Thesis: Urvashi D. Heramun (2026) "Advances in Double Quantum and Singlet Nuclear Magnetic Resonance", University of Southampton, Faculty of Engineering and Physical Sciences, School of Chemistry and Chemical Engineering, PhD Thesis. DOI: https://doi.org/10.5258/SOTON/01/T061.

UNIVERSITY OF SOUTHAMPTON

Faculty of Engineering and Physical Sciences

School of Chemistry and Chemical Engineering

Advances in Double Quantum and Singlet Nuclear Magnetic Resonance

by

Urvashi Devi Heramun

ORCiD: 0009-0007-7524-6098

A thesis submitted for the degree of
Doctor of Philosophy

May 2026

University of Southampton

Abstract

Faculty of Engineering and Physical Sciences
School of Chemistry and Chemical Engineering

Doctor of Philosophy

Advances in Double Quantum and Singlet Nuclear Magnetic Resonance

by Urvashi Devi Heramun

This thesis explores the experimental application of two pulse sequence families that effectively excite double-quantum coherence in near-equivalent spin-1/2 pairs in solution nuclear magnetic resonance. The established methods are inefficient in this coupling regime, leading to substantial relaxation losses.

The first procedure, GeoDQ, uses the geometric Aharonov-Anandan phase, exploiting a rotation through π about the z-axis in the zero-quantum subspace spanned by the $\{|S_0\rangle, |T_0\rangle\}$ states. We combine double-quantum filtering and singlet order excitation to study the $^{13}C_2$ relaxation of singlet order within a previously inaccessible molecule. This decays slower than longitudinal order, since it is protected against common relaxation mechanisms.

We report pH-dependent isotope shifts due to ^{18}O and ^{13}C isotopic substitution. Furthermore, we use GeoDQ to investigate chiral guest binding as a symmetry-breaking mechanism between two diastereotopic $^{19}F_2$ nuclei.

The second procedure, Spinor-DQ, uses the spinor behaviour of two-level quantum systems, exploiting a rotation through 2π in the single-quantum subspace spanned by the $\{|S_0\rangle, |T_{+1}\rangle\}$ states. These are the SLIC, and PulsePol pulse sequences originally used to excite singlet order, including a SLIC variant that is well-compensated against deviations in the rf field amplitude.

We apply the GeoDQ and Spinor-DQ sequences to study $^{13}C_2$ and $^{19}F_2$ near-equivalent spin-pairs, achieving good double-quantum filtering efficiency.

Contents

Declaration of Authorship

I declare that this thesis and the work presented in it is my own and has been generated by me as the result of my own original research.

I confirm that:

1. This work was done wholly or mainly while in candidature for a research degree at this University;
2. Where any part of this thesis has previously been submitted for a degree or any other qualification at this University or any other institution, this has been clearly stated;
3. Where I have consulted the published work of others, this is always clearly attributed;
4. Where I have quoted from the work of others, the source is always given. With the exception of such quotations, this thesis is entirely my own work;
5. I have acknowledged all main sources of help;
6. Where the thesis is based on work done by myself jointly with others, I have made clear exactly what was done by others and what I have contributed myself;
7. Parts of this work have been published as:

   U. D. Heramun, M. Sabba, C. Bengs, G. A. I. Moustafa, and M. H. Levitt, *The Journal of Chemical Physics*, 2025, **163**, 074201. [1]

   U. D. Heramun, M. Sabba, D. Yamano, C. Bengs, B. Legrady, G. Pileio, S. Thompson, and M. H. Levitt, *The Journal of Chemical Physics*, 2026, **164**, 064201. [2]

Signed: .... Date: ....

Acknowledgements

I could not have completed this research project without the unwavering support of my supervisor, Malcolm Levitt. Thank you for your enthusiasm, patience, and involvement in all the projects we worked on over the past four years. I had a lot of fun doing some great science, and learnt a lot from you.

I had the privilege of working with Mohamed Sabba, to whom I owe a lot. I benefited immensely from his theoretical and experimental NMR expertise, wise life advice, and from his extensive knowledge of *SpinDynamica*.

In addition, I would like to thank George Bacanu, who first taught me the basic theoretical principles of NMR, and with whom I set up my very first NMR experiment as an undergraduate student.

For their advice and help with NMR theory and experiments, I thank Laurynas Dagys, Christian Bengs, Bonifac Legrady, James Whipham, and Marek Plata, who were always available to answer my questions, and help me troubleshoot the many problems that can arise during an experiment.

I wish to thank Gamal Moustafa, Dolnapa Yamano, and Sam Thompson for their skill in organic synthesis, and assistance in preparing samples. I am very grateful for the unique insight and suggestions.

For their encouragement and advice, I thank Giuseppe Pileio, Marina Carravetta, Marcel Utz, Michael Tayler, Kirill Sheberstov, and James Eills.

I would like to thank Oksana Bondar, Geoffrey Hyett, Harry Harbor-Collins, Thomas Robertson, and Anupama Acharya, for the many light-hearted conversations we had in the office, and general good humour.

Lastly, I would like to thank my family for always believing in me, and for their endless support and patience as I climbed this mountain.

List of Abbreviations

CSA Chemical Shift Anisotropy.

CW Continuous Wave.

DD Dipole-Dipole.

DQ Double-Quantum.

DQ2S Double-Quantum-to-Singlet.

DQC(s) Double-Quantum Coherence(s).

DQF Double-Quantum Filtering.

DQP Double-Quantum Precursor.

GeoDQ Geometric Double-Quantum.

INADEQUATE Incredible Natural Abundance DoublE QUAntum Transfer Experiment.

IST Inner Singlet-Triplet.

LLS Long-Lived States.

LO Longitudinal Order.

M2S Magnetisation-to-Singlet.

NMR Nuclear Magnetic Resonance.

OST Outer Singlet-Triplet.

ppb parts-per-billion.

ppm parts-per-million.

rf radio-frequency.

S2DQ Singlet-to-Double-Quantum.

S2M Singlet-to-Magnetisation.

SLIC Spin-Lock Induced Crossing.

SO Singlet Order.

SOD Singlet Order Destruction.

SQC(s) Single-Quantum Coherence(s).

SR Spin-Rotation.

ZQ Zero-Quantum.

I have not yet lost a feeling of wonder, and of delight, that this delicate motion should reside in all the ordinary things around us, revealing itself only to him who looks for it. I remember, in the winter of our first experiments, just seven years ago, looking on snow with new eyes. There the snow lay around my doorstep - great heaps of protons quietly precessing in the earth's magnetic field. To see the world for a moment as something rich and strange is the private reward of many a discovery.

Edward M. Purcell
Nobel Lecture, 11th December 1952

Chapter 1

Nuclear Magnetic Resonance

The phenomenon of nuclear magnetic resonance (NMR) was first detected by Rabi[3] and colleagues in 1938, though Gorter[4] had almost discovered this effect one year prior. In 1946, independent demonstrations of NMR in condensed matter were contemporarily made by Bloch[5], and Purcell[6].

NMR spectroscopy exploits the magnetic properties of nuclei to obtain valuable information regarding the structure and dynamics of the molecules being studied. The proton (^{1}H), deuterium (^{2}H), carbon (^{13}C), nitrogen (^{15}N), fluorine (^{19}F), and phosphorus (^{31}P) nuclei may all be studied using NMR. Since these nuclei can all be found, or introduced relatively easily into biologically relevant systems, NMR is widely used in the pharmaceutical industry in the context of ligand and protein-based screening methods[7].

The most widely known application of NMR is, however, magnetic resonance imaging[8–10] (MRI), where the spatial distribution of nuclei can be mapped out using magnetic field gradients. This non-invasive technique is used to create detailed images of soft tissues and organs, which revolutionised medical diagnostics. The technique can also be applied to study lithium-ion batteries[11], and has found use in the oil and gas industry[12].

In this chapter, some foundational concepts of NMR are introduced. The Levitt[13], Freeman[14], Keeler[15], and Kowalewski[16] seminal textbooks were consulted to provide a basic overview of the mechanics underpinning NMR.

1.1 Introduction

In quantum mechanics, mathematical operators represent physical observables[17]. In some cases, operators are applied to a function, and the outcome is the same function, multiplied by a numerical factor. This type of equation is an *eigenquation*, where the function is an *eigenfunction* of the operator, and the numerical factor is an *eigenvalue*. Quantum mechanical operators, denoted by $\hat{Q}$, are hermitian: $\hat{Q} = \hat{Q}^{\dagger}$, where † indicates the adjoint/conjugate transpose. Consequently, these operators have *real* eigenvalues.

Position, momentum, and energy are all examples of observables. The quantum mechanical operator that corresponds to the total energy of the system is given by the *Hamiltonian*, denoted by $\hat{H}$. Electronic motion and nuclear motion occur on different timescales. In NMR, it is possible to simplify[13] the overall Hamiltonian, by removing terms that do not depend from the direction of the nuclear spin polarisations.

The time-dependent Schrödinger equation is written as follows[18]:

$$\frac{\mathrm{d}}{\mathrm{d}t} \left|\psi\left(t\right)\right\rangle = -i\hat{H} \left|\psi\left(t\right)\right\rangle, \tag{1.1}$$

in angular frequency units, therefore $\hbar$ does not appear. The spin state of the nuclei $\left|\psi\left(t\right)\right\rangle$ can be expressed as the following linear combination:

$$\left|\psi\left(t\right)\right\rangle = \sum_{i}^{n} c_i(t) \left|i\right\rangle, \tag{1.2}$$

where $c_i(t)$ is the time-dependent coefficient, and n is the dimension of this space, called Hilbert space, $\mathcal{H}$. The evolution of a state in time is given by:

$$\left|\psi\left(t\right)\right\rangle = \hat{U}(t) \left|\psi\left(0\right)\right\rangle, \tag{1.3}$$

where $\hat{U}(t)$ is the propagator, which is unitary, $\hat{U}^{\dagger} = \hat{U}^{-1}$, and is given by:

$$\hat{U}(t) = \exp\left\{-i\hat{H}t\right\}. \tag{1.4}$$

1.2 Nuclear Spin

Spin is a form of angular momentum that does not arise from the rotation of a particle, but is an intrinsic property of the particle itself, much like mass, electric charge, and magnetism. The nuclear dipole magnetic moment $\hat{\boldsymbol{\mu}}$, and the nuclear spin angular momentum $\hat{\boldsymbol{I}}$ operators are related to each other. The equation is given as follows:

$$\hat{\boldsymbol{\mu}} = \gamma \hat{\boldsymbol{I}}, \tag{1.5}$$

where γ is the magnetogyric ratio of the nucleus, specified in units of rad s^{-1} T^{-1}.

Most atomic nuclei have $\gamma > 0$, meaning that the magnetic moment and the angular momentum have the same direction. The nuclear spin quantum number I represents the total angular momentum of an atomic nucleus, which can be obtained by combining the spins of its nucleons. An odd number of nucleons leads to nuclei $I > 0$, which are detectable by NMR spectroscopy.

However, many isotopes that are present in high natural abundance in nature, such as ^{12}C, and ^{16}O, have nuclear spin $I = 0$. Such spins are denominated NMR *silent*/non-magnetic, since they do not possess a magnetic moment. One of the most important nuclei used in NMR spectroscopy is the proton, ^{1}H, which has nuclear spin $I = \frac{1}{2}$. Protons, electrons, and neutrons are elementary particles with spin $S = \frac{1}{2}$, and are *fermions*. Photons have spin $S = 1$, and are *bosons*. Figure 1.1 depicts the concept of nuclear spin.

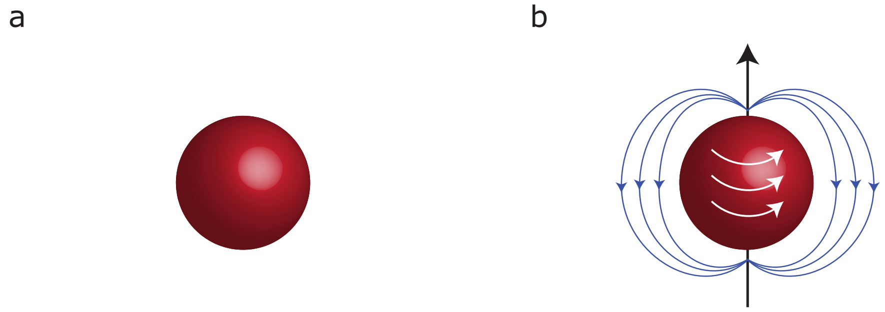

Figure 1.1: Visualisation of the spin angular momentum properties. (**a**) A nucleus with $I = 0$ does not have a magnetic moment. (**b**) A nucleus with $I = \frac{1}{2}$ has a magnetic moment, and generates a magnetic field around itself.

1.3 Larmor Precession

Each spin $I > 0$ is associated with a tiny magnetic moment. The magnetic moment, summed over all the spins present in the sample, is given by the macroscopic[14] magnetisation vector $\boldsymbol{M}$, which has the following x, y, and z-components: $\{M_x, M_y, M_z\}$.

In the absence of an external magnetic field, the direction of each spin angular momentum present in a sample containing nuclei with $I > 0$ is evenly distributed in space/isotropic. In the presence of an external magnetic field $\boldsymbol{B}$, a degree of polarisation is acquired, and the vector $\boldsymbol{M}$ becomes aligned to the direction of the magnetic field.

The interaction between the nuclear magnetic dipole moment $\boldsymbol{\mu}$, with the external field $\boldsymbol{B}$, imposes a torque $\hat{\boldsymbol{\tau}} = \hat{\boldsymbol{\mu}} \times \boldsymbol{B} = \gamma \hat{\boldsymbol{I}} \times \boldsymbol{B}$ on the magnetic moment. As a result, the vector $\boldsymbol{M}$ starts *precessing* in a conical trajectory around the direction of the magnetic field, keeping a constant angle with it.

In practice, the z-axis of this *laboratory frame* is chosen to be aligned with the magnetic field. The z-component of the external field $\boldsymbol{B}$ is denoted B^0. The frequency of precession of the bulk magnetisation vector is given by the following equation:

$$\omega^0 = -\gamma B^0, \tag{1.6}$$

where ω^0 is the Larmor frequency. For $\gamma > 0$, the direction of the precession is clockwise, and therefore negative. Figure 1.2 illustrates this concept.

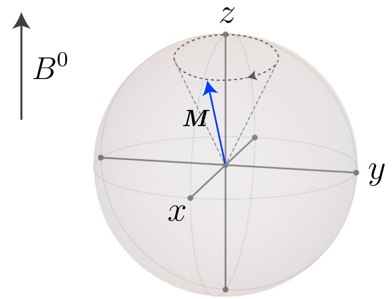

Figure 1.2: Larmor precession of a $\gamma > 0$ nucleus. The macroscopic magnetisation vector $\boldsymbol{M}$ precesses in a clockwise direction around the magnetic field applied along the z-axis, B^0, at the Larmor frequency, ω^0.

1.4 Boltzmann Distribution

For a single spin-$1/2$ nucleus, the number of degenerate states is equal to $2I + 1 = 2$, in the absence of a magnetic field. The degeneracy of the states is lifted once the magnetic field B^0 is applied, and the energy levels become separated by $\Delta E = \hbar\omega^0$. The splitting of the energy levels, and the quantisation of energy in the presence of a magnetic field is named Zeeman effect. If the system is irradiated using electromagnetic radiation that matches ΔE, the *resonance* condition has been met, inducing an energy transition. In NMR, this is induced by a radiofrequency (rf) field, denoted B^1.

The Boltzmann equation governs the population distribution:

$$\frac{N_\beta}{N_\alpha} = \exp\left(-\frac{\Delta E}{k_B T}\right) = \exp\left(-\frac{\gamma\hbar B^0}{k_B T}\right), \tag{1.7}$$

where N_β and N_α are the populations within the upper and lower energy level, respectively, k_B is the Boltzmann constant, and T the temperature. At room temperature, the lower energy state $|\alpha\rangle$ is slightly more populated than the upper energy state $|\beta\rangle$. The population difference between the two states gives rise to net magnetisation along the z-axis, where $M_z \propto (N_\alpha - N_\beta)$.

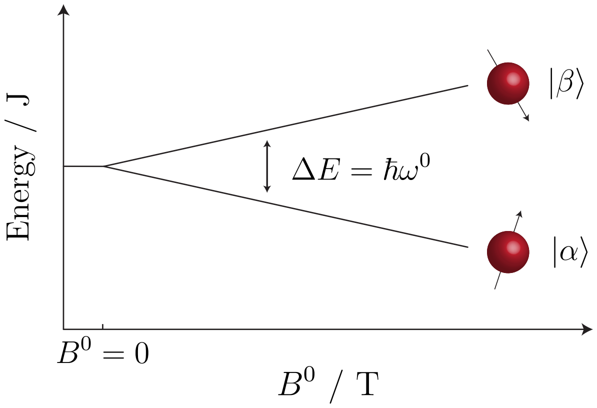

Figure 1.3: The Zeeman effect for a single spin-$1/2$ system as a function of the external magnetic field B^0.

1.5 Spin Angular Momentum Operators

Within a system of isolated spin-1/2 nuclei, the x, y, and z-components of the nuclear spin angular momentum operator $\hat{\boldsymbol{I}}$ are represented by their respective Cartesian angular momentum operators $\hat{I}_x$, $\hat{I}_y$, and $\hat{I}_z$. They are related by the following commutation relations:

$$[\hat{I}_x, \hat{I}_y] = i\hat{I}_z \qquad [\hat{I}_y, \hat{I}_z] = i\hat{I}_x \qquad [\hat{I}_z, \hat{I}_x] = i\hat{I}_y \tag{1.8}$$

The total spin angular momentum $\hat{\boldsymbol{I}}^2$ is equal to the following:

$$\hat{\boldsymbol{I}}^2 = \hat{I}_x^2 + \hat{I}_y^2 + \hat{I}_z^2, \tag{1.9}$$

and:

$$\hat{\boldsymbol{I}}^2 \hat{I}_z = \hat{I}_z \hat{\boldsymbol{I}}^2, \tag{1.10}$$

which means that the two operators commute. As a consequence, they share the same eigenfunctions $|I, m\rangle$. The following eigenequation applies for $\hat{\boldsymbol{I}}^2$:

$$\hat{\boldsymbol{I}}^2 |I, m\rangle = I(I+1) |I, m\rangle \,. \tag{1.11}$$

The following eigenequation applies for $\hat{I}_z$:

$$\hat{I}_z |I, m\rangle = m |I, m\rangle \,, \tag{1.12}$$

where m is the magnetic spin quantum number, and $m = \{-I, -I{+}1, ..., +I\}$. This is associated with the projection of $\hat{\boldsymbol{I}}$, along a specific axis.

The Zeeman eigenstates are given in the following $|I, m\rangle$ notation:

$$|\alpha\rangle = \left|\frac{1}{2}, \frac{1}{2}\right\rangle \qquad |\beta\rangle = \left|\frac{1}{2}, -\frac{1}{2}\right\rangle \tag{1.13}$$

The following eigenequations are obeyed:

$$\hat{I}_z |\alpha\rangle = +\frac{1}{2} |\alpha\rangle \qquad \hat{I}_z |\beta\rangle = -\frac{1}{2} |\beta\rangle \,. \tag{1.14}$$

A spin that is in the state $|\alpha\rangle$ is said to be polarised along the z-axis, i.e. “spin up”, while a spin that is in the state $|\beta\rangle$ is said to be polarised along the $-z$-axis, i.e. “spin down”. The Hilbert space, $\mathcal{H}$, spanned by the two states has a dimension of 2^N, where N is the number of spins.

The matrix representations of the three angular momentum operators in the Zeeman eigenbasis $\{|\alpha\rangle, |\beta\rangle\}$ are given in the following:

$$\hat{I}_x = \frac{1}{2}\begin{pmatrix} 0 & 1 \\ 1 & 0 \end{pmatrix} \qquad \hat{I}_y = \frac{1}{2}\begin{pmatrix} 0 & i \\ -i & 0 \end{pmatrix} \qquad \hat{I}_z = \frac{1}{2}\begin{pmatrix} 1 & 0 \\ 0 & -1 \end{pmatrix} \tag{1.15}$$

where each matrix is a Pauli spin matrix, σ_x, σ_y, and σ_z, respectively. The unity operator $\hat{\mathbb{1}}$ is given by the following:

$$\frac{1}{2}\hat{\mathbb{1}} = \frac{1}{2}\begin{pmatrix} 1 & 0 \\ 0 & 1 \end{pmatrix}. \tag{1.16}$$

The raising ($\hat{I}^+$) operator increases the quantum number m in steps of 1, whereas the lowering ($\hat{I}^-$) operator decreases m in steps of 1:

$$\hat{I}^+ = \hat{I}_x + i\hat{I}_y \qquad \hat{I}^- = \hat{I}_x - i\hat{I}_y \tag{1.17}$$

where:

$$\begin{aligned} \hat{I}^+ |\alpha\rangle &= 0, \\ \hat{I}^- |\alpha\rangle &= |\beta\rangle, \\ \hat{I}^+ |\beta\rangle &= |\alpha\rangle, \\ \hat{I}^- |\beta\rangle &= 0. \end{aligned} \tag{1.18}$$

The operators have the following matrix representations:

$$\hat{I}^+ = \begin{pmatrix} 0 & 1 \\ 0 & 0 \end{pmatrix} \qquad \hat{I}^- = \begin{pmatrix} 0 & 0 \\ 1 & 0 \end{pmatrix} \tag{1.19}$$

The operators $\hat{I}_x$ and $\hat{I}_y$ are related to the shift operators, as follows:

$$\hat{I}_x = \frac{1}{2}(\hat{I}^+ + \hat{I}^-) \qquad \hat{I}_y = \frac{1}{2i}(\hat{I}^+ - \hat{I}^-) \tag{1.20}$$

It is convenient to define the projection operators, $\hat{I}^{\alpha}$, and $\hat{I}^{\beta}$ as well:

$$\hat{I}^{\alpha} = \frac{1}{2}\hat{\mathbb{1}} + \hat{I}_z \qquad \hat{I}^{\beta} = \frac{1}{2}\hat{\mathbb{1}} - \hat{I}_z \tag{1.21}$$

The operators have the following matrix representations:

$$\hat{I}^{\alpha} = \begin{pmatrix} 1 & 0 \\ 0 & 0 \end{pmatrix} \qquad \hat{I}^{\beta} = \begin{pmatrix} 0 & 0 \\ 0 & 1 \end{pmatrix} \tag{1.22}$$

where:

$$\begin{aligned} \hat{I}^{\alpha} \left|\alpha\right\rangle &= \left|\alpha\right\rangle, \\ \hat{I}^{\beta} \left|\alpha\right\rangle &= 0, \\ \hat{I}^{\alpha} \left|\beta\right\rangle &= 0, \\ \hat{I}^{\beta} \left|\beta\right\rangle &= \left|\beta\right\rangle. \end{aligned} \tag{1.23}$$

The operators $\hat{I}_x$, $\hat{I}_y$, $\hat{I}_z$, and half the unity operator $\hat{\mathbb{1}}$, are related to the shift and polarisation operators, as follows:

$$\begin{aligned} \hat{I}_x &= \frac{1}{2}(\hat{I}^{+} + \hat{I}^{-}) = \frac{1}{2}(\left|\alpha\right\rangle\left\langle\beta\right| + \left|\beta\right\rangle\left\langle\alpha\right|) \\ \hat{I}_y &= \frac{1}{2i}(\hat{I}^{+} - \hat{I}^{-}) = \frac{1}{2i}(\left|\alpha\right\rangle\left\langle\beta\right| - \left|\beta\right\rangle\left\langle\alpha\right|) \\ \hat{I}_z &= \frac{1}{2}(\hat{I}^{\alpha} - \hat{I}^{\beta}) = \frac{1}{2}(\left|\alpha\right\rangle\left\langle\alpha\right| - \left|\beta\right\rangle\left\langle\beta\right|) \\ \frac{1}{2}\hat{\mathbb{1}} &= \frac{1}{2}(\hat{I}^{\alpha} + \hat{I}^{\beta}) = \frac{1}{2}(\left|\alpha\right\rangle\left\langle\alpha\right| + \left|\beta\right\rangle\left\langle\beta\right|). \end{aligned} \tag{1.24}$$

Generally, the spin-1/2 particle exists in a superposition of the two energy eigenstates, of the following form:

$$\left|\psi\right\rangle = c_{\alpha}\left|\alpha\right\rangle + c_{\beta}\left|\beta\right\rangle, \tag{1.25}$$

where c_{α} and c_{β} are the complex superposition coefficients. Note that the following normalisation condition must apply:

$$|c_{\alpha}|^2 + |c_{\beta}|^2 = 1. \tag{1.26}$$

The state $|\psi\rangle$ may be written as the following vector:

$$|\psi\rangle = \begin{pmatrix} c_\alpha \\ c_\beta \end{pmatrix}. \tag{1.27}$$

Consequently, the Zeeman eigenstates can be written in the following form:

$$|\alpha\rangle = \begin{pmatrix} 1 \\ 0 \end{pmatrix} \qquad |\beta\rangle = \begin{pmatrix} 0 \\ 1 \end{pmatrix}. \tag{1.28}$$

The state $|\psi\rangle$ of a pair of coupled spins-1/2 is described by the following:

$$|\psi\rangle = c_{\alpha\alpha}\,|\alpha\alpha\rangle + c_{\alpha\beta}\,|\alpha\beta\rangle + c_{\beta\alpha}\,|\beta\alpha\rangle + c_{\beta\beta}\,|\beta\beta\rangle\,, \tag{1.29}$$

where $|\alpha\alpha\rangle$, $|\alpha\beta\rangle$, $|\beta\alpha\rangle$, and $|\beta\beta\rangle$ are the four Zeeman product states, since the Hilbert space has now a dimension of $2^2 = 4$.

In the case of the $|\alpha\beta\rangle$ notation, α means that the z-angular momentum of the spin I_1 has a value of $\frac{1}{2}$, whereas β indicates a value of $-\frac{1}{2}$ of the same quantity in the case of the spin I_2. The complex coefficients $c_{\alpha\alpha}$, $c_{\alpha\beta}$, $c_{\beta\alpha}$, and $c_{\beta\beta}$ are normalised, as follows:

$$|c_{\alpha\alpha}|^2 + |c_{\alpha\beta}|^2 + |c_{\beta\alpha}|^2 + |c_{\beta\beta}|^2 = 1. \tag{1.30}$$

The total angular momentum operators are given by the following:

$$\hat{I}_x = \hat{I}_{1x} + \hat{I}_{2x} \qquad \hat{I}_y = \hat{I}_{1y} + \hat{I}_{2y} \qquad \hat{I}_z = \hat{I}_{1z} + \hat{I}_{2z} \tag{1.31}$$

The matrix representation of the $\hat{I}_{1z}$ operator is given by the Kronecker product of the matrices of the single-spin z-angular momentum operator, and the unity operator, as follows:

$$\hat{I}_{1z} = \hat{I}_z \otimes \hat{\mathbb{1}} = \frac{1}{2}\begin{pmatrix} +1 & 0 & 0 & 0 \\ 0 & +1 & 0 & 0 \\ 0 & 0 & -1 & 0 \\ 0 & 0 & 0 & -1 \end{pmatrix}, \tag{1.32}$$

where the following convention[19] was used:

$$\begin{pmatrix} a & b \\ c & d \end{pmatrix} \otimes \begin{pmatrix} \alpha & \beta \\ \gamma & \delta \end{pmatrix} = \begin{pmatrix} a\begin{pmatrix} \alpha & \beta \\ \gamma & \delta \end{pmatrix} & b\begin{pmatrix} \alpha & \beta \\ \gamma & \delta \end{pmatrix} \\ c\begin{pmatrix} \alpha & \beta \\ \gamma & \delta \end{pmatrix} & d\begin{pmatrix} \alpha & \beta \\ \gamma & \delta \end{pmatrix} \end{pmatrix} = \begin{pmatrix} a\alpha & a\beta & b\alpha & b\beta \\ a\gamma & a\delta & b\gamma & b\delta \\ c\alpha & c\beta & d\alpha & d\beta \\ c\gamma & c\delta & d\gamma & d\delta \end{pmatrix}. \tag{1.33}$$

In NMR, a pulse sequence consists of a series of rf pulses and delays that are designed to manipulate the nuclear spins to give a desired experimental outcome. When dealing with multiple spins, it is helpful to use Cartesian product operators[15,20] to describe the quantum states during the experiment, as shown in Table 1.1 for a two spin-1/2 system. The multiple-quantum coherence terms are not observable during acquisition.

Table 1.1: Cartesian product operators for a two spin-1/2 system.

Operator	**Description**
$\frac{1}{2}\hat{\mathbb{1}}$	unity operator
$\hat{I}_{1z}$	z-magnetisation on I_1
$\hat{I}_{1x}$, $\hat{I}_{1y}$	x and y-in-phase magnetisation on I_1
$2\hat{I}_{1x}\hat{I}_{2z}$, $2\hat{I}_{1y}\hat{I}_{2z}$	x and y-antiphase magnetisation on I_1
$\hat{I}_{2z}$	z-magnetisation on I_2
$\hat{I}_{2x}$, $\hat{I}_{2y}$	x and y-in-phase magnetisation on I_2
$2\hat{I}_{1z}\hat{I}_{2x}$, $2\hat{I}_{1z}\hat{I}_{2y}$	x and y-antiphase magnetisation on I_2
$2\hat{I}_{1z}\hat{I}_{2z}$	longitudinal zz-order
$2\hat{I}_{1x}\hat{I}_{2x}$, $2\hat{I}_{1y}\hat{I}_{2y}$, $2\hat{I}_{1x}\hat{I}_{2y}$, $2\hat{I}_{1y}\hat{I}_{2x}$	multiple-quantum coherence

1.6 Spin Density Operator

The quantum state of the system can be described as a statistical ensemble[21] of spin systems by the density matrix operator $\hat{\rho}$, defined as follows:

$$\hat{\rho} = \overline{|\psi\rangle \langle\psi|}, \tag{1.34}$$

where the overbar indicates the ensemble *average*, and $|\psi\rangle$ is the quantum state of one individual spin system. The average contribution of each ensemble member to the observable is defined by the expectation value. For an operator $\hat{Q}$, this is given by the following:

$$\left\langle \hat{Q} \right\rangle = \mathrm{Tr}\{\hat{\rho}\hat{Q}\}. \tag{1.35}$$

The matrix representation of the density operator can be obtained by calculating the matrix elements $\rho_{\alpha\beta} = \langle\alpha| \hat{\rho} |\beta\rangle$, for the $|\alpha\rangle$ and $|\beta\rangle$ basis states. The matrix representation of the density operator for these two states is given as follows, for a single spin-1/2:

$$\begin{aligned} \hat{\rho}_\alpha &= \overline{|\alpha\rangle \langle\alpha|} = \begin{pmatrix} 1 \\ 0 \end{pmatrix} \otimes \begin{pmatrix} 1 & 0 \end{pmatrix} = \begin{pmatrix} 1 & 0 \\ 0 & 0 \end{pmatrix}, \\ \hat{\rho}_\beta &= \overline{|\beta\rangle \langle\beta|} = \begin{pmatrix} 0 \\ 1 \end{pmatrix} \otimes \begin{pmatrix} 0 & 1 \end{pmatrix} = \begin{pmatrix} 0 & 0 \\ 0 & 1 \end{pmatrix}. \end{aligned} \tag{1.36}$$

For an ensemble of single spin-1/2 nuclei, the matrix representation of the density matrix in Hilbert space takes the following form:

$$\hat{\rho} = \begin{pmatrix} \rho_{\alpha\alpha} & \rho_{\alpha\beta} \\ \rho_{\beta\alpha} & \rho_{\beta\beta} \end{pmatrix}, \tag{1.37}$$

where the diagonal elements of the density matrix $\rho_{\alpha\alpha}$ and $\rho_{\beta\beta}$ represent the *populations* of the states $|\alpha\rangle$ and $|\beta\rangle$, respectively. On the other hand, the off-diagonal elements of the density matrix $\rho_{\alpha\beta}$ and $\rho_{\beta\alpha}$ are the *coherences* between the $|\alpha\rangle$ and $|\beta\rangle$ states.

The thermal equilibrium density matrix for isolated spins-1/2 is given by, approximately:

$$\hat{\rho}^{eq} \approx \begin{pmatrix} \frac{1}{2} + \frac{1}{4}\mathbb{B} & 0 \\ 0 & \frac{1}{2} - \frac{1}{4}\mathbb{B} \end{pmatrix}, \tag{1.38}$$

where the Boltzmann factor is given by the compact notation $\mathbb{B} = \frac{\hbar\gamma B^0}{k_\mathrm{B}T}$. This corresponds to:

$$\hat{\rho}^{eq} = \frac{1}{2}\hat{\mathbb{1}} + \frac{1}{2}\mathbb{B}\hat{I}_z, \tag{1.39}$$

which is the *thermal equilibrium density operator* that is the starting point of most NMR experiments and simulations.

A quantum system evolves in time according to the time-dependent Schrödinger equation (Equation 1.1). The evolution of the density matrix is given by the Liouville von Neumann equation of motion, as follows:

$$\frac{d}{dt}\hat{\rho}(t) = -i[\hat{H}(t), \hat{\rho}(t)], \tag{1.40}$$

which has the following solution:

$$\hat{\rho}(t) = \hat{U}(t)\hat{\rho}^0\hat{U}^{-1}(t), \tag{1.41}$$

where $\hat{\rho}^0$ is the density matrix at $t = 0$, and U is the propagator (Equation 1.4).

The Liouville von Neumann equation in Liouville space takes the following form:

$$i\hbar\frac{\partial}{\partial t}\left|\rho\left(t\right)\right\rangle = \hat{\mathcal{L}}\left|\rho\left(t\right)\right\rangle, \tag{1.42}$$

where $\hat{\mathcal{L}}$ is the commutator with the Hamiltonian $\hat{\mathcal{L}} = [H, \bullet]$, known as the Liouvillian superoperator. In Liouville space, which has a dimension of $2^{(2N)}$ N-spins, superoperators[22] are able to transform operators into other operators. In Hilbert space, the dimension is given by 2^N N-spins, and operators transform vectors into other vectors.

In the absence of a radiofrequency field being applied, the populations reach thermal equilibrium, and the coherences progressively decay to zero.

1.7 The NMR Signal

The precessing transverse magnetisation generated after the application of a radiofrequency pulse induces a current in the coil that is arranged perpendicularly to the static magnetic field B^0. This oscillating electric current is the NMR signal, or Free Induction Decay (FID). For easier analysis, this time-domain signal is converted into a frequency-domain signal by Fourier Transformation (FT).

The Fourier transform of the FID signal generates the familiar absorption Lorentzian that is characteristic of NMR spectra:

$$S(\omega) = \frac{\lambda}{\lambda^2 + (\omega - \omega^0)^2}, \tag{1.43}$$

where λ is the coherence decay rate constant, and is given by:

$$\lambda = \frac{1}{T_2}. \tag{1.44}$$

The intensity of the peak is maximised when the frequency parameter is equal to the Larmor frequency. In addition, the full-width at half-height of a peak contains information regarding the T_2 relaxation time constant, as shown in Figure 1.4.

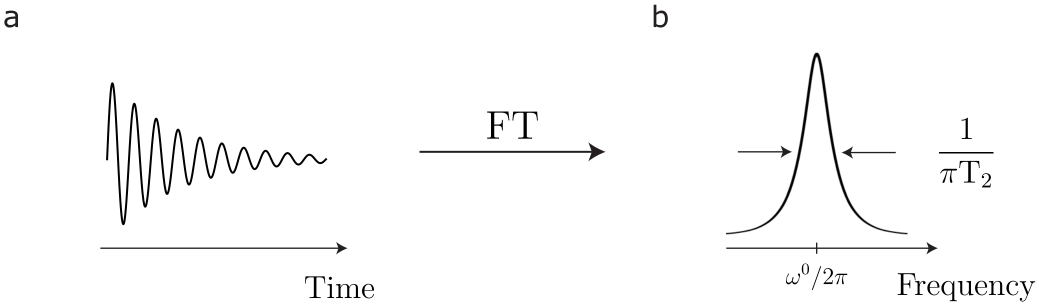

Figure 1.4: Fourier transform of the FID, into the characteristic NMR absorption Lorentzian peak.

1.8 Relaxation

Relaxation governs the return of a spin system to thermal equilibrium, which is described by the T_1, and T_2 relaxation time constants. The longitudinal relaxation time T_1 governs the return to equilibrium of the component of the magnetisation vector that is aligned along the direction of the static magnetic field B^0, usually the longitudinal magnetisation.

The energy levels of a homonuclear two spin-1/2 system of the AX type (see Figure 1.8) are arranged as illustrated in Figure 1.5. Relaxation processes are governed by the T_1 time constant.

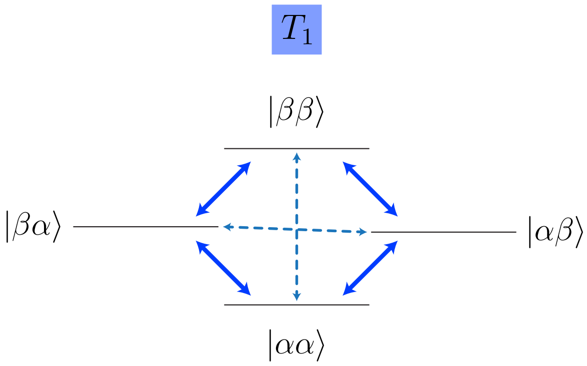

Figure 1.5: Energy levels of a homonuclear two spin-1/2 system with $\gamma > 0$, in the case of strong magnetic inequivalence (AX type). The forbidden zero and double-quantum transitions are indicated by the dashed lines.

The transverse relaxation time T_2 governs the rate at which the transverse magnetisation components decay to zero, and lose phase coherence. In addition, T_2 determines the width of the NMR resonance line, as seen in Figure 1.4. Generally, $T_1 \geq T_2$.

The evolution of the magnetisation vector is given by the Bloch equations[5,18,23], given as following:

$$\dot{\boldsymbol{M}}(t) = \gamma \boldsymbol{M}(t) \times \boldsymbol{B}(t) - \frac{M_x}{T_2}\hat{\boldsymbol{\imath}} - \frac{M_y}{T_2}\hat{\boldsymbol{\jmath}} - \frac{M_z - M_0}{T_1}\hat{\boldsymbol{k}}, \tag{1.45}$$

where M_0 denotes the thermal equilibrium z-magnetisation.

1.8.1 Spin-Lattice Relaxation Time

The solution of the Bloch equations involving the longitudinal magnetisation component is given in the following:

$$M_z(t) = M_z^{eq} + (M_z(0) - M_z^{eq}) \exp\{-t/T_1\}. \tag{1.46}$$

The inversion recovery pulse sequence allows the determination of the T_1 relaxation time, as follows:

$$(\pi)_x - \tau - (\pi/2)_x, \tag{1.47}$$

where the delay τ is varied incrementally. Starting from thermal equilibrium conditions, a π pulse is applied. After the magnetisation is inverted, this is allowed to recover for a time τ, after which a $\pi/2$ pulse, of the same phase, is applied. The integral of each peak is plotted along a time-axis, after which the T_1 time is extracted by linear least squares fitting. A typical experiment is shown in Figure 1.6.

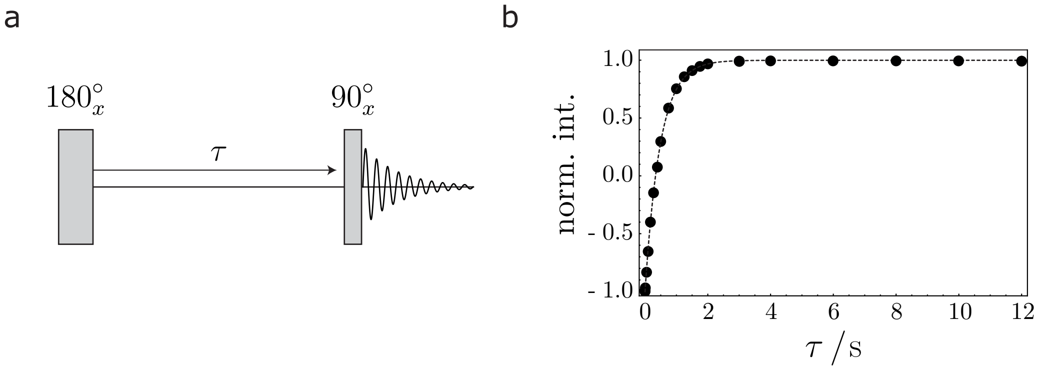

Figure 1.6: (**a**) The inversion recovery pulse sequence. (**b**) A typical inversion recovery experiment. The data points were simulated to obtain $T_1 \approx 0.48$ s.

1.8.2 Spin-Spin Relaxation Time

The solutions of the Bloch equations involving the transverse magnetisation components are given in the following:

$$\begin{aligned} M_x(t) &= M_x(0) \exp\{-t/T_2\}, \\ M_y(t) &= M_y(0) \exp\{-t/T_2\}. \end{aligned} \tag{1.48}$$

To measure the T_2 relaxation time, the Hahn spin echo[24] method was first used. The pulse sequence is as follows:

$$(\pi/2)_y - \tau - (\pi)_y - \tau. \tag{1.49}$$

However, this method is prone to artefacts arising from diffusion due to the spins experiencing inhomogeneities in the magnetic field, leading to imperfect refocusing of the magnetisation, and a shorter T_2 than the true value. To reduce the error arising from diffusion, Carr and Purcell[25] proposed the following scheme:

$$(\pi/2)_y - [\tau/2 - (\pi)_y - \tau/2]_n, \tag{1.50}$$

where n is the repetition number. In this experiment, the n parameter is incrementally varied. The amplitude of the successive echoes decays exponentially with the T_2 time constant. A significant drawback of this method, however, is that deviations in the amplitude of the rf field of the π-pulses leads to the accumulation of errors over the course of the echo train being applied, because the successive echoes rotate the polarisation vectors further away from the xy-plane.

A modification of this method was proposed by Meiboom and Gill[26], as follows:

$$(\pi/2)_y - [\tau/2 - (\pi)_x - \tau/2]_n. \tag{1.51}$$

A simple phase shift by $\pi/2$ of the π-pulse. During the sequence, the amplitude of the echoes decreases with the T_2 relaxation time. A typical T_2 spin echo decay experiment is shown in Figure 1.7.

The Carr-Purcell-Meiboom-Gill (CPMG) spin echo[25,26] is one of the most

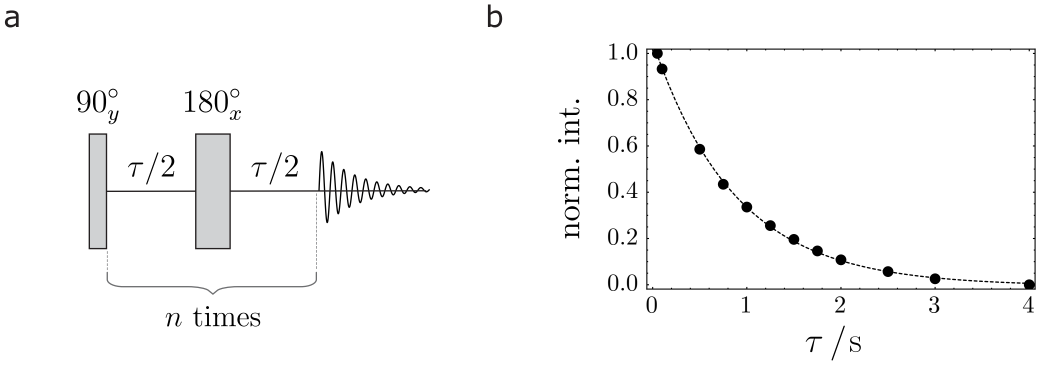

Figure 1.7: (**a**) CPMG spin echo decay sequence for the determination of the T_2 relaxation time constant. (**b**) A typical spin echo decay experiment. The data points were simulated to obtain $T_2 \approx 1.01$ s.

important pulse sequence building blocks in NMR.

1.9 Coupling Regimes

The relationship between the chemical shift frequency difference Δ, and the J-coupling is important, as it governs the behaviour of homonuclear spin-1/2 pairs of nuclei. There are three such cases, as illustrated in Figure 1.8.

The first case is that of *weak-coupling*, or strong magnetic inequivalence. In these conditions, the chemical shift difference is much larger than the J-coupling. This type of system is labelled AX, using the Pople notation[28].

The second case is that of *strong-coupling*. In this regime, the chemical shift difference is of approximately the same magnitude, or smaller than the J-coupling. This type of system is labelled AB. In the case where $\Delta \ll J$, such a system is said to belong to the *near-equivalence regime*. Much of the work described in this thesis was carried out in these conditions.

The third case is that of *identical chemical shifts*. This type of system is given the A_2 label. In the case where the two spins also have identical couplings to all the other spins within the molecule, the two spins are said to be *magnetically equivalent*[13]. In the case where two spins belong to the same isotopic species, and the two spins can be exchanged by a molecular symmetry operation, then the two spins are said to be *chemically equivalent*[13].

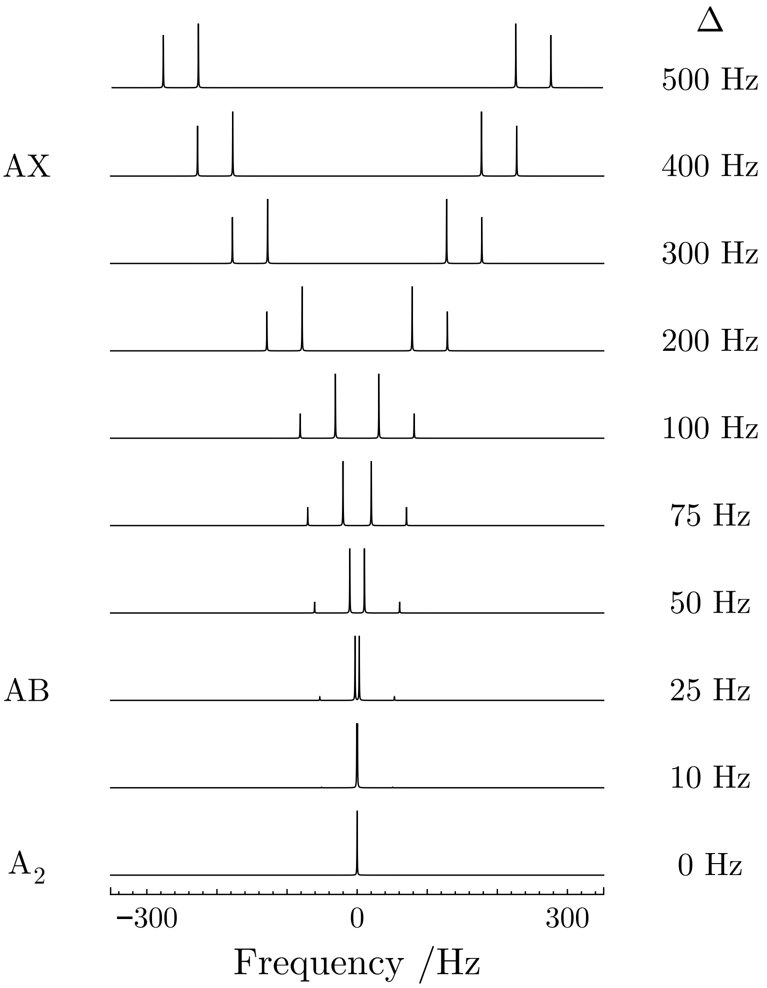

Figure 1.8: Spectra of a two spin-1/2 homonuclear system in an isotropic liquid as a function of the chemical shift difference Δ. The simulations were carried out using *SpinDynamica*[27], where $J = 50$ Hz.

1.10 The NMR Hamiltonians

In this section, a brief overview of the Hamiltonians[29–31] relevant to the treatment of spin systems in isotropic liquid media is presented.

1.10.1 Rotating Frame

To remove the time-dependence of the spin Hamiltonian under the effect of an external rf field, the laboratory frame of reference is transformed into a *rotating frame*.

In the laboratory frame, the magnetisation vector precesses very fast at the Larmor frequency ω^0. In a rotating frame, however, the precession occurs at a much reduced frequency Ω^0, denoted the *resonance offset*, or *offset frequency*. This is the difference between the Larmor frequency, and the frequency of the frame ω^{ref}, written as follows[13]:

$$\Omega^0 = \omega^0 - \omega^{\mathrm{ref}}. \tag{1.52}$$

The *exact resonance* condition applies when $\omega^0 = \omega^{\mathrm{ref}}$, and therefore $\Omega^0 = 0$.

1.10.2 Spin Hamiltonian

The Zeeman Hamiltonian, in the absence of an rf field, is given by:

$$\hat{H}_Z = \hat{H}^0 = -\gamma B^0 \hat{I}_z = \omega^0 \hat{I}_z. \tag{1.53}$$

The rotating frame spin Hamiltonian is expressed as follows:

$$\hat{\tilde{H}}^0 = \Omega^0 \hat{I}_z, \tag{1.54}$$

where the tilde denotes the rotating frame conditions.

1.10.3 Chemical Shift Hamiltonian

Electrons surrounding nuclei generate their own magnetic field, which adds or subtracts from the external applied field B^0. The chemical shift therefore accounts for the surrounding electronic environment around the nucleus[32,33]. The chemical shift Hamiltonian can be written in the following form:

$$\hat{H}_{CS} = -\gamma \hat{\boldsymbol{I}} \cdot \boldsymbol{\delta} \cdot \boldsymbol{B}, \tag{1.55}$$

where $\boldsymbol{\delta}$ is the chemical shift tensor:

$$\boldsymbol{\delta} = \begin{pmatrix} \delta_{xx} & \delta_{yx} & \delta_{zx} \\ \delta_{xy} & \delta_{yy} & \delta_{zz} \\ \delta_{xz} & \delta_{yz} & \delta_{zz} \end{pmatrix}. \tag{1.56}$$

The components of $\boldsymbol{\delta}$ depend on the orientation of the molecule. This rank 2 tensor can be written as the sum of three irreducible Cartesians operators, of rank 0, 1, and 2. In isotropic liquids, the rapid molecular tumbling averages out the rank 1 and 2 components.

The isotropic chemical shift is contained within the first part, where δ_{iso} is the mean of the three principal values, as follows: $\delta_{\text{iso}} = [(\delta_{xx} + \delta_{yy} + \delta_{zz})/3]$, where, if all three values are equal, $\boldsymbol{\delta}$ is said to be isotropic. If two, or more, values are different, the tensor $\boldsymbol{\delta}$ is said to anisotropic. The chemical shift anisotropy (CSA) is contained within the rank 2 component of the chemical shift tensor, and is defined as the largest deviation[34] in chemical shift from the isotropic value, $\delta_{\text{aniso}} = \delta_{zz} - \delta_{\text{iso}}$.

The biaxiality parameter, $0 < \eta < 1$, quantifies the difference between δ_{yy} and δ_{xx}, and is given by the following:

$$\eta = \frac{\delta_{yy} - \delta_{xx}}{\delta_{\text{aniso}}}. \tag{1.57}$$

The chemically shifted Larmor frequency is given by:

$$\omega^0 = -\gamma B^0 (1 + \delta_{\text{iso}}). \tag{1.58}$$

1.10.4 Hamiltonian During a Pulse

The rotating frame rf Hamiltonian is given by the following:

$$\hat{\hat{H}}_{rf} = \omega_{\text{nut}}(\hat{I}_x \cos\phi_{\text{p}} + \hat{I}_y \sin\phi_{\text{p}}), \tag{1.59}$$

where ϕ_{p} is the phase of the rf pulse, and $\omega_{\text{nut}} = |\frac{1}{2}\gamma B_{\text{rf}}|$ is the *nutation frequency*, where B_{rf} represents the amplitude of the applied rf field.

The frame transformation removes the time-dependent nature of this interaction. The spin Hamiltonian takes the following form:

$$\hat{\hat{H}} = \hat{\hat{H}}^0 + \hat{\hat{H}}_{rf} = \Omega^0 \hat{I}_z + \omega_{\text{nut}}(\hat{I}_x \cos\phi_{\text{p}} + \hat{I}_y \sin\phi_{\text{p}}). \tag{1.60}$$

In the case of an on-resonance ($\Omega^0 = 0$), strong pulse of phase 0, the rotating frame spin Hamiltonian during the pulse is reduced to the following:

$$\hat{\hat{H}} = \omega_{\text{nut}} \hat{I}_x. \tag{1.61}$$

For a strong pulse of duration τ_{p}, the pulse flip angle β_{p} is given by:

$$\beta_{\text{p}} = \omega_{\text{nut}} \tau_{\text{p}}. \tag{1.62}$$

The pulse propagators are given as the following rotation operators, which are the exponentials of the spin angular momentum operators:

$$\begin{aligned} \hat{R}_x(\beta_{\text{p}}) &= \exp\left\{-i\beta_{\text{p}}\hat{I}_x\right\}, \\ \hat{R}_y(\beta_{\text{p}}) &= \exp\left\{-i\beta_{\text{p}}\hat{I}_y\right\}, \\ \hat{R}_z(\beta_{\text{p}}) &= \exp\left\{-i\beta_{\text{p}}\hat{I}_z\right\}. \end{aligned} \tag{1.63}$$

The spin-1/2 matrix representation of $\hat{R}_x(\beta_{\text{p}})$ is given as follows:

$$\hat{R}_x(\beta_{\text{p}}) = \begin{pmatrix} \cos\frac{1}{2}\beta_{\text{p}} & -i\sin\frac{1}{2}\beta_{\text{p}} \\ -i\sin\frac{1}{2}\beta_{\text{p}} & \cos\frac{1}{2}\beta_{\text{p}} \end{pmatrix}. \tag{1.64}$$

1.10.5 Scalar Coupling Hamiltonian

The scalar J-coupling arises from the interaction of pairs of nuclear spins through bonding electrons. The J-coupling Hamiltonian for a single spin-pair is given as follows:

$$\hat{H}_{J_{12}} = 2\pi \boldsymbol{\hat{I}_1} \cdot \boldsymbol{J}_{12} \cdot \boldsymbol{\hat{I}_2}, \tag{1.65}$$

where $\boldsymbol{J}_{12}$ is the J-coupling tensor. Like the chemical shift tensor, this rank 2 tensor can also be reduced to three components: a rank 0 component containing the isotropic J-coupling, a rank 1 antisymmetric component, and a rank 2 anisotropic component. In isotropic liquids, this tensor is averaged out by molecular tumbling, and the Hamiltonian is written as follows:

$$\hat{H}_J = 2\pi J_{12}(\boldsymbol{\hat{I}_1} \cdot \boldsymbol{\hat{I}_2}), \tag{1.66}$$

where $J_{12} = [\left(J^{12}_{xx} + J^{12}_{yy} + J^{12}_{zz}\right)/3]$, which is the isotropic J-coupling.

1.10.6 Dipolar Coupling Hamiltonian

Each nuclear spin-1/2 has a magnetic dipole moment, and generates a magnetic field that is experienced by another nucleus in close proximity. The dipole-dipole Hamiltonian between a pair of spins is given as follows:

$$\hat{H}_{DD} = \left(\frac{3\; b_{12}(\boldsymbol{\hat{I}_1} \cdot \boldsymbol{r_{12}})(\boldsymbol{\hat{I}_2} \cdot \boldsymbol{r_{12}})}{r^2_{12}} - \boldsymbol{\hat{I}_1} \cdot \boldsymbol{\hat{I}_2} \right). \tag{1.67}$$

The dipolar coupling constant b_{12} defines the magnitude of the through space interaction between spins 1 and 2, and is given by:

$$b_{12} = -\frac{\gamma_1 \gamma_2 \hbar}{r^3_{12}} \frac{\mu_0}{4\pi}, \tag{1.68}$$

where μ_0 is the vacuum permittivity, r_{12} is the internuclear distance between the two spins, and γ_1, γ_2 are the respective magnetogyric ratios.

In isotropic liquids, the short-range intermolecular dipolar couplings average to zero. The contribution from the long-range dipole-dipole couplings is very small, and can be neglected.

1.10.7 Total Hamiltonian

The isotropic[30] part of the Hamiltonian $\hat{H}_0$ is made up by $\hat{H}_Z$, $\hat{H}_{CS}$ and $\hat{H}_J$. The Zeeman contribution, along with the isotropic parts of the chemical shift and scalar coupling Hamiltonians are rank 0. The rank 2 components of the chemical shift and scalar coupling Hamiltonians are anisotropic, and form some of the terms within the *fluctuating* part of the Hamiltonian $\hat{H}_2(t)$, which contains the relaxation terms and is time-dependent. The previously mentioned dipole-dipole Hamiltonian $\hat{H}_{DD}$ is also of rank 2.

The total spin Hamiltonian, in the laboratory frame, is given by:

$$\begin{aligned}
\hat{H}(t) &= \hat{H}_0 + \hat{H}_1(t) + \hat{H}_2(t), \\
\hat{H}_0 &= \hat{H}_Z + \hat{H}_{CS} + \hat{H}_J, \\
\hat{H}_1(t) &= \hat{H}_{rf}(t), \\
\hat{H}_2(t) &= \hat{H}_{DD}(t) + \hat{H}_{CS}^{aniso}(t) + \hat{H}_J^{aniso}(t) + \hat{H}_{SR}(t) + \hat{H}_{RDM}(t),
\end{aligned} \tag{1.69}$$

where $\hat{H}_{SR}(t)$ is the spin-rotation Hamiltonian. The spin-rotation mechanism arises due to the interaction between the nuclear spin, and the magnetic field generated by the rotation of the molecule itself. It is particularly relevant in small molecules. An indicator of this relaxation mechanism is the decrease in the T_1 relaxation time as a sample is heated.

The random field motion Hamiltonian, $\hat{H}_{RDM}(t)$, is given by the random generation of localised magnetic fields due to molecular motion. For spin-1/2 nuclei, the quadrupolar spin Hamiltonian $\hat{H}_Q$ is zero. It however becomes important for non spin-1/2 nuclei, where the electric charge distribution is not spherically symmetrical. Consequently, the interaction of the nuclear quadrupole moment is orientation-dependent.

1.11 Coherence Order Selection

In NMR experiments, a pulse sequence is applied to manipulate the spins to obtain the desired effect. At the end of this pulse sequence, an NMR spectrum is acquired. To obtain a better signal-to-noise ratio, the pulse sequence can be applied several times, for as many transients as are required, and the resulting free-induction decay (FID) signals are added to produce the final spectrum. In this case, the pulse sequence is applied exactly in the same way for each transient.

On the other hand, there is a technique called *phase cycling*, where the pulse sequence is repeated, and all frequency and delays are identical, while exclusively varying the phases of the pulses. After the experiment is repeated multiple times, in proportion to the number of steps in the phase list, the resulting FID signals are summed. If the phases are cycled correctly, unwanted signals cancel out, and the desired spectrum is obtained.

This method has been used as a means to suppress imperfections in NMR spectra due to artifacts, such as "phantom" and "ghost" signals due to imperfect refocusing pulses creating transverse magnetisation[35]. The procedure, however, is more importantly used for coherence pathway *selection*[36].

A coherence transfer pathway diagram can be used to visualise how the coherences p are evolving as pulses are applied. Groups of pulses can be gathered together in "blocks", where the overall phase of the block is cycled with other blocks' phases. The coherence transfer pathway diagram in Figure 1.9 illustrates the principle for the refocused INADEQUATE pulse sequence[37].

Radiofrequency pulses induce changes in the coherence order, and each coherence p conserves its quantum number during free precession. The route of a particular coherence forms a coherence transfer pathway. The system starts at thermal equilibrium, where $p = 0$. For convenience, the $\hat{}$ symbols on operators will now be omitted. The zero order coherence level indicates Zeeman polarisation, with the I_{1z} and I_{2z} operators for a homonuclear two-spin-1/2 system. Other terms are the longitudinal two-spin order $2I_{1z}I_{2z}$, and zero-quantum coherence $I_1^+ I_2^-$ or $I_1^- I_2^+$. Only single quantum coherences $p = \pm 1$ are observable. Specifically, the $p = -1$ coherence is what is detected

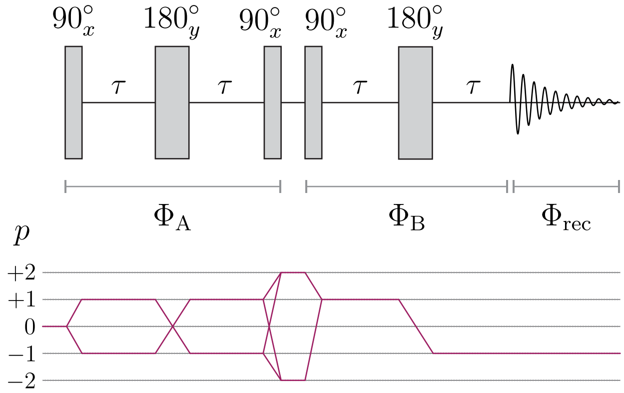

Figure 1.9: Coherence transfer pathway diagram for the one-dimensional refocused INADEQUATE pulse sequence, where $\tau \approx (4J)^{-1}$. At thermal equilibrium, $p = 0$. The first block, "A", consists of $90^\circ_x 180^\circ_y 90^\circ_x$ pulses, at the end of which the double-quantum coherences $p = \pm 2$ are obtained. This is cycled with an overall phase Φ_A. The $90^\circ_x 180^\circ_y$ pulses form block "B", with an overall phase Φ_B. From double-quantum, the coherence level $p = -1$ is reached for quadrature detection. The receiver is cycled with the phase Φ_rec.

by quadrature detection. Part of the $p = +1$ coherence may be detected[38], if the receiver channels are imbalanced (imperfect quadrature detection). We are interested in the double-quantum coherences $p = \pm 2$, where the relevant operators are $2I_{1x}I_{2y}$, and $2I_{1y}I_{2x}$. After a phase cycle is complete, single-quantum coherences are suppressed, and double-quantum terms are made observable.

Phase cycling proved fundamental in the resonance assignment of the carbon backbone of organic molecules. INADEQUATE proved to be particularly useful, since it allowed the observation of natural abundance ^{13}C spins in biologically relevant molecules, where ^{13}C isotopic labelling can be difficult, in some cases. The method traditionally works well for weakly-coupled systems, with a double-quantum coherence excitation time $T \simeq 1/(2J)$.

Using the refocused INADEQUATE sequence above (Figure 1.9) as our example, we see that there are three blocks in total: A, B, and the receiver "rec", with phases Φ_A, Φ_B, and Φ_rec, respectively. The change in coherence order for the blocks is: Δp_A and Δp_B for A and B, respectively. These are written as following:

$$\begin{aligned}\Delta p_A &= p_{AB} - 0 = +2,\\ \Delta p_B &= -1 - p_{AB} = -3,\end{aligned} \tag{1.70}$$

where we have chosen the coherence pathway passing through the $p = +2$ double-quantum coherence. The receiver phase is always set to $\phi_{rec} = 1$.

The "master equation" is written[39] as follows:

$$\Phi^{(m)}\left(\boldsymbol{p}\right) = \text{constant}, \tag{1.71}$$

where m is the cycle counter, and $\boldsymbol{p}$ represents the coherence transfer pathway.

The number of $\Delta p = 4$ steps in the coherence transfer diagram suggests that our phase cycle needs four transients to complete one cycle. The phase shift step in the phase cycle is given by: $\left(2\pi\right)/\Delta p = \pi/2$. This is a 90° step between each successive transient.

For our system, we write the equation as following:

$$\begin{aligned}\Phi\left(\boldsymbol{p}\right) &= \Delta p_A \phi_A + \Delta p_B \phi_B + \phi_{rec},\\ 0 &= \Delta p_A \phi_A + \Delta p_B \phi_B + \phi_{rec}.\end{aligned} \tag{1.72}$$

Substituting the values, and keeping the phase of the block A stationary $(\phi_A = 0)$ gives:

$$\begin{aligned}0 &= -3\phi_B + \phi_{rec},\\ \phi_{rec} &= 3\phi_B.\end{aligned} \tag{1.73}$$

It is convenient to construct a table containing the phase list, such as the one shown in Table 1.2. This particular phase cycle selects for both double-quantum coherences $\Delta p = \pm 2$.

Table 1.2: Phase list for the selection of double-quantum coherences.

Phase counter m	$\boldsymbol{\Phi}_{\mathrm{A}}$	$\boldsymbol{\Phi}_{\mathrm{B}}$	$\boldsymbol{\Phi}_{\mathrm{rec}}$
1	0	0	0
2	0	$\frac{\pi}{2}$	$\frac{3\pi}{2}$
3	0	π	π
4	0	$\frac{3\pi}{2}$	$\frac{\pi}{2}$

1.12 Composite Pulses

The Bloch sphere trajectories of the magnetisation after a 90°, and 180° pulse are given in Figure 1.10. This is for the case of "perfect" pulses. The first pulse rotates the magnetisation vector onto the x-axis, and the second inverts it along the $-z$-axis.

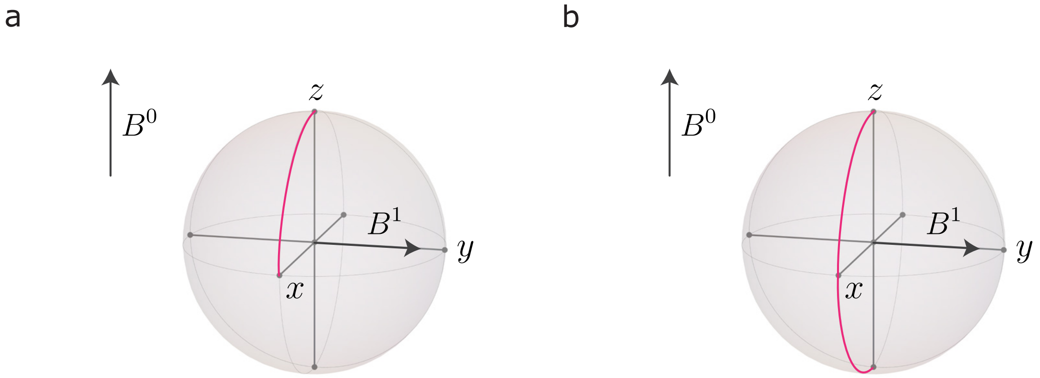

Figure 1.10: Bloch sphere trajectories of the I_x, I_y, and I_z operators under the influence of an exact rf field B^1, starting from the I_z operator at thermal equilibrium. The static magnetic field B^0 is oriented along the z-axis. (**a**) In the case of a $(\pi/2)_y$ pulse. (**b**) In the case of a $(\pi)_y$ pulse.

In practice, however, B^1 inhomogeneity, and resonance offset errors can lead to the rotation imposed being of a different angle to the desired one.

This can be due to user error, such as missetting the length of the pulse due to errors in calibration, or problematic hardware.

To compensate for these pulse imperfections, *composite pulses* were devised, such as the Levitt composite[40] 180° pulse, of the following structure:

$$(\pi)_y = (\pi/2)_y(\pi)_x(\pi/2)_y. \tag{1.74}$$

This simple scheme accounts for both rf misset, and resonance offset effects, as depicted in Figure 1.11.

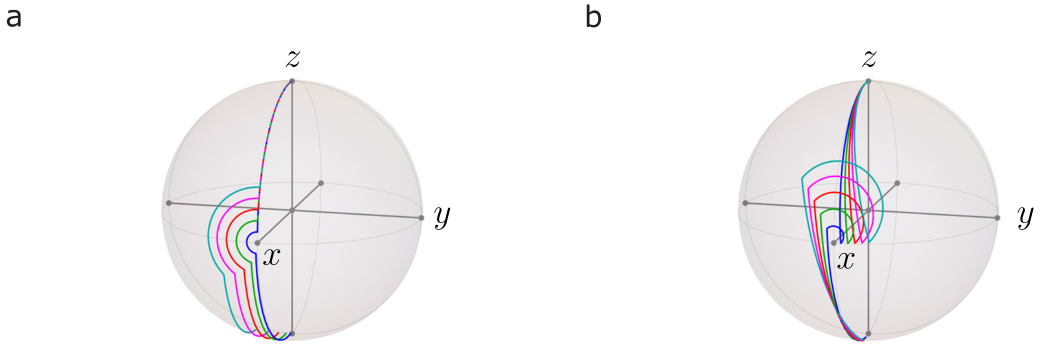

Figure 1.11: Bloch sphere trajectories of the I_x, I_y, and I_z operators during a Levitt composite $(\pi)_y$ pulse[40], starting from the I_z operator at thermal equilibrium. (**a**) In the case of misset radiofrequency pulse length. (**b**) In the case of resonance offset.

Another type of composite pulse is the broadband (BB) composite[41,42] pulse 1: BB$_1$. For a pulse with an angle θ, the symmetrised sequence has the following structure:

$$(\theta)_y(\pi)_{\phi_1}(2\pi)_{\phi_2}(\pi)_{\phi_1}(\theta)_y \ , \tag{1.75}$$

where $\phi_1 = \arccos(-\theta/4\pi)$, and $\phi_2 = 3\phi_1$. For a 90° pulse, the sequence has the following form:

$$\mathrm{BB}_1(90^\circ_{90^\circ}) = 45^\circ_{90^\circ}180^\circ_{97.2^\circ}360^\circ_{291.5^\circ}180^\circ_{97.2^\circ}45^\circ_{90^\circ} \ . \tag{1.76}$$

The 180° pulse is given as follows:

$$\mathrm{BB}_1(180^\circ_{90^\circ}) = 90^\circ_{90^\circ}180^\circ_{104.5^\circ}360^\circ_{313.4^\circ}180^\circ_{104.5^\circ}90^\circ_{90^\circ} \ . \tag{1.77}$$

The contour plots shown in Figure 1.12 depict the performance of a 180° pulse with respect to the B^1 field inhomogeneity, and resonance offset, for an “ideal” pulse, a Levitt composite pulse, and a BB_1 composite pulse.

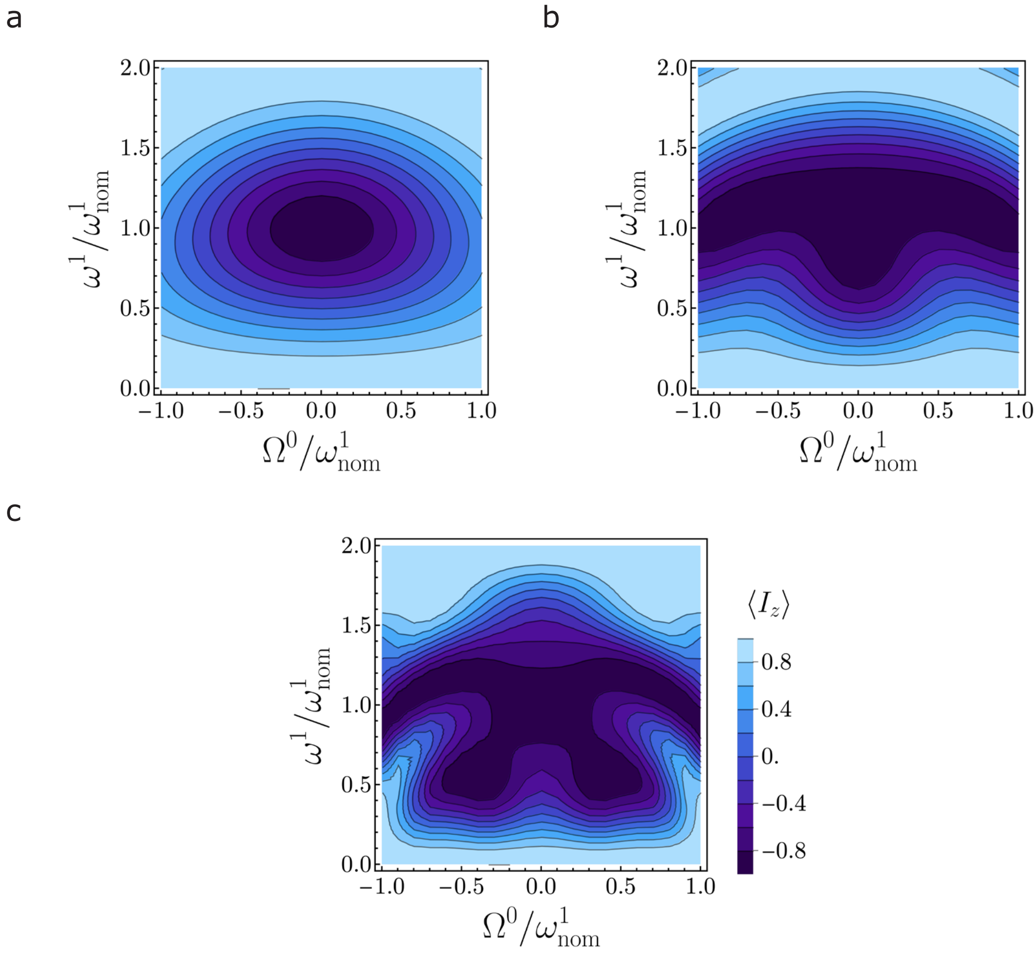

Figure 1.12: Contour plots of various magnetisation inversion schemes, showing the performance of the sequences with respect to B^1 field inhomogeneity, and resonance offset. The darker regions correspond to a better magnetisation inversion. (**a**) A simple 180° pulse. (**b**) A Levitt composite 180° pulse (Equation 1.74). (**c**) A BB_1 180° composite pulse (Equation 1.77).

Chapter 2

Long-Lived Nuclear Spin States

Relaxation processes govern the return of a spin system to thermal equilibrium with its surrounding environment. Two prominent relaxation time constants are T_1 and T_2. The T_1 longitudinal, or spin-lattice, relaxation time constant describes the time required for the spin-populations of a system to reach thermal equilibrium. On the other hand the T_2, or spin-spin, relaxation time constant describes the time required for the phase-coherence of the spins in the system to be lost. Generally, $T_1 \geq T_2$.

Hence, the spin memory of the system in question, and therefore the time available to perform the NMR experiments themselves are constrained to a small multiple of T_1. Beyond 3-5 T_1, spin order is lost irreversibly. A pathway that leads to extended relaxation lifetimes involves exploiting *long-lived states*[43,44] (LLS). The singlet state is one such example, consisting of non-magnetic (total spin quantum number $I = 0$) nuclear spin-1/2 pairs that are resistant to prominent dissipation mechanisms, such as intramolecular dipole-dipole relaxation.

In this chapter, singlet and triplet states are introduced, along with a variety of pulse sequences that have been used to excite singlet order in the past, and some of the most prominent singlet order relaxation mechanisms.

2.1 Introduction

The Zeeman states discussed in the previous chapter may be combined to construct one singlet state $|S_0\rangle$, with total nuclear spin $I = 0$ (antiparallel arrangement), and three triplet states $|T_{+1}\rangle, |T_0\rangle, |T_{-1}\rangle$, with $I = 1$ (parallel arrangement). They are written in the following form:

$$\begin{aligned}
&\text{Singlet state:} \quad I = 0 \quad \left\{ |1\rangle = |S_0\rangle = \frac{1}{\sqrt{2}}\left(|\alpha\beta\rangle - |\beta\alpha\rangle\right), \right. \\
&\text{Triplet states:} \quad I = 1 \quad \left\{ \begin{aligned} &|2\rangle = |T_{+1}\rangle = |\alpha\alpha\rangle, \\ &|3\rangle = |T_0\rangle = \frac{1}{\sqrt{2}}\left(|\alpha\beta\rangle + |\beta\alpha\rangle\right), \\ &|4\rangle = |T_{-1}\rangle = |\beta\beta\rangle, \end{aligned} \right.
\end{aligned} \tag{2.1}$$

where α and β denote the two spin angular momentum $\pm(\hbar/2)$ projections along an external axis, and the subscripts $\{+1, 0, -1\}$ refer to the value of the magnetic spin quantum number $m = \{I, I-1, ..., -I\}$.

The dihydrogen molecule, H_2, exists as two nuclear spin isomers. The nuclear singlet state belongs to the *para*-hydrogen spin isomer, whereas the three triplet states belong to the *ortho*-hydrogen spin isomer. The two possible arrangements of the spin angular momenta are shown in Figure 2.1.

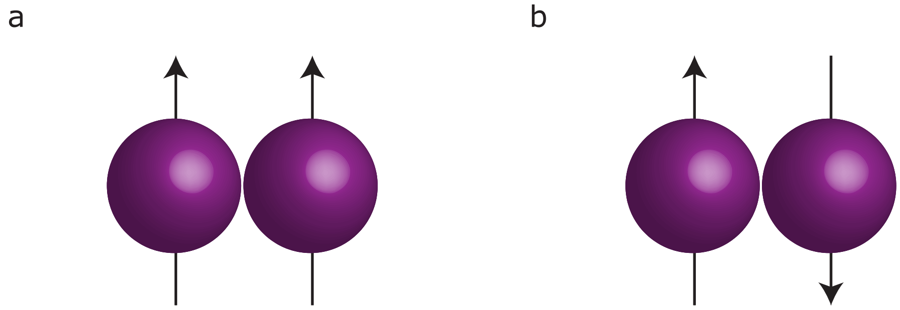

Figure 2.1: The two spin isomers of dihydrogen. (**a**) The *ortho*-hydrogen spin isomer, where $I = 1$. (**b**) The *para*-hydrogen spin isomer, where $I = 0$.

The singlet state $|S_0\rangle$ behaves as a non-magnetic spin-0 particle[45], and is invariant under rotation, as seen in the following eigenequations:

$$\begin{aligned} I_z \left| S_0 \right\rangle &= 0, \\ \boldsymbol{I^2} \left| S_0 \right\rangle &= 0. \end{aligned} \tag{2.2}$$

Therefore, this state does not generate an NMR signal. In the dihydrogen case, the signal observed is due to exclusively the triplet states, which behave akin to the three states of a spin-1 particle. The following eigenquations apply in this case:

$$\begin{aligned} I_z \left| T_M \right\rangle &= M \left| T_M \right\rangle, \\ \boldsymbol{I^2} \left| T_M \right\rangle &= 2 \left| T_M \right\rangle, \end{aligned} \tag{2.3}$$

where $M = \{+1, 0, -1\}$.

The singlet and each of the triplet states have different symmetry under exchange of the two spins 1 and 2 after the permutation operator (12) is applied. The singlet state is *antisymmetric* with respect to exchange:

$$(12) \left| S_0 \right\rangle = - \left| S_0 \right\rangle, \tag{2.4}$$

whereas the three triplet states are *symmetric* under exchange:

$$(12) \left| T_M \right\rangle = \left| T_M \right\rangle. \tag{2.5}$$

To convert the exchange antisymmetric singlet state, into any of the triplet exchange symmetric states, the conversion mechanism itself must be exchange antisymmetric. As mentioned in the previous chapter, through space dipole-dipole couplings can be the most prominent source of spin order relaxation. Highly magnetic nuclei, such as protons, generate strong dipolar interactions due to their high γ.

The dipole-dipole Hamiltonian may be written[46] in the following form:

$$H_{DD} = \boldsymbol{I_1} \cdot \boldsymbol{D_{12}} \cdot \boldsymbol{I_2} = \boldsymbol{I_2} \cdot \boldsymbol{D_{21}} \cdot \boldsymbol{I_1}, \tag{2.6}$$

where $\boldsymbol{D_{12}}$ is the dipole-dipole coupling tensor between spins 1 and 2.

This Hamiltonian is symmetric upon exchange of the two spins 1 and

2, since there is no change in sign. Therefore, the singlet state remains isolated, while the populations of the triplet states undergo rapid exchange under the dipole-dipole relaxation mechanism. In practice, the decay of singlet order, described by the relaxation constant T_S, occurs due to the slow equilibration between either of the $|T_{+1}\rangle, |T_0\rangle$, and $|T_{-1}\rangle$ populations, with the $|S_0\rangle$ population.

Consequently, the singlet order relaxation lifetime T_S is generally $T_\mathrm{S} \gg T_1$, since T_1 processes occur exclusively within the triplet manifold. The diagram in Figure 2.2 illustrates this concept.

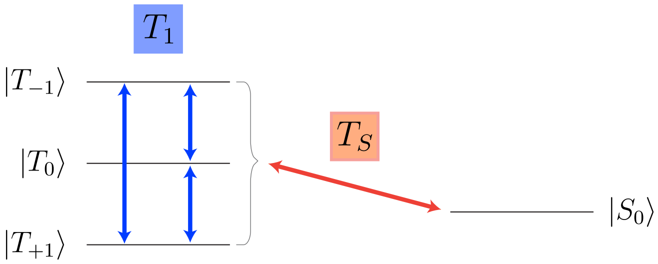

Figure 2.2: T_1 relaxation occurs within the rapidly interchanging triplet manifold $|T_{+1}\rangle, |T_0\rangle$, and $|T_{-1}\rangle$. The decay of singlet order, described by the relaxation constant T_S, occurs due to the slow equilibration between either of the $|T_{+1}\rangle, |T_0\rangle$, and $|T_{-1}\rangle$ populations, with the $|S_0\rangle$ population. Hence, singlet order is generally longer-lived than longitudinal spin order.

Applications of singlet NMR have ranged from the study of chemical exchange[47,48], slow diffusion processes[49], weak ligand-protein interactions[50], to MRI imaging[51]. Long-lived spin order has also been used for the storage of hyperpolarised spin order[52–54].

Singlet NMR methods are not constrained to exotic spin isomers, or complicated molecular systems. In fact, long-lived states can be accessed within relatively ordinary molecules, and using conventional radiofrequency pulses that can be programmed in a standard NMR experiment. The later sections will examine a few of the most common pulse sequences used to access and manipulate the singlet state.

In historical singlet NMR experiments, a remarkable singlet order time constant of almost 25 minutes was measured in nitrous oxide[55], and of over one hour[56] in a naphthalene derivative at room temperature.

2.2 Magnetically Equivalent Spin-Pairs

The spin Hamiltonian for a two spin-1/2 A_2 system can be written as follows:

$$H = \omega^0 I_z + 2\pi J(\boldsymbol{I_1} \cdot \boldsymbol{I_2}). \tag{2.7}$$

The matrix representation of H is given as follows, in the singlet-triplet basis:

$$H = \begin{array}{c} \begin{array}{cccc} |S_0\rangle & |T_{+1}\rangle & |T_0\rangle & |T_{-1}\rangle \end{array} \\ \begin{pmatrix} -\frac{3}{2}\pi J & 0 & 0 & 0 \\ 0 & \omega^0 + \frac{1}{2}\pi J & 0 & 0 \\ 0 & 0 & \frac{1}{2}\pi J & 0 \\ 0 & 0 & 0 & -\omega^0 + \frac{1}{2}\pi J \end{pmatrix} \end{array}, \tag{2.8}$$

where the basis kets have been given above every matrix column.

At zero magnetic field, the Larmor frequency $\omega^0 = 0$, and the three triplet states become degenerate, with a separation of $|\gamma B^0|$ between each other. The separation between $|S_0\rangle$ and $|T_0\rangle$ is given by $|2\pi J|$. In this coupling regime, the singlet and triplet states are eigenstates of the spin Hamiltonian.

Magnetic equivalence occurs when two spins have the same chemical and magnetic environment[13,57]. To exploit the singlet state, magnetic inequivalence[13,57] between the two spins is required.

2.3 Magnetically Inequivalent Spin-Pairs

At high magnetic field, the spin Hamiltonian for a two spin-1/2 AB system can be written as follows:

$$H = \omega^0(1 + \delta_1)I_{1z} + \omega^0(1 + \delta_2)I_{2z} + 2\pi J(\boldsymbol{I_1} \cdot \boldsymbol{I_2}), \tag{2.9}$$

where δ_1 is the chemical shift of spin 1, and δ_2 is the chemical shift of spin 2.

The matrix representation of H, in the singlet-triplet basis, is as follows:

$$H = \begin{pmatrix} -\frac{3}{2}\pi J & 0 & \frac{1}{2}\omega^0\Delta & 0 \\ 0 & \omega^0(1+\frac{1}{2}\Sigma)+\frac{1}{2}\pi J & 0 & 0 \\ \frac{1}{2}\omega^0\Delta & 0 & \frac{1}{2}\pi J & 0 \\ 0 & 0 & 0 & -\omega^0(1+\frac{1}{2}\Sigma)+\frac{1}{2}\pi J \end{pmatrix}, \quad (2.10)$$

where the sum Σ, and difference Δ between the chemical shifts is given, as follows:

$$\begin{aligned} \Sigma &= \delta_1 + \delta_2, \\ \Delta &= \delta_1 - \delta_2. \end{aligned} \quad (2.11)$$

The off-diagonal terms of the Hamiltonian contain the chemical shift difference term, which connect the $|S_0\rangle$ and $|T_0\rangle$ states, inducing transitions between the two states.

The singlet and triplet states are not exact eigenstates of the Hamiltonian at high magnetic field. The eigenstates are given by the following:

$$\begin{aligned} |S_0'\rangle &= |S_0\rangle \cos(\theta_{\mathrm{ST}}/2) + |T_0\rangle \sin(\theta_{\mathrm{ST}}/2), \\ \left|T_{+1}'\right\rangle &= |T_{+1}\rangle, \\ |T_0'\rangle &= |T_0\rangle \cos(\theta_{\mathrm{ST}}/2) - |S_0\rangle \sin(\theta_{\mathrm{ST}}/2), \\ \left|T_{-1}'\right\rangle &= |T_{-1}\rangle, \end{aligned} \quad (2.12)$$

where $|S_0'\rangle$, $\left|T_{+1}'\right\rangle$ $|T_0'\rangle$, and $\left|T_{-1}'\right\rangle$ are the perturbed states. These are equal to the unperturbed states when the chemical shift difference $\Delta = 0$. The singlet-triplet mixing angle θ_{ST} is given[58] by the following:

$$\theta_{\mathrm{ST}} = \arctan\left(\frac{\Delta}{J}\right). \quad (2.13)$$

This angle approaches $\pi/2$ for weakly-coupled spins, and $\theta_{\mathrm{ST}} \lesssim 30^\circ$ for strongly-coupled spins. A very strongly-coupled spin-pair is said to be *near-equivalent*.

2.4 Singlet Order

A spin state can be represented by $|\psi\rangle$. The population operator for this spin state is given by:

$$P_\psi = |\psi\rangle \langle\psi| . \tag{2.14}$$

The population operator for the singlet state P_{S_0} is can be written in all the following forms[59]:

$$\begin{aligned} P_{S_0} &= |S_0\rangle \langle S_0| \\ &= \frac{1}{2}\left(|\alpha\beta\rangle \langle\alpha\beta| - |\alpha\beta\rangle \langle\beta\alpha| - |\beta\alpha\rangle \langle\alpha\beta| + |\beta\alpha\rangle \langle\beta\alpha|\right) \\ &= \frac{1}{4}\mathbb{1} - \boldsymbol{I_1} \cdot \boldsymbol{I_2} \\ &= \frac{1}{4}\mathbb{1} - \frac{1}{2}[\left(I_1^- \cdot I_2^+ + I_1^+ \cdot I_2^-\right) + 2\left(I_{1z} \cdot I_{2z}\right)] \\ &= \frac{1}{4}\mathbb{1} + \sqrt{3}\mathbf{T^{12}_{00}}, \end{aligned} \tag{2.15}$$

where $\mathbf{T^{12}_{00}}$ represents the rank 0 spherical tensor operator for the I_1 and I_2 spins, and $\mathbb{1}$ is the identity operator. These equalities are expressed in multiple bases for completeness. First is the singlet triplet basis, then the Cartesian product operator basis, shift operator basis, and finally the spherical tensor operator basis.

A table containing the spherical tensor operators for a homonuclear two-spin-1/2 system can be found in Appendix A.

The remaining population operators $P_{T_{+1}}$, P_{T_0} and $P_{T_{-1}}$ can be written in an analogous manner, shown elsewhere[59]. We focus our attention on the population differences between the states.

Longitudinal order (**LO**) is the population difference between the outer triplet states $|T_{-1}\rangle$ and $|T_{+1}\rangle$:

$$\begin{aligned} \mathbf{LO} &= P_{T_{+1}} - P_{T_{+1}} \\ &= |T_{+1}\rangle \langle T_{+1}| - |T_{-1}\rangle \langle T_{-1}| \\ &= I_{1z} + I_{2z}. \end{aligned} \tag{2.16}$$

We define singlet order as the population difference between the singlet state, and the mean of the three triplet states:

$$\begin{aligned}
\mathbf{SO} &= P_{S_0} - \frac{P_{T_{+1}} + P_{T_0} + P_{T_{-1}}}{3} \\
&= \left|S_0\right\rangle\left\langle S_0\right| - \frac{\left|T_{+1}\right\rangle\left\langle T_{+1}\right| + \left|T_0\right\rangle\left\langle T_0\right| + \left|T_{-1}\right\rangle\left\langle T_{-1}\right|}{3} \\
&= -\frac{4}{3}\boldsymbol{I_1} \cdot \boldsymbol{I_2} \\
&= -\frac{2}{3}[\left(I_1^- \cdot I_2^+ + I_1^+ \cdot I_2^-\right) + 2\left(I_{1z} \cdot I_{2z}\right)] \\
&= \frac{2}{\sqrt{3}}\mathbf{T_{00}^{12}}.
\end{aligned} \tag{2.17}$$

The aim of singlet NMR experiments is to convert **LO** into **SO** at will, and the reverse transformation to obtain observable magnetisation. However, some of the routine pulse sequences that allow for magnetisation-to-singlet and singlet-to-magnetisation conversion often do not produce pure singlet order alone. These procedures exploit the $|S_0\rangle$, $|T_0\rangle$ population imbalance, which generates pseudo-singlet order (**pSO**). This is calculated as following:

$$\begin{aligned}
\mathbf{pSO} &= P_{S_0} - P_{T_0} \\
&= \left|S_0\right\rangle\left\langle S_0\right| - \left|T_0\right\rangle\left\langle T_0\right| \\
&= -\frac{2[\left(I_1^- \cdot I_2^+ + I_1^+ \cdot I_2^-\right) + 2\left(I_{1z} \cdot I_{2z}\right)]}{\sqrt{3}} + \\
&+ \frac{[-\left(I_1^- \cdot I_2^+\right) - I_1^+ \cdot I_2^- + 4\left(I_{1z} \cdot I_{2z}\right)]}{3} \\
&= \frac{2}{\sqrt{3}}\mathbf{T_{00}^{12}} + \frac{\sqrt{6}}{3}\mathbf{T_{20}^{12}}.
\end{aligned} \tag{2.18}$$

The presence of the spherical tensor operator of rank 2 can then be removed by a filtering stage during experiments, such as the T_{00} filter, illustrated in Figure 2.14. This allows only the isotropic magnetisation to pass, removing any rank 1 and rank 2 spherical tensor operators[60].

The theoretical maximum efficiency[59,61] that can be achieved in experiments with the conversion pathway **LO** → **SO** → **LO** is 2/3. The **LO** → **SO** pathway has a conversion efficiency of 1, however the backward **SO** → **LO** transformation has a conversion efficiency of 2/3. The bounds[62] on each transformation are different, since the two operators have two different norms[59,61]. The two efficiencies are multiplied together to obtain the 2/3 conversion efficiency value for the overall conversion pathway.

2.5 Singlet Filtered NMR Spectroscopy

In the magnetic equivalence regime, the singlet state cannot be observed, since it is non-magnetic. In this regime, the singlet and triplet states exchange rapidly, and the special long-lived character of the singlet state is not revealed, since the triplet states undergo rapid relaxation.

To prepare, and then observe singlet order, the symmetry of the spin Hamiltonian must be switched[63] at determined points during the experiment by suppressing the chemical shift terms. The next stage involves reinstating the symmetry to prevent further singlet-triplet coherences from occurring. The equilibration of populations between the two states would destroy singlet order, since the population *imbalance* is evened.

In the first demonstration of a singlet NMR experiment in 2004 by Carravetta[44,58] *et al.*, the sample was adiabatically transported within the fringe field of the spectrometer. Using this method, magnetic equivalence was imposed between the proton spin-pair within the 2,3-dibromothiophene AX type molecular system. Doing so suppresses any chemical shift effects, maintaining symmetry. The pulse sequence is given in Figure 2.3.

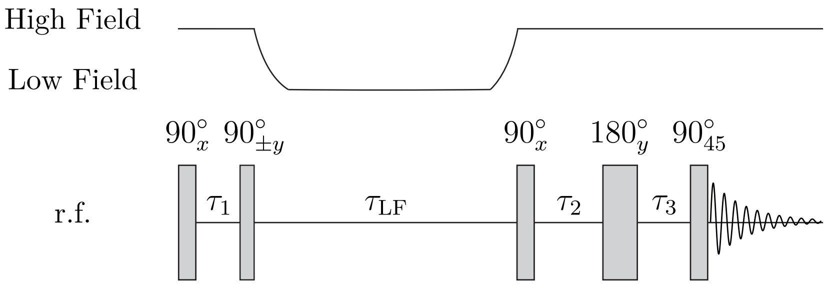

Figure 2.3: The first pulse sequence used to excite singlet order[44] at low magnetic field, between weakly-coupled pairs of spins.

The first part of the sequence creates the zero-quantum coherence between the $|S_0\rangle$ and $|T_0\rangle$ states, where $\tau_1 = \pi/\Delta\delta$. The second part of the sequence allows the NMR signal readout, where $\tau_2 = \pi/(2\Delta\delta)$, and $\tau_3 = 1/(4J)$.

During a low-field storage time τ_{LF}, singlet order decays with its characteristic longer lifetime T_{S}, compared to T_1. While the exchange symmetry is in force, singlet NMR signals cannot be observed, since this form of spin order is not magnetic. As a consequence, the symmetry is broken again by applying a high magnetic field, and the singlet-triplet transitions resume. Following further rf pulses, singlet order is transformed into longitudinal order, which can then be made observable by NMR.

At high magnetic field, the singlet and triplet states are eigenstates of the Hamiltonian, provided that an rf spin-locking field of an amplitude larger than the difference between the chemical shift frequency difference between the spins is applied[64,65]. In these conditions, the spin-lock suppresses the chemical shift terms within the spin Hamiltonian. The pulse sequence[43,65] is depicted in Figure 2.4.

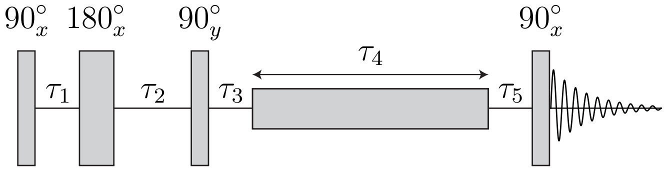

Figure 2.4: The first pulse sequence used to excite singlet order[43] at high magnetic field, between weakly-coupled pairs of spins.

At the start of the pulse sequence, the thermal equilibrium density operator $\rho_1 = I_{1z} + I_{2z}$. The first part of the sequence consists of three pulses and delays: $90_x - \tau_1 - 180_x - \tau_2 - 90_y - \tau_3$, where $\tau_1 = 1/(4J)$, $\tau_2 = 1/(4J) + \pi/\Delta$, and $\tau_3 = \pi/(2\Delta)$. The density operator ρ_2 can be written as follows:

$$\rho_2 = -(I_1^+ I_2^- + I_1^- I_2^+), \tag{2.19}$$

which is a zero-quantum coherence. This state is allowed to evolve under a resonant rf field of low power for a time τ_4, which suppresses the chemical shift difference. In the singlet-triplet basis, ρ_2 is expressed as follows:

$$\rho_2 = |S_0\rangle\langle S_0| - |T_0\rangle\langle T_0|\,, \tag{2.20}$$

which corresponds to pseudo-singlet order (Equation 2.18). After the spin-lock, the delay $\tau_5 = \pi/(2\Delta)$ and a 90°_y pulse are applied, which convert the singlet population into observable antiphase single-quantum coherences.

2.6 Singlet NMR of Near-Equivalent Spins

The pulse sequences introduced in the previous section work well in AX molecular spin systems, where the chemical shifts are well-resolved in the NMR spectrum. In this section, we briefly introduce pulse sequences that are able to operate in the strong-coupling regime, where the chemical shifts are not well-resolved. Such spectra display an AB pattern, or even a pseudo-A_2 type single peak. Working within this regime presents some advantages, such as not needing to suppress the chemical shift difference by field-cycling, or applying a spin-lock.

To follow the transformation of one state into another during the application of a pulse sequence, it is convenient to work with single-transition operators[66,67]. For a two-level subspace of the states $|r\rangle$ and $|s\rangle$, these are defined as follows:

$$\begin{aligned} I_x^{rs} &= \frac{1}{2}\left(|r\rangle\langle s| + |s\rangle\langle r|\right), \\ I_y^{rs} &= \frac{1}{2i}\left(|r\rangle\langle s| - |s\rangle\langle r|\right), \\ I_z^{rs} &= \frac{1}{2}\left(|r\rangle\langle r| - |s\rangle\langle s|\right), \\ \frac{1}{2}\mathbb{1}^{rs} &= \frac{1}{2}\left(|r\rangle\langle r| + |s\rangle\langle s|\right). \end{aligned} \tag{2.21}$$

2.6.1 M2S-S2M

To generate an AB molecular system, the symmetry of the molecule can be broken by several methods. One example consists of dissolving $^{13}C_2$-oxalate[68] into a mixture of $D_2{}^{16}O$ and $H_2{}^{18}O$. The substitution of ^{16}O nuclei for ^{18}O

nuclei within the molecule results in changes in the vibrational wavefunction. The change in fractional mass results in small isotope shifts, of the order of parts-per-billion, to be generated. Other symmetry-breaking mechanisms employ a remote stereogenic centre within the molecule[69], and a slightly asymmetrical functional group distribution[70] around the singlet spin-pair, which we will encounter in the following chapters.

The small difference between the chemical shifts is sufficient for the M2S-S2M pulse sequence to prepare singlet order. The full pulse sequence is drawn in Figure 2.5. Generally, singlet NMR pulse sequences display this type of structure. First, singlet order is prepared. This is followed by a relaxation delay τ_{relax}, where singlet order is allowed to evolve/decay. The T_{S} time may be extracted by the incremental variation of the τ_{relax} delay, and subsequent fitting of the integrated signal to an exponential decay function. The last step of the sequence involves singlet order being converted back into longitudinal magnetisation, after which the NMR signal is acquired.

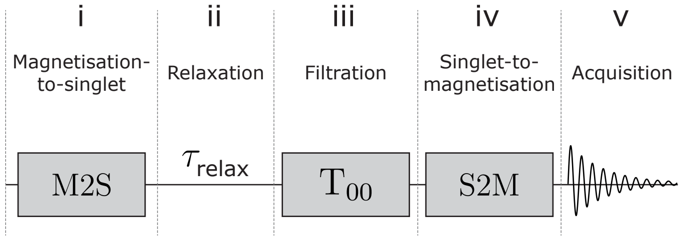

Figure 2.5: (**i**) The M2S pulse block excites singlet order. (**ii**) Singlet order evolves during the relaxation time τ_{relax}. (**iii**) A T_{00} filter removes any non-singlet operators. (**iv**) A time-reversed M2S sequence is applied: S2M, with the omission of the final 90°_{y} pulse (see Figure 2.6). (**v**) The NMR signal is acquired.

The magnetisation-to-singlet[69,71,72] (M2S) part of the sequence employs J-synchronised spin-echo train of pulses to induce singlet-triplet transitions. The singlet-to-magnetisation (S2M) sequence is the time-reversed M2S sequence, which converts singlet order back into longitudinal magnetisation. Figure 2.6 illustrates the M2S and S2M blocks of pulses.

The initial 90°_{y} pulse generates singlet-quantum coherences within the triplet manifold. Then, a J-synchronised train of spin echoes (JSE) is applied

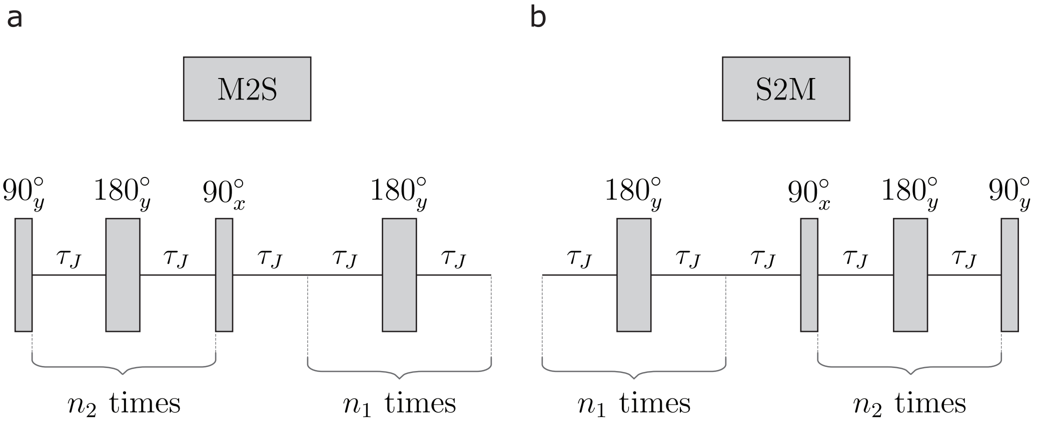

Figure 2.6: (**a**) Magnetisation-to-Singlet (M2S) pulse block structure. An initial 90°_y pulse is applied, followed by a J-synchronised echo train, where $\tau_J \approx (4J)^{-1}$, is applied for $n_2 \approx 2 \times [\text{round}\,(\pi/4\theta_{\text{ST}})]$ times. After a 90°_x pulse and another delay τ_J, a second J-synchronised echo train is applied for n_2 times, where $n_2 = 2n_1$. (**b**) Singlet-to-Magnetisation (S2M) pulse block structure. This is the chronological reverse of the M2S sequence.

n_2 times, which converts the single-quantum coherences into outer singlet-triplet (OST) coherences[73] ($|T_{+1}\rangle$-$|S_0\rangle$ or $|T_{-1}\rangle$-$|S_0\rangle$). The desired $|T_0\rangle$-$|S_0\rangle$ zero-quantum coherence is then generated by the 90°_x pulse. After a delay $\tau_J \approx (4J)^{-1}$, the second echo train is applied n_1 times to create the population difference between $|T_0\rangle$ and $|S_0\rangle$, which is singlet order.

The procedure can be visualised as a trajectory taking place in the zero-quantum subspace spanned by the $|S_0\rangle$ and $|T_0\rangle$ states. The overall effect of the JSE train of pulses results in the $|S_0\rangle$ and $|T_0\rangle$ states mixing. This is governed exclusively by the chemical shift difference, and the more magnetically-equivalent the two spins, the longer the singlet-triplet conversion, increasing the likelihood of encountering relaxation losses.

After an evolution time τ_{relax}, the S2M sequence (without the final 90°_y pulse) shown in Figure 2.6, is applied for readout. The trajectories of the operators involved in the pulse sequence are illustrated in Figure 2.8. This simple simulation does not include a T_{00} filtering step. In this case, the spin order is fully converted back to transverse magnetisation I_x, because the norm of the density operator is preserved throughout the sequence. If

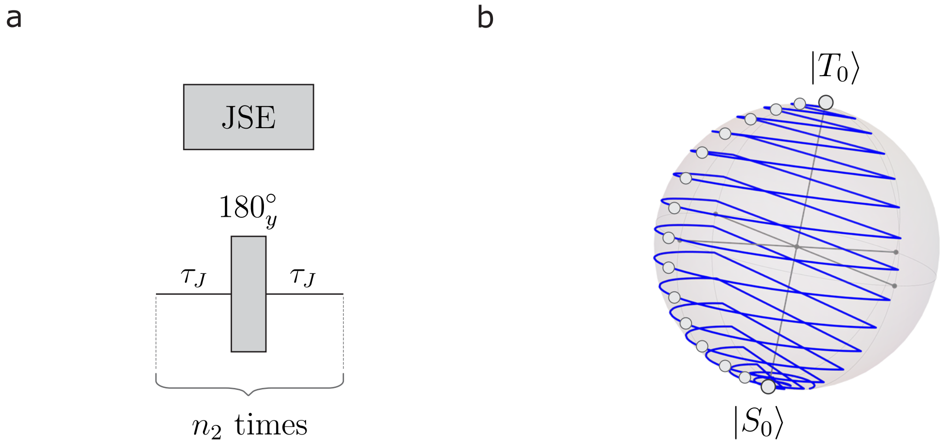

Figure 2.7: Bloch sphere trajectory of a JSE train of echoes, during the M2S pulse sequence. (**a**) Structure of a J-synchronised echo (JSE). This is repeated by an echo number n_2. (**b**) The buildup of the echoes causes the $|S_0\rangle$ and $|T_0\rangle$ states to mix. The overall effect is that of a π_z^{ZQ} rotation in the zero-quantum subspace spanned by the $|S_0\rangle$ and $|T_0\rangle$ states. The *SpinDynamica*[27] parameters used were $\Delta = 4.05$ Hz, $J = 40.1$ Hz, and $n_2 = 16$.

singlet order filtration had been employed at the midpoint of the sequence, selecting for the operator $-4/3\ (\boldsymbol{I_1} \cdot \boldsymbol{I_2})$ (whose operator norm is $\sqrt{(2/3)}$ times the operator norm of I_x), only a maximum of $2/3$ of the magnetisation could have been observed at the end of the sequence.

The M2S-S2M pulse sequence is designed to operate at high magnetic field, and in the strong-coupling/near-equivalence regime. A modification of the M2S sequence achieves robust singlet order excitation for systems well into the intermediate coupling regime, where the chemical shift difference and the J-coupling are of similar magnitude. This is the generalised magnetisation-to-singlet[74] (gM2S) procedure. For readout, the chronological reverse of gM2S, gS2M is applied.

A pulse sequence devised to achieve magnetisation-to-singlet conversion strictly within the weak-coupling/strong inequivalence regime is known as the Sarkar[47] pulse sequence, which involves a composite pulse decoupling[75] step. This procedure does not work very well outside strong inequivalence conditions.

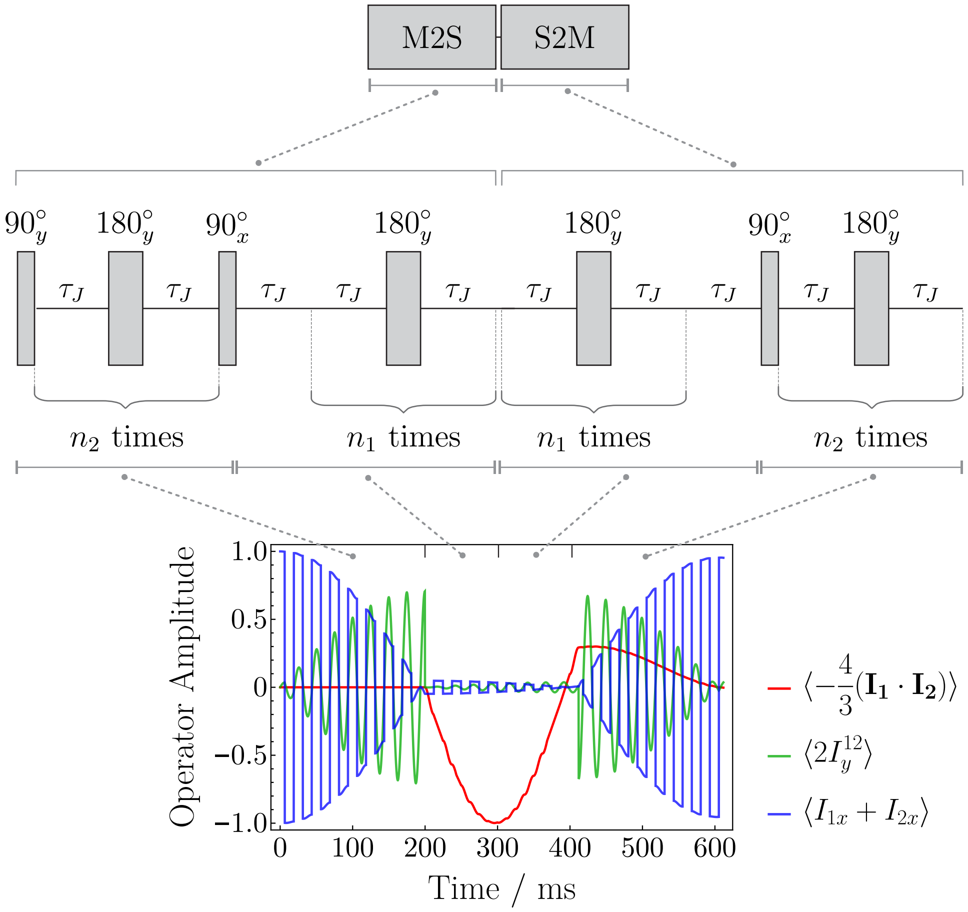

Figure 2.8: Time evolution of the singlet order operator $(-\frac{4}{3}(\mathbf{I_1} \cdot \mathbf{I_2}))$, the single-transition operator for one of the outer singlet-triplet coherences $2I_y^{12}$, and the x-magnetisation operator during the M2S-S2M pulse sequence. The *SpinDynamica*[27] parameters used are given in Table B.5 for 1,3-^{13}C$_2$-squarate.

2.6.2 SLIC

Spin-Lock Induced Crossing (SLIC)[76–81] is another method of exciting singlet order. After an initial 90°_ϕ pulse to generate transverse magnetisation, a spin-lock is applied. This is the SLIC block. The sequence is depicted in Figure 2.9.

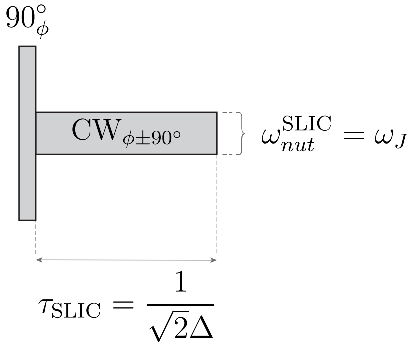

Figure 2.9: After an initial 90°_ϕ pulse, a continuous-wave (CW) pulse is applied, a spin-lock. This SLIC block must satisfy two requirements: First, its nutation frequency $\omega_{nut}^{\text{SLIC}} = \omega_J$, and second, the duration of the pulse $\tau_{\text{SLIC}} = (\sqrt{2}\Delta)^{-1}$. A 90° phase shift is applied with respect to the initial excitation pulse.

The following matching conditions[76,82] must be satisfied:

1. The nutation frequency ω_{nut} of the SLIC pulse must equal the intra-pair J-coupling $\omega_J = 2\pi J$ between the spin-pair being studied.
2. The duration τ_{SLIC} is synchronised with the chemical shift difference Δ between the spin-pair under consideration, as follows: $\tau_{\text{SLIC}} = (\sqrt{2}\Delta)^{-1}$.

Figure 2.10 shows SLIC integrated inside a wider pulse sequence for the purposes of singlet filtering and readout. After exciting singlet order, this evolves during a storage time τ_{relax}. This time can be varied in incremental steps to ultimately extract the singlet relaxation lifetime T_{S}. The filtration procedure removes any non rank 0 spin operators by the means of a T_{00} filter (Figure 2.14). A second SLIC pulse generates observable magnetisation again, and the signal can be readout.

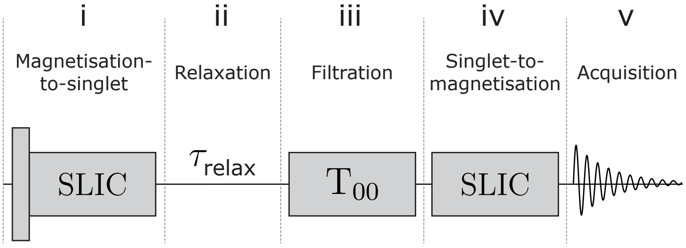

Figure 2.10: (**i**) Following an initial 90° pulse, the first SLIC pulse block excites singlet order, as described in Figure 2.9. (**ii**) Singlet order evolves during the relaxation time τ_{relax}. (**iii**) A T_{00} filter (Figure 2.14) removes any non-singlet operators. (**iv**) The second SLIC block allows the system to return to observable magnetisation for readout. (**v**) The NMR signal is acquired.

To draw an analogy with M2S, in this case the M2S echo trains have been replaced by a spin-lock, whose nutation frequency is matched to the J-coupling between the two spins. During the spin lock, polarisation transfer occurs between the singlet and one of the triplet states. SLIC generates singlet order faster compared to M2S, since $\tau_{\text{SLIC}} = \left(\sqrt{2}\Delta\right)^{-1} > \tau_{\text{M2S}} = [(3\pi)\,/\,(8\Delta)]$, where Δ is the chemical shift difference between the two spins. However, the method is especially sensitive to rf field inhomogeneities and resonance offset effects. Therefore, it is less robust with respect to experimental imperfections, compared to M2S.

2.6.3 PulsePol

The PulsePol[83] sequence was originally engineered for optimal electron-nuclei polarization transfer in the study of nitrogen-vacancy (NV) centres in diamond[84]. Recently, it has been adapted by Sabba[85] *et al.* for singlet order excitation[85–88]. The pulse sequence consists of $\mathcal{R}$-elements, repeated in alternating phases. This notation is already known[89,90] from symmetry-based recoupling theory, originally developed for MAS solid-state NMR[91–94].

An RN_n^ν sequence is constructed from two basic $\mathcal{R}$-elements: $\mathcal{R}_\phi^0$ and $\mathcal{R}_{-\phi}^{0'}$. Each element is required to induce a total π rotation of the spins about the x-axis. The simplest $\mathcal{R}$-element is therefore just a simple 180°

pulse, with a phase $\phi = (\pi\nu)/N$ radians. Each $\mathcal{R}$-element must achieve the required rotation within a duration $\tau_R = n/(NJ)$. The second $\mathcal{R}$-element, $\mathcal{R}^{0'}_{-\phi}$, is built by changing the sign of all phases of the pulses belonging to the first $\mathcal{R}$-element. Each pair of elements is repeated $N/2$ times. The symmetry numbers N, n, and ν are integers. These define the selection rules by which the RN^{ν}_{n} sequence operates, which are described elsewhere[85,92]. Figure 2.11 shows the process of building an RN^{ν}_{n} sequence.

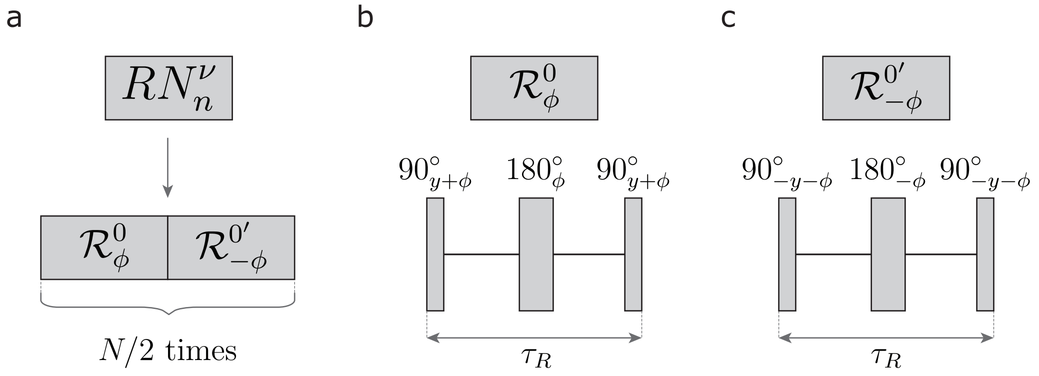

Figure 2.11: (**a**) A RN^{ν}_{n} sequence is constructed from two basic $\mathcal{R}$-elements: $\mathcal{R}^{0}_{\phi}$ and $\mathcal{R}^{0'}_{-\phi}$. The pair is repeated $N/2$ times.(**b**) Each $\mathcal{R}$-element must have the effect of generating an overall π rotation of the spins about the x-axis, with a duration of the $\mathcal{R}$-element $\tau_R = n/(NJ)$. This can be achieved by a π pulse, sandwiched between two $\pi/2$ pulses, each shifted by 90° in phase. The phase ϕ is given by $\phi = (\pi\nu)/N$ radians.(**c**) The second $\mathcal{R}$-element, $\mathcal{R}^{0'}_{-\phi}$, is built by giving a sign change to all the phases of the first $\mathcal{R}$-element, $\mathcal{R}^{0}_{\phi}$.

Although other combinations of symmetry numbers were examined[85], the $R4^{1}_{3}$ specific $\mathcal{R}$-element has shown the highest efficiency in exciting singlet order in solution, especially in its “riffled” implementation[85]. This is achieved by introducing an additional 180° phase shift on the central pulse within the second $\mathcal{R}$-element. As a result, this sequence is more robust compared to M2S-S2M with respect to rf error compensation. Figure 2.12 shows the general structure of the riffled implementation mode of PulsePol.

Similarly to other singlet NMR pulse sequences, PulsePol can also be included inside a pulse sequence module that allows for singlet order excitation, storage, filtration, and readout, as depicted in Figure 2.13.

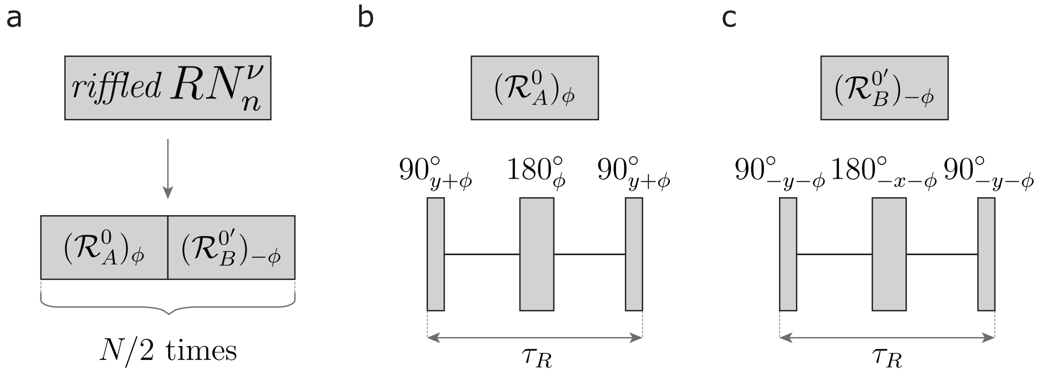

Figure 2.12: (**a**) A RN_n^ν sequence is constructed from two basic $\mathcal{R}$-elements: $(\mathcal{R}_A^0)_\phi$ and $(\mathcal{R}_B^{0'})_{-\phi}$. The pair is repeated $N/2$ times. (**b**) Each $\mathcal{R}$-element must have the effect of generating an overall π rotation of the spins about the x-axis, with a duration of the $\mathcal{R}$-element $\tau_R = n/(NJ)$. This can be achieved by a π pulse, sandwiched between two $\pi/2$ pulses, each shifted by 90° in phase. The phase ϕ is given by $\phi = (\pi\nu)/N$ radians. (**c**) The second $\mathcal{R}$-element, $(\mathcal{R}_B^{0'})_{-\phi}$, is built by giving a π phase shift to the central 180° pulse, and a sign change to all the phases compared to the first $\mathcal{R}$-element.

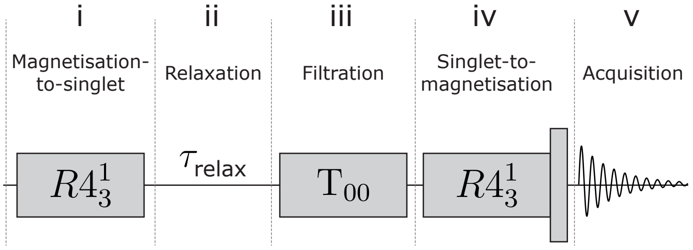

Figure 2.13: (**i**) The $R4_3^1$ sequence, known as "PulsePol", excites singlet order. This can be the standard implementation, or riffled. (**ii**) Singlet order evolves during the relaxation time τ_{relax}. (**iii**) A T_{00} filter removes any non-singlet operators. (**iv**) PulsePol is applied again to return to z-magnetisation, and a final 90° pulse is applied for readout. (**v**) The NMR signal is acquired.

Chapter 4 illustrates a new application of the PulsePol and SLIC pulse sequences. These procedures are well-established in the singlet NMR of nearly-equivalent spins, and have now been adapted[2] to excite double-quantum coherence in this coupling regime, since the standard methods are inefficient. We present a new variant of SLIC that is more robust with respect to deviations in the rf field amplitude[95], compared to the standard SLIC method.

2.6.4 Rank 0 Spin Order Selection/Suppression

In cases where singlet NMR experiments require repetition, such as when acquiring multiple transients, or measuring the singlet order decay time constant T_{S}, a waiting time of 3-5 T_{S} between transients is recommended. This exceeds the ordinary 3-5 T_1 requirement, since singlet relaxation is generally slower than longitudinal relaxation.

A time-efficient way of carrying out such experiments involves removing residual singlet order by applying a Singlet Order Destruction[96] (SOD) filter prior to the start of the pulse sequence, as described in Figure 2.14.

Firstly, the populations of the three triplet states are equalised with a T_{00} filter. This consists of a series of alternating hard pulses with well-defined phases, and gradient pulses, resulting in any non-singlet order being destroyed. Secondly, the populations between the singlet state, and the central triplet state are exchanged *via* a J-synchronised CPMG-based sequence.

This is repeated a number of $m \simeq (2\pi/3)/(2\theta_{\mathrm{ST}})$ times to achieve maximum destruction of singlet order. The j parameter is optional, and where it is included in the sequence, its value is chosen to be between $3-5$. The T_{00} filter and J-synchronised block can be further repeated as a whole for j times optionally, usually up to five loops, to maximise the SOD effectiveness.

The T_{00} filter consists of a series of alternating pulsed field gradients and radio-frequency pulses that aim to dephase any operators that do not have the symmetry of the T_{00} operator indicative of singlet order, thereby allowing only singlet operators to pass through. It can be written in the following form:

$$G_1 - 90°_{\theta_m} - G_2 - 90^\circ_{\theta_m} - 90^\circ_{-x} - G_3, \tag{2.22}$$

where $\theta_m \approx \arctan\sqrt{2}$, or the magic-angle (54.7°).

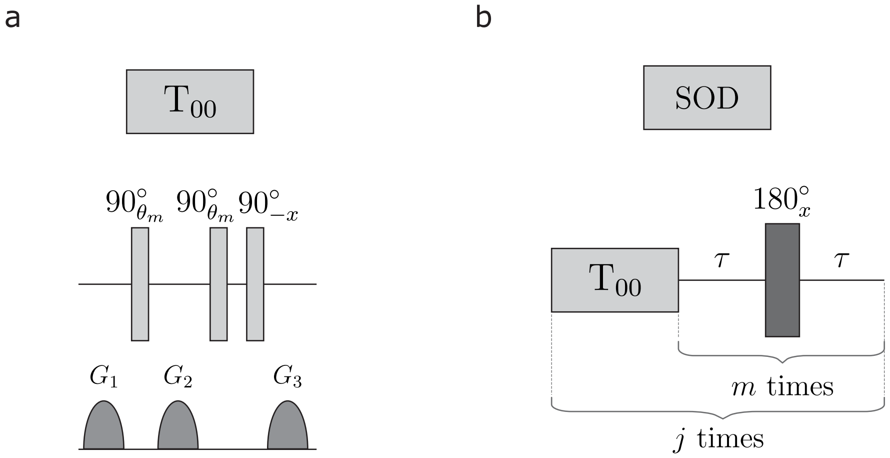

Figure 2.14: Singlet order filtering modules. (**a**) Description of the T_{00} filter used in singlet NMR experiments, where the phase $\theta_m \approx 54.7°$, the magic angle, and G_1, G_2 and G_3 indicate field gradients. (**b**) Singlet order destruction[96] (SOD) filter, used to remove residual singlet order from the system. The delay $\tau \simeq (4J)^{-1}$. The darker colour indicates the implementation of a composite 180° pulse[40]. Adapted from Heramun *et al.*[1], *J. Chem. Phys.* 163, 074201 (2025), Supporting Info; licensed under a Creative Commons Attribution (CC BY) license.

2.7 Singlet Order Relaxation Mechanisms

The following sections briefly summarise the major singlet order relaxation mechanisms. These are the dipole-dipole, chemical shift anisotropy, and spin rotation mechanisms. Other mechanisms that contribute to singlet order relaxation include interactions with paramagnetic species, such as oxygen, and fast-relaxing quadrupolar nuclei[97].

2.7.1 Intra-Pair Dipole-Dipole Mechanism

This mechanism involves the dipole-dipole interactions between the two spins in the singlet pair. The contributions to the longitudinal relaxation rate $R_1^{\mathrm{i-DD}}$, and the singlet order relaxation rate $R_S^{\mathrm{i-DD}}$ are given[98] as follows:

$$\begin{aligned} R_1^{\mathrm{i-DD}} &= \frac{3}{2} b_{12}^2 \tau_2, \\ R_S^{\mathrm{i-DD}} &= 0, \end{aligned} \tag{2.23}$$

where τ_2 is the rotational correlation time for this rank 2 interaction. Singlet order is unaffected by the intra-pair dipole-dipole relaxation mechanism.

The rotational correlation time τ_c corresponds, roughly, to the mean time required for the molecule to perform a rotation by one radian. In the extreme narrowing limit, $\omega^0 \tau_c \ll 1$, and T_1 is inversely proportional to τ_c.

2.7.2 Out-of-Pair Dipole-Dipole Mechanism

This mechanism presents itself from the dipole-dipole coupling of spins 1 and 2 within the singlet pair, and a third spin 3, within the same molecule. The contributions to the longitudinal relaxation rate $R_1^{\mathrm{op-DD}}$, and the singlet order relaxation rate $R_S^{\mathrm{op-DD}}$ are given[98] as follows, for spins 1, 2, and 3:

$$\begin{aligned} R_1^{\mathrm{op-DD}} &= \frac{1}{2}(3b_{12}^2 + b_{13}^2 + b_{23}^2)\tau_2, \\ R_S^{\mathrm{op-DD}} &= (b_{13}^2 + b_{23}^2 - 2b_{13}b_{23}\mathcal{P}_2 \cos(\Theta_{13,23}))\tau_2, \end{aligned} \tag{2.24}$$

where $\mathcal{P}_2(x) = 1/2(3x^2 - 1)$ is a Legendre polynomial[99], and $\Theta_{13,23}$ is the angle between the vectors connecting spins 1 and 3, and spins 2 and 3.

The contribution of the out-of-pair dipole-dipole mechanism decreases with a r^{-8} dependence, where r is the distance between spin 3, and the centre of the singlet spin-pair. In the context of synthesising ideal molecules containing spin-pairs that are able to form a long-lived state, it is important that the singlet spin-pair is sufficiently isolated from other spins.

2.7.3 Chemical Shift Anisotropy Mechanism

As previously mentioned in Chapter 1, the chemical shift tensor $\boldsymbol{\delta}$ (Equation 1.56) can be further reduced to three components: a rank 0 isotropic component δ_{iso}, a rank 1 antisymmetric component δ^{-}, and a rank 2 symmetric component δ^{+}, written as follows for a single spin:

$$\begin{aligned}\boldsymbol{\delta} = \delta_{\text{iso}} \begin{pmatrix} 1 & 0 & 0 \\ 0 & 1 & 0 \\ 0 & 0 & 1 \end{pmatrix} + \begin{pmatrix} 0 & \Delta_{xy} & \Delta_{xz} \\ -\Delta_{xy} & 0 & \Delta_{yz} \\ -\Delta_{xz} & -\Delta_{yz} & 0 \end{pmatrix} + \\ \begin{pmatrix} \delta_{xx} - \delta_{\text{iso}} & (\delta_{xy} + \delta_{yx})/2 & (\delta_{xz} + \delta_{zx})/2 \\ (\delta_{xy} + \delta_{yx})/2 & \delta_{yy} - \delta_{\text{iso}} & (\delta_{yz} + \delta_{zy})/2 \\ (\delta_{xz} + \delta_{zx})/2 & (\delta_{yz} + \delta_{zy})/2 & \delta_{zz} - \delta_{\text{iso}} \end{pmatrix},\end{aligned} \tag{2.25}$$

where $\Delta_{xy} = (\delta_{xy} - \delta_{yx})/2$, $\Delta_{xz} = (\delta_{xz} - \delta_{zx})/2$, and $\Delta_{yz} = (\delta_{yz} - \delta_{zy})/2$.

Both the symmetric and antisymmetric components cause the relaxation of longitudinal and singlet order. In special circumstances, however, singlet order remains unaffected by this relaxation mechanism. The detailed derivation of the expressions given below is explored elsewhere[59,98], and is herein reported to provide a better understanding of the mechanisms underlying singlet order relaxation.

If the δ^{+} symmetric component of the chemical shift tensor is identical for two spins, 1 and 2, the contribution of the CSA^{+} mechanism to singlet order relaxation vanishes, while the contribution to longitudinal order relaxation persists, as follows[98]:

$$\begin{aligned} R_1^{\text{CSA}^+} &= \frac{9}{45}\gamma_1\gamma_2(B^0)^2\tau_2(\delta_{\text{aniso}})^2(3+\eta^2), \\ R_S^{\text{CSA}^+} &= 0. \end{aligned} \tag{2.26}$$

If the biaxiality parameter η_1 for spin 1, and η_2 for spin 2 are both zero, the contribution of the CSA^{+} mechanism to the singlet order relaxation depends exclusively on the angle Θ between the two principal z-axes of the δ^{+} tensors of each nucleus making up the singlet spin-pair, as follows[98]:

$$R_S^{\mathrm{CSA}^+} = \frac{2}{27}\gamma_1\gamma_2(B^0)^2\tau_2\left[2(\delta^1_{\mathrm{aniso}})^2 + 2(\delta^2_{\mathrm{aniso}})^2 - \delta^1_{\mathrm{aniso}}\delta^2_{\mathrm{aniso}}(1+3\cos(2\Theta))\right]. \tag{2.27}$$

The contribution of the CSA- mechanism to the longitudinal and singlet order relaxation rates is given as follows[98], for two spins 1 and 2:

$$\begin{aligned} R_1^{\mathrm{CSA}^-} &= \frac{1}{3}\gamma_1\gamma_2(B^0)^2\tau_1[(\Delta^1_{xy})^2 + (\Delta^2_{xy})^2 + (\Delta^1_{xz})^2 + (\Delta^2_{xz})^2 + (\Delta^1_{yz})^2 + (\Delta^2_{yz})^2],\\ R_S^{\mathrm{CSA}^-} &= \frac{4}{9}\gamma_1\gamma_2(B^0)^2\tau_1[(\Delta^1_{xy} - \Delta^2_{xy})^2 + (\Delta^1_{xz} - \Delta^2_{xz})^2 + (\Delta^1_{yz} - \Delta^2_{yz})^2], \end{aligned} \tag{2.28}$$

where τ_1 is the rotational correlation time for this rank 1 interaction. The contribution of the CSA- mechanism to singlet order relaxation can therefore be minimised, if the antisymmetric part of the chemical shift tensor for each of the two nuclei making up the spin-pair is similar to the other.

Note that the rotational correlation times for interactions of differing ranks are different[98], as follows:

$$\tau_1 = 3\tau_2, \tag{2.29}$$

which may result in the CSA- mechanism having a greater effect on longitudinal and singlet order relaxation, compared to the CSA$^+$ mechanism.

The expressions for the CSA$^{\pm}$ [1] mechanisms on the rate of singlet order relaxation can be written as follows[98]:

$$\begin{aligned} R_S^{\mathrm{CSA}^+} &= \frac{4}{9}\gamma_1\gamma_2(B^0)^2\tau_2||\Delta\delta^+||^2,\\ R_S^{\mathrm{CSA}^-} &= \frac{2}{9}\gamma_1\gamma_2(B^0)^2\tau_1||\Delta\delta^-||^2, \end{aligned} \tag{2.30}$$

where $\Delta\delta^+$ and $\Delta\delta^-$ are the difference between the symmetric/antisymmetric parts of the chemical shift tensor, and are calculated as follows for spins 1 and 2:

$$\begin{aligned} \Delta\delta^+ &= \delta_1^+ - \delta_2^+,\\ \Delta\delta^- &= \delta_1^- - \delta_2^-, \end{aligned} \tag{2.31}$$

in the molecular reference frame, and where the Frobenius norm applies. For a 4x4 matrix $\boldsymbol{Q}$, $||\boldsymbol{Q}|| = \sqrt{\mathrm{Tr}(\boldsymbol{Q}\boldsymbol{Q}^\dagger)}$.

2.7.4 Spin-Rotation Mechanism

The spin-rotation relaxation mechanism is especially prominent in small, symmetrical molecules in non-viscous solvents, or in the gas phase. It arises due to the coupling between the singlet spin-pair nuclei, and the magnetic field generated due to the rotation of the molecule itself as it tumbles.

One of the most notable examples of a molecule that displays a dominant spin-rotation contribution to the relaxation of its singlet order is $^{15}N_2O$, nitrous oxide. It has been shown[45,55] that, in the case of pure spin-rotation, the following ratio between T_S and T_1 applies:

$$\frac{T_S}{T_1} = \frac{C_1^2 + C_2^2}{2(C_1 - C_2)^2}, \tag{2.32}$$

where C_1 and C_2 are the magnitudes of the spin-rotation couplings for the two inequivalent ^{15}N sites within nitrous oxide.

Chapter 3

Singlet NMR in a Case of High Molecular Symmetry

Coupled pairs of spin-1/2 nuclei support one singlet state, and three triplet states. Singlet order is defined as the mean population difference between the singlet and triplet manifolds. Nuclear singlet order decays with a relaxation time constant T_S, that in suitable conditions may be slower than the decay of longitudinal magnetisation, characterised by the T_1 relaxation time constant.

In this chapter, we explore the nuclear singlet relaxation of a highly symmetrical isotopologue of the squarate molecule in high pH conditions. The 1,3-$^{13}C_2$-squarate species of interest is present in minor quantities in an aqueous solution of $^{13}C_1$-squarate. To break the symmetry of this molecule, ^{18}O-enrichment was used, providing access to $^{13}C_2$ double-quantum coherence, and $^{13}C_2$ singlet order. Secondary isotope shifts of the ^{13}C NMR resonance were measured in high and low pH solutions.

The ^{13}C signals from the ^{18}O-enriched 1,2-$^{13}C_2$-squarate and 1,3-$^{13}C_2$-squarate species were selectively acquired by applying the geometric double-quantum (GeoDQ) filtering pulse sequence. The double-quantum coherence was subsequently converted to singlet order, and back again, using the double-quantum-to-singlet (DQ2S) and singlet-to-double-quantum (S2DQ) pulse sequences. We report the $^{13}C_2$-singlet lifetime measurement of ^{18}O-enriched 1,3-$^{13}C_2$-squarate in high pH conditions, and at high magnetic field.

3.1 Introduction

The squarate dianion is the conjugate base of squaric acid. Squarate is planar and rigid, thanks to resonance stabilisation from π-electron delocalisation within the ring, as shown in Figure 3.1. This highly symmetric structure possesses $D_{4\mathrm{h}}$ point group symmetry[100]:

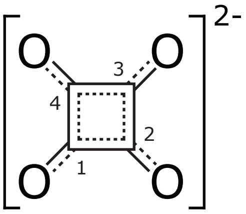

Figure 3.1: Molecular structure of the squarate dianion (IUPAC: 3,4-Dihydroxycyclobut-3-ene-1,2-dione).

Within this molecule, the long-lived state of two different pairs of $^{13}C_2$-spins in solution is available to access: 1,2-$^{13}C_2$-squarate, or 1,3-$^{13}C_2$-squarate. The first structure has previously been studied[48] by singlet NMR, where proton exchange effects were shown to induce premature singlet relaxation. When the exchange effects were minimised, namely at high pH, singlet order was successfully generated, and the singlet lifetime relaxation constant T_S was measured. The second species remains unexplored so far.

The two ^{13}C sites within 1,2-$^{13}C_2$-squarate are related to each other by a $\pi/2$ rotation about the C_4 principal rotation axis perpendicular to the centre of squarate. Their respective CSA tensors have the same values. However, the principal axes of the two CSA tensors are not identical, since they are also related by a $\pi/2$ rotation about the C_4 axis. The ^{13}C CSA tensors of 1,2-$^{13}C_2$-squarate were calculated using ORCA[101], and are represented by ovaloids[102,103]. These are overlaid with the squarate backbone in Figure 3.3(a). Since the two ^{13}C tensors have different orientations, the difference between the two CSA tensors, which contributes to singlet order relaxation[63,104–106], is non-zero. Therefore, even though the squarate dianion itself is highly symmetrical, the two ^{13}C nuclei of 1,2-$^{13}C_2$-squarate are not positioned in the favourable configuration that results in the suppression of the CSA contribu-

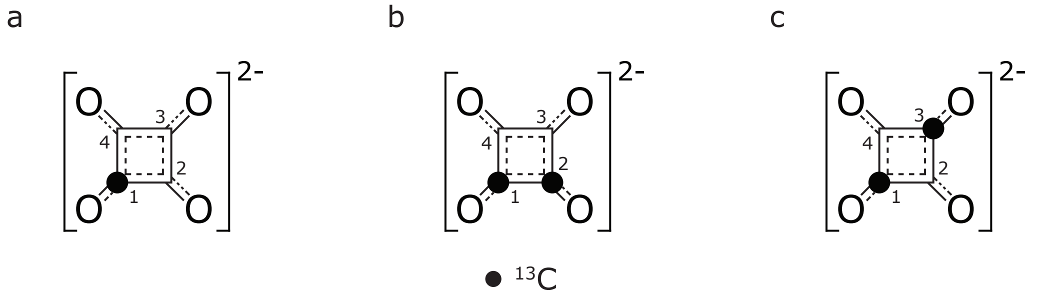

Figure 3.2: Molecular structures of the squarate dianion, containing one or two ^{13}C atoms, indicated by filled circles. The squarate dianion is the dominant species in high-pH solutions of squaric acid. (**a**) $^{13}C_1$-squarate; (**b**) 1,2-$^{13}C_2$-squarate, as studied in Ref.[48]; (**c**) 1,3-$^{13}C_2$-squarate. In the current work, double-quantum filtering is used to suppress the ^{13}C NMR signals of $^{13}C_1$-squarate, allowing the observation of signals from the 1,2-$^{13}C_2$-squarate and 1,3-$^{13}C_2$-squarate isotopologues. Adapted from Heramun *et al.*[1], *J. Chem. Phys.* 163, 074201 (2025); licensed under a Creative Commons Attribution (CC BY) license.

tion to singlet relaxation. This applies to the contribution of the spin-rotation mechanism[64] to singlet relaxation as well.

On the other hand, the $^{13}C_2$ nuclei within the 1,3-$^{13}C_2$-squarate isotopologue, shown in Figure 3.2(c), are arranged in the optimal symmetry required for the effective suppression of CSA relaxation. The two ^{13}C sites are related by inversion of symmetry operation about the inversion centre i lying in the centre of squarate, in addition to a π rotation about the two C_2 rotation axes, and $2 * \pi/2$ rotations about the C_4 principal rotation axis. Generally, any two molecular sites related by inversion have identical CSA and spin-rotation tensors[107], as shown in Figure 3.3(b). As a consequence, the CSA and spin-rotation contributions to the $^{13}C_2$ singlet relaxation of 1,3-$^{13}C_2$-squarate is completely eliminated, assuming the molecule remains rigid.

To ultimately study the $^{13}C_2$ singlet order of 1,3-$^{13}C_2$-squarate by experiment, a few more steps are required. First of all, the 1,3-$^{13}C_2$-squarate species could not be synthesised directly, due to difficulties during the synthesis. In order to overcome this challenge, we instead examined a sample containing $^{13}C_1$-squarate where, of the four positions in the carbon skeleton (C1-C4 (Figure 3.1)), one was carbon-13 labelled (C1) during the synthetic procedure.

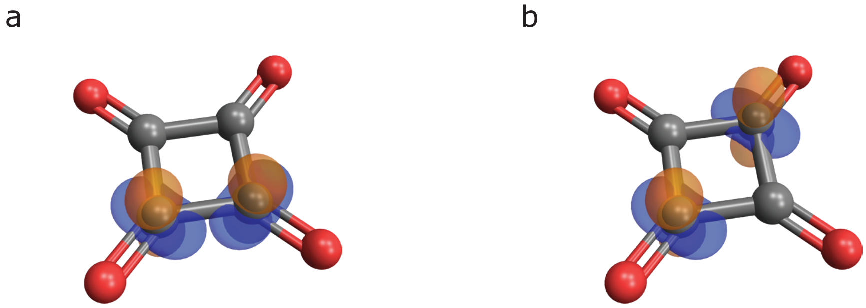

Figure 3.3: Ovaloid representations[102,103] of the ^{13}C CSA tensors, superimposed on the structure of the squarate dianion ($C_2O_4{}^{2-}$). (**a**) The ^{13}C CSA tensors of 1,2-$^{13}C_2$-squarate. (**b**) The ^{13}C CSA tensors of 1,3-$^{13}C_2$-squarate. Further details on the tensor calculations are given in Appendix B.1.1. Adapted from Heramun *et al.*[1], *J. Chem. Phys.* 163, 074201 (2025); licensed under a Creative Commons Attribution (CC BY) license.

However, this results in the smaller signals arising from the $^{13}C_2$-squarate isotopologues being obscured by the strong signals given by the $^{13}C_1$-squarate species in the ^{13}C NMR spectrum. Fortunately, double-quantum filtration methods such as the INADEQUATE pulse sequence[108] have been used extensively to selectively detect natural-abundance ^{13}C signals from coupled $^{13}C_2$ species, while suppressing the large signals from $^{13}C_1$ uncoupled species. This pulse sequence is shown in Figure 3.4, and was previously encountered in Chapter 1 to explain phase cycling.

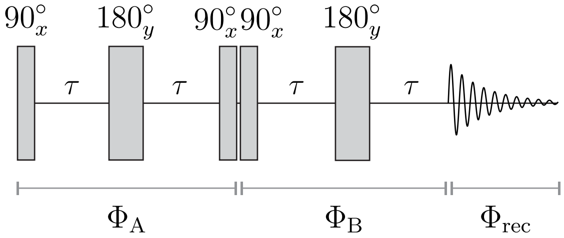

Figure 3.4: Refocused INADEQUATE pulse sequence. For weakly-coupled systems, $\tau \simeq (4J)^{-1}$. For near-equivalent and strongly-coupled systems, $\tau \simeq J/(2\Delta^2)$. The phases of the pulses may be grouped in "blocks": Φ_A, Φ_B and Φ_{rec} as the receiver phase.

Second, the symmetrical structure of squarate must be broken prior to applying suitable rf pulses to generate double-quantum coherences. To this end, random oxygen-18 enrichment was used, as previously done for the singlet NMR studies of $^{13}C_2$-oxalate[68], 1,2-$^{13}C_2$-squarate[48], and $^{103}Rh_2$-paddlewheel complexes[87]. The substitution of the lighter ^{16}O isotope for the ^{18}O heavier isotope modifies the vibronic motion within the molecular environment, causing small secondary *isotope shifts* of the ^{13}C chemical shift value[109–115]. The upcoming section examines the properties of the isotope shifts in NMR.

3.2 Isotope Shifts in NMR

Isotopes of the same element have the same atomic number, but differ in their mass number, since heavier isotopes contain additional neutrons.

Changes in the chemical shift (Subsection 1.10.3) due to the perturbation of the vibrational wavefunction of the molecule upon substitution of one or more atoms for one of its isotopes are denoted *isotope shift effects*.

Primary isotope shift effects occur when the nucleus directly under observation is substituted. Secondary isotope shift effects are those where a nucleus in proximity to the resonant NMR nucleus is switched for one of its isotopes.

The following observations and general trends were reported in a review[110] of the isotope shifts in NMR by Batiz-Hernandez in the 1960s, and later verified in the work of Jameson[111]:

1. Heavier isotope substitution shifts the NMR signal of the nucleus under observation to a higher magnetic field (i.e. upfield).

2. The magnitude of the isotope shift depends on the distance from the isotopically substituted site to the nucleus under observation. The largest isotope shifts are observed for a substitution site one bond away from the resonant nucleus.

3. The magnitude of the isotope shift reflects the range of chemical shifts that a particular nucleus experiences. Resonant nuclei with higher sensitivity to shielding will experience an isotope shift higher in magnitude than nuclei with narrower chemical shift ranges. For example, isotope

shifts in ^{59}Co are of the order of parts-per-million[116], whereas in ^{13}C and ^{1}H, the observed isotope shifts are of the order of parts-per-billion.

4. The magnitude of the isotope shift is the largest where the change in the mass fraction upon isotopic substitution has been the most substantial.
5. The magnitude of the isotope shift is generally proportional to the amount of atoms (of the same type) within the molecule that have undergone substitution.

In addition to the through-bond isotope shift effects, solvent-induced isotope shift effects for ^{19}F-substituted derivatives of benzene have been observed[117] in mixtures containing 1:1 H_2O:D_2O. The change in chemical shift is caused by hydrogen bonding of the fluorobenzene with the solvent, since deuterium has a different vibrational behaviour than water. Electron-donating substituents attached to the benzene ring, especially in the *ortho*-positions, have been observed to increase solvent-induced isotope shift effects. This is due to the additional negative charge placed on the ^{19}F-nucleus by mesomerism, which strengthens intermolecular hydrogen bonding.

Pinchas and Meshulan first observed[118] ^{18}O-induced isotope shifts of the ^{1}H nucleus in ^{1}H NMR spectra. Later in the same decade, Risley and van Etten observed[119] ^{18}O-induced isotope shifts of ^{13}C in ^{13}C NMR. Isotope shifts arising from the presence of ^{18}O have been observed[120] to affect ^{55}Mn and ^{95}Mo NMR spectra, as well as ^{31}P spectra[121].

Attempts at predicting isotope shifts have been made[122], however these effects depend on too many variables to allow for a systematic prediction method to be established.

3.3 Double-Quantum Excitation in the Near-Equivalence Regime

The standard double-quantum filtering method is not suitable for our particular case. The INADEQUATE sequence requires a large chemical shift difference Δ between the two coupled spins, relative to the scalar coupling J between them. This is the *weak-coupling* case[123]. Figure 3.5 illustrates the theoretical amplitude buildup of the double-quantum coherence operator, written as $-2(I_{1x}I_{2y} + I_{1y}I_{2x})$ in Cartesian form, as a function of the chemical shift difference Δ for the INADEQUATE pulse sequence.

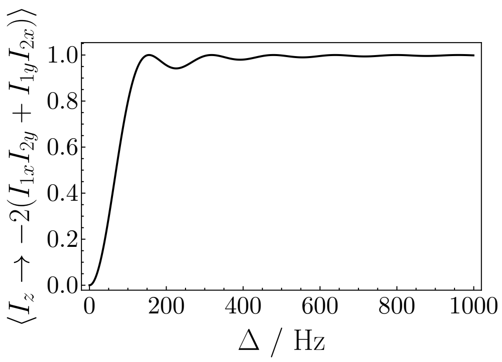

Figure 3.5: Dependence of the double-quantum amplitude buildup (Equation 3.1) on the chemical shift difference Δ for the INADEQUATE pulse sequence (Figure 1.9). The *SpinDynamica*[27] simulation used $J = 40.1$ Hz.

This simulation employs the `TransformationAmplitude` routine within *SpinDynamica*[27], which outputs the amplitude for the conversion of operator A, in this case the thermal equilibrium z-magnetisation, into operator B, the double-quantum coherence, by the unitary transformation U. This is the *transformation amplitude*[124] operation $\langle A \xrightarrow{U} B\rangle$, which is defined as follows:

$$\langle A \xrightarrow{U} B\rangle = \frac{(B|UAU^\dagger)}{(B|B)}, \tag{3.1}$$

where the Liouville bracket[22] is given by:

$$(B|A) = \mathrm{Tr}\{B^\dagger A\}. \tag{3.2}$$

The rotating-frame spin Hamiltonian for a homonuclear spin-1/2 pair, in the absence of a radiofrequency field, is given by the following:

$$H^0 = \Omega_1 I_{1z} + \Omega_2 I_{2z} + H_J. \tag{3.3}$$

The J-coupling Hamiltonian H_J is given by:

$$H_J = \omega_J \, \mathbf{I}_1 \cdot \mathbf{I}_2, \tag{3.4}$$

where:

$$\begin{aligned} \omega_J &= 2\pi J, \\ \omega_\Delta &= 2\pi\Delta, \\ \Omega_{\mathrm{ST}} &= 2\pi\sqrt{J^2+\Delta^2}. \end{aligned} \tag{3.5}$$

The chemical shift difference is Δ, and the effective frequency of the system is Ω_{ST}. The resonance offset frequencies for the spins are defined as follows:

$$\begin{aligned} \Omega_1 &= \omega^0(\delta_1 - \delta_{\mathrm{ref}}), \\ \Omega_2 &= \omega^0(\delta_2 - \delta_{\mathrm{ref}}). \end{aligned} \tag{3.6}$$

The terms $\{\delta_1, \delta_2, \delta_{\mathrm{ref}}\}$ indicate the chemical shift of spin I_1, spin I_2, and the rf reference frequency, respectively.

The Hamiltonian can be expressed in the following form as well:

$$H^0 = \frac{\Omega_{\mathrm{ST}}}{2} \sin(\theta_{\mathrm{ST}})\left(I_{1z} - I_{2z}\right) + \Omega_{\mathrm{ST}} \cos(\theta_{\mathrm{ST}})\left(\mathbf{I_1} \cdot \mathbf{I_2}\right). \tag{3.7}$$

Systems where $\theta_{\mathrm{ST}} \gtrsim 70^\circ$ are said to be *weakly coupled.* Systems where $\theta_{\mathrm{ST}} \lesssim 70^\circ$ are said to be *strongly coupled.* The extreme strong-coupling regime $\theta_{\mathrm{ST}} \lesssim 30^\circ$ is the main focus here, the *near-equivalence*[56,69] case. The singlet-triplet mixing angle is small in magnitude for a near-equivalent AB system, approaching $\pi/2$ for the weak-coupling AX case.

The ^{18}O-induced secondary isotope shifts of ^{13}C-squarate are small, of the order of a few parts-per-billion (ppb). The $^{13}C_2$ coupled systems subsequently generated are of the *near-equivalence* or *extreme strong coupling* type. This means that the chemical shift frequency difference is much smaller compared to the J-coupling[69]. The standard INADEQUATE (Figure 3.4) pulse sequence[123] has very poor efficiency in the near-equivalence regime. The simulation in Figure 3.6 shows the buildup of the double-quantum operator as a function of the singlet-triplet mixing angle θ_{ST} (Equation 2.13).

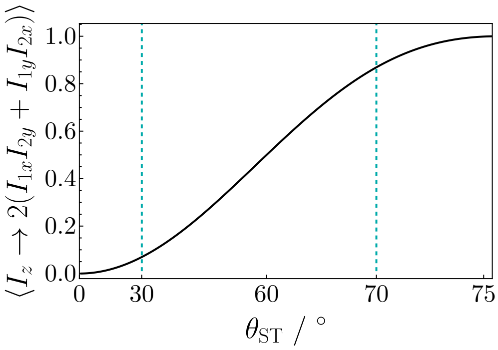

Figure 3.6: Dependence of the double-quantum amplitude buildup (Equation 3.1) on the singlet-triplet mixing angle θ_{ST} for the refocused INADEQUATE pulse sequence. The *SpinDynamica*[27] simulation used $J = 40.1$ Hz.

The Nakai-McDowell modified implementation[125] of the INADEQUATE pulse sequence was devised to excite double-quantum coherence in strongly-coupled spin systems, as depicted in Figure 3.7(b).

Figure 3.8 shows the time evolution of the double-quantum *precursor* DQP operator for the traditional INADEQUATE sequence in part (a), and the Nakai-McDowell method in part (b). In the Cartesian operator form, this is written as $2(I_{1x}I_{2z} + I_{1z}I_{2x})$, or $2(I_{1y}I_{2z} + I_{1z}I_{2y})$, depending on the phase of the initial rf pulse. Following a 90° pulse, the double-quantum operator is obtained, explaining the name. The standard INADEQUATE sequence fails to generate the double-quantum precursor operator required, but by greatly extending the double-quantum excitation time, it is possible to obtain a maximum amplitude of the DQP operator. This however massively extends the time employed to excite double-quantum coherence, leading to considerable T_2 relaxation losses.

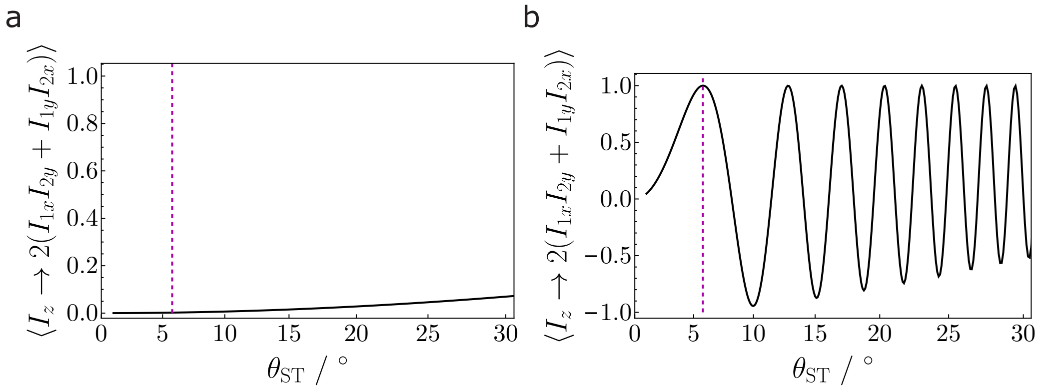

Figure 3.7: Dependence of the double-quantum amplitude buildup (Equation 3.1) on the singlet-triplet mixing angle θ_{ST} for the refocused INADEQUATE pulse sequence (Figure 1.9), applied to a strongly-coupled/near-equivalent spin system. The *SpinDynamica*[27] parameters used were $\Delta = 4.05$ Hz and $J = 40.1$ Hz to create these conditions, where the resulting $\theta_{\mathrm{ST}} \simeq 5.8°$ is indicated by a dashed line. (**a**) Traditional INADEQUATE implementation, where $\tau \simeq (4J)^{-1}$. (**b**) Nakai-McDowell implementation of the INADEQUATE sequence, where $\tau \simeq J/(2\Delta^2)$.

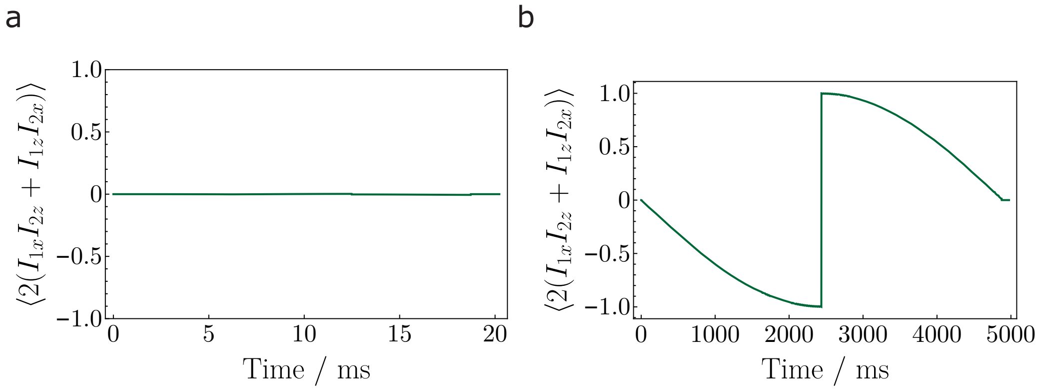

Figure 3.8: Time evolution of the double-quantum precursor amplitude operator (Equation 3.1) for the refocused INADEQUATE pulse sequence (Figure 1.9), applied to a strongly-coupled/near-equivalent spin system. The *SpinDynamica*[27] parameters used were $\Delta = 4.05$ Hz and $J = 40.1$ Hz to create these conditions. (**a**) Traditional INADEQUATE implementation, where $\tau \simeq (4J)^{-1}$. (**b**) Nakai-McDowell implementation of the INADEQUATE sequence, where $\tau \simeq J/(2\Delta^2)$.

Fortunately, a technique known as geometric double-quantum excitation (GeoDQ) exploits the geometric Aharanov-Anandan[126,127] quantum phase to generate double-quantum coherences with high efficiency in near-equivalent spin-1/2 pairs[128]. This is a generalisation[129] of the Berry phase[130,131], for non-adiabatic systems, which is the regime that applies to NMR experiments.

In the work described below, we used GeoDQ to selectively detect the small $^{13}C_2$ signals from a sample containing $^{13}C_1$-squarate, while suppressing the intense signals from the uncoupled ^{13}C nuclei. The DQCs were converted into singlet order by manipulating the spins further, allowing study of the $^{13}C_2$ long-lived state of 1,2-$^{13}C_2$-squarate, and 1,3-$^{13}C_2$-squarate.

The ^{18}O enrichment employed as the symmetry-breaking mechanism generates a multitude of isotopologues. We measured pH dependent secondary isotope shifts due to the ^{18}O substitution at low and high pH, and ^{13}C-induced isotope shifts from the natural abundance second ^{13}C site for the high pH case. The evidence suggests that an additional mechanism is present at low pH, where the acid-base equilibrium is perturbed by the ^{16}O to ^{18}O substitution in sites where protonation occurs. The combination of the dynamic and vibronic mechanisms result in the measured secondary isotope shift values.

The GeoDQ sequence was successfully implemented to selectively detect the ^{13}C NMR signals from the ^{18}O-enriched isotopologues of 1,2-$^{13}C_2$-squarate and 1,3-$^{13}C_2$-squarate, which are AB type molecular systems. In both cases, the chemical shift difference between the two ^{13}C spins is not well-resolved.

The GeoDQ pulse sequence was further modified, and the GeoDQ-singlet variant allowed the excitation of double-quantum filtered singlet order, and back for readout. This procedure allowed the measurement of the $^{13}C_2$ singlet lifetimes of 1,2-$^{13}C_2$-squarate, and 1,3-$^{13}C_2$-squarate, the latter for the first time, in high magnetic field.

3.4 Materials and Methods

3.4.1 Sample Preparation

The samples consisted of 4.6 mg of $^{13}C_1$-squaric acid, dissolved in 400 μL of a 1:1 mixture of $H_2{}^{18}O$:$D_2{}^{16}O$ to make up a 0.1 M solution. The isotopic purity of $H_2{}^{18}O$ was 97.1 %. The solutions were incubated at 80°C for two hours, to allow the $^{16}O/^{18}O$ exchange process to reach a dynamic equilibrium. Samples with differing pH values were prepared by step-wise addition of a 2 M solution of sodium hydroxide. For each instance, the volume did not exceed 65 μL, and therefore any effects on sample concentration were deemed negligible. The pH measurements were carried out with a Hamilton SpinTrode pH electrode (www.hamiltoncompany.com). The calibration of the pH meter was verified over the full pH range, using standard buffers. Where degassed relaxation lifetimes are shown, this was achieved using the standard freeze-thaw procedure under inert atmosphere.

3.4.2 Instrumental Details

The solution-state NMR experiments used Bruker Neo Avance systems of 400 MHz and 700 MHz. The first is equipped with a 5 mm Bruker BBO probe, the second with a Bruker TCI prodigy 5 mm cryoprobe. The 90° pulse length was optimised to (9.2 ± 0.1) μs at 400 MHz, and (12.8 ± 0.1) μs at 700 MHz.

3.5 Results

Squaric acid ($C_4O_4H_2$), the hydrogen squarate ($C_4O_4H^-$) monoanion, and the squarate ($C_4O_4{}^{2-}$) dianion are in a dynamic equilibrium with each other. Squaric acid is most abundant below the $pKa_1 = 1.5$. Beyond $pKa_2 = 3.4$, squarate prevails. Between pKa_1 and pKa_2 hydrogen squarate dominates the distribution of species in solution. Figure 3.9 shows the fractional composition of the three species in solution.

We observed the ^{13}C NMR signal position of ^{18}O-enriched $^{13}C_1$-squarate

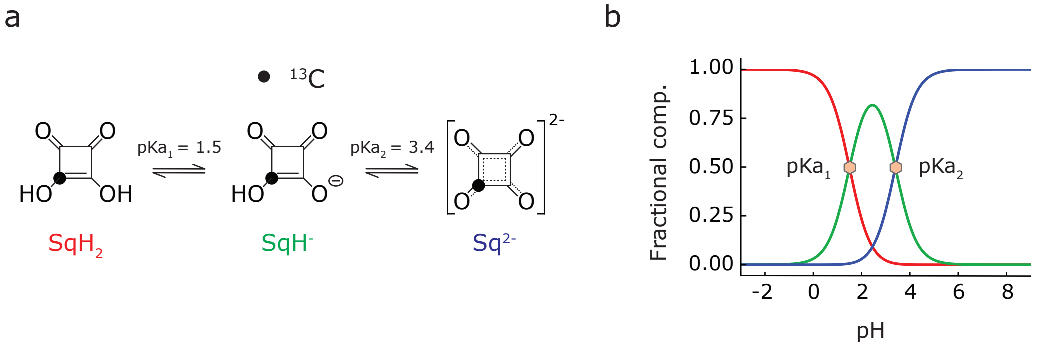

Figure 3.9: (**a**) Dynamic equilibrium displayed by $^{13}C_1$-squaric acid in solution. The diprotic squaric acid SqH_2 (red) is most abundant below $pKa_1 = 1.5$, while the squarate dianion Sq^{2-} (blue) dominates beyond $pKa_2 = 3.4$. Between the two extremes is the singly-protonated species hydrogen squarate SqH^- (green). (**b**) Fractional composition diagram showing the distribution of the various species of squaric acid at different pH values. Each pKa value equals the pH at the corresponding half-equivalence point. Adapted from Heramun *et al.*[1], *J. Chem. Phys.* 163, 074201 (2025); licensed under a Creative Commons Attribution (CC BY) license.

shifting downfield (i.e. to higher values of the chemical shift δ_{iso}) as the pH is increased, as shown in Figure 3.10(a). The mean ^{13}C chemical shift changed by $\approx +7.7$ ppm as the pH increased from 0.9 to 13.3. The aromatic character of the molecule increases with more electron delocalisation as the protons ionise, leaving the ^{13}C nucleus under observation increasingly deshielded.

The ^{18}O-enrichment gives rise to isotope shifts of the ^{13}C signal extending over one, two, and three bonds. Furthermore, we observed one and two-bond isotope shifts of the ^{13}C resonance due to the presence of natural abundance carbon-13 nuclei one or two bonds away from the ^{13}C isotopic label.

Contrary to the fact that isotope shift effects generally weaken in strength with increasing distance from the substituted nucleus, the ^{18}O-induced two-bond secondary isotope shift of ^{13}C at pH 0.9 was observed to be smaller in magnitude than the three-bond ^{18}O-induced isotope shift of ^{13}C. Secondly, the observed peak pattern of the pH 13.3 sample suggests that the ^{18}O-induced two-bond secondary isotope shift of ^{13}C is very small.

The experimentally measured isotope shift values at pH 0.9 and pH 13.3 are summarised in Tables 3.1, and 3.2, respectively. The change of the ^{13}C

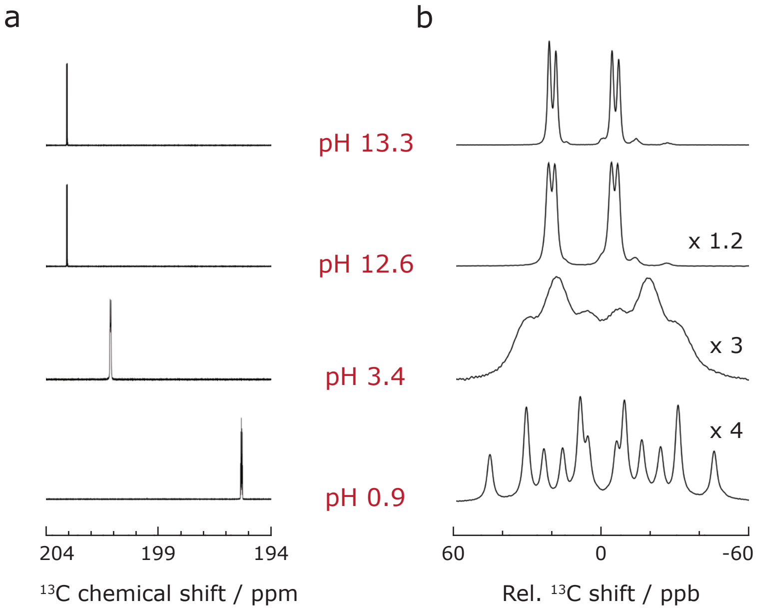

Figure 3.10: (**a**) Variation in the ^{13}C chemical shift positions as a function of pH for samples of ^{18}O-enriched $^{13}C_1$-squaric acid dissolved in 1:1 $H_2{}^{18}O$:$D_2{}^{16}O$. Each spectrum was acquired for 200 transients at 9.4 T and 298 K. (**b**) Expansion of the relevant spectral region for each pH point shown, spanning 120 ppb. The chemical shift scale at pH 0.9 is centred around 195.32 ppm, 201.12 ppm at pH 3.4, and 203.05 ppm at pH 12.6 and pH 13.3. The vertical scales are given with respect to the pH 13.3 spectrum. Adapted from Heramun *et al.*[1], *J. Chem. Phys.* 163, 074201 (2025); licensed under a Creative Commons Attribution (CC BY) license.

chemical shift as a function of pH is due to the dynamic equilibrium between the squarate dianion, hydrogen squarate ($C_2O_4H^-$), and squaric acid ($C_2O_4H_2$) molecules, as shown in Figure 3.9. The observed ^{13}C chemical shift is a population-weighted average of the ^{13}C chemical shifts of the rapidly exchanging species in solution. This leads to a strong pH dependence of the mean ^{13}C chemical shift, as shown in Figure 3.10(a).

There are two relevant mechanisms that govern the secondary isotope shifts, the *vibronic* and *dynamic* mechanisms, as explored in Section 3.2. In the low pH case, both mechanisms are active, which could explain the unusually low value of the two bond $^2\Delta^{13}C(^{18}O)$ isotope shift. In the high pH case, the isotope shifts are largely due to the vibronic mechanism alone, since there are very few protonation events.

The secondary isotope shifts are described according to the convention previously set by the studies concerning ^{18}O-enriched oxalate[68], 1,2-$^{13}C_2$-squarate[48], and rhodium paddlewheel complexes[87], as following:

$$^{n}\Delta \mathrm{X}(h) = \delta_{\mathrm{X}}(h) - \delta_{\mathrm{X}}(l), \tag{3.8}$$

where Δ represents the chemical shift difference after substitution, X the nucleus being observed, h the heavier isotope, l the lighter isotope, and n the number of chemical bonds separating X and h.

The upcoming spectra show stylised squarate structures that are not representative of the exact ionic species in solution, but merely indicate the positions of the ^{18}O, ^{16}O and ^{13}C nuclei with respect to each other.

3.5.1 pH 0.9

The ^{13}C spectrum of ^{18}O-enriched squarate at pH 0.9 is shown in Figure 3.11.

Peaks 1-12 were successfully matched to their corresponding isotopomer by measuring the displacement of the NMR resonance from the left-most peak. The isotope shifts are additive, therefore the peak that was most downfield/less shielded was taken as the reference isotopomer, since it is not affected by any isotope shift interactions. The other peaks were referenced to the left-most peak according to the number of isotope shift interactions that are present in each isotopomer, subsequently matching each peak. The carbon-13 “satellite” peaks indicative of coupled ^{13}C nuclei were not directly visible from this spectrum. Therefore, only the isotope shifts of ^{13}C due to ^{18}O substitution were measurable.

The detailed assignment procedure for each isotopomer is illustrated in Appendix B.2.1. The experimentally measured isotope shifts are reported in Table 3.1, where the uncertainties were estimated using half of the width of the NMR signal at half of the height of the peak. Using these values, the spectrum was simulated to a close approximation with *SpinDynamica*[27].

Generally, $^{1}\Delta^{13}\mathrm{C}(^{18}\mathrm{O}) > {}^{2}\Delta^{13}\mathrm{C}(^{18}\mathrm{O}) > {}^{3}\Delta^{13}\mathrm{C}(^{18}\mathrm{O})$. However, in this case the two bond isotope shift $^{2}\Delta^{13}\mathrm{C}(^{18}\mathrm{O})$ was smaller than the three bond

Table 3.1: Experimentally measured secondary isotope shifts of ^{18}O-enriched ^{13}C$_1$-squarate at pH 0.9 (Figure 3.11), in a magnetic field of 9.4 T and a sample temperature of 298 K. The isotope shift convention is given in Equation 3.8.

^{13}C Isotope Shift	**Value /ppb**	**Value /Hz**
$^{1}\Delta^{13}\mathrm{C}(^{18}\mathrm{O})$	-40.1 ± 0.5	-4.03 ± 0.05
$^{2}\Delta^{13}\mathrm{C}(^{18}\mathrm{O})$	-14.9 ± 0.5	-1.50 ± 0.05
$^{3}\Delta^{13}\mathrm{C}(^{18}\mathrm{O})$	-22.1 ± 0.5	-2.23 ± 0.05

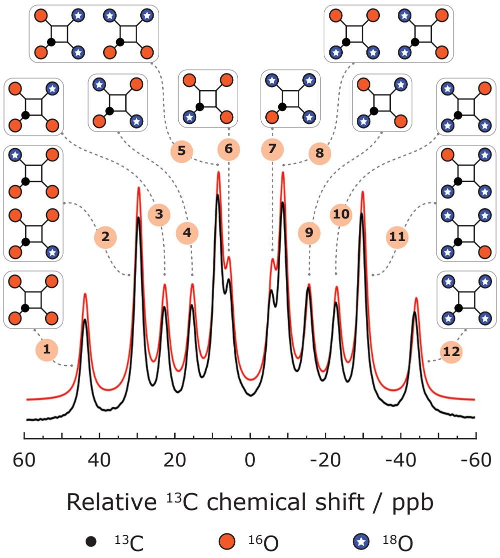

Figure 3.11: The isotopologues of ^{18}O-enriched ^{13}C$_1$-squarate, and their correspondence with the ^{13}C spectrum at pH 0.9. The filled black circles denote ^{13}C atoms. The filled orange circles denote ^{16}O atoms, while the blue stars denote ^{18}O atoms. The experimental spectrum at 9.4 T (black, 512 scans), is compared with a *SpinDynamica*[27] simulation of the spectrum (red). The ^{13}C chemical shift scale is centred at 195.32 ppm. Adapted from Heramun *et al.*[1], *J. Chem. Phys.* 163, 074201 (2025); licensed under a Creative Commons Attribution (CC BY) license.

shift ${}^3\Delta^{13}C(^{18}O)$. The explanation behind this effect was attributed to the complex interplay between the dynamic and vibronic isotope shift mechanisms, and was not analysed further.

3.5.2 pH 3.4

The ^{13}C spectrum of ^{18}O-enriched squarate at pH 3.4 is shown in Figure 3.10(b). The broad peaks arise due to the rapid protonation events occurring at this pH.

3.5.3 pH 13.3

The ^{13}C spectrum of ^{18}O-enriched squarate at pH 13.3 is shown in Figure 3.12(a), showing four intense peaks. These signals arise from the $^{13}C_1$-squarate isotopologues, and that we aim to suppress using DQF methods. This particular splitting pattern is unusual, since it corresponds to a negligibly small two bond ^{18}O isotope shift ${}^2\Delta^{13}C(^{18}O)$, for reasons that are currently unknown. The stylised squarate structures in Figure 3.12 show the the positions two bonds away from the ^{13}C nucleus under observation can contain either ^{18}O or ^{16}O. These are greyed out, since it was not possible to confirm which oxygen isotope is present.

Table 3.2: Estimated values of the ^{18}O and ^{13}C-induced ^{13}C isotope shifts of ^{18}O-enriched $^{13}C_1$-squarate at pH 13.3 (Figure 3.12) at 9.4 T and 298 K. Note the negligible magnitude of the two-bond ^{18}O-induced isotope shift ${}^2\Delta^{13}C(^{18}O)$. The isotope shift convention is given in Equation 3.8.

^{13}C Isotope Shift	**Value /ppb**	**Value /Hz**
${}^1\Delta^{13}C(^{18}O)$	-25.7 ± 0.5	-2.59 ± 0.05
${}^2\Delta^{13}C(^{18}O)$	0.0 ± 0.5	0.00 ± 0.05
${}^3\Delta^{13}C(^{18}O)$	-2.7 ± 0.5	-0.28 ± 0.05
${}^1\Delta^{13}C(^{13}C)$	-21.3 ± 0.5	-2.15 ± 0.05
${}^2\Delta^{13}C(^{13}C)$	-7.1 ± 0.5	-0.72 ± 0.05

Figure 3.12(b) shows the placements of the $^{13}C_2$-squarate isotopologues. These are the species that generate the smaller signals surrounding the pseudo doublet of doublets indicative of the $^{13}C_1$-squarate isotopologues, and that we aim to magnify. Peak 4 and Peak 7 contain the $^{13}C_2$ species of interest: ^{18}O-enriched 1,3-$^{13}C_2$-squarate, and 1,2-$^{13}C_2$-squarate, respectively.

The detailed assignment procedure for each isotopomer is illustrated in Appendix B.2.2. The experimentally measured isotope shifts are reported in Table 3.2, where the uncertainties were estimated using half of the width of the NMR signal at half of the height of the peak. Using these values, the spectrum was simulated to a close approximation with *SpinDynamica*[27].

3.6 Double-Quantum Filtered NMR

The intense signals arising from the $^{13}C_1$-squarate isotopologues in the pH 13.3 spectrum (Figure 3.12), posed a significant challenge to the goal of observing the small signals from the 1,3-$^{13}C_2$-squarate isotopologue. To suppress the NMR signals from the $^{13}C_1$ uncoupled spin-1/2 nuclei, and select those from $^{13}C_2$ coupled spin-1/2 pairs, two methods may be used.

One method employs double-quantum filtered NMR techniques, such as the INADEQUATE pulse sequence (Figure 3.4), which has been used extensively to selectively observe $^{13}C_2$ signals[37,108,123,132]. The other method exploits singlet order[44,45]. The choice of parameters allows the suppression of unwanted background NMR signals, while selecting those from the desired spin-pair capable of supporting singlet order.

Although both avenues were explored (see Appendix B.4), the double-quantum filtering route was found to be more effective in selecting either the 1,2-$^{13}C_2$-squarate or 1,3-$^{13}C_2$-squarate species, and efficiently suppressing the large signals from the $^{13}C_1$-squarate isotopologues.

There is however a challenge ahead. In our particular systems of interest, the chemical shift difference Δ between the two ^{13}C nuclei was estimated to be approximately 4.1 Hz at 9.4 T field strength. This was calculated by subtracting the one-bond $^{1}\Delta^{13}C(^{18}O) \approx -25.7$ ppb secondary isotope shift from the three-bond secondary isotope shift $^{3}\Delta^{13}C(^{18}O) \approx -2.7$ ppb, as

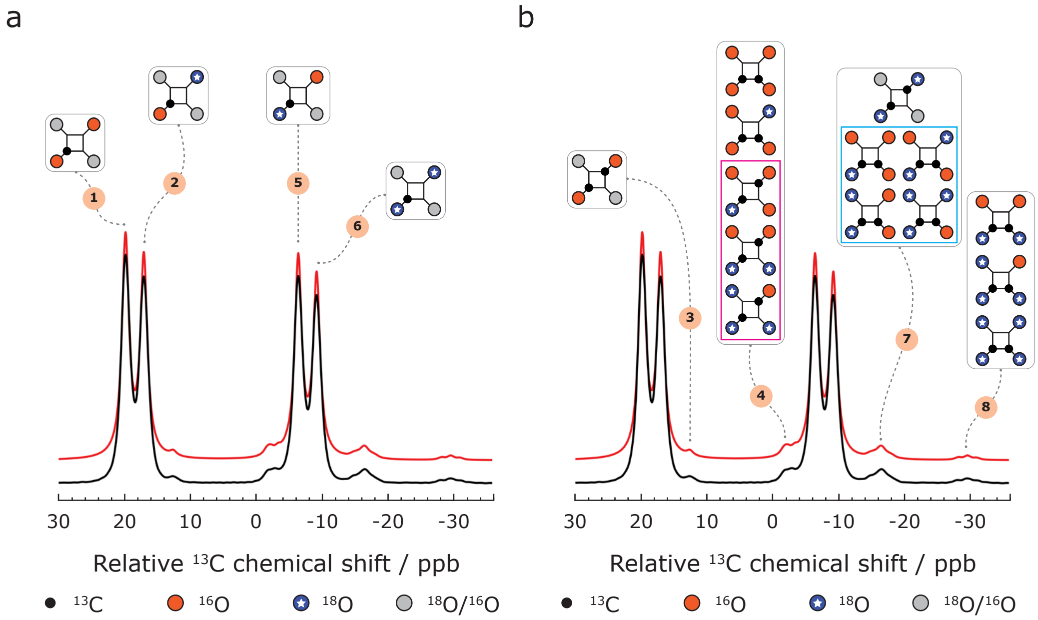

Figure 3.12: (**a**) The ^{18}O isotopologues of $^{13}C_1$-squarate, and their correspondence with the ^{13}C spectrum at pH 13.3. (**b**) The ^{18}O isotopologues of $^{13}C_2$-squarate, and their correspondence with the ^{13}C spectrum at pH 13.3. The filled black circles denote ^{13}C atoms. The filled orange circles denote ^{16}O atoms, while the white stars denote ^{18}O atoms. Filled grey circles denote oxygen atoms which may be either ^{16}O or ^{18}O, since the two-bond isotope shift $^{2}\Delta^{13}C(^{18}O)$ is negligible (see Table 3.2), the isotopic nature of these oxygen atoms does not affect the ^{13}C spectrum. The experimental spectrum at 9.4 T (black, 512 scans), is compared with a *SpinDynamica*[27] simulation of the spectrum (red). The ^{13}C chemical shift scale is centred at 203.05 ppm. Singlet NMR can be performed on the isotopologues further enclosed in a second box. This is pink for 1,3-$^{13}C_2$-squarate, and blue for 1,2-$^{13}C_2$-squarate. Adapted from Heramun *et al.*[1], *J. Chem. Phys.* 163, 074201 (2025); licensed under a Creative Commons Attribution (CC BY) license.

follows:

$$\Delta = [({}^1\Delta^{13}\mathrm{C}(^{18}\mathrm{O}) - {}^3\Delta^{13}\mathrm{C}(^{18}\mathrm{O}))] \cdot |\omega^0| \ , \tag{3.9}$$

where $|\omega^0|$ is the absolute value of the Larmor frequency of ^{13}C in Hertz, for an external magnetic field $B^0 = 9.4$ T (see Equation 1.6):

$$|\omega^0| \simeq (1.01 \cdot 10^6) \text{ Hz} \ . \tag{3.10}$$

For 1,2-^{13}C$_2$-squarate, $^1J_{\mathrm{CC}} \simeq 55.0$ Hz, and for 1,3-^{13}C$_2$-squarate, $^2J_{\mathrm{CC}} \simeq 40.1$ Hz. Hence, the chemical shift difference $\Delta \simeq 4.1$ Hz is much smaller in magnitude, than the J-coupling. Consequently, each ^{13}C$_2$ isotopologue is in the near-equivalence coupling regime (see Figure 1.8).

The standard INADEQUATE method[123] is unsuitable for this strong-coupling regime, and although the double-quantum excitation time can be greatly extended in the Nakai-McDowell implementation of the pulse sequence[125] (see Figure 3.8(b)), this leads to significant relaxation losses, and therefore poor signal quality.

To overcome this difficulty, we chose to use a method that was recently shown to be effective for the double-quantum excitation in nearly-equivalent AB type spin systems. This is the geometric double-quantum (GeoDQ) excitation pulse sequence[128], shown in Figure 3.13.

Theoretical expressions for the pulse sequence intervals τ_1^{Geo} and τ_2^{Geo}, and the loop number n, are given by[128]:

$$\begin{aligned} \tau_1^{\mathrm{Geo}} &= \pi/(2\Omega_{\mathrm{ST}}), \\ \tau_2^{\mathrm{Geo}} &= 2\tau_1^{\mathrm{Geo}}, \\ n &= 2 \times \mathrm{round}(\pi/(4\theta_{\mathrm{ST}})). \end{aligned} \tag{3.11}$$

The last equation ensures that n is an even number, which leads to the most robust performance of the sequence[133]. In practice, these parameters were optimised experimentally to selectively filter the ^{18}O-enriched 1,2-^{13}C$_2$-squarate signal, or the ^{18}O-enriched 1,3-^{13}C$_2$-squarate signal. The two isotopologues have the same chemical shift difference Δ, but different J-couplings, and therefore different $\tau_1^{\mathrm{Geo}}, \tau_2^{\mathrm{Geo}}$, and n parameters.

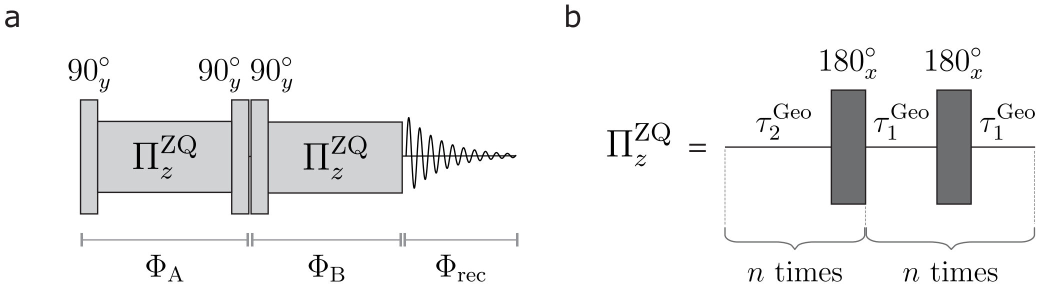

Figure 3.13: (**a**) Geometric double-quantum-filtering pulse sequence. The phases of the blocks were cycled as an overall four-step cycle: $\Phi_{\mathrm{A}} = \{0, 0, 0, 0\}$, $\Phi_{\mathrm{B}} = \{0, \pi/2, \pi, 3\pi/2\}$ and $\Phi_{\mathrm{rec}} = \{0, 3\pi/2, \pi, \pi/2\}$. (**b**) Structure of the Π_z^{ZQ} sequence. The darker colour indicates the implementation of a composite 180° pulse[40]. Theoretical expressions for τ_1^{Geo}, τ_2^{Geo} and n are given in Equation 3.11. The parameters used in the experiments are given in Table 3.3. Adapted from Heramun *et al.*[1], *J. Chem. Phys.* 163, 074201 (2025); licensed under a Creative Commons Attribution (CC BY) license.

The density operator transformations performed by the sequence shown in Figure 3.13 are detailed below, and graphically illustrated in Figure 3.14.

The thermal equilibrium density operator ρ_1 is characterised by a population excess in the $|2\rangle = |T_{+1}\rangle$ state, and a depleted population in the $|4\rangle = |T_{-1}\rangle$ state, for $\gamma > 0$. It may be written as follows:

$$\rho_1 = I_z = 2I_z^{24} = \begin{pmatrix} 0 & 0 & 0 & 0 \\ 0 & 1 & 0 & 0 \\ 0 & 0 & 0 & 0 \\ 0 & 0 & 0 & -1 \end{pmatrix}. \tag{3.12}$$

This state is depicted in Pane 1 of Figure 3.14, where the darker balls represent an enhanced population, while the lighter balls represent a depleted population. The GeoDQ sequence starts by applying an initial $(\pi/2)_y$ strong pulse, as shown in Figure 3.13(b). This generates single-quantum coherences between adjacent pairs of triplet states. The corresponding operator may be

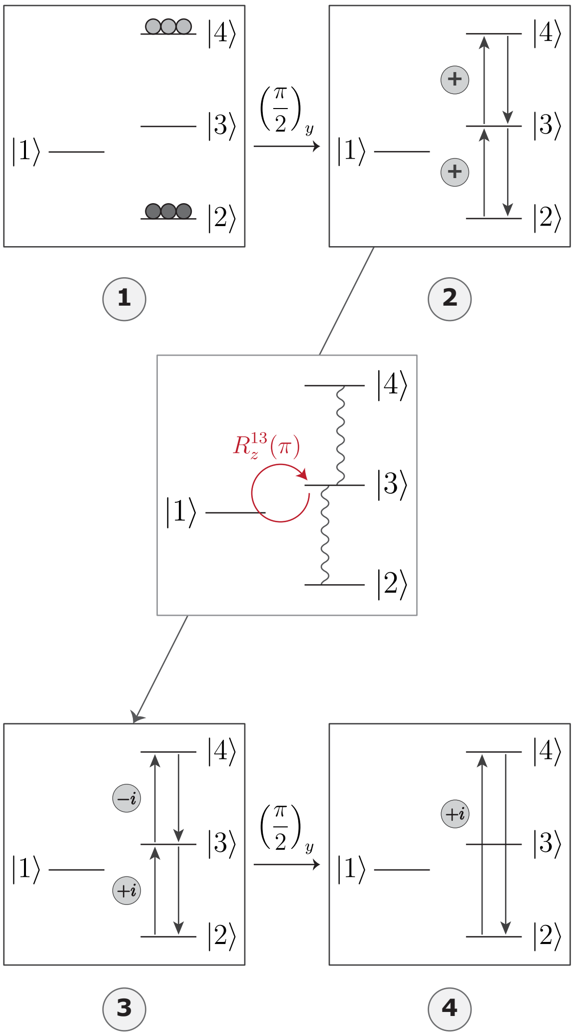

Figure 3.14: Geometric double-quantum excitation. An ensemble of spin-$1/2$ pairs is at thermal equilibrium in a strong magnetic field (pane 1). In-phase single-quantum triplet-triplet coherences are generated by a $\pi/2$ y-pulse (pane 2). This is converted into a *double-quantum precursor state* of antiphase triplet-triplet coherences (pane 3). A final $\pi/2$ y-pulse generates double-quantum coherence between the states $|T_{\pm1}\rangle$ (pane 4). The transformation from the state in pane 2 to that in pane 3 is achieved by generating a cyclic trajectory with geometric phase π in the zero-quantum subspace spanned by the singlet state $|S_0\rangle = |1\rangle$ and the central triplet state $|T_0\rangle = |3\rangle$. This transformation corresponds to a rotation through π about the z-axis of the zero-quantum subspace. Adapted from Heramun *et al.*[2], *J. Chem. Phys.* 164, 064201 (2026); licensed under a Creative Commons Attribution (CC BY) license.

written using Cartesian, and single-transition operators, as follows:

$$\begin{aligned}
\rho_2 &= R_y(\pi/2)\rho_1 R_y(\pi/2)^\dagger \\
&= I_x \qquad (3.13)\\
&= \sqrt{2}(I_x^{23} + I_x^{34}) \\
&= \frac{1}{\sqrt{2}}\{|2\rangle\langle 3| + |3\rangle\langle 2| + |3\rangle\langle 4| + |4\rangle\langle 3|\} \\
&= \frac{1}{\sqrt{2}}\begin{pmatrix} 0 & 0 & 0 & 0 \\ 0 & 0 & 1 & 0 \\ 0 & 1 & 0 & 1 \\ 0 & 0 & 1 & 0 \end{pmatrix},
\end{aligned}$$

where the $|T_{+1}\rangle\langle T_0| = |2\rangle\langle 3|$, $|T_0\rangle\langle T_{+1}| = |3\rangle\langle 2|$, $|T_0\rangle\langle T_{-1}| = |3\rangle\langle 4|$, and $|T_{-1}\rangle\langle T_0| = |4\rangle\langle 3|$ single-quantum triplet-triplet coherences are all generated with the same sign. This is depicted in Pane 2 of Figure 3.14.

In order to excite double-quantum coherence, the density operator ρ_2, which has the same signs for all the triplet-triplet SQCs, must be converted into a state ρ_3 where the SQCs have opposite signs. These are the desired antiphase triplet-triplet single-quantum coherences, also called the *double-quantum precursor state*, DQP, as seen earlier in the chapter.

This important transformation is accomplished during the Π_z^{ZQ} section of the GeoDQ sequence (Figure 3.13). A sequence of π pulses with timings τ_1^{Geo}, τ_2^{Geo}, and n repetitions (Equation 3.11), generates a cyclic trajectory in the zero-quantum (ZQ) subspace $\{|S_0\rangle, |T_0\rangle\}$ spanned by the singlet state $|1\rangle = |S_0\rangle$ and the central triplet state $|3\rangle = |T_0\rangle$, as depicted in the central pane of Figure 3.14.

The cyclic trajectory encloses a solid angle of π subtended by the zero-quantum Bloch-sphere trajectory, which leads to a geometric Aharonov-Anandan phase – a generalisation of the Berry phase[130,134] for non-adiabatic conditions – of $\pi/2$ for the states $|1\rangle$ and $|3\rangle$. The overall effect is equivalent to a z-rotation on the Bloch sphere of the $|T_0\rangle$ and $|S_0\rangle$ zero-quantum transition[128], indicated by $R_z^{13}(\pi)$. In this instance, the specific trajectory shape traced by the system is a *spherical lune*[128], or *orange slice*[135], which has an opening angle of $\gamma = \pi/2$, so that the trajectory subtends a solid angle $\mathbf{\Omega} = \pi$ at the origin.

The triplet-triplet coherences $|3\rangle\langle 4|$ and $|2\rangle\langle 3|$ acquire opposite phase shifts of $\pm\pi/2$ upon completion of the cyclic zero-quantum trajectory, leading to a state with triplet-triplet coherences of opposite sign, as shown in Pane 3 of Figure 3.14).

A visual representation of this process is depicted in Figure 3.15.

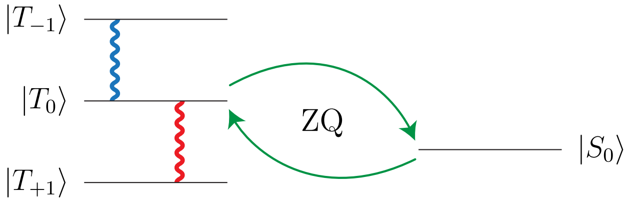

Figure 3.15: A zero-quantum cycle between the $|T_0\rangle$ and $|S_0\rangle$ states creates the desired triplet-triplet antiphase single-quantum coherences required to excite double-quantum coherence. The phase difference is denoted by different colours, and coherences by the wavy lines.

The density operator of the DQP state ρ_3 is given as follows:

$$\begin{aligned}
\rho_3^{\text{geo}} &= R_z^{13}(\pi)\,\rho_2\,R_z^{13}(\pi)^\dagger \\
&= \sqrt{2}R_z^{13}(\pi)\left(I_x^{23} + I_x^{34}\right)R_z^{13}(\pi)^\dagger \\
&= 2I_{1y}I_{2z} + 2I_{1z}I_{2y} \\
&= \sqrt{2}\left(I_y^{23} - I_y^{34}\right) \\
&= \frac{1}{\sqrt{2}}\{-|2\rangle\langle 3| + |3\rangle\langle 2| + |3\rangle\langle 4| - |4\rangle\langle 3|\} \\
&= \frac{i}{\sqrt{2}}\begin{pmatrix} 0 & 0 & 0 & 0 \\ 0 & 0 & -1 & 0 \\ 0 & 1 & 0 & 1 \\ 0 & 0 & -1 & 0 \end{pmatrix}.
\end{aligned} \tag{3.14}$$

This transformation is possible thanks to the commutation relationships of single-transition operators[66,67]:

$$\begin{aligned}
[I_z^{13}, I_x^{23}] &= \tfrac{1}{2} i I_y^{23}, \\
[I_z^{13}, I_y^{23}] &= -\tfrac{1}{2} i I_x^{23}, \\
[I_z^{13}, I_x^{34}] &= -\tfrac{1}{2} i I_y^{34}, \\
[I_z^{13}, I_y^{34}] &= \tfrac{1}{2} i I_x^{34}.
\end{aligned} \tag{3.15}$$

The double-quantum precursor state ρ_3 is then converted into double-quantum coherence by the second $(\pi/2)_y$ pulse shown in Figure 3.13(b):

$$\begin{aligned}
\rho_4 &= R_y(\pi/2)\, \rho_3, R_y(\pi/2)^\dagger \\
&= R_y(\pi/2)\, (2I_{1y}I_{2z} + 2I_{1z}I_{2y}) R_y(\pi/2)^\dagger \\
&= 2I_{1x}I_{2y} + 2I_{1y}I_{2x} \\
&= 2I_y^{24} \\
&= -i(I_1^+ I_2^+ - I_1^- I_2^-) \\
&= -i(|2\rangle \langle 4| - |4\rangle \langle 2|) \\
&= \frac{i}{\sqrt{2}} \begin{pmatrix} 0 & 0 & 0 & 0 \\ 0 & 0 & 0 & -1 \\ 0 & 0 & 0 & 0 \\ 0 & 1 & 0 & 0 \end{pmatrix}.
\end{aligned} \tag{3.16}$$

The corresponding graphical representation of this transformation is shown in Pane 4 of Figure 3.14. The double-quantum excitation procedure generates a unitary transformation U of the density operator, where $U^\dagger = U^{-1}$, without taking into account relaxation effects. The *double-quantum excitation amplitude* a_{DQ} for a particular sequence is defined as follows:

$$a_{\mathrm{DQ}} = \langle 2| U \rho_1 U^\dagger |4\rangle , \tag{3.17}$$

which may also be written in the following form:

$$a_{\mathrm{DQ}} = \left\langle I_z \xrightarrow{U} |2\rangle \langle 4| \right\rangle. \tag{3.18}$$

The *transformation amplitude* was previously defined in Equation 3.1. The final state corresponds to double-quantum excitation of maximal amplitude, assuming a correct implementation of the pulse sequence, ignoring certain numerical factors, and without relaxation effects being taken into account.

$$\begin{aligned} a_{\mathrm{DQ}} &= \langle 2|\, \rho_4 \,|4\rangle = -i, \\ a^*_{\mathrm{DQ}} &= \langle 4|\, \rho_4 \,|2\rangle = +i. \end{aligned} \tag{3.19}$$

The time evolution of the DQP operator during the GeoDQ sequence, using the 1,3-$^{13}C_2$-squarate parameters at pH 13.3, is explored in Figure 3.16. As described above, the sequence successfully generates the maximum amplitude of the $2(I_{1y}I_{2z} + I_{1z}I_{2y})$ operator, which is then converted into double-quantum coherence after the final $(\pi/2)_y$ pulse.

The GeoDQ pulse sequence was successfully applied to detect the $^{13}C_2$-squarate isotopologues (Figure 3.2(b-c)) from a sample of ^{18}O-enriched $^{13}C_1$-squarate at pH 13.3. The DQF ^{13}C NMR spectrum of ^{18}O-enriched 1,2-$^{13}C_2$-squarate is shown in Figure 3.17(b), while the DQF ^{13}C NMR spectrum of ^{18}O-enriched 1,3-$^{13}C_2$-squarate is shown in Figure 3.17(e). In both cases, the degree of selectivity and the suppression of the intense signals due to the $^{13}C_1$-squarate isotopologues was excellent.

In Figure 3.17(e), the 1,2-$^{13}C_2$-squarate signal also appears in this spectrum, though with reduced intensity. This is expected, since the double-quantum filter allows the signals from both $^{13}C_2$ species to pass through it. The experimentally optimised parameters for both systems are given in Table 3.3. In all cases, the DQF efficiencies could not be determined, since each peak position was indicative of other isotopologues as well, as previously illustrated in Figure 3.12(b).

The J-couplings were also estimated using DFT calculations, given in Table 3.3 as J_{calc}. Further details are given in Appendix B.1.2.

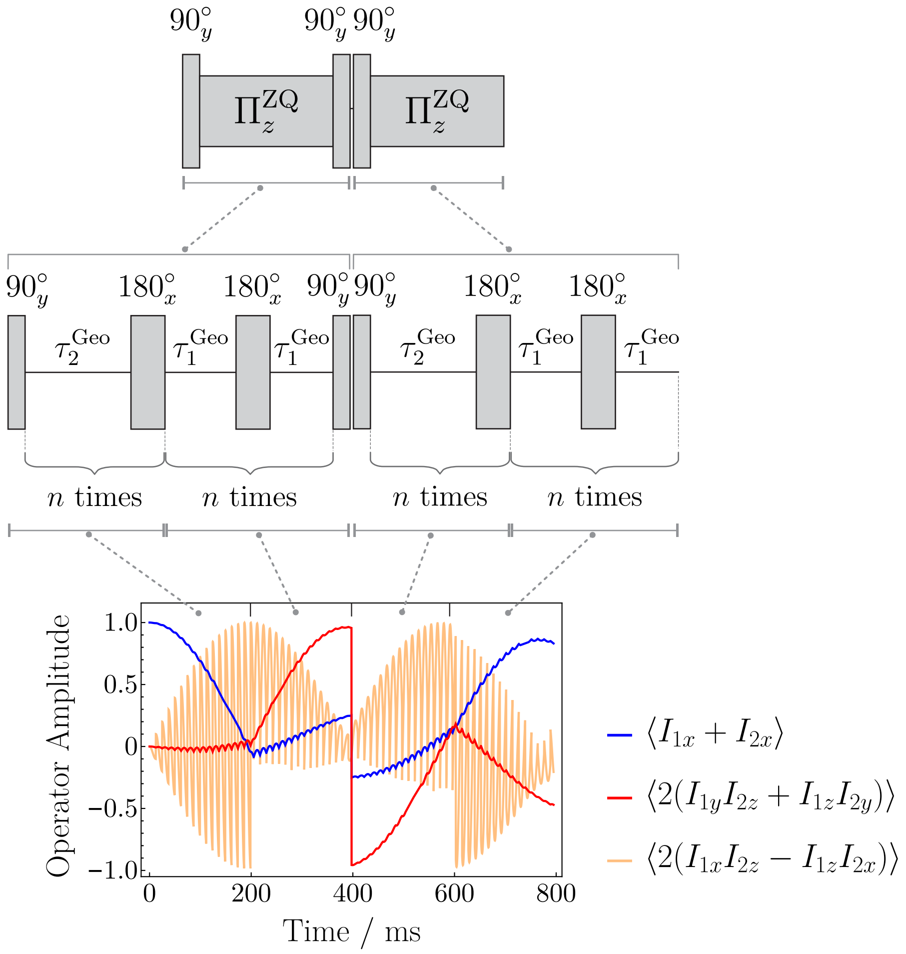

Figure 3.16: Time evolution of the x-magnetisation operator, the double-quantum precursor operator $(2(I_{1y}I_{2z} + I_{1z}I_{2y}))$, and the outer singlet-triplet coherence operator $(2(I_{1x}I_{2z} - I_{1z}I_{2x}))$ during the GeoDQ pulse sequence. The *SpinDynamica*[27] parameters used are described in Table 3.3, for the 1,3-$^{13}C_2$-squarate species.

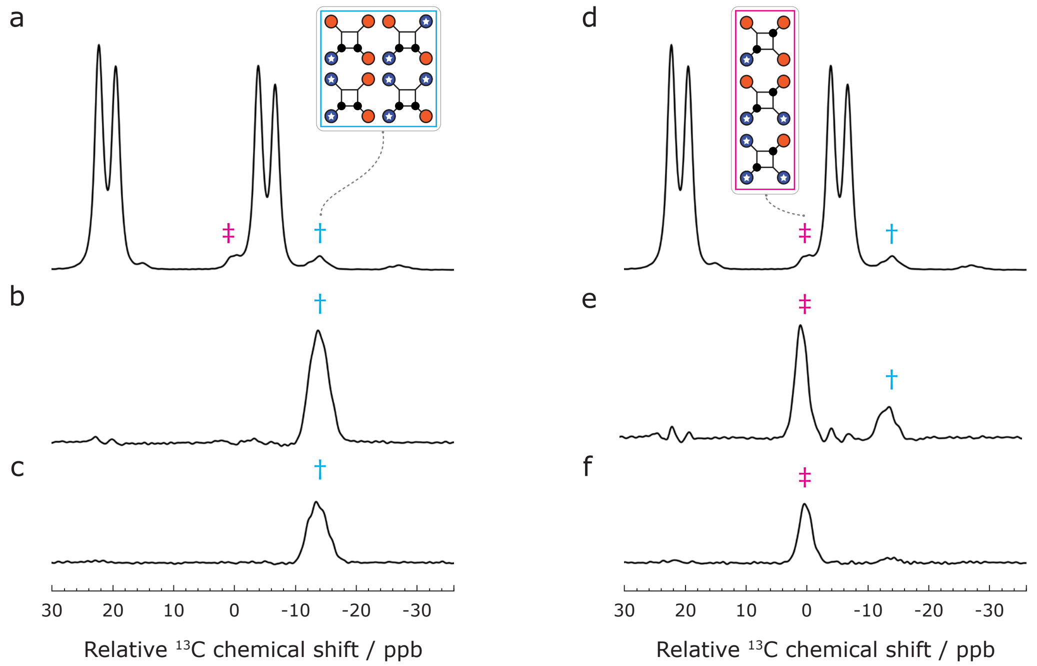

Figure 3.17: Selective ^{13}C NMR of squarate. All spectra are of a solution of $^{13}C_1$ squarate at pH 13.3 and 298 K. The chemical shift scale is centred at 203.05 ppm. Blue dagger: 1,2-$^{13}C_2$ squarate signals; Magenta double-dagger: 1,3-$^{13}C_2$ squarate signals. The experimentally optimised pulse sequence parameters are given in Table 3.3. (**a**),(**d**) A 90° pulse-acquire ^{13}C NMR spectrum of the $^{13}C_1$-squarate solution at 9.4 T, averaged over 512 transients. Only given as a positional reference for the 1,2-$^{13}C_2$-squarate and 1,3-$^{13}C_2$-squarate signals. (**b**) Double-quantum filtered spectrum obtained using the GeoDQ pulse sequence (1024 transients at 16.4 T), using parameters optimised for 1,2-$^{13}C_2$-squarate. (**c**) Singlet-filtered spectrum obtained using the GeoDQ-singlet pulse sequence (1024 transients at 16.4 T), using parameters optimised for 1,2-$^{13}C_2$-squarate. (**e**) Double-quantum filtered spectrum obtained using the GeoDQ pulse sequence (1024 transients at 16.4 T), using parameters optimised for 1,3-$^{13}C_2$-squarate. (**f**) Singlet-filtered spectrum obtained using the GeoDQ-singlet pulse sequence (1024 transients at 16.4 T), using parameters optimised for 1,3-$^{13}C_2$-squarate. Adapted from Heramun *et al.*[1], *J. Chem. Phys.* 163, 074201 (2025); licensed under a Creative Commons Attribution (CC BY) license.

Table 3.3: First three rows: Pulse sequence parameters used for the geometric double-quantum filtration experiments at 16.4 T and 298 K for a pH 13.3 sample. Next five rows: spin system parameters deduced from the optimised values of the pulse sequence parameters, using Equation 3.11. The small values of θ_{ST} indicate $^{13}C_2$ spin-pairs in the near-equivalence regime. Last row: estimated values of the ^{13}C-^{13}C *J*-couplings using computational chemistry methods (see Appendix B.1.2). Adapted from Heramun *et al.*[1], *J. Chem. Phys.* 163, 074201 (2025); licensed under a Creative Commons Attribution (CC BY) license.

Parameter	**1,2-^{13}C$_2$-sq.**	**1,3-^{13}C$_2$-sq.**
τ_1^{Geo} /ms	4.53	6.21
τ_2^{Geo} /ms	9.06	12.42
n	20	16
J /Hz	55.0 ± 0.1	40.1 ± 0.1
Δ /Hz	4.1 ± 0.1	4.1 ± 0.1
$\Omega_{\mathrm{ST}}/(2\pi)$ /Hz	55.0 ± 0.1	40.1 ± 0.1
$\Delta\delta$ /ppb	5.8 ± 0.1	5.8 ± 0.1
$\theta_{\mathrm{ST}}/^\circ$	4.2 ± 0.2	5.8 ± 0.2
J_{calc} /Hz	56.5 ± 0.5	47.8 ± 0.5

3.7 Double-Quantum Filtered Singlet NMR

The geometric double-quantum filtering scheme (Figure 3.13) can be integrated into a wider module that enables the excitation of singlet order, from double-quantum coherence. This is especially useful to study the singlet order relaxation of the 1,2-$^{13}C_2$ squarate and 1,3-$^{13}C_2$-squarate isotopologues, without the signals arising from the $^{13}C_1$-squarate isotopologues interfering.

The phase cycle is identical to that of the GeoDQ sequence, where the second GeoDQ blocks and the receiver phases are cycled in a four-step cycle to filter for double-quantum coherences, suppressing undesired operators. The geometric double-quantum-filtered singlet (GeoDQ-singlet) pulse sequence is shown in Figure 3.18.

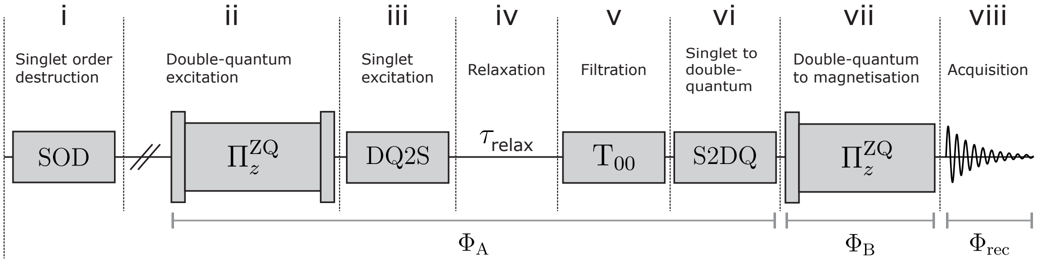

Figure 3.18: Geometric double-quantum filtering singlet pulse sequence. (**i**) The singlet-order destruction (SOD) block[96] removes any longitudinal magnetisation and residual singlet order. (**ii**) Following a relaxation delay to re-establish longitudinal magnetisation, double-quantum coherence is generated by a geometric double-quantum excitation block, with an overall phase shift Φ_A. (**iii**) The double-quantum-to-singlet (DQ2S) block converts double-quantum coherence to singlet order. (**iv**) Singlet order decays during the relaxation interval τ_{relax}. (**v**) A T_{00} filter removes signals which do not pass through any rank-0 spherical tensor operators. (**vi**) The singlet-to-double-quantum (S2DQ) block converts singlet order to double-quantum coherence. (**vii**) A second geometric double-quantum pulse block is applied, with an overall phase shift Φ_B. (**viii**) The NMR signal is acquired and digitised, with receiver phase Φ_{rec}. The phases of the blocks are cycled as an overall four-step cycle: $\Phi_A = \{0, 0, 0, 0\}$, $\Phi_B = \{0, \pi/2, \pi, 3\pi/2\}$ and $\Phi_{rec} = \{0, 3\pi/2, \pi, \pi/2\}$. Adapted from Heramun *et al.*[1], *J. Chem. Phys.* 163, 074201 (2025); licensed under a Creative Commons Attribution (CC BY) license.

The pulse sequence is subdivided into eight sections, as follows:

(i) Singlet Order Destruction (SOD). This pulse block consists of a sequence of rf pulses and gradients[96] employed to remove residual longitudinal and singlet order (see Figure 2.14(b)). This step is especially important as a time-saving measure in experiments with extended T_S relaxation lifetimes, and to ensure that every transient acquired begins from the same starting point. Further details on the parameters used in the experiments are given in Appendix B.3.

(ii) Geometric Double-Quantum Excitation. Following a relaxation delay of 3-5 times T_1 to allow the system to reach thermal equilibrium, a geometric double-quantum excitation sequence Π_z^{ZQ} is applied to generate double-quantum coherence (Figure 3.13(b)).

(iii) Double-Quantum To Singlet (DQ2S) conversion. A 90°_{-y} and 45°_x pulses are initially applied, followed by a J-synchronised spin echo sequence (JSE), repeated for n times. Analogously to the JSE used in the M2S pulse sequence (Figure 2.6(a)) for converting longitudinal magnetisation into singlet order[71], this completes the steps to access singlet order, from double-quantum coherence. This block is shown in Figure 3.19(a).

(iv) Relaxation. Singlet order can be allowed to evolve/decay for a time τ_{relax}. This relaxation interval τ_{relax} is varied in a series of experiments in order to study the decay of $^{13}C_2$-singlet order in 1,2-$^{13}C_2$-squarate and 1,3-$^{13}C_2$-squarate, described later in Figure 3.21.

(v) Filtration. The T_{00} filter consists of a sequence of rf pulses and gradients[68,136] used to suppress any non rank 0 spherical tensor operator signals (see Figure 2.14(a)). Consequently, signals arising from the 1,2-$^{13}C_2$-squarate and 1,3-$^{13}C_2$-squarate singlet order pass through the filter, while other magnetisation components are suppressed instead. Further details on the parameters used in the experiments are given in Appendix B.3.

(vi) Singlet To Double-Quantum (S2DQ) conversion. This sequence converts singlet order back into double-quantum coherence by acting in the reverse chronological order of the DQ2S sequence, similar to the S2M sequence (see Figure 2.6(b)). This pulse sequence block is shown in Figure 3.19(b), and is the chronological reverse of the DQ2S sequence.

(**vii**) Double-Quantum to Magnetisation. A second geometric double-quantum sequence Π_z^{ZQ} converts the double-quantum coherence into observable magnetisation. The sequence was illustrated in Figure 3.13(b). The parameters used for the singlet-filtered experiments of 1,2-$^{13}C_2$-squarate and 1,3-$^{13}C_2$-squarate are given in Table 3.3.

(**viii**) Acquisition. The ^{13}C NMR signal is observed.

3.7.1 DQ2S-S2DQ

The DQ2S and S2DQ pulse blocks are described in Figure 3.19(a). The theoretical value of τ_1^{Geo}, and the loop number n were given in Equation 3.11.

The transformations performed by these singlet excitation modules can be

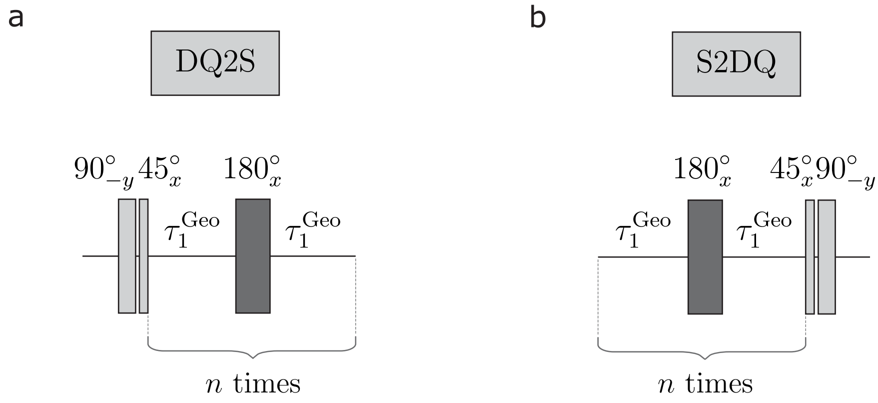

Figure 3.19: (**a**) The double-quantum to singlet (DQ2S) block converts double-quantum coherence into singlet order. (**b**) The singlet to double-quantum (S2DQ) block is the chronological reverse of the DQ2S block, and converts singlet order back to double-quantum coherence. The darker colour indicates the implementation of a composite 180° pulse[40]. The theoretical values of τ_1^{Geo} and n are given in Equation 3.11. The parameters used in the experiments are given in Table 3.3. Adapted from Heramun *et al.*[1], *J. Chem. Phys.* 163, 074201 (2025); licensed under a Creative Commons Attribution (CC BY) license.

explored using density operators. The density operator ρ_4 that contains the DQC generated by the GeoDQ sequence was given in Equation 3.16. The first $(\pi/2)_{-y}$ pulse within the DQ2S block converts double-quantum coherence, back into antiphase triplet-triplet coherences:

$$\rho_5 = R_y(-\pi/2)\rho_4 R_y(+\pi/2) = \frac{i}{\sqrt{2}} \begin{pmatrix} 0 & 0 & 0 & 0 \\ 0 & 0 & -1 & 0 \\ 0 & +1 & 0 & +1 \\ 0 & 0 & -1 & 0 \end{pmatrix}. \tag{3.20}$$

The subsequent $(\pi/4)_x$ pulse converts ρ_5, into the state ρ_6. This has the effect of depleting the population of the central triplet state $|T_0\rangle$, compared to the two outer triplet states $|T_{+1}\rangle$ and $|T_{-1}\rangle$:

$$\rho_6 = R_x(\pi/4)\rho_5 R_x(-\pi/4) = \frac{1}{2} \begin{pmatrix} 0 & 0 & 0 & 0 \\ 0 & +1 & 0 & +1 \\ 0 & 0 & -2 & 0 \\ 0 & +1 & 0 & +1 \end{pmatrix}. \tag{3.21}$$

The next element of the DQ2S sequence is a J-synchronised multiple spin echo sequence, as shown in Figure 3.19(a). A JSE of a suitable duration (i.e. J-synchronous), induces a π rotation about the x-axis of the ZQ subspace made up by the $|S_0\rangle, |T_0\rangle$ states[69,71]. This transformation results in a population exchange between the singlet $|S_0\rangle$ and central triplet $|T_0\rangle$ states:

$$\rho_7 = R_x^{\mathrm{ZQ}}(\pi)\rho_7 R_x^{\mathrm{ZQ}}(-\pi) = \frac{1}{2} \begin{pmatrix} -2 & 0 & 0 & 0 \\ 0 & +1 & 0 & +1 \\ 0 & 0 & 0 & 0 \\ 0 & +1 & 0 & +1 \end{pmatrix}. \tag{3.22}$$

The state ρ_7 contains the desired singlet order. Therefore, the sequence of pulses shown in Figure 3.19(a) are able to convert double-quantum coherence into singlet order. The S2DQ sequence (see Figure 3.19(b)), operates by reversing the transformations performed by the DQ2S block, allowing a return to double-quantum coherence.

The time evolution of several operators during the GeoDQ-singlet pulse sequence, using the 1,3-$^{13}C_2$-squarate parameters at pH 13.3, is explored in Figure 3.16. As described above, the sequence successfully generates the maximum amplitude of the double-quantum precursor operator, which is then converted into the unobservable double-quantum operator, then into the singlet order operator, and ultimately back into transverse magnetisation for readout.

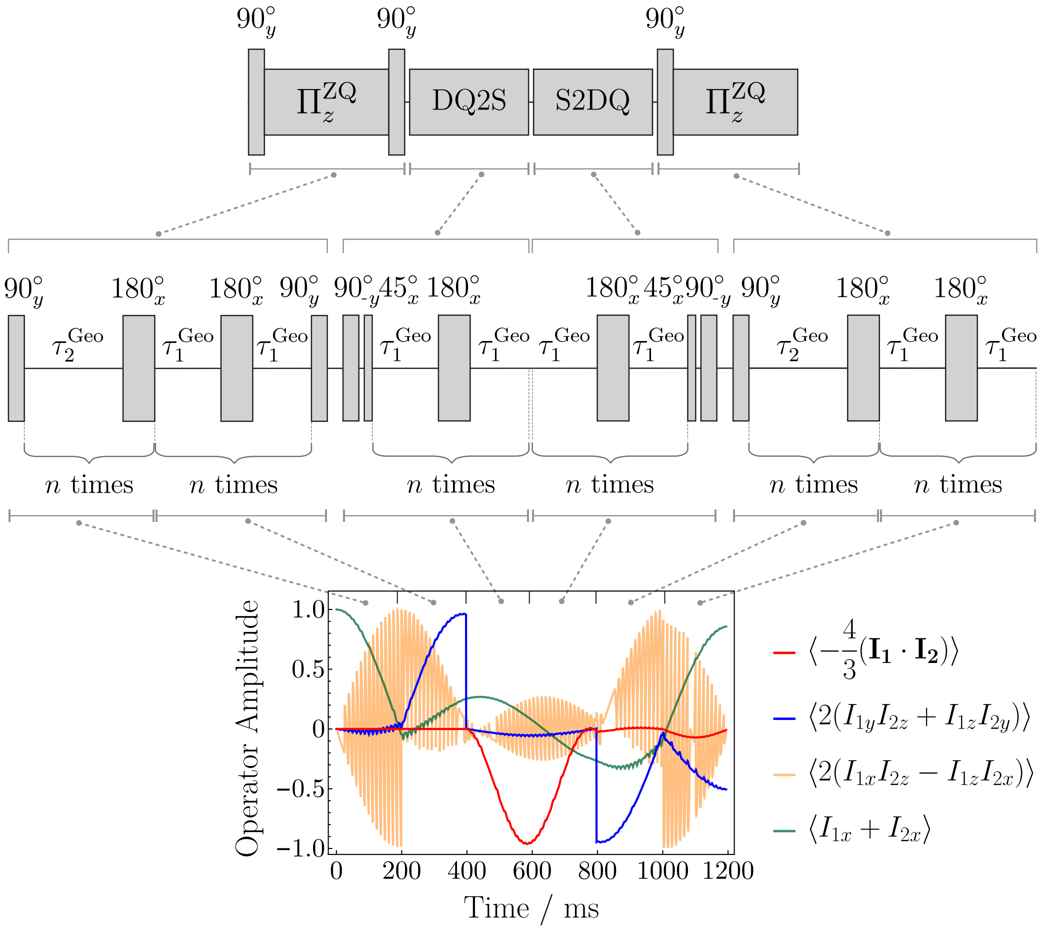

Figure 3.20: Time evolution of the singlet order operator ($-\frac{4}{3}(\mathbf{I_1} \cdot \mathbf{I_2})$), the double-quantum precursor operator ($2(I_{1y}I_{2z} + I_{1z}I_{2y})$), the outer singlet-triplet coherence operator ($2(I_{1x}I_{2z} - I_{1z}I_{2x})$), and the x-magnetisation operator during the GeoDQ-singlet pulse sequence. The *SpinDynamica*[27] parameters used are described in Table 3.3, for the 1,3-$^{13}C_2$-squarate species.

The overall theoretical efficiency for the DQ2S-S2DQ sequences to convert double-quantum coherence into singlet order, and back to double-quantum coherence again, is 2/3. This is the maximum achievable by consecutive unitary transformations[61,62], as previously explained in Chapter 2. However, as previously described in Subsection 2.6.1, the absence of the T_{00} filtering step in this simulation results in the maximum reconversion of singlet order, into transverse magnetisation.

Figure 3.17(c) and (f) show ^{13}C NMR spectra acquired after applying the pulse sequence shown in Figure 3.18, without a relaxation delay τ_{relax}. These NMR signals derive from the ^{13}C magnetisation of the 1,2-$^{13}C_2$-squarate and 1,3-$^{13}C_2$-squarate isotopologues which have passed through both double-quantum coherence and singlet order, sequentially. The sequences are seen to be highly selective and efficient. Additional NMR spectra, showing comparisons with the refocused INADEQUATE, and M2S-S2M pulse sequences are given in Figures B.1 and B.2 in Appendix B.4.

3.8 Relaxation Measurements

To study the decay of $^{13}C_2$-singlet order in 1,2-$^{13}C_2$-squarate and 1,3-$^{13}C_2$-squarate, the relaxation interval τ_{relax} shown in Figure 3.18(iv) was varied in a series of experiments. The decay curves are shown in Figure 3.21.

Singlet order was observed to decay faster in the 1,2-$^{13}C_2$-squarate isotopologue ($T_{\mathrm{S}} \simeq (125 \pm 20)$ s), compared to the 1,3-$^{13}C_2$-squarate isotopologue ($T_{\mathrm{S}} \simeq (200 \pm 26)$ s). This is due to the higher degree of symmetry of 1,3-$^{13}C_2$-squarate, compared to 1,2-$^{13}C_2$-squarate. The presence of the inversion centre i removes the prominent contribution of relaxation arising from CSA to the decay of $^{13}C_2$ singlet order. Paramagnetic impurities were removed *via* degassing. The T_1 time constants were estimated by using a standard inversion-recovery sequence (see Figure 1.6), followed by geometric double-quantum filtration. This method allowed the selective observation of either 1,2-$^{13}C_2$-squarate, or 1,3-$^{13}C_2$-squarate, where ($T_1 \approx (29 \pm 1)$ s) for both isotopologues, suggesting that the longitudinal magnetisation of both species decayed between 6 to 10 times faster than singlet order.

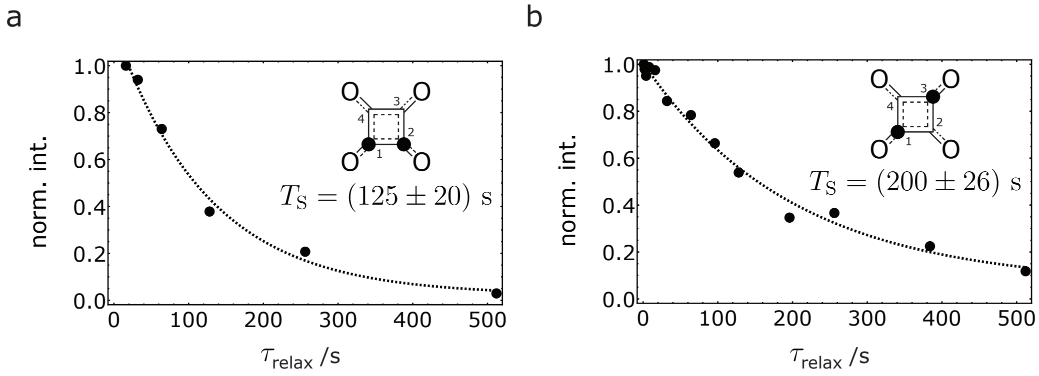

Figure 3.21: (**a**) Decay curve for the $^{13}C_2$-singlet order of the 1,2-$^{13}C_2$-squarate isotopologue. (**b**) Decay curve for the $^{13}C_2$-singlet order of the 1,3-$^{13}C_2$-squarate isotopologue. All results were obtained on a degassed solution of $^{13}C_1$-squarate at 16.4 T and 298 K, by applying the GeoDQ-singlet pulse sequence shown in Figure 3.18. The monoexponential decays of the signal intensities were fitted using non-linear least squares. Adapted from Heramun *et al.*[1], *J. Chem. Phys.* 163, 074201 (2025); licensed under a Creative Commons Attribution (CC BY) license.

3.9 Discussion

The squarate dianion molecular system is attractive due to its high degree of molecular symmetry and the absence of other NMR active nuclei surrounding the spins of interest, thereby removing any sources of intramolecular relaxation in singlet NMR experiments. Carbon-13 labelling of one site within the structure creates $^{13}C_1$-squarate. Further ^{18}O random enrichment of $^{13}C_1$-squarate breaks the symmetry of the molecule due to the difference in mass between ^{16}O and ^{18}O, allowing the study of the 1,2-$^{13}C_2$-squarate and 1,3-$^{13}C_2$-squarate isotopologues in a high pH aqueous solution.

We observed numerous isotopologues due to the variety of ^{18}O-induced and ^{13}C-induced ^{13}C secondary isotope shifts that change the position of the ^{13}C NMR resonance by a few parts-per-billion. The ^{13}C isotope shifts were measured over one and two bonds at high pH. The ^{18}O isotope shifts were measured over one, two, and three bonds in both high and low pH cases, demonstrating a strong pH dependence. This is due to a combination of the vibronic and dynamic isotope shift mechanisms, which creates the complex peak splitting that was observed in the pH 0.9 and pH 13.3 ^{13}C spectra.

In the dynamic mechanism, the substitution of one ^{16}O atom by ^{18}O at a location where protonation occurs changes the average ^{13}C chemical shifts throughout the molecule by moving the acid-base equilibrium. The dynamic mechanism's contribution to the isotope shifts vanishes at high pH, since the squarate dianion $C_4O_4^{2-}$ is most abundant in solution, with minimal protonation events occurring. In this pH regime the vibronic two-bond $^2\Delta^{13}C(^{18}O)$ secondary isotope shift is negligibly small, unlike the one-bond, $^1\Delta^{13}C(^{18}O)$, and the three-bond $^3\Delta^{13}C(^{18}O)$ shifts, for unknown reasons.

The GeoDQ pulse sequence was successfully applied to selectively detect the signals from the 1,2-$^{13}C_2$-squarate and 1,3-$^{13}C_2$-squarate isotopologues, while efficiently suppressing the more intense signals from the $^{13}C_1$ species. This procedure was demonstrated to be more effective in exciting double-quantum coherences in the near-equivalence regime, compared to the traditional INADEQUATE pulse sequence. Using this method, we were able to study the 1,3-$^{13}C_2$-squarate species that was previously inaccessible. The customised DQ2S and S2DQ procedures were integrated into the wider GeoDQ-singlet excitation sequence for the geometric double-quantum singlet filtered experiments. The conversion of $^{13}C_2$ double-quantum coherence into $^{13}C_2$ singlet order, and backwards, was demonstrated with good efficiency.

The singlet relaxation time constants T_S for both the 1,2-$^{13}C_2$-squarate and 1,3-$^{13}C_2$-squarate isotopologues greatly exceeded the T_1 values. The T_S value for 1,3-$^{13}C_2$-squarate was measured to be ≈ 200 s in a high pH aqueous solution, at 16.4 T field strength. The long T_S time may be due to the inversion symmetry of 1,3-$^{13}C_2$-squarate, which removes the large contribution of the chemical shift anisotropy mechanism to singlet relaxation, even at high magnetic fields. However, even though T_S is unusually long for a species in high magnetic field in aqueous solution, the intermolecular interactions with solvent protons and other species, combined with the relatively high viscosity of the aqueous environment, still limit the singlet relaxation time to a few minutes, even for this highly favourable species.

Chapter 4

Spinor Double-Quantum Excitation

A family of double-quantum excitation schemes is described for the solution nuclear magnetic resonance (NMR) of near-equivalent spin-1/2 pairs. These new methods exploit the spinor behaviour of 2-level systems, whose signature is the change of sign of a quantum state upon a 2π rotation.

The spinor behaviour is used to manipulate the phases of single-quantum coherences, in order to prepare a double-quantum precursor state which is rapidly converted into double-quantum coherence by a straightforward $\pi/2$ rotation.

One set of spinor-based methods exploits symmetry-based pulse sequences, while the other set exploits SLIC (Spin-Lock Induced Crossing), in which the nutation frequency under a resonant radiofrequency field is matched to the spin-spin coupling. A variant of SLIC is introduced which is well-compensated for deviations in the radiofrequency field amplitude.

The methods are demonstrated by performing double-quantum-filtered ^{19}F NMR on two different molecular systems containing a pair of diastereotopic ^{19}F nuclei each, and ^{13}C NMR on a naphthalene derivative. We compare the new methods with existing techniques.

4.1 Introduction

In the previous chapter, the geometric double-quantum excitation pulse sequence (see Figure 3.13) was used to selectively detect the signals from near-equivalent $^{13}C_2$-pairs in ^{13}C NMR spectra[1,128]. This method facilitates DQ-excitation in this coupling regime through a π rotation about the z-axis in the zero-quantum subspace ($R_z^{13}(\pi)$) to generate a geometric Aharonov-Anandan phase. Despite its superior performance to the INADEQUATE sequence (Figure 3.4), the set-up of the GeoDQ sequence requires detailed knowledge of the spin-system parameters, complicating its optimisation.

A group of procedures which operate differently to the GeoDQ technique, but which also achieve efficient double-quantum excitation in the near-equivalence regime are introduced in this chapter. This is the Spinor-DQ excitation technique, named after its mechanism, which exploits the spinor property of two-level quantum systems. This DQ-excitation pathway involves a 2π rotation of a quantum state in the singlet-outer triplet state manifold (C^{12}) to create the antiphase triplet-triplet coherences required for double-quantum excitation, as illustrated in Figure 4.1. This operation returns the system to the original state, with a sign change. This property[127,137] is characteristic of a spinor, which requires a 4π rotation to restore its original state. Spinor behaviour has been reported numerous times in NMR[138–143].

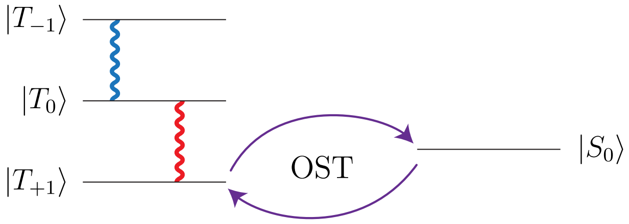

Figure 4.1: Outer Singlet-Triplet (OST) transitions[73] may be induced between the $|T_{+1}\rangle$ and $|S_0\rangle$ states. A 2π cycle between the states leads to a sign change for one of the triplet-triplet coherences. This creates the desired triplet-triplet antiphase single-quantum coherences required to excite double-quantum coherence. The phase difference is denoted by different colours, and coherences by the wavy lines. Another 2π rotation between the states returns the system to its original state, adding up to a 4π rotation in total.

Two different implementations of Spinor-DQ excitation are herein demonstrated. The first implementation involves the PulsePol sequence, first devised for the transfer of polarisation from the electron to the nucleus in nitrogen-vacancy centres in diamonds[83,144]. Additionally, PulsePol has been effectively adapted for singlet NMR studies of coupled spin-1/2 pairs in solution[85–88], as described in Subsection 2.6.3.

The second implementation of Spinor-DQ excitation uses the SLIC method, as described in Subsection 2.6.2. This pulse sequence was originally developed to excite singlet order by applying a resonant radiofrequency field, such that the nutation frequency of the spins matches the J-coupling between them[73,76,77,80–82,97,124,145–152]. The SLIC sequence shows high selectivity, but is disadvantaged by its high sensitivity to rf amplitude mismatch. An rf-compensated variant, "cSLIC", was devised by Sabba[95] *et al.*, which is more robust with respect to deviations from the radiofrequency field amplitude.

The structures of the INADEQUATE, geometric DQ-excitation, and spinor DQ-excitation schemes are illustrated in Figure 4.2.

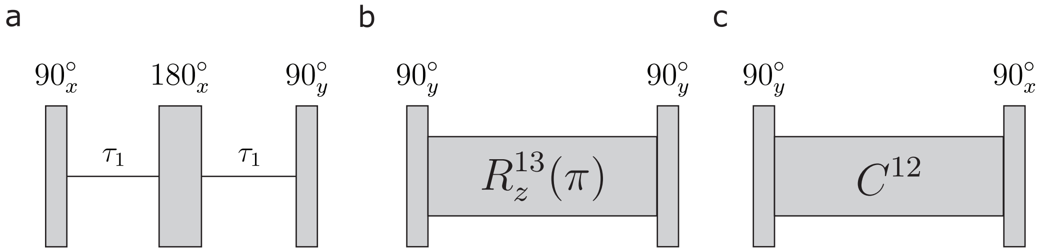

Figure 4.2: Double-quantum excitation schemes for spin-1/2 pairs. (**a**) The INADEQUATE three-pulse method. (**b**) The geometric double-quantum excitation method. (**c**) One version of the spinor double-quantum-excitation method. Adapted from Heramun *et al.*[2], *J. Chem. Phys.* 164, 064201 (2026); licensed under a Creative Commons Attribution (CC BY) license.

The experimental demonstrations given further along this chapter examine $^{19}F_2$ and $^{13}C_2$ near-equivalent molecular systems. The corresponding double-quantum filtered spectra obtained from applying the INADEQUATE, Spinor-DQ, and GeoDQ sequences are compared. Both Spinor-DQ and GeoDQ procedures excite DQC in all the spin systems examined, with much higher efficiency than the conventional INADEQUATE sequence.

4.1.1 Spin Hamiltonian

The rotating-frame spin Hamiltonian for a homonuclear spin-1/2 pair in the absence of a radiofrequency field is written as follows:

$$H^0 = \Omega_1 I_{1z} + \Omega_2 I_{2z} + H_J, \tag{4.1}$$

where the J-coupling Hamiltonian is given by:

$$H_J = \omega_J \, \mathbf{I}_1 \cdot \mathbf{I}_2, \tag{4.2}$$

and the resonance offset frequencies for the two spins are defined as follows:

$$\begin{aligned} \Omega_1 &= \omega^0(\delta_1 - \delta_{\text{ref}}), \\ \Omega_2 &= \omega^0(\delta_2 - \delta_{\text{ref}}). \end{aligned} \tag{4.3}$$

The terms $\{\delta_1, \delta_2, \delta_{\text{ref}}\}$ are the chemical shift of spins I_1, spin I_2, and the rf reference frequency, respectively. The other symbols are specified in Equation 3.5.

The spin Hamiltonian may be written as the sum of two terms, as follows:

$$H^0 = H_\Sigma + (H_\Delta + H_J). \tag{4.4}$$

where:

$$\begin{aligned} H_\Sigma &= \omega_\Sigma \, \tfrac{1}{2} \left(I_{1z} + I_{2z} \right), \\ H_\Delta &= \omega_\Delta \, \tfrac{1}{2} \left(I_{1z} - I_{2z} \right).. \end{aligned} \tag{4.5}$$

The sum and difference of the resonance offset frequencies are defined as follows:

$$\begin{aligned} \omega_\Sigma &= \Omega_1 + \Omega_2, \\ \omega_\Delta &= \Omega_1 - \Omega_2. \end{aligned} \tag{4.6}$$

The singlet and triplet states were defined and numbered in Equation 2.1.

Rotation operators for single transitions are defined as follows:

$$R_{\mu}^{rs}\left(\beta\right)=\exp\!\left(-i\beta I_{\mu}^{rs}\right), \tag{4.7}$$

where $\mu\in\{x,y,z\}$ denotes the axis of rotation. The operator for a cycle $\mathcal{C}$, i.e. a rotation through an angle of 2π, is particularly relevant. A cycle in the $\{\left|r\right\rangle,\left|s\right\rangle\}$ subspace is independent of the axis, and is described by the following operator:

$$\mathcal{C}^{rs}=R_{\mu}^{rs}(2\pi), \tag{4.8}$$

which may be written as follows:

$$\mathcal{C}^{rs}=-\mathbb{1}^{rs}+\sum_{u\neq\{r,s\}}\left|u\right\rangle\left\langle u\right|, \tag{4.9}$$

where the second term involves a summation over all states which are outside the rotated 2-level system. The cycle operator C^{12} for the $\{\left|S_0\right\rangle,\left|T_{+1}\right\rangle\}=\{\left|1\right\rangle,\left|2\right\rangle\}$ subspace, is given by:

$$C^{12}=-\mathbb{1}^{12}+\mathbb{1}^{34}. \tag{4.10}$$

The negative sign of the first term is a consequence of spinor behaviour.

The spin Hamiltonian H^0 can be expressed in terms of single-transition operators, as follows:

$$\begin{aligned}H^0=&-\Omega_{\mathrm{ST}}R_y^{13}(-\theta_{\mathrm{ST}})I_z^{13}R_y^{13}(+\theta_{\mathrm{ST}})+\omega_{\Sigma}I_z^{24}\\&+\tfrac{1}{4}\omega_J(\mathbb{1}^{24}-\mathbb{1}^{13}),\end{aligned} \tag{4.11}$$

where Ω_{ST} and θ_{ST} were given in Equation 3.5.

4.2 Double-Quantum Filtering Schemes

The double-quantum filtering amplitude a_{DQF} is equal to the absolute squared of the double-quantum excitation amplitude[124,153] a_{DQ}, as follows:

$$a_{\mathrm{DQF}} = |a_{\mathrm{DQ}}|^2 = |\left\langle 2\right| U\rho_1 U^\dagger \left|4\right\rangle|^2 = |\left\langle \rho_1 \xrightarrow{U} \left|2\right\rangle \left\langle 4\right| \right\rangle|^2. \tag{4.12}$$

Although a_{DQ} (Equation 3.18) is a complex number in general, the double-quantum filtering amplitude a_{DQF} is a real and positive value, which approaches 1 for a DQ-excitation sequence of maximum efficiency.

The double-quantum excitation time is denoted by T in all the schemes illustrated in this chapter. Ideally, T should be as short as possible to minimise relaxation losses. For near-equivalent systems, however, large values of a_{DQF} often require a long T.

4.2.1 INADEQUATE

The INADEQUATE pulse sequence is shown in Figure 4.2(a), and given in Figure 4.3 as it was implemented in the current experiments.

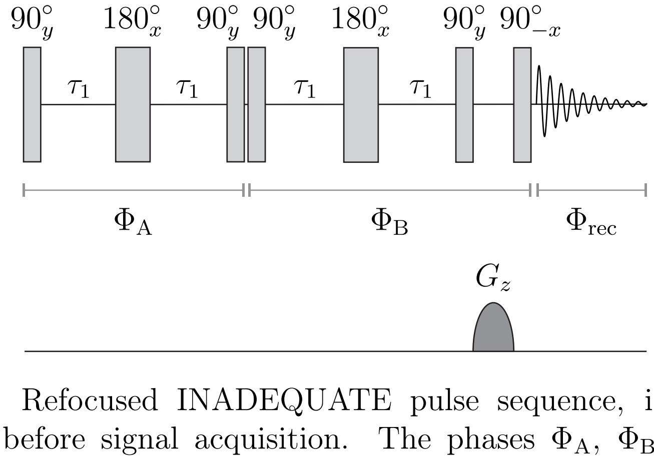

Figure 4.3: Refocused INADEQUATE pulse sequence, including a z-filtering step before signal acquisition. The phases Φ_{A}, Φ_{B} and Φ_{rec} are cycled in 4 steps to implement double-quantum filtering. Adapted from Heramun *et al.*[2], *J. Chem. Phys.* 164, 064201 (2026); licensed under a Creative Commons Attribution (CC BY) license.

Although the standard INADEQUATE sequence performs well for weakly-coupled spin-1/2 pairs ($T \simeq (2J)^{-1}$), significant double-quantum excitation is only achieved in the near-equivalence regime when the total duration T of INADEQUATE is inversely proportional to the inner peak splitting:

$$T \sim |\pi/\Delta\omega_{\mathrm{inner}}| \simeq |J/\Delta^2|. \tag{4.13}$$

This implementation, as discussed in Chapter 3, leads to a large value of T in the near-equivalence limit, and correspondingly large relaxation losses. Several authors[108,125,154,155] have independently derived an expression for the double-quantum excitation amplitude of INADEQUATE in the general case. This may be written as follows:

$$\begin{aligned} a_{\mathrm{DQ}}^{\mathrm{INADQ}} = {} & i\cos(\theta_{\mathrm{ST}})\sin(\Omega_{\mathrm{ST}}\tau_1)\cos(\omega_J\tau_1) \\ & - i\left(\sin^2(\theta_{\mathrm{ST}}) + \cos^2(\theta_{\mathrm{ST}})\cos(\Omega_{\mathrm{ST}}\tau_1)\right)\sin(\omega_J\tau_1). \end{aligned} \tag{4.14}$$

Two methods can be used to achieve faster double-quantum excitation in the near-equivalence regime: geometric double-quantum excitation, described in Chapter 3, and spinor double-quantum excitation, described in this chapter.

4.2.2 GeoDQ

The geometric double-quantum excitation pulse sequence (GeoDQ) previously introduced in Chapter 3 is shown in Figure 4.2(b), and given in Figure 4.4 as it was implemented in the current experiments. The GeoDQ sequence employs a cyclic trajectory between the $|T_0\rangle$ and $|S_0\rangle$ states to ultimately create a phase difference between the $|T_{+1}\rangle\langle T_0| = |2\rangle\langle 3|$, and $|T_0\rangle\langle T_{-1}| = |3\rangle\langle 4|$ coherences, as depicted in Figure 3.14.

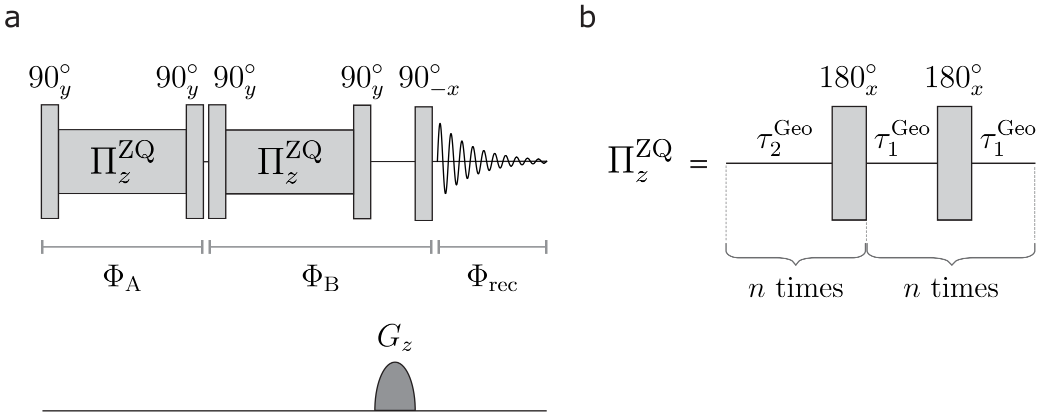

Figure 4.4: (**a**) GeoDQ pulse sequence, including a z-filtering step before signal acquisition. (**b**) Structure of the Π_z^{ZQ} block. Theoretical expressions for τ_1^{Geo}, τ_2^{Geo} and n are given in Equation 3.11. The phases Φ_A, Φ_B and Φ_{rec} are cycled in 4 steps to implement double-quantum filtering. Adapted from Heramun *et al.*[2], *J. Chem. Phys.* 164, 064201 (2026); licensed under a Creative Commons Attribution (CC BY) license.

4.2.3 Spinor Double-Quantum Excitation Schemes

The first two steps of the spinor DQ excitation scheme are the same as for geometric DQ excitation. The starting point is thermal equilibrium, which is associated with the density operator ρ_1 shown in Equation 3.12. Following a $\pi/2$ pulse, ρ_2 is obtained, described in Equation 3.13. The in-phase SQCs are depicted in Pane 2 of Figure 3.14 for GeoDQ, and Figure 4.5 for Spinor-DQ.

The spinor double-quantum excitation method prepares the double-quantum precursor state using a different method to that used in GeoDQ. Instead of implementing a π rotation in the $\{|1\rangle, |3\rangle\}$ subspace, Spinor-DQ implements a 2π rotation in an outer singlet-triplet subspace. This can be either of two subspaces. The lower subspace, spanned by the states $\{|S_0\rangle, |T_{+1}\rangle\} = \{|1\rangle, |2\rangle\}$, and the upper subspace, spanned by the states $\{|S_0\rangle, |T_{-1}\rangle\} = \{|1\rangle, |4\rangle\}$.

In this chapter, it is assumed that a cycle is implemented in the $\{|1\rangle, |2\rangle\}$ subspace, as shown in the central pane in Figure 4.5. The key element to implement this rotation is shown as $C^{12}(\pi)$ in Figure 4.2(c). The relevant transformation of the spin density operator is as follows:

$$\begin{aligned}
\rho_3^{\text{spinor}} &= C^{12}\,\rho_2\,C^{12\dagger} \\
&= \sqrt{2}C^{12}\left(I_x^{23} + I_x^{34}\right)C^{12\dagger} \\
&= \sqrt{2}\left(-I_x^{23} + I_x^{34}\right) \\
&= -2I_{1x}I_{2z} - 2I_{1z}I_{2x} \qquad\qquad (4.15) \\
&= \frac{1}{\sqrt{2}}\{-|2\rangle\langle 3| - |3\rangle\langle 2| + |3\rangle\langle 4| + |4\rangle\langle 3|\} \\
&= \frac{1}{\sqrt{2}}\begin{pmatrix} 0 & 0 & 0 & 0 \\ 0 & 0 & -1 & 0 \\ 0 & -1 & 0 & 1 \\ 0 & 0 & 1 & 0 \end{pmatrix}.
\end{aligned}$$

This transformation follows from the properties of the single-transition cycle operator previously given in Equation 4.10:

$$\begin{aligned}
C^{12}\,|2\rangle &= -\,|2\rangle\,, \\
C^{12}\,|3\rangle &= +\,|3\rangle\,, \\
C^{12}\,|4\rangle &= +\,|4\rangle\,. \qquad (4.16)
\end{aligned}$$

The change in sign of state $|2\rangle$ after applying the cycle operator C^{12} to it is a manifestation of spinor behaviour. A graphical representation of ρ_3^{spinor} is shown in Pane 3 of Figure 4.5. The DQP state ρ_3^{spinor} is converted into double-quantum coherence by a final $(\pi/2)_x$ pulse, as follows:

$$\begin{aligned}
\rho_4 &= R_x(\pi/2)\,\rho_3^{\text{spinor}}\,R_x(\pi/2)^\dagger \\
&= -R_x(\pi/2)\,(2I_{1x}I_{2z} + 2I_{1z}I_{2x})R_x(\pi/2)^\dagger \\
&= 2I_{1x}I_{2y} + 2I_{1y}I_{2x} \qquad (4.17)\\
&= 2I_y^{24} \\
&= -i(I_1^+I_2^+ - I_1^-I_2^-) \\
&= -i(|2\rangle\langle 4| - |4\rangle\langle 2|) \\
&= \frac{i}{\sqrt{2}}\begin{pmatrix} 0 & 0 & 0 & 0 \\ 0 & 0 & 0 & -1 \\ 0 & 0 & 0 & 0 \\ 0 & 1 & 0 & 0 \end{pmatrix}.
\end{aligned}$$

This is the same final state that was obtained for the geometric double-quantum excitation (Equation 3.16) sequence. A graphical representation is shown in Pane 4 of Figure 4.5. Therefore, both GeoDQ and Spinor-DQ generate double-quantum coherence with maximum amplitude, without taking into account pulse imperfections and relaxation losses.

In singlet NMR, two pulse sequences excite OST to populate the singlet state, ultimately accessing singlet order. These are the SLIC[73,76], and PulsePol[85] pulse sequences. We adapt these sequences to excite DQC in systems in the near-equivalence coupling regime. The OST cycle described earlier requires a 4π-rotation to return to its original state, like a spinor.

4.2.4 PulsePol/Symmetry-Based Implementation

The first implementation of Spinor-DQ involves the PulsePol/symmetry-based $R4_3^1$ sequence. PulsePol consists of the following sequence of delays and pulses[83], as follows:

$$\text{PulsePol} = 90_{90} - \tau_2 - 180_0 - \tau_2 - 90_{90} - 90_{180} - \tau_2 - 180_{90} - \tau_2 - 90_{180}. \quad (4.18)$$

As discussed by Sabba[85] *et al.*, PulsePol is closely related to the $R4_3^1$

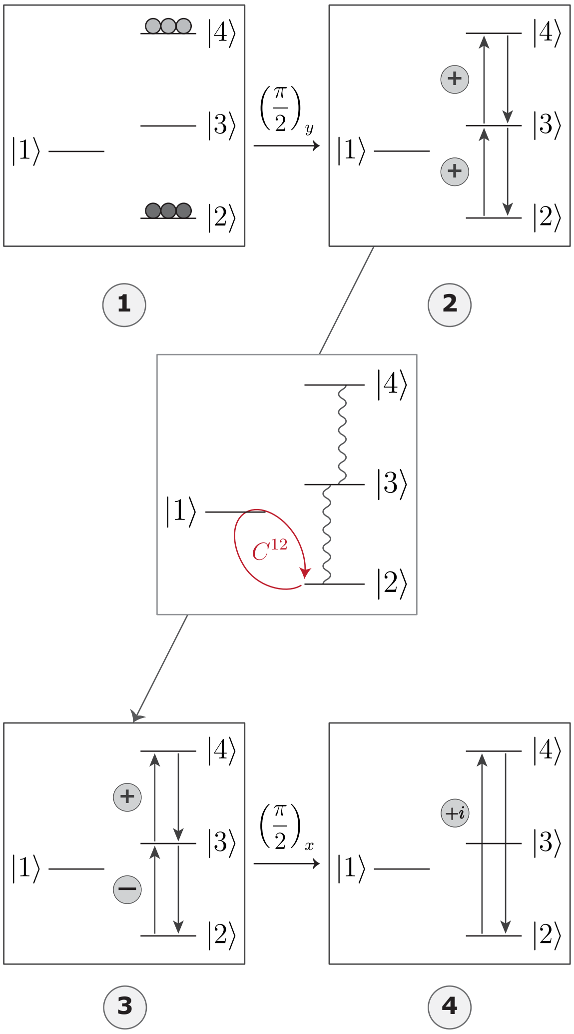

Figure 4.5: Spinor double-quantum excitation. An ensemble of spin-1/2 pairs is at thermal equilibrium in a strong magnetic field (pane 1). In-phase single-quantum triplet-triplet coherences are generated by a $\pi/2$ y-pulse (pane 2). This is converted into a *double-quantum precursor state* of antiphase triplet-triplet coherences (pane 3). A final $\pi/2$ x-pulse generates double-quantum coherence between the states $|T_{\pm 1}\rangle$ (pane 4). This method uses a rotation through 2π in the single-quantum subspace spanned by the singlet state $|S_0\rangle = |1\rangle$ and the outer triplet state $|T_{+1}\rangle = |2\rangle$. The rotation corresponds to the single-transition cycle operator C^{12} (Equation 4.10). Adapted from Heramun *et al.*[2], *J. Chem. Phys.* 164, 064201 (2026); licensed under a Creative Commons Attribution (CC BY) license.

symmetry-based sequence:

$$R4_3^1 = \left[\, 90_{135} - \tau_2 - 180_{45} - \tau_2 - 90_{135} - 90_{-135} - \tau_2 - 180_{135} - \tau_2 - 90_{-135} \,\right]^2, \tag{4.19}$$

where the superscript indicates 2 repetitions. This sequence conforms to $R4_3^1$ symmetry when applied to spin-1/2 pairs in solution NMR if the delay τ_2 obeys the following:

$$\tau_2 = \tfrac{3}{8}\tau_J, \tag{4.20}$$

in the limit of short rf pulses. The J-coupling period τ_J is given by:

$$\tau_J = \frac{2\pi}{|\omega_J|} = |J|^{-1}. \tag{4.21}$$

The construction of an R-sequence was explained in Chapter 2. The basic $\mathcal{R}$-element of $R4_3^1$ in Equation 4.19, is given by:

$$\mathcal{R}^0 = 90_{90} - \tau_2 - 180_0 - \tau_2 - 90_{90}\ . \tag{4.22}$$

For $R4_3^1$, the symmetry numbers are $\{N, n, \nu\} = \{4, 3, 1\}$. Therefore, the complete $R4_3^1$ sequence consists of four $\mathcal{R}$-elements, with a duration of three J-periods. The phases of the $\mathcal{R}$-elements alternate between the values $\pm\phi$, where $\phi = \pi\nu/N = \pi/4$ in the case of $R4_3^1$. The total duration of the $R4_3^1$ sequence is given by:

$$T_{R4} = 3\tau_J. \tag{4.23}$$

Several alternative combinations of symmetry numbers are also possible, as specified in Table 1 of Ref.[85]. This rational, symmetry-based, construction procedure leads to well-defined selection rules for the average Hamiltonian $\overline{H}^{(1)}$, which governs the dynamical properties of the pulse sequence, within certain approximations[93,94].

The $R4_3^1$ and PulsePol sequences are related as follows:

$$R4_3^1 = \left[(\text{PulsePol})_{\phi=\pi/4}\right]^2\ . \tag{4.24}$$

The $R4_3^1$ sequence consists of a phase-shifted PulsePol sequence, repeated twice. In this chapter, the $R4_3^1$ sequence in Equation 4.19 is considered, not PulsePol (Equation 4.18). This allows the direct application of symmetry-based pulse sequence theory[91–94].

Figure 4.6 shows the pulse sequence as it was implemented during the experiments. This sequence was constructed using a *riffled* variant of $R4_3^1$ (see Subsection 2.6.3), which improves the robustness[85]. Nevertheless, in the limit of short rf pulses, the symmetry properties and selection rules for the $R4_3^1$ symmetry are still valid, and the sequence is called "PulsePol-DQ".

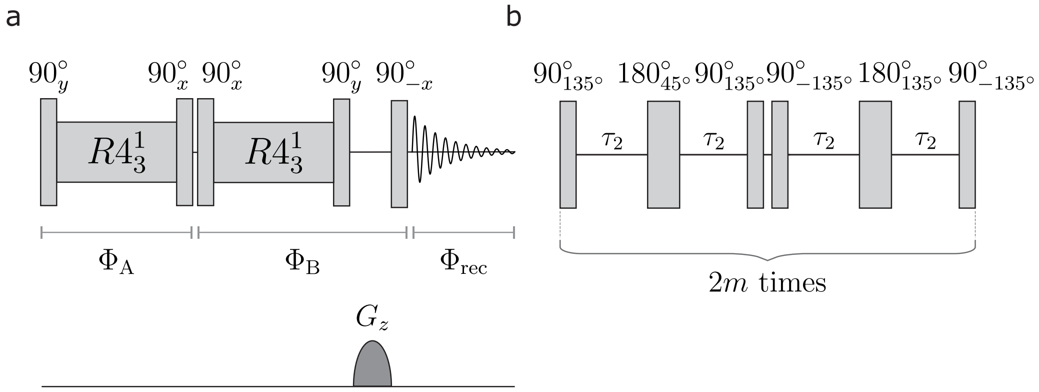

Figure 4.6: (**a**) Double-quantum-filtering pulse sequence, using PulsePol/$R4_3^1$ for double-quantum excitation, including a z-filtering step before signal acquisition. (**b**) Structure of the $R4_3^1$ sequence, broken down as shown in Equation 4.19. The pair of $\mathcal{R}$-elements is repeated $2m$ times. Adapted from Heramun *et al.*[2], *J. Chem. Phys.* 164, 064201 (2026); licensed under a Creative Commons Attribution (CC BY) license.

The cycle element C^{12} shown in Figure 4.2(c) is given by m repetitions of the $R4_3^1$ sequence (i.e. $2m$ repetitions of a PulsePol sequence, shifted by $\pi/4$ in phase):

$$C^{12} = \left[R4_3^1\right]^m . \tag{4.25}$$

As described by Sabba[85] *et al.*, the theory of $R4_3^1$ in the current context proceeds by describing the chemical shift Hamiltonians H_Δ and H_Σ in the interaction frame of the J-coupling and rf fields:

$$\begin{aligned}\tilde{H}_\Delta &= U_{\mathrm{rf}}(t)^\dagger U_J(t)^\dagger H_\Delta U_J(t) U_{\mathrm{rf}}(t),\\ \tilde{H}_\Sigma &= U_{\mathrm{rf}}(t)^\dagger U_J(t)^\dagger H_\Sigma U_J(t) U_{\mathrm{rf}}(t),\end{aligned} \tag{4.26}$$

where $U_{\mathrm{rf}}(t)$ is the propagator under the rf fields of the pulse sequence. The propagator under the J-coupling Hamiltonian is defined as follows:

$$U_J(t) = \exp\{-iH_J t\}. \tag{4.27}$$

The propagator for the spin system, at any time point t, may be approximated as follows:

$$U(t) \simeq U_J(t) U_{\mathrm{rf}}(t) \times \exp\{-i\overline{H}^{(1)} t\}, \tag{4.28}$$

where $\overline{H}^{(1)}$ is the average Hamiltonian[34,156,157] of the chemical shift terms over a single $R4_3^1$ sequence:

$$\overline{H}^{(1)} = \overline{H}^{(1)}_\Delta + \overline{H}^{(1)}_\Sigma, \tag{4.29}$$

with:

$$\overline{H}^{(1)}_\Delta = T_{R4}^{-1} \int_0^{T_{R4}} \tilde{H}_\Delta(t)\, dt, \tag{4.30}$$

and similarly for $\overline{H}^{(1)}_\Sigma$. The numbering convention used here for the average Hamiltonian terms is that of Hohwy *et al.*[157], superseding an earlier convention[34,156]. The selection rules associated with the symmetry number combinations given in Table 1 of Ref.[85] lead to an average Hamiltonian with the following form:

$$\overline{H}^{(1)} = \overline{H}^{(1)}_{1111} + \overline{H}^{(1)}_{1\,-11\,-1}, \tag{4.31}$$

where:

$$\begin{aligned}\overline{H}^{(1)}_{1111} &= \tfrac{1}{2}\kappa_{1111}\omega_\Delta \left|2\right\rangle \left\langle 1\right|,\\ \overline{H}^{(1)}_{1\,-11\,-1} &= -\tfrac{1}{2}\kappa_{1\,-11\,-1}\omega_\Delta \left|1\right\rangle \left\langle 2\right|.\end{aligned} \tag{4.32}$$

Note that the $R4_3^1$ symmetry causes all terms derived from H_Σ to vanish. The scaling factors $\kappa_{1\,\pm 1 1\,\pm 1}$ depend on the symmetry numbers $\{N, n, \nu\}$ of the pulse sequence and the details of the basic element $\mathcal{R}^0$. In the limit of short rf pulses, its scaling factors $\kappa_{1\,\pm 1 1\,\pm 1}$ are given by[85]:

$$\begin{aligned} \kappa_{1111} &= -\kappa_{1\,-11\,-1} = (-1)^p \frac{\sqrt{2}N}{\pi n} \sin^2\left(\frac{\pi n}{2N}\right), \\ p &= \frac{n-\nu}{N} - \tfrac{1}{2}; \quad p \in \mathbb{Z}, \end{aligned} \tag{4.33}$$

where $\mathbb{Z}$ is the set of all integers.

For the $R4_3^1$ sequence, $\{N, n, \nu\} = \{4, 3, 1\}$, the scaling factors evaluate to:

$$\kappa_{1111} = -\kappa_{1\,-11\,-1} = \frac{2(1+\sqrt{2})}{3\pi} \simeq 0.512\ . \tag{4.34}$$

The first-order average Hamiltonian $\overline{H}^{(1)}$ for the $R4_3^1$ sequence is therefore given by:

$$\overline{H}^{(1)} = \omega_{\mathrm{nut}}^{12} I_x^{12}, \tag{4.35}$$

where the single-transition nutation frequency $\omega_{\mathrm{nut}}^{12}$ is proportional to the chemical shift difference frequency ω_Δ:

$$\omega_{\mathrm{nut}}^{12} = \kappa_{1111}\omega_\Delta \simeq 0.512\,\omega_\Delta. \tag{4.36}$$

The selection rules imposed by $R4_3^1$ symmetry ensure that the average Hamiltonian is selective for the $\{|1\rangle, |2\rangle\}$ transition. The real values of the scaling factors $\kappa_{1\,\pm 1 1\,\pm 1}$ indicate that the $R4_3^1$ sequence generates a rotation about the x-axis of the $\{|1\rangle, |2\rangle\}$ subspace. In contrast, the effective rotation axis of the PulsePol sequence (Equation 4.18) is rotated away from the x-axis by 45°. From Equation 4.28, the propagator for a single $R4_3^1$ sequence is given by:

$$U(R4_3^1) \simeq U_J(T_{R4}) U_{\mathrm{rf}}(R4_3^1) R_x^{12}(\omega_{\mathrm{nut}}^{12} T_{R4}), \tag{4.37}$$

where the single-transition rotation angle is given by:

$$\omega_{\text{nut}}^{12} T_{R4} = 8\omega_{\text{nut}}^{12} \tau_2, \tag{4.38}$$

and the single-transition rotation operator R_x^{12} was defined in Equation 4.7.

After being taken over the entire $R4_3^1$ sequence, the propagators U_J and U_{rf} become unity operators. Hence, the propagator for a complete $R4_3^1$ sequence is given by just a rotation around the x-axis of the $\{|1\rangle, |2\rangle\}$ subspace. Equation 4.37 simplifies to:

$$U(R4_3^1) \simeq R_x^{12}(\omega_{\text{nut}}^{12} T_{R4}). \tag{4.39}$$

If the $R4_3^1$ sequence is repeated m times, the total duration T is given by:

$$T = mT_{R4} = 3m\tau_J = 24m\tau_2, \tag{4.40}$$

since $3\tau_J$ periods occur within the same time as $8\tau_2$ delays. The overall spin propagator is given by:

$$U(\left[R4_3^1\right]^m) \simeq R_x^{12}(\beta^{12}), \tag{4.41}$$

where the total rotation angle in the $\{|1\rangle, |2\rangle\}$ subspace is:

$$\beta^{12} = \omega_{\text{nut}}^{12} T. \tag{4.42}$$

The density operator ρ_2 (Equation 3.13), is transformed as follows:

$$\begin{aligned}\rho_3(T) &\simeq R_x^{12}(\beta^{12})\,\rho_2\,R_x^{12}(\beta^{12})^\dagger \\ &= 2^{1/2} R_x^{12}(\beta^{12})\left(I_x^{23} + I_x^{34}\right) R_x^{12}(\beta^{12})^\dagger \\ &= 2^{1/2}\left(I_x^{23}\cos\left(\tfrac{1}{2}\beta^{12}\right) + I_y^{13}\sin\left(\tfrac{1}{2}\beta^{12}\right) + I_x^{34}\right). \end{aligned} \tag{4.43}$$

Note the 4π-periodicity with respect to β^{12} in Equation 4.43, which is a signature of spinor behaviour. The last equation follows from the commutation relationships[66,67]:

$$\begin{aligned}
[I_x^{12}, I_x^{23}] &= \tfrac{1}{2} i I_y^{13}, \\
[I_x^{12}, I_y^{13}] &= -\tfrac{1}{2} i I_x^{23}, \\
[I_x^{12}, I_x^{34}] &= 0. \qquad (4.44)
\end{aligned}$$

The total rotation angle β^{12} may be set to $\approx 2\pi$ by choosing the repetition number m as follows:

$$m = \mathrm{round}\left(\frac{2\pi}{8|\kappa_{1111}\,\omega_\Delta|\tau_2}\right) \simeq \mathrm{round}\left(0.651\frac{J}{\Delta}\right). \qquad (4.45)$$

This way, the propagator for the repeated $R4_3^1$ sequences approximates a cycle C^{12}:

$$U(\left[R4_3^1\right]^m) \simeq R_x^{12}(2\pi) = C^{12}. \qquad (4.46)$$

Under these conditions, the transformations of Equations 4.15 and 4.17 are possible, and double-quantum coherence can be generated by applying a final $(\pi/2)_x$ pulse. The duration T required to excite DQC is twice compared to the singlet order excitation time[85]. This is due to the fact that Spinor-DQ excitation requires a 2π rotation in the $\{|1\rangle, |2\rangle\}$ subspace, while the generation of singlet order by PulsePol only requires a π rotation. The spin density operator at the end of the complete sequence has the following form:

$$\begin{aligned}
\rho_4(T) &= R_x(\pi/2)\rho_3(T)R_x^\dagger(\pi/2) \\
&\simeq 2I_y^{24}\sin^2(\tfrac{1}{4}\beta^{12}) + \ldots, \qquad (4.47)
\end{aligned}$$

which shows the excitation of double-quantum coherence, plus other terms (omitted for simplicity).

The double-quantum amplitude for the PulsePol-DQ sequence, over the duration T is given as follows:

$$a_{\mathrm{DQ}}^{\mathrm{PulsePol}}(T) \simeq -i\sin^2\left(\tfrac{1}{4}\omega_{\mathrm{nut}}^{12}T\right). \qquad (4.48)$$

The double-quantum filtering amplitude for the PulsePol-DQ sequence is given, in the absence of relaxation, by the square magnitude of Equation 4.48:

$$a_{\mathrm{DQF}}^{\mathrm{PulsePol}}(T) \simeq \sin^4\left(\tfrac{1}{4}\omega_{\mathrm{nut}}^{12}T\right). \tag{4.49}$$

4.2.5 SLIC Implementation

The second implementation of Spinor-DQ involves the SLIC sequence, plus its variants, as shown in Figure 4.7.

SLIC-DQ: Single Pulse Implementation

The first type of implementation of SLIC as a Spinor-DQ sequence is shown in Figure 4.7(a). Double-quantum excitation, in this case, is induced by a weak rf field with phase $\phi = 0$, and with an amplitude that satisfies the SLIC condition (see Subsection 2.6.2) $\omega_{\mathrm{nut}}^{\mathrm{SLIC}} = \omega_J$ for a total DQ-excitation time T. This pulse is not preceded by a 90° pulse, nor is it followed by one. Instead, the SLIC pulse is applied to thermal equilibrium magnetisation I_z, directly generating DQC without any further manipulations. The SLIC phenomenon has been widely exploited in the preparation and study of long-lived states[73,76,77,80–82,97,124,145–151,158], and is now used to excite DQC.

The spin Hamiltonian in the presence of the SLIC pulse is given by:

$$H = H_\Sigma + H_\Delta + H_J + \omega_{nut} I_x. \tag{4.50}$$

The individual Hamiltonian terms are specified in Equations 4.2 and 4.5.

The SLIC pulse is applied to a thermal-equilibrium spin system in high magnetic field, described by the density operator $\rho_1 = I_z$ (Equation 3.12). The final density operator for a SLIC pulse with duration T is given by:

$$\rho_f(T) = U(T)\, I_z\, U^\dagger(T)\ , \tag{4.51}$$

where the SLIC propagator, without accounting for relaxation, is:

$$U(T) = \exp\{-iHT\}. \tag{4.52}$$

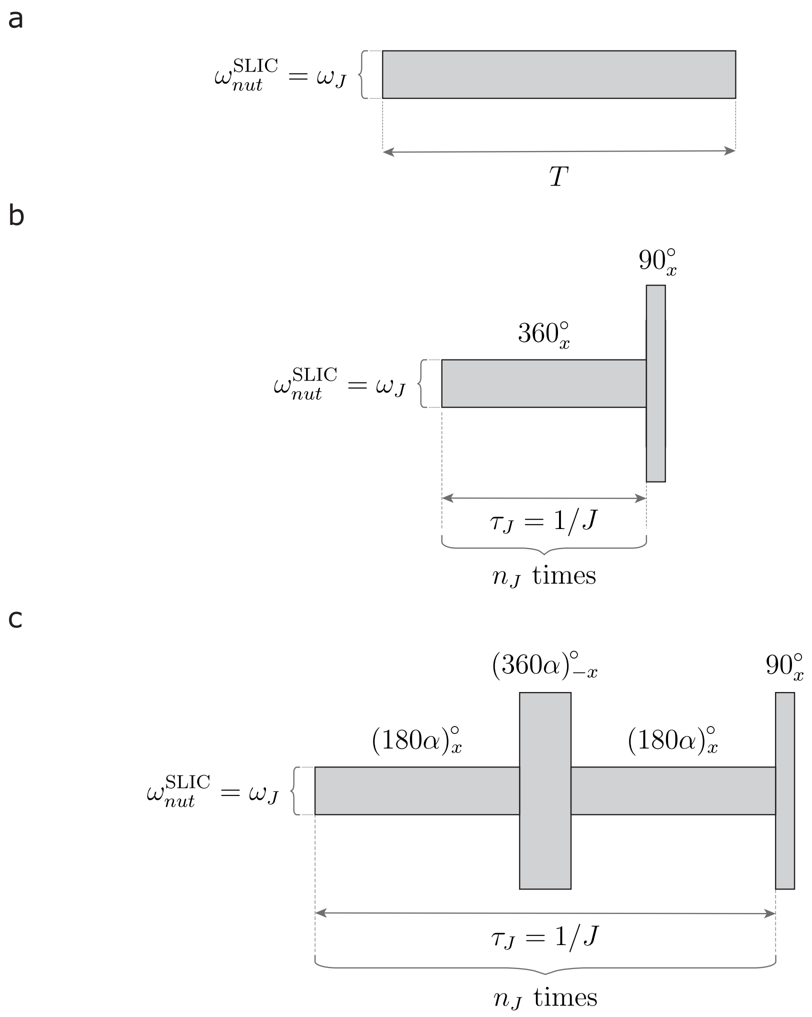

Figure 4.7: (**a**) Double-quantum excitation is induced by a weak rf field satisfying the SLIC condition $\omega_{\mathrm{nut}}^{\mathrm{SLIC}} = \omega_J$ for a total duration T. (**b**) A strong 90° pulse is appended to the SLIC pulse, without a change of phase. The SLIC pulse is subdivided into a series of n_J 360°_x pulses to ensure stroboscopic evolution. Optimal double-quantum excitation is achieved when the repeat number n_J satisfies Equation 4.76. (**c**) Double-quantum excitation scheme using cSLIC, with compensation against rf amplitude errors. A strong central pulse with a 180° phase shift is inserted at the centre point of the SLIC pulse. The flip angle multiplier α, with $\alpha \lesssim 1$, is defined in equation 4.79 and takes into account the finite duration of the central compensation pulse. The strong and weak pulses provide equal and opposite rotations, leaving no net rotation even in the presence of an rf amplitude error. For an infinitely short central pulse, $\alpha = 1$, and the central pulse has a flip angle of 360°. Adapted from Heramun *et al.*[2], *J. Chem. Phys.* 164, 064201 (2026); licensed under a Creative Commons Attribution (CC BY) license.

The Hamiltonian then undergoes a transformation into a periodic interaction frame, defined by the following unitary transformation of spin operators:

$$\tilde{Q} = W(t)^{\dagger}\, Q\, W(t), \tag{4.53}$$

where the time-dependent transformation operator $W(t)$ is defined as follows:

$$W(t) = R_y(-\pi/2) U_J(t) R_z(-\omega_J t), \tag{4.54}$$

where U_J is given by Equation 4.27 and $0 \leq t \leq T$. The frame has a period corresponding to one J-revolution $\tau_J = |J|^{-1}$.

The following property holds for all time-independent operators Q and times t:

$$\tilde{Q}(t + k\tau_J) = \tilde{Q}(t)\ ; \quad k \in \mathbb{Z}. \tag{4.55}$$

The Liouville von Neumann equation of motion of the spin density operator in the interaction frame is given by the following:

$$\frac{d}{dt}\tilde{\rho} = -i\big[\tilde{H}, \tilde{\rho}\big], \tag{4.56}$$

where the interaction-frame spin Hamiltonian $\tilde{H}(t)$ is given by:

$$\tilde{H}(t) = W(t)^{\dagger}\, H\, W(t) - i\, W(t)^{\dagger}\Big(\frac{d}{dt}W(t)\Big). \tag{4.57}$$

The second term in Equation 4.57 corrects for the non-inertial motion of the frame, playing a similar role to the Coriolis force in classical mechanics[159–161]. These equations may be combined to obtain the interaction frame Hamiltonian $\tilde{H}(t)$, as follows:

$$\begin{aligned}\tilde{H}(t) &= W(t)^{\dagger} H W(t) - H_J + \omega_J I_z \\ &= \tilde{H}_{\Delta}(t) + \tilde{H}_{\Sigma}(t) - (\omega_{\text{nut}} - \omega_J) I_z \\ &= \tilde{H}_{\Delta}(t) + \tilde{H}_{\Sigma}(t) - \epsilon_{\text{rf}}\, \omega_J I_z, \end{aligned} \tag{4.58}$$

where the fractional rf amplitude mismatch ϵ_{rf} is defined as follows:

$$\epsilon_{\mathrm{rf}} = \frac{\omega_{\mathrm{nut}} - \omega_J}{\omega_J}. \tag{4.59}$$

This value goes to zero for an exact SLIC condition match. The interaction-frame chemical shift terms are given by:

$$\begin{aligned}\tilde{H}_\Delta(t) &= \tfrac{1}{2}\omega_\Delta\, W(t)^\dagger\,(I_{1z} - I_{2z})\, W(t),\\ \tilde{H}_\Sigma(t) &= \tfrac{1}{2}\omega_\Sigma\, W(t)^\dagger\,(I_{1z} + I_{2z})\, W(t).\end{aligned} \tag{4.60}$$

The interaction-frame chemical shift Hamiltonian terms may be written in terms of single-transition operators (Equation 2.21), as follows:

$$\begin{aligned}\tilde{H}_\Delta(t) &= 2^{-1/2}\omega_\Delta\big(-I_x^{12} + I_x^{14}\cos(2\omega_J t) + I_y^{14}\sin(2\omega_J t)\big),\\ \tilde{H}_\Sigma(t) &= \tfrac{1}{2}\omega_\Sigma\big(I_x\cos(\omega_J t) + I_y\sin(\omega_J t)\big).\end{aligned} \tag{4.61}$$

The average Hamiltonian for SLIC, in the interaction frame, is given by:

$$\begin{aligned}\overline{H}^{(1)} &= \tau_J^{-1}\int_0^{\tau_J}\tilde{H}(t)\,dt\\ &= -\frac{1}{\sqrt{2}}\,\omega_\Delta I_x^{12} - \epsilon_{\mathrm{rf}}\,\omega_J I_z\\ &= -\kappa_{\mathrm{SLIC}}\,\omega_\Delta I_x^{12} - \epsilon_{\mathrm{rf}}\,\omega_J I_z.\end{aligned} \tag{4.62}$$

The propagator $U(T)$ for the spin system over the time T can be estimated from the interaction frame Hamiltonian averaged over one period, if the shift frequencies ω_Δ and ω_Σ are small compared to ω_J, and $|\epsilon_{\mathrm{rf}}| \ll 1$.

$$U(T) \simeq W(T)\exp\{-i\overline{H}^{(1)}T\}W(0)^\dagger. \tag{4.63}$$

When the SLIC matching condition is met, a rotation in the $\{|1\rangle, |2\rangle\}$ subspace is induced by the SLIC pulse in the interaction frame. This is identical to the rotation generated by the $R4_3^1$ sequence in the ordinary rotating frame (Equation 4.35). The nutation frequency is given by the negative chemical shift frequency difference ω_Δ, multiplied by a scaling factor κ_{SLIC}:

$$\kappa_{\mathrm{SLIC}} = \frac{1}{\sqrt{2}}. \tag{4.64}$$

Averaging the Hamiltonian over one J-period results in the oscillatory terms present in Equation 4.61 vanishing.

The second term in Equation 4.62 represents the deviation of the rf field amplitude from the exact SLIC condition. Therefore, the rf mismatch term interferes with the desirable subspace rotation, suggesting that the SLIC-DQ is highly susceptible to such deviations.

For DQ-excitation by a single on-resonance SLIC pulse, as shown in Figure 4.7(a), with an exact SLIC match ($\epsilon_{\mathrm{rf}} = 0$), Equation 4.51 may be implemented in three steps. The application of $W(0)^\dagger$ (Equation 4.63) gives:

$$\begin{aligned} W(0)^\dagger \, I_z \, W(0) &= R_y(\pi/2) \, I_z \, R_y^\dagger(\pi/2) = I_x \\ &= 2^{1/2}(I_x^{23} + I_x^{34}). \end{aligned} \tag{4.65}$$

This is identical to the density operator obtained in Pane 2 of the general scheme for Spinor-DQ excitation (Figure 4.5).

The propagator under the average Hamiltonian $\overline{H}^{(1)}$ for an interval T, in the case $\epsilon_{\mathrm{rf}} = 0$, is given by:

$$\exp\{-i\overline{H}^{(1)}T\} = R_x^{12}(\beta^{12}), \tag{4.66}$$

where the rotation angle in the $\{|1\rangle, |2\rangle\}$ subspace is given for SLIC by:

$$\beta^{12} = -\kappa_{\mathrm{SLIC}}\omega_\Delta T, \tag{4.67}$$

and the SLIC scaling factor $\kappa_{\mathrm{SLIC}} = 2^{-1/2}$. Hence, the transformation under the average Hamiltonian is given by:

$$R_x^{12}(\beta^{12}) I_x R_x^{12\,\dagger}(\beta^{12}) = \sqrt{2}\big(I_x^{23}\cos\big(\tfrac{1}{2}\beta^{12}\big) + I_y^{13}\sin\big(\tfrac{1}{2}\beta^{12}\big) + I_x^{34}\big). \tag{4.68}$$

This expression has a period of 4π with respect to the angle β^{12}, a signature of spinor behaviour. This transformation is similar to that given by a $R4_3^1$ sequence (Equation 4.43). The total rotation angle β^{12} may be set to $\approx -2\pi$ by the following choice of T:

$$T \simeq \mathrm{round}\left(\frac{2\pi J}{|\kappa_{\mathrm{SLIC}}\,\omega_\Delta|}\right)\tau_J \simeq \mathrm{round}\left(\left|\frac{\sqrt{2}J}{\Delta}\right|\right)\tau_J. \tag{4.69}$$

For this specific T, the evolution under the SLIC average Hamiltonian approximates a cycle, the spinor behaviour is activated, and Equation 4.68 evaluates to:

$$R_x^{12}(\beta^{12}) I_x R_x^{12\,\dagger}(\beta^{12}) \simeq \sqrt{2}\big(-I_x^{23} + I_x^{34}\big). \tag{4.70}$$

The opposite signs indicate the generation of the double-quantum precursor state (antiphase single-quantum coherence), which corresponds to Pane 3 of Figure 4.5.

In general, the spin density operator at the end of the SLIC pulse may be calculated by applying the operator $W(T)$ to the right-hand side of Equation 4.68. This leads to:

$$\rho_f(T) = -2I_y^{24}\sin(\omega_J T)\sin^2(\tfrac{1}{4}\beta^{12}) + \ldots, \tag{4.71}$$

which contains the DQC operator I_y^{24}.

The double-quantum excitation amplitude for the simplest implementation of SLIC shown in Figure 4.7(a) is as follows:

$$\begin{aligned} a_{\mathrm{DQ}}^{\mathrm{SLIC(a)}}(T) &= \langle 2|\,\rho_f(T)\,|4\rangle \\ &\simeq i\sin(\omega_J T)\sin^2(\tfrac{1}{4}\beta^{12}). \end{aligned} \tag{4.72}$$

where the SLIC rotation angle is given by Equation 4.67.

The SLIC double-quantum excitation amplitude contains two oscillating terms. The “fast” oscillating term has a frequency ω_J, whereas the “slow” oscillating term has a frequency $2^{-1/2}\omega_\Delta$. Optimal double-quantum excitation requires setting T to satisfy Equation 4.69, which maximises the value of the “slow” oscillation, while simultaneously maximising the value of the "fast" oscillation, by satisfying the condition:

$$\text{SLIC-DQ(a)}: \; T = (k \pm \tfrac{1}{4})\,\tau_J \;; \quad k \in \mathbb{Z}. \tag{4.73}$$

In general, the conditions of Equations 4.69 and 4.73 cannot simultaneously be satisfied exactly. A good compromise is to use a value of T which satisfies Equation 4.73 exactly, while also satisfying Equation 4.69 reasonably well. An unusual constraint of Equation 4.73 is that DQ-excitation is achieved when T is a multiple of τ_J, plus or minus a quarter of a rotation period.

The derivation above shows that double-quantum excitation by SLIC is a form of Spinor-DQ excitation. Instead of the explicit $\pi/2$ pulses shown in Figure 4.2(c) and 4.5, the $\pi/2$ rotations involved in SLIC are concealed in the interaction frame transformation. Nevertheless, the basic principles of Spinor-DQ excitation are evident. Equation 4.72 shows that, although a single SLIC pulse does generate DQC with high efficiency when applied to longitudinal magnetisation, the dependence on the SLIC pulse duration is highly oscillatory.

It is important to remember that the sequence duration T required to achieve SLIC-DQ excitation is twice what is required to achieve the generation of singlet order by SLIC[76].

SLIC-DQ: Two-pulse implementation

Attempting to choose a duration T to fit the constraint imposed by Equation 4.73 can be a little awkward, and prone to human error. To correct this, the version of SLIC-DQ shown in Figure 4.7(b) was devised. In this case, the SLIC pulse is followed by a strong $\pi/2$ pulse, of the same phase as the SLIC pulse. The DQ-excitation amplitude is given by:

$$a_{\mathrm{DQ}}^{\mathrm{SLIC(b)}}(T) \simeq i\cos(\omega_J T)\sin^2(\tfrac{1}{4}\beta^{12}), \tag{4.74}$$

where the SLIC rotation angle β^{12} is given by Equation 4.67.

In this implementation, optimal double-quantum excitation is achieved when T is an integer multiple of the period $\tau_J = |J^{-1}|$, while being as close as possible to the optimum value given in Equation 4.69. The SLIC duration is given by:

$$\text{SLIC-DQ(b)}: \; T = n_J \tau_J \; ; \; n_J \in \mathbb{Z}, \tag{4.75}$$

where the optimal number of cycles may be estimated as follows, in the absence of relaxation:

$$n_J \simeq \text{round}\left(\left| \frac{\sqrt{2}J}{\Delta} \right| \right). \tag{4.76}$$

The double-quantum filtering amplitude by SLIC-DQ is given by the square magnitude of Equation 4.74:

$$a_{\text{DQF}}^{\text{SLIC(b)}}(T) = |a_{\text{DQ}}^{\text{SLIC(b)}}(T)|^2 \simeq \cos^2(\omega_J T) \sin^4(\tfrac{1}{4}\beta^{12}). \tag{4.77}$$

cSLIC-DQ: Amplitude-Error Compensation

Figure 4.8(a) shows the performance of the SLIC-DQ sequence as a function of resonance offset $\Delta\omega = \frac{1}{2}\omega_\Sigma$. Exact SLIC match is assumed, $\epsilon_{\text{rf}} = 0$. The simulation shows that double-quantum excitation by SLIC is strongly frequency-selective, with an excitation bandwidth roughly equal to 0.3 times the J-coupling.

Figure 4.8(b) compares analytical results with numerical simulations of the double-quantum excitation, as a function of the rf field amplitude. A strong oscillatory dependence is superimposed on the typically narrow excitation profile of SLIC. This renders SLIC-DQ extremely sensitive to small deviations of the rf amplitude from the exact SLIC match condition - even more sensitive than other applications of SLIC. As shown below, this hypersensitivity to the rf field amplitude strongly degrades the experimental performance of SLIC-DQ.

The high sensitivity of SLIC-DQ to deviations in the rf field amplitude from the exact SLIC condition presents a serious challenge. Fortunately, an effective scheme for rf error compensation is available, and is shown in Figure 4.7(c). This method, which is called here compensated-SLIC (cSLIC), uses an rf pulse sequence employing two different amplitude levels. First, a weak rf field matching the SLIC condition is applied, then a much stronger rf field provides a compensating counter-rotation in the centre of the sequence, followed by a second weak rf field matching the SLIC condition. The cSLIC module has a total duration of $\tau_J = |J^{-1}|$, repeated n_J times (Equation 4.76).

The general form of the cSLIC sequence has the following form:

$$\text{cSLIC} = (\alpha\pi)_x - (\alpha 2\pi)^{\text{strong}}_{-x} - (\alpha\pi)_x, \tag{4.78}$$

where the factor $\alpha = 1$ for an infinitely short pulse, and is given by:

$$\alpha = \frac{\omega^{\text{strong}}_{\text{nut}}}{\omega^{\text{strong}}_{\text{nut}} + \omega_J}. \tag{4.79}$$

The cSLIC sequence is compensated for any excess nutation caused by rf amplitude mismatch. Under ideal conditions, the weak SLIC field generates an exact 2π rotation upon every cycle, and the central pulse generates an equal and opposite 2π rotation. When the rf field amplitude is larger than expected, the excess rotation induced by the misset SLIC field is compensated by the equal and opposite excess rotation caused by the misset strong pulse – and similarly when the rf field is weaker. This compensation mechanism assumes that the weak and strong rf fields experience the rf amplitude errors in the same proportion. This is the case when both fields are generated by the same radiofrequency coil, and when the deviations are caused by spatial variations in the rf field strength. This is the usual experimental situation.

The dependence of the cSLIC-DQ excitation amplitude on the total sequence duration T and rf amplitude error ϵ_{rf} is given by:

$$a^{\text{cSLIC}}_{\text{DQ}} \simeq +i\cos\theta_\epsilon \sin^2\left(\tfrac{1}{4}\kappa'\omega_\Delta T\right) \ , \tag{4.80}$$

where the parameters θ_ϵ and κ' are defined as follows:

$$\begin{aligned} \theta_\epsilon &= 2 \ \arctan\left(\frac{\epsilon_{\text{rf}}}{2+\epsilon_{\text{rf}}}\right), \\ \kappa' &= 2^{-1/2}\text{sinc}\left(\pi\epsilon_{\text{rf}}\right)\sec\left(\theta_\epsilon\right). \end{aligned} \tag{4.81}$$

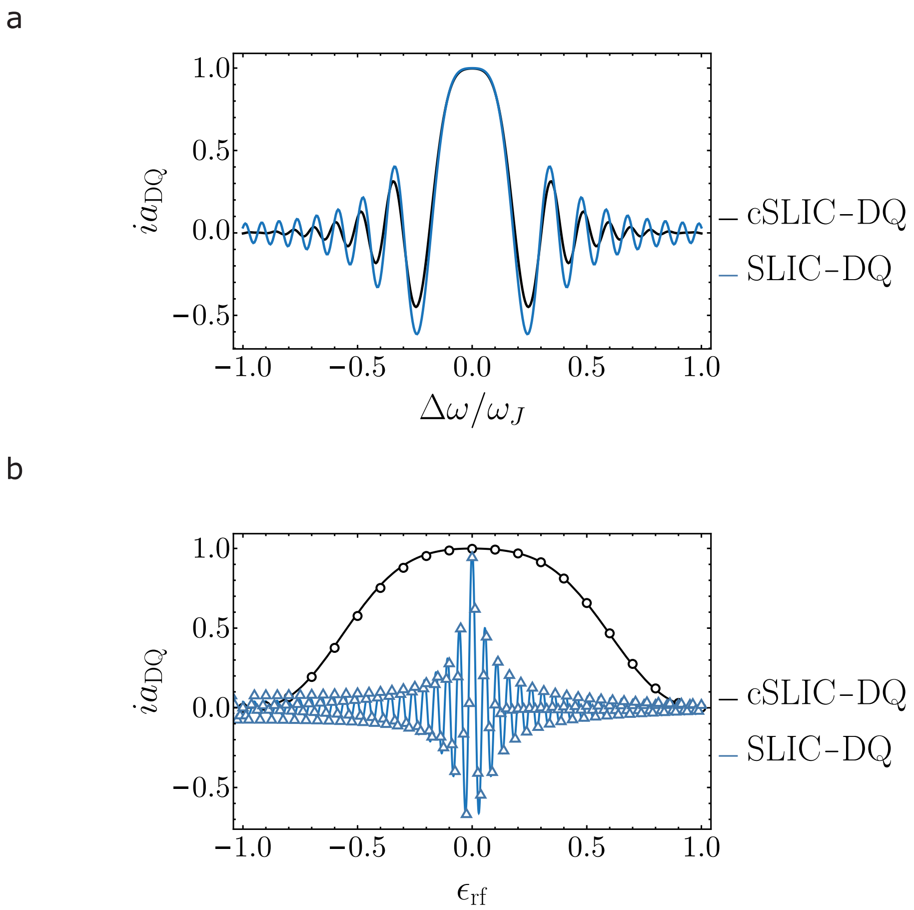

Figure 4.8: (**a**) Double-quantum excitation as a function of $\Delta\omega/\omega_J$, where the resonance offset is defined as $\Delta\omega = \omega_\Sigma/2$, for the same sequences. (**b**) Double-quantum excitation as a function of rf amplitude error ϵ_{rf} (Equation 4.59) for the standard SLIC-DQ implementation shown in Figure 4.7(a) as well as the cSLIC-DQ sequence shown in Figure 4.7(c). The resonance offset is set to zero in both cases, $\omega_\Sigma = 0$. The total duration of the conventional SLIC-DQ sequence is $T = 79.12\,\mathrm{ms}$, corresponding to $T = (20 + \frac{1}{4})\tau_J$. For the compensated SLIC-DQ sequence, the total duration is $T = 78.14\,\mathrm{ms}$, corresponding to $T = 20\tau_J$. The nutation frequency of the hard pulses in the cSLIC-DQ sequence was 25.0 kHz. Solid lines: analytical expressions. Open markers: numerical simulations. All simulations use $J = 255.94$ Hz and $\Delta = 17.8$ Hz. Adapted from Heramun *et al.*[2], *J. Chem. Phys.* 164, 064201 (2026); licensed under a Creative Commons Attribution (CC BY) license.

In the case of exact SLIC match ($\epsilon_{\mathrm{rf}} \to 0$), these parameters tend to the values $\theta_\epsilon \to 0$ and $\kappa' \to \kappa$, so that cSLIC has the same behaviour as SLIC.

This leads to the double-quantum-filtered signal amplitude:

$$a_{\mathrm{DQF}}^{\mathrm{cSLIC}}(T) = |a_{\mathrm{DQ}}^{\mathrm{cSLIC}}(T)|^2 \simeq \cos^2(\theta_\epsilon)\sin^4(\tfrac{1}{4}\kappa'\omega_\Delta T). \tag{4.82}$$

The strong-pulse limit with $\alpha = 1$ can only be approached if the duration of the central pulse is negligible, which requires a very strong radiofrequency field amplitude. A compromise for the finite-pulse case, which works well in practice, is to slightly reduce the durations, and hence the flip angles, of the two outer pulses, while simultaneously reducing the flip angle of the central strong pulse, in order to match the sum of the flip angles of the outer pulses. The overall duration of the three pulses remains fixed at τ_J. This leads to the compromise solution in Equation 4.78 and Figure 4.7(c).

The greatly improved robustness of cSLIC-DQ with respect to rf amplitude errors is shown by the numerical simulations in Figure 4.8(a). The resonance-offset dependence of uncompensated SLIC-DQ and cSLIC-DQ are similar, as shown by the simulations in Figure 4.8(b).

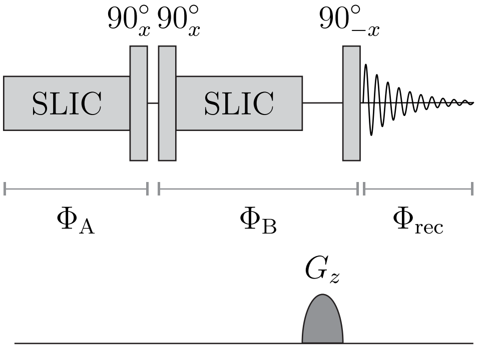

Figure 4.9: Double-quantum-filtering pulse sequence, using SLIC for double-quantum excitation, including a z-filtering step before signal acquisition. The SLIC element can either be the uncompensated version, as in Figure 4.7(b), or the compensated cSLIC sequence, as in Figure 4.7(c). Adapted from Heramun *et al.*[2], *J. Chem. Phys.* 164, 064201 (2026); licensed under a Creative Commons Attribution (CC BY) license.

4.3 Materials and Methods

4.3.1 Sample Preparation

Details regarding the preparation of the samples are given in the list below.

$^{13}C_2$-DAND: The ^{13}C NMR experiments were performed on a 30 mM solution of a $^{13}C_2$-labelled deutero-alkoxy naphthalene derivative ($^{13}C_2$-DAND) dissolved in 350 μL of isopropanol-d_8, where $^{13}C_2$-DAND is the abbreviated form of: ($1, 2, 3, 4, 5, 6, 8$-heptakis(methoxy-d_3)-7-((propan-2-yl-d_7)oxy)naphthalene-4a,8a-[$^{13}C_2$]). The synthesis of $^{13}C_2$-DAND is given by Hill-Cousins[162] *et al.*

I: The ^{19}F NMR experiments were performed on a 0.13 M solution of **I** dissolved in 450 μL of $CDCl_3$, where **I** is the abbreviated form of: (tert-butyl (2,2-difluoro-2-phenylacetyl)-L-alaninate). The synthetic procedure of the molecule is given in the Supporting Information of Ref.[2].

K: The ^{19}F NMR experiments were performed on a 70 mM solution of **K** dissolved in 450 μL of $CDCl_3$, where **K** is the abbreviated form of: (benzyl (2,2-difluoro-2-phenylacetyl)-L-valinate). The synthetic procedure of the molecule is left to be described in a future publication.

4.3.2 NMR Instrumentation

The ^{13}C solution-state NMR experiments were carried out on a 400 MHz Bruker Neo Avance system equipped with a 5 mm Bruker BBO probe. The 90° pulse length τ_{90} was optimised to $(8.8 \pm 0.1\ \mu\text{s})$ at 400 MHz.

The ^{19}F solution-state NMR experiments were carried out on a 600 MHz Bruker Avance system equipped with a 5 mm Bruker TBO He probe. The 90° pulse length τ_{90} at 600 MHz was optimised to (10.0 ± 0.1) μs for **I**, and (11.0 ± 0.1) μs for **K** at 600 MHz. No ^{1}H decoupling was used throughout the experiments. Regarding the z-filter, the strength of the z-gradient G_z applied was 15%, applied for a duration of 4.4 ms for all experiments.

4.4 Results

The following section illustrates the implementation of the double-quantum filtering schemes described earlier. Three different molecular systems are examined:

1. A near-equivalent ^{19}F spin-1/2 pair, denoted **I**.
2. A strongly-coupled ^{19}F spin-1/2 pair, denoted **K**.
3. A near equivalent ^{13}C spin-1/2 pair, denoted ^{13}C$_2$-DAND.

4.4.1 ^{19}F NMR: Near-Equivalence Case

The molecular structure of **I**, with its associated parameters, is given in Table 4.1. The ^{19}F spin-pair exhibits a small singlet-triplet mixing angle θ_{ST}, placing it within the near-equivalence regime. The symmetry of this molecule is broken by the presence of a chiral site within the molecular structure. This symmetry-breaking mechanism was first exploited by Tayler *et al.*[69] in the context of the singlet NMR of a ^{1}H spin-pair within a tripeptide.

The conventional 90° ^{19}F NMR spectrum of **I** is given in Figures 4.10(a), and 4.11(a). The spectrum consists of a single, strong peak. The chemical shift difference between the ^{19}F nuclei is so small, that the outer peaks of the AB type pattern can only be observed directly after acquiring many transients, and with additional magnification, as shown in Figure 4.10(b).

The DQF-schemes illustrated earlier in the chapter were applied to this spin system. A series of ^{19}F NMR spectra of **I** are shown in Figure 4.11. The 90° pulse-acquire spectrum, refocused INADEQUATE, GeoDQ, PulsePol-DQ, SLIC-DQ, and cSLIC-DQ spectra are depicted together. The pulse sequence parameters are given in Table 4.2.

Figure 4.11(b) shows a DQF ^{19}F NMR spectrum obtained using the refocused INADEQUATE pulse sequence (Figure 4.3). Even after optimisation of the pulse sequence delays τ_1, only approximately 5 % of the magnetisation is retained after passing through the double-quantum filter.

Table 4.1: Molecular structure of tert-butyl (2,2-difluoro-2-phenylacetyl)-L-alaninate, referred to as **I**, and associated parameters. The singlet-triplet mixing angle is given in Equation 2.13. The values of Δ and θ_{ST} assume a field of 14.1 T. Adapted from Heramun *et al.*[2], *J. Chem. Phys.* 164, 064201 (2026); licensed under a Creative Commons Attribution (CC BY) license.

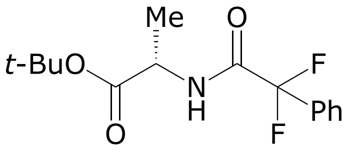

Parameter	Value
$^2J_{\mathrm{FF}}$ /Hz	255.9 ± 0.3
$\Delta\delta$ /ppb	32.0 ± 2.0
Δ /Hz	18.0 ± 1.0
$\theta_{\mathrm{ST}}/°$	4.1 ± 0.2

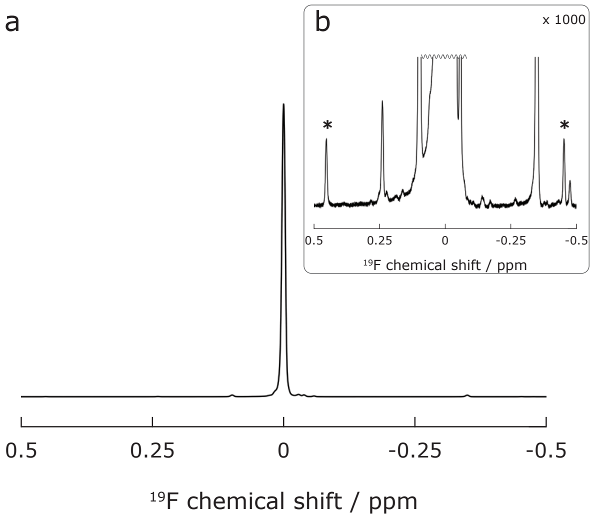

Figure 4.10: (**a**) A 90° pulse-acquire ^{19}F NMR spectrum of **I** (Table 4.1), acquired at 14.1 T, 298 K, and averaged over 5120 transients. The frequency scale is centred around -102.931 ppm. (**b**) A zoomed in view of the spectrum shown in part a. The vertical scale is given. The asterisks indicate the position of the AB outer peaks.

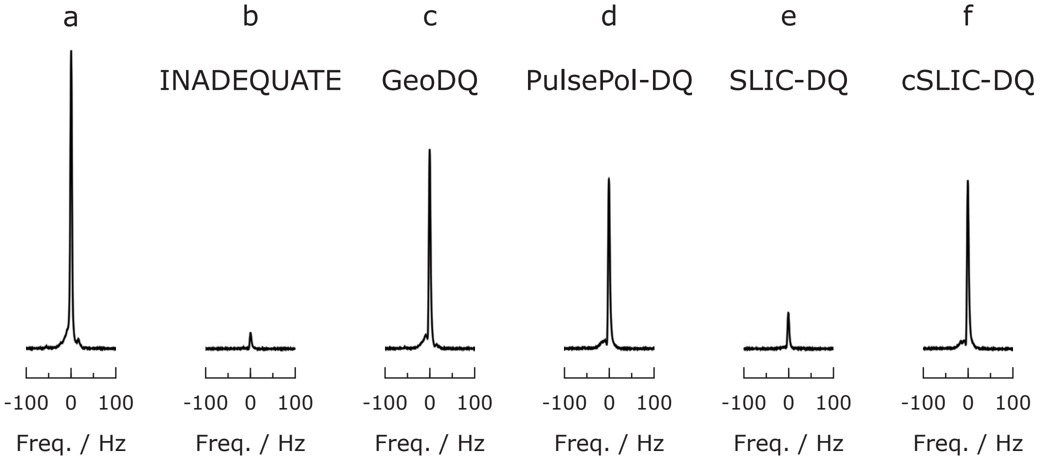

Figure 4.11: ^{19}F spectra of a solution of **I** in CDCl$_3$, acquired at 14.1 T, 298 K, and averaged over 4 transients. ^{1}H decoupling was not used. The frequency axis is centred around -102.931 ppm. All spectra have the same vertical scale. Double-quantum-filtering amplitudes are in parentheses. All pulse sequence parameters are given in Table 4.2. (**a**) A 90° pulse-acquire spectrum. (**b**) Double-quantum-filtered spectrum obtained using the refocused INADEQUATE pulse sequence (Figure 4.3) [5.4%]. (**c**) Double-quantum-filtered spectrum obtained using the GeoDQ pulse sequence (Figure 4.4) [66.6%]. (**d**) Double-quantum-filtered spectrum obtained using the PulsePol-DQ pulse sequence (Figure 4.6) [56.5%]. (**e**) Double-quantum-filtered spectrum obtained using the SLIC-DQ pulse sequence (Figure 4.9) [15.0%]. (**f**) Double-quantum-filtered spectrum obtained using the cSLIC-DQ pulse sequence (Figure 4.9) [56.2%]. Adapted from Heramun *et al.*[2], *J. Chem. Phys.* 164, 064201 (2026); licensed under a Creative Commons Attribution (CC BY) license.

The dependence of the DQF signals of **I** on the DQ-excitation time T is plotted in Figure 4.12 for the refocused INADEQUATE, PulsePol-DQ, SLIC-DQ, and cSLIC-DQ pulse sequences. The experimental curve, theoretical curve, and simulated data points are depicted together. The experimentally optimised value of T for each method is shown by a dashed line.

Figure 4.12(a) shows the experimental dependence of the DQF signal intensity on the sequence duration T for the INADEQUATE pulse sequence. The theoretical curve (blue line), and simulated points (open symbols) continue to increase at large T values, while the experimental curve intensity (black line) is heavily damped, shortening the optimal τ_1. Consequently, the experimental T for INADEQUATE ($T \approx 290$ ms) is much shorter than the theoretical optimum ($T \approx 808$ ms), where relaxation was not accounted for.

Figure 4.11(c) shows the DQF spectrum obtained using the GeoDQ pulse sequence (Figure 4.4). In this case, approximately 67% of the magnetisation is retained after passing through the double-quantum filter. This is roughly 13 times more than that generated by INADEQUATE. The improved efficiency may be attributed to the much faster double-quantum excitation by GeoDQ ($T \approx 86$ ms), compared to that achieved by INADEQUATE ($T \approx 290$ ms).

Figure 4.11(d) shows the DQF spectrum obtained using the PulsePol-DQ pulse sequence (Figure 4.6). The DQF signal amplitude is greater than for INADEQUATE, but is slightly less than that achieved by GeoDQ. This is attributed to PulsePol-DQ having a longer excitation duration T than GeoDQ. Figure 4.12(b) shows the experimental dependence of the DQF signal intensity on the sequence duration T for the PulsePol-DQ pulse sequence. There is a good correspondence between theory and experiment, except for the damping of the curves due to relaxation effects.

Figure 4.11(e) shows the DQF spectrum obtained using the SLIC-DQ pulse sequence (Figure 4.9).

Figure 4.12(c) shows the experimental dependence of the DQF signal intensity on the sequence duration T for the SLIC-DQ pulse sequence. Although SLIC-DQ is faster than GeoDQ and PulsePol-DQ, in the final DQF spectrum only approximately 5% of the magnetisation is retained after pass-

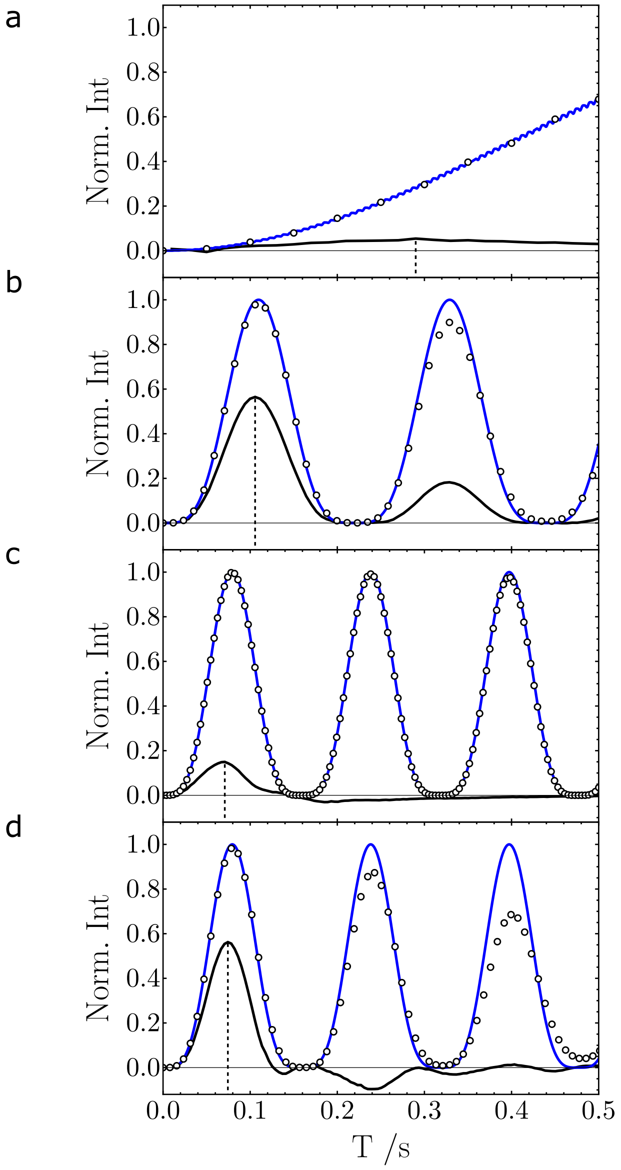

Figure 4.12: Dependence of DQF signals on the DQ-excitation duration T for different pulse sequences. Analytical functions (blue curves), simulated points (open circles), both neglecting relaxation, and experimental data for **I** (black lines). (a): INADEQUATE (blue curve: $|a_{\mathrm{DQ}}^{\mathrm{INADQ}}(T)|^2$, where $a_{\mathrm{DQ}}^{\mathrm{INADQ}}(T)$ is given by Equation 4.14); (b): PulsePol-DQ sequence (blue curve: Equation 4.49); (c): SLIC-DQ sequence, using the implementation in Figure 4.7(b) (blue curve: Equation 4.77); (d): cSLIC-DQ sequence (blue curve: Equation 4.82). All simulations use $J = 255.94$ Hz and $\Delta = 17.8$ Hz. The experimentally optimised values of T are shown by vertical dashed lines. Adapted from Heramun *et al.*[2], *J. Chem. Phys.* 164, 064201 (2026); licensed under a Creative Commons Attribution (CC BY) license.

Table 4.2: Pulse sequence parameters used for the double-quantum filtering experiments on the solution of $^{19}\mathrm{F}_2$-**I** 14.1 T. The GeoDQ parameters $\{\tau_1^{\mathrm{Geo}}, \tau_2^{\mathrm{Geo}}, n\}$ correspond to Figure 4.4. The factor α for cSLIC is defined in Equation 4.79. SLIC-DQ used the implementation shown in Figure 4.7(b). The uncertainties in the nutation frequencies were estimated from the experimental nutation spectrum. Adapted from Heramun *et al.*[2], *J. Chem. Phys.* 164, 064201 (2026); licensed under a Creative Commons Attribution (CC BY) license.

Pulse Sequence	Parameter	Value
Hard pulses	$\omega_{\mathrm{nut}}/(2\pi)$ / kHz	25.0 ± 0.3
INADEQUATE	τ_1 / ms	145.00
	T / ms	290.00
GeoDQ	τ_1^{Geo} /ms	926.0
	τ_2^{Geo} / μs	1852
	n	22
	T / ms	85.88
PulsePol-DQ	τ_2 / μs	1407.5
	m	9
	T / ms	105.66
SLIC-DQ	$\omega_{\mathrm{nut}}^{\mathrm{SLIC}}/(2\pi)$ / Hz	256 ± 3
	n_J	19
	T / ms	70.866
cSLIC-DQ	$\omega_{\mathrm{nut}}^{\mathrm{SLIC}}/(2\pi)$ / Hz	256 ± 3
	n_J	19
	τ_J / μs	3916
	T / ms	74.404
	α	0.940

ing through the double-quantum filter. These losses are due to the extreme sensitivity of SLIC-DQ to rf amplitude deviations, as illustrated by the simulations in Figure 4.8. In addition, the rf inhomogeneity averages out the rapid rf-induced oscillations, meaning they are not observed. Furthermore, small variations of the rf field amplitude across the sample lead to premature decay of the DQF signal. The SLIC-DQ sequence is the fastest DQ-excitation module explored here, with $T \approx 71$ ms.

The cSLIC-DQ sequence (Figure 4.7(c)) largely overcomes the limitations presented by SLIC-DQ. Figure 4.11(f) shows the DQF spectrum obtained using the cSLIC-DQ pulse sequence (Figure 4.9). In this case, the compensating pulse removes the rapid rf-induced oscillations, meaning they are not observed. The DQF signal amplitude is approximately equal to that of PulsePol-DQ. The cSLIC-DQ sequence is the second fastest DQ-excitation module explored here, with $T \approx 74$ ms.

Figure 4.12(d) shows the experimental dependence of the DQF signal intensity on the sequence duration T for the cSLIC-DQ pulse sequence. At longer times T, the experimental curve deviates significantly from theory, even going negative from $T \simeq 0.25$ s. The reasons for this deviation are currently unknown.

4.4.2 ^{19}F NMR: Strong-Coupling Case

The molecular structure of **K**, with its associated parameters, is given in Table 4.3. The ^{19}F spin-pair is at the upper limit of the strong-coupling regime, since the singlet-triplet mixing angle $\theta_{\mathrm{ST}} \geq 30^\circ$. The structure of **K** is similar to that of **I**, where the two molecules only have different chiral side-chains, where **K** has a bulkier functional group. This key difference in molecular weight between the two functional groups is the cause behind the larger symmetry-breaking effect observed in **K**, resulting in a higher θ_{ST}.

The conventional 90° ^{19}F NMR spectrum of **K** is given in Figures 4.13, and and 4.14(a). A classic AB pattern is readily observed.

The DQF-schemes illustrated earlier in the chapter were applied to this spin system. A series of ^{19}F NMR spectra of **K** are shown in Figure 4.14. The

Table 4.3: Molecular structure of benzyl (2,2-difluoro-2-phenylacetyl)-L-valinate, referred to as **K**, and associated parameters. The singlet-triplet mixing angle can be calculated from Equation 2.13. The values of Δ and θ_{ST} assume a field of 14.1 T.

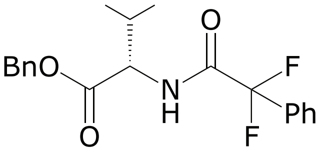

Parameter	**Value**
$^{2}J_{\mathrm{FF}}$ /Hz	255.3 ± 0.1
$\Delta\delta$ /ppb	279.9 ± 2.0
Δ /Hz	158.1 ±1.0
$\theta_{\mathrm{ST}}/^{\circ}$	31.8 ± 0.2

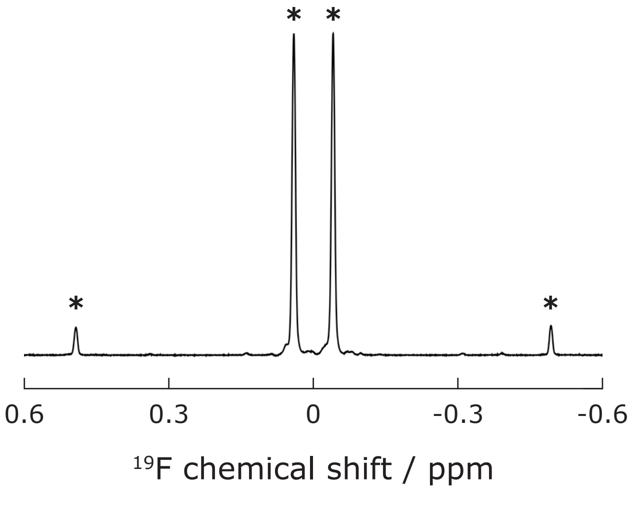

Figure 4.13: A 90° pulse-acquire ^{19}F NMR spectrum of a solution of **K** in $CDCl_3$ (Table 4.3), acquired at 14.1 T, 298 K, and averaged over 4 transients. The frequency scale is centred around -102.974 ppm. The asterisks indicate the position of the outer AB peaks, and of the two main peaks.

90° pulse-acquire spectrum, refocused INADEQUATE, GeoDQ, PulsePol-DQ, SLIC-DQ, and cSLIC-DQ spectra are depicted together. The pulse sequence parameters are given in Table 4.4.

Figure 4.14(b) shows a double-quantum-filtered ^{19}F NMR spectrum obtained using the refocused INADEQUATE pulse sequence (Figure 4.3). After optimisation of the pulse sequence delays τ_1, only $\approx 80\%$ of the magnetisation is retained after passing through the double-quantum filter. In this coupling regime, the INADEQUATE sequence remains effective for DQ-excitation.

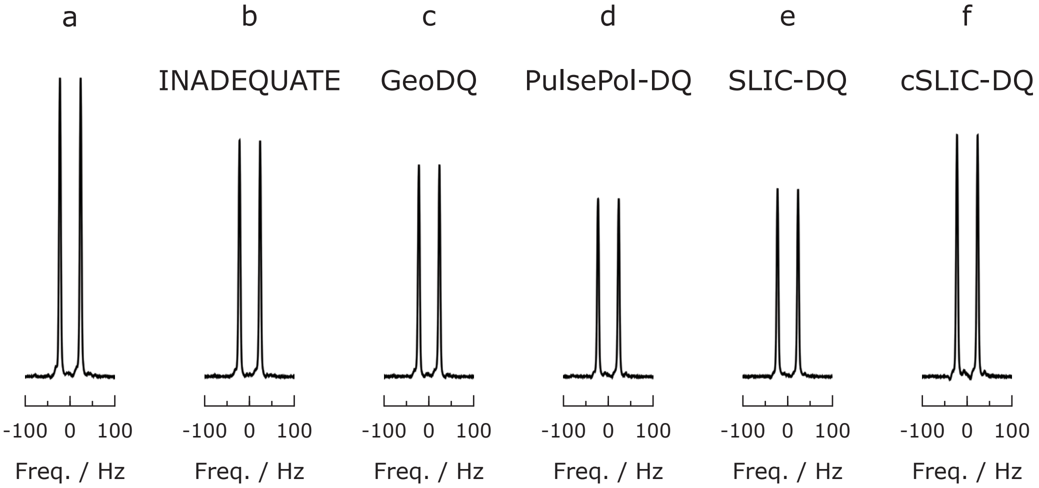

Figure 4.14: ^{19}F spectra of a solution of **K** in CDCl$_3$, acquired at 14.1 T, 298 K, and averaged over 4 transients. ^{1}H decoupling was not used. The frequency axis is centred around -102.974 ppm. All spectra have the same vertical scale. Double-quantum-filtering amplitudes are in parentheses. All pulse sequence parameters are given in Table 4.4. (**a**) A 90° pulse-acquire spectrum. (**b**) Double-quantum-filtered spectrum obtained using the refocused INADEQUATE pulse sequence (Figure 4.3) [79.1%]. (**c**) Double-quantum-filtered spectrum obtained using the GeoDQ pulse sequence (Figure 4.4) [70.9%]. (**d**) Double-quantum-filtered spectrum obtained using the PulsePol-DQ pulse sequence (Figure 4.6) [59.6%]. (**e**) Double-quantum-filtered spectrum obtained using the SLIC-DQ pulse sequence (Figure 4.9) [63.0%]. (**f**) Double-quantum-filtered spectrum obtained using the cSLIC-DQ pulse sequence (Figure 4.9) [80.9%].

Figure 4.14(c) shows the DQF spectrum obtained using the GeoDQ pulse sequence (Figure 4.4). In this case, approximately 70% of the magnetisation is retained after passing through the double-quantum filter. In this case, GeoDQ ($T \approx 27$ ms) excites DQC slower than INADEQUATE ($T \approx 13$ ms), resulting in relaxation losses.

Figure 4.14(d) shows the DQF spectrum obtained using the PulsePol-DQ pulse sequence (Figure 4.6). In this case, approximately 60% of the magnetisation is retained after passing through the double-quantum filter. The DQF signal amplitude is greatly reduced compared to INADEQUATE, and PulsePol-DQ is the worst performing sequence of those presented here, even though $T \approx 25$ ms, which is close to the GeoDQ sequence. The reasons behind this discrepancy are unknown.

Figure 4.14(e) shows the DQF spectrum obtained using the SLIC-DQ pulse sequence (Figure 4.9), the fastest DQ-excitation method of the five shown. The DQF signal is slightly higher than that of PulsePol-DQ. The moderate signal loss of SLIC-DQ due to rf inhomogeneity is partially recovered by the cSLIC-DQ sequence shown in Figure 4.7(c). The optimised cSLIC-DQ spectrum is shown in Figure 4.14(f), and has a DQF signal amplitude of approximately 81%, unexpectedly outperforming all the other DQ-excitation sequences. The double-quantum excitation time T for cSLIC-DQ is the second shortest of all the sequences explored here.

Table 4.4: Pulse sequence parameters used for the double-quantum filtering experiments on the solution of **K** at 14.1 T and 298 K. The GeoDQ parameters $\{\tau_1^{\mathrm{Geo}}, \tau_2^{\mathrm{Geo}}, n\}$ correspond to Figure 4.4. SLIC-DQ used the implementation shown in Figure 4.7(b). The factor α for cSLIC is defined in Equation 4.79. The uncertainties in the nutation frequencies were estimated from the experimental nutation spectrum.

Pulse Sequence	**Parameter**	**Value**
Hard pulses	$\omega_{\mathrm{nut}}/(2\pi)$ / kHz	22.7 ± 0.3
INADEQUATE	τ_1 /ms	6.50
	T /ms	13.0
GeoDQ	τ_1^{Geo} /ms	0.85
	τ_2^{Geo} /ms	1.70
	n	8
	T /ms	27.2
PulsePol-DQ	τ_2 /ms	1.55
	m	2
	T /ms	24.8
SLIC-DQ	$\omega_{\mathrm{nut}}^{\mathrm{SLIC}}/(2\pi)$ / Hz	255 ± 3
	n_J	2
	T /ms	8.94
cSLIC-DQ	$\omega_{\mathrm{nut}}^{\mathrm{SLIC}}/(2\pi)$ / Hz	255 ± 3
	n_J	2
	τ_J /ms	3.916
	T /ms	9.39
	α	0.989

4.4.3 ^{13}C NMR: Near-Equivalence Case

A naphthalene derivative, $^{13}C_2$-DAND[162], is an excellent candidate for double-quantum filtering experiments. This molecule displays a high degree of symmetry. To break the symmetry and generate a small chemical shift difference Δ between the two ^{13}C nuclei at the centre of the structure, one of the OCD_3 groups is substituted in place of an $OCD(CD_3)_2$ group. The slight asymmetry introduced by a remote functional group substitution is sufficient to break the symmetry of the molecule. The $^{13}C_2$-DAND molecular system has been used extensively[70,73,85,96,128] in the past for singlet NMR studies, and displayed a singlet relaxation lifetime T_S of over one hour[70] in solution. Its molecular structure, and associated parameters, is given in Table 4.5.

Table 4.5: Molecular structure of (1,2,3,4,5,6,8-heptakis(methoxy-d_3)-7-((propan-2-yl-d_7)oxy)naphthalene-4a,8a-[$^{13}C_2$]), referred to as $^{13}C_2$-DAND, and associated parameters. The singlet-triplet mixing angle can be calculated from Equation 2.13. The values of Δ and θ_{ST} assume a field of 9.4 T.

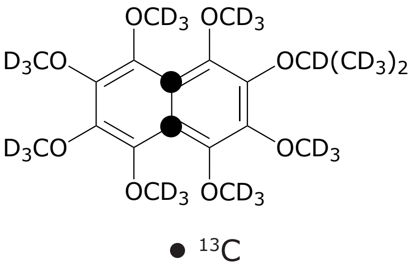

Parameter	Value
$^1J_{CC}$ /Hz	54.4 ± 0.1
$\Delta\delta$ /ppb	75.0 ± 2.0
Δ /Hz	7.5 ± 1.0
$\theta_{ST}/°$	7.8 ± 0.2

The DQF-schemes illustrated earlier in the chapter were applied to this spin system. A series of ^{13}C NMR spectra of $^{13}C_2$-DAND are shown in Figure

4.15. The 90° pulse-acquire spectrum, refocused INADEQUATE, GeoDQ, PulsePol, SLIC, and compensated SLIC spectra are depicted together. The pulse sequence parameters are given in Table 4.6. The conventional 90° ^{13}C NMR spectrum of $^{13}C_2$-DAND is given in Figure 4.15(a).

Figure 4.15(b) shows a DQF ^{13}C NMR spectrum obtained using the refocused INADEQUATE pulse sequence (Figure 4.3). Even after optimisation of the pulse sequence delays τ_1, approximately 27% of the magnetisation is retained after passing through the double-quantum filter.

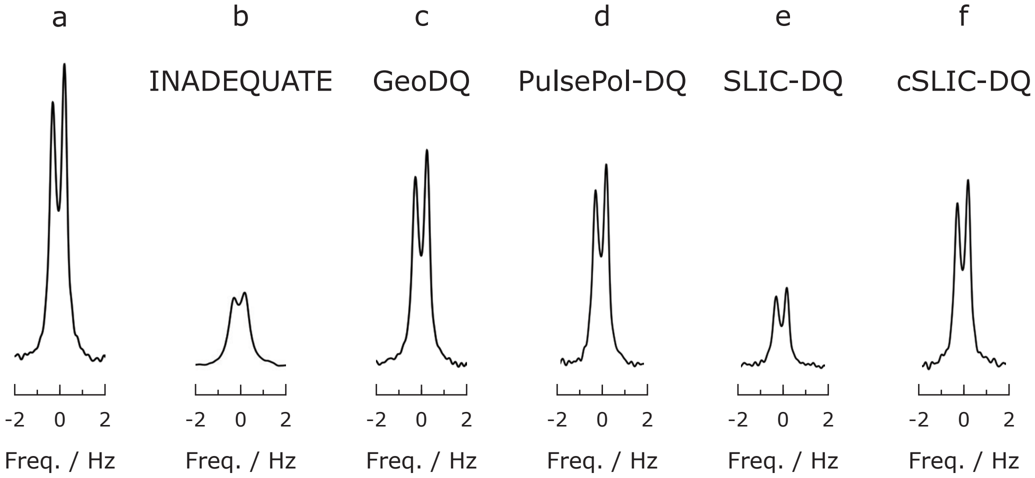

Figure 4.15: ^{19}F spectra of a solution of $^{13}C_2$-DAND in ipa-d_8, acquired at 9.4 T, 298 K, and averaged over 4 transients. The frequency axis is centred around 119.031 ppm. All spectra have the same vertical scale. Double-quantum-filtering amplitudes are in parentheses. All pulse sequence parameters are given in (**a**) A 90° pulse-acquire spectrum. (**b**) Double-quantum-filtered spectrum obtained using the refocused INADEQUATE pulse sequence (Figure 4.3) [27.0%]. (**c**) Double-quantum-filtered spectrum obtained using the GeoDQ pulse sequence (Figure 4.4) [78.2%]. (**d**) Double-quantum-filtered spectrum obtained using the PulsePol-DQ pulse sequence (Figure 4.6) [73.1%]. (**e**) Double-quantum-filtered spectrum obtained using the SLIC-DQ pulse sequence (Figure 4.9) [28.7%]. (**f**) Double-quantum-filtered spectrum obtained using the cSLIC-DQ pulse sequence (Figure 4.9) [67.5%].

Figure 4.15(c) shows the DQF spectrum obtained using the GeoDQ pulse sequence (Figure 4.4). with the parameters given in Table 4.6. In this case, approximately 78% of the magnetisation is retained after passing through the double-quantum filter. This is roughly 3 times more than that generated by INADEQUATE. The improved efficiency may be attributed to the much faster double-quantum excitation by GeoDQ ($T \approx 147$ ms), compared to that achieved by INADEQUATE ($T \approx 760$ ms).

Figure 4.15(d) shows the DQF spectrum obtained using the PulsePol-DQ pulse sequence (Figure 4.6). The DQF signal amplitude is greater than for INADEQUATE, but is slightly less than that achieved by GeoDQ. This is attributed to PulsePol-DQ having a longer excitation duration T than GeoDQ.

Figure 4.15(e) shows the DQF spectrum obtained using the SLIC-DQ pulse sequence (Figure 4.9). Although SLIC-DQ is faster than GeoDQ and PulsePol-DQ, in the final DQF spectrum only approximately 29% of the magnetisation is retained after passing through the double-quantum filter. These losses are due to the extreme sensitivity of SLIC-DQ to rf amplitude deviations, as illustrated by the simulations in Figure 4.8(b). Small variations of the rf field amplitude across the sample lead to premature decay of the DQF signal. The SLIC-DQ sequence is the fastest DQ-excitation module explored here, with $T \approx 150$ ms.

The cSLIC-DQ sequence (Figure 4.7(c)) largely overcomes the limitations presented by SLIC-DQ. Figure 4.15(f) shows the DQF spectrum obtained using the cSLIC-DQ pulse sequence (Figure 4.9). The DQF signal amplitude is approximately equal to that of PulsePol-DQ. The cSLIC-DQ sequence is the second fastest DQ-excitation module explored here, with $T \approx 179$ ms.

Appendix C.2 contains simulated and experimental double-quantum amplitude buildup curves of $^{13}C_2$-DAND, for the pulse sequences used above.

Table 4.6: Pulse sequence parameters used for the double-quantum filtering experiments on the solution of ^{13}C$_2$-DAND at 9.4 T and 298 K. The GeoDQ parameters $\{\tau_1^{\mathrm{Geo}}, \tau_2^{\mathrm{Geo}}, n\}$ correspond to Figure 4.4. The factor α for cSLIC is defined in Equation 4.79. SLIC-DQ used the implementation shown in Figure 4.7(b). The uncertainties in the nutation frequencies were estimated from the experimental nutation spectrum.

Pulse Sequence	**Parameter**	**Value**
Hard pulses	$\omega_{\mathrm{nut}}/(2\pi)$ / kHz	28.4 ± 0.2
INADEQUATE	τ_1 / ms	380.0
	T / ms	760.0
GeoDQ	τ_1^{Geo} /ms	4.60
	τ_2^{Geo} / ms	9.21
	n	12
	T / ms	147.4
PulsePol-DQ	τ_2 / ms	6.90
	m	9
	T / ms	248.4
SLIC-DQ	$\omega_{\mathrm{nut}}^{\mathrm{SLIC}}/(2\pi)$ / Hz	54 ± 3
	n_J	10
	T / ms	149.8
cSLIC-DQ	$\omega_{\mathrm{nut}}^{\mathrm{SLIC}}/(2\pi)$ / Hz	54 ± 3
	n_J	10
	τ_J / ms	18.39
	T / ms	178.9
	α	0.998

4.5 Discussion

Conventional double-quantum excitation methods, such as the three-pulse INADEQUATE[123,132,163] pulse sequence, work well in spin systems where the chemical shift difference is much larger than the J-coupling (i.e. the "weak-coupling" regime). This no longer applies in cases where the chemical shift difference is very small, compared to the J-coupling (i.e. the "strong-coupling" regime). In this thesis, we examine the case of double-quantum excitation primarily in the *extreme* strong-coupling regime, or "near-equivalence".

In the previous chapter, we explored the implementation of the geometric double-quantum excitation procedure[1,128] GeoDQ, to isolate signals arising from $^{13}C_2$-squarate species from a solution of $^{13}C_1$-squarate at high pH. The GeoDQ pulse sequence exploits the Aharanov-Anandan geometric phase. Such a phase may be acquired by quantum states when performing a cyclic trajectory in the zero-quantum (ZQ) subspace spanned by the singlet and central triplet states, which subtends a solid angle at the origin of the Bloch sphere.

In this chapter, however, we exploited spinor behaviour to excite double-quantum coherence. This means that a quantum state changes sign after undergoing a 2π rotation in a subspace spanned by the singlet state, and either of the outer triplet states. This variety of DQC-excitation was called Spinor-DQ. Both the GeoDQ and Spinor-DQ procedures may be employed to manipulate strongly coupled spin-1/2 pairs, with the goal of exciting double-quantum coherence faster than the standard method allows.

We explored two broad types of Spinor-DQ excitation. In the first method, the PulsePol[85] pulse sequence, interpreted as a symmetry-based pulse sequence, was used to generate a single-transition rotation through an angle of 2π. This realises the spinor property, allowing efficient DQC-excitation. In the second method, a single radiofrequency pulse, matched to the SLIC condition[76], was used. The direct excitation of double-quantum coherence by SLIC has not been described before, although related multiple-quantum excitation effects have been noted when double-frequency radiofrequency fields are applied to coupled spin systems[164–169].

A few variants of SLIC-DQ excitation were introduced. These include a repeating three-pulse sequence that uses two different radiofrequency field amplitudes. This compensated SLIC, "cSLIC", variant accounts for deviations of the rf field amplitude from the exact SLIC condition, although effects such as radiofrequency droop and phase transients remain problematic after multiple repetitions of the sequence. More recently, the cSLIC sequence has been adapted for singlet order excitation as well, achieving good error compensation[95].

The various double-quantum filtering schemes described above were experimentally implemented on three different molecular systems in solution at high magnetic field, and room temperature. The first is a near-equivalent ^{19}F spin-1/2 pair, denoted **I**. The second is a ^{19}F spin-1/2 pair of the intermediate coupling regime, denoted **K**. The third system was a near equivalent ^{13}C spin-1/2 pair, denoted ^{13}C$_2$-DAND.

A small chemical shift difference was induced between the two ^{19}F nuclei within **I**, due to the presence of a stereogenic centre within the molecule. The two ^{19}F nuclei are said to be *diastereotopic*. The same mechanism applies to **K** as well, although the symmetry-breaking interaction is of greater magnitude in this case, due to the heavier weight of the stereogenic side-chain. The ^{19}F spectrum of **I** displayed a pseudo-A$_2$-type pattern, since the chemical shift difference was not big enough to result in a well-resolved split peak of the AB-type.

Nevertheless, DQC was successfully excited in **I** using the GeoDQ, PulsePol-DQ, cSLIC-DQ, SLIC-DQ, and INADEQUATE methods, here ordered from the highest observed DQF signal amplitude, to the lowest. The INADEQUATE pulse sequence performed the worst, since the long DQC-excitation time in the near-equivalence regime results in prominent relaxation losses. The SLIC-DQ pulse sequence is extremely sensitive to rf amplitude mismatch, which results in a poor DQF signal amplitude being observed. This issue is largely overcome by using the cSLIC-DQ variant, which performed similarly to GeoDQ, and PulsePol-DQ, though problems with accumulating phase errors, and power droop issues may have hindered the operation of this sequence. The PulsePol-DQ pulse sequence performed slightly worse than

GeoDQ, due to its longer DQC-excitation time, thereby losing some DQF signal due to relaxation effects. Overall, the SLIC-DQ sequences displayed the shortest double-quantum coherence excitation time.

A similar behaviour was observed for the near-equivalent $^{13}C_2$-DAND molecule. On the other hand, we observed good DQF signal amplitude for all sequences for the less strongly-coupled molecule **K**. In these conditions, DQC-excitation using the conventional INADEQUATE sequence is still the optimal method. In this case, the GeoDQ and PulsePol-DQ procedures display long DQC-excitation times, and were therefore vulnerable to relaxation losses. On the other hand, while the SLIC-DQ sequences were faster than INADEQUATE to excite DQC, these were not as robust as the refocused INADEQUATE pulse sequence with respect to rf amplitude deviations, therefore showing a weaker performance in DQF spectra.

A selection of pulse sequences are now available to be used for double-quantum coherence excitation in the strong-coupling/near-equivalence regime. The choice is between the GeoDQ, and the Spinor-DQ category of sequences. Experimental demonstrations have shown good efficiency from both sequence families. Potential applications may involve, for example, diastereotopic ^{1}H pairs, which are common in the NMR of biomolecules such as proteins. The glycine residues in flexible peptide backbones, such as found in flexible termini or loops, contain inherently diastereotopic CH_2 groups. In some cases, the chemical shift difference between the diastereotopic ^{1}H nuclei are too small to give a resolved spectral splitting. DQF using the methods described above could allow the editing of NMR spectra, as an alternative to techniques that exploit long-lived singlet states[145,170]. *In vivo* and MRI applications are conceivable[171–173]. The sequences described here are also likely to be applicable to systems of more than 2 coupled spins. For example, various implementations of SLIC have been applied successfully for the study of long-lived states in systems of the $AA'XX'$ and $AA'MM'XX'$ kind[82,149–151,158].

Another potential application of these techniques is for molecular binding assays. It has been found that, in some cases, the reversible association of an achiral molecule with a chiral one induces diastereotopicity in moieties of the achiral partner[174]. In principle, this phenomenon could be detected by double-quantum-filtered NMR experiments on the free achiral molecule in solution. As demonstrated above, double-quantum filtering is discriminatory even when the ordinary NMR spectrum displays no obvious symptom of diastereotopicity. Double-quantum filtering, using GeoDQ or Spinor-DQ methods, could therefore detect the reversible association of some types of molecules in solution. In the context of drug discovery, this could provide a complement to existing NMR-based methods, which typically exploit either transient magnetisation transfer in the bound complex, enhancements in the decay rates of magnetisation or long-lived spin order, or binding-induced perturbations of diffusion rates and chemical shifts[50,175–179]. Double-quantum filtering might provide a cleaner and less ambiguous discrimination in some cases.

Chapter 5

Double-Quantum Excitation Facilitated by Chiral Guest Binding

A combination of Coulombic and hydrogen bonding interactions between a fluorinated achiral carboxylic acid and a chiral amine are able to break the symmetry between two previously equivalent nuclei in the achiral molecule, inducing diastereotopicity.

The conventional pulse-acquire ^{19}F NMR spectrum of this solution does not show signs of inequivalence between the $^{19}F_2$ nuclei. The two diastereotopic nuclei under observation are strongly-coupled, since the chemical shift difference between them is small, relative to the J-coupling.

Nonetheless, we demonstrate the detection of binding between the two molecules using the geometric double-quantum filtering, and singlet filtering methods on isotropic solutions containing varying ratios of a fluorinated carboxylic acid, and a chiral amine at high magnetic field, and room temperature. In addition, we report T_1 and T_S relaxation lifetime measurements.

5.1 Introduction

Chiral molecules possess two enantiomers, which are non superimposable mirror images of each other, and cannot be distinguished by NMR[180] directly. Remarkably, however, the addition of a chiral molecule to a solution containing a *prochiral* molecule can cause a splitting of the NMR signal. Such a molecule may, for example, have the following form: $CF_2R_1R_2$. This structure is achiral, but binding to a chiral agent causes the mirror symmetry of the molecule to be removed, and a non-equivalence in chemical shifts is imposed between the two ^{19}F nuclei. The two sites now occupy different environments, generating separate signals in the corresponding ^{19}F NMR spectrum. The chemical shift difference Δ is dependent on the amount of chiral solvating agent added, also denoted as *enantiomeric excess*, *ee*.

This phenomenon has been reported in liquid crystal media[181–184], and isotropic liquids[174,185,186] more recently. One of the very first[187] reported observations of the splitting of an NMR signal into an AB quartet due to the presence of a chiral agent was made over fifty years ago, however.

In this chapter, we examine the case of a prochiral molecule in isotropic solution, to which varying amounts of a single enantiomer of a chiral molecule are added. The molecular structure of the fluorinated phenoxyacetic acid **FPA**, and the chiral amine **CA** under consideration are given in Figure 5.1.

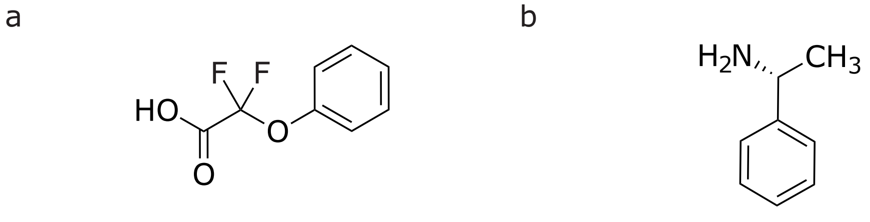

FPA

CA

Figure 5.1: The prochiral molecule, and chiral “guest”. (**a**) Molecular structure of 2, 2-difluoro-2-phenoxyacetic acid, “**FPA**”. (**b**) Molecular structure of (S)-1-phenylethan-1-amine, “**CA**”.

The choice to use ^{19}F NMR to study this binding mechanism is intentional. The ^{19}F nucleus has a gyromagnetic ratio ≈ 40.1 MHz T^{-1}, meaning it is almost as sensitive as protons, where $\gamma \approx 42.6$ MHz T^{-1}, but with the advantage of being relatively free of background NMR signals that are common in ^{1}H NMR. In addition, the chemical shift range of ^{19}F NMR spectra can span over hundreds of ppm, compared to $\approx 10 - 15$ ppm for proton spectra. This means that NMR signals are better resolved from one another, in comparison to ^{1}H NMR, and with the important advantage that any perturbation to the ^{19}F chemical shift is more readily observable. Importantly, many biologically relevant compounds often contain fluorine atoms.

The symmetry between the two ^{19}F nuclei in **FPA** is broken by non-covalent bonding interactions between the prochiral molecule **FPA**, and the chiral guest **CA**. The symmetry of **FPA** breaks down when undergoing fast exchange with the chiral amine **CA** in solution, where diastereotopicity is induced in the **FPA** substrate. This is caused by two intermolecular forces acting together, as illustrated in Figure 5.2.

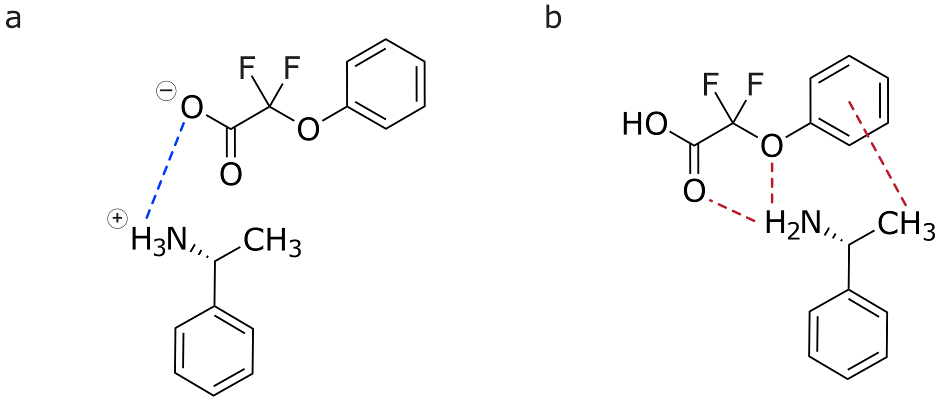

Figure 5.2: FPA-CA binding interaction forces. (**a**) Coulombic attraction between the cationic form of **FPA**, and the anionic form of the chiral guest **CA**. (**b**) Hydrogen bonding interaction between **FPA** and **CA**.

The first contributing force is Coulombic attraction, which arises from the acid-base interactions between the **FPA** carboxylic acid, and the **CA** amine, as shown in Figure 5.2(a). The second contribution is due to hydrogen bonding between the two molecules, where the CH-π interaction is included as well, as shown in Figure 5.2(b). The design of the prochiral and chiral "guest" molecules is pivotal for the success of this type of symmetry-breaking interaction, as discussed in Ref.[174]. In particular, it was noted that the presence of a phenoxy group in the α position with respect to the carboxylic acid group is especially important to ensure that the appropriate intermolecular forces are present that fix the **FPA**/**CA** conformation.

A racemic mixture of enantiomers possesses 0 % enantiomeric excess, whereas a single, pure enantiomer has an enantiomeric excess of 100 %. In this work, we operate within the 100 % *ee* conditions. The conventional 90° pulse-acquire ^{19}F NMR spectrum of **FPA** displays a strong, single peak of an A_2 type system. As the solution is progressively titrated with increasing amounts of **CA**, the spectral pattern remains unchanged. However, we observed the perturbation of the isotropic chemical shift δ_{iso}, suggesting that binding has occurred, and we were able to further confirm this using double-quantum filtered NMR. We were unable to extract the dissociation constant K_{D} from the binding isotherm, due to not having enough data points.

The procedure was implemented on the various near-equivalent systems using the geometric double-quantum filtering pulse sequence, GeoDQ, that was discussed in previous chapters. In addition, we were able to perform singlet filtering experiments, and measure the singlet relaxation time constant T_{S}. The short T_1, and therefore T_2 relaxation time constants meant that the double-quantum filtering efficiency was generally very low, and worse in the systems with a small θ_{ST} angle, which resulted in long double-quantum excitation time T_{DQ}, and therefore major relaxation losses. Nonetheless, the detection of these reversible and non-covalent binding interactions on the mM scale may be an addition to existing NMR methods.

5.2 Materials and Methods

5.2.1 Sample Preparation

The ^{19}F NMR experiments were performed on solutions 20 mM of **FPA**, and varying concentrations of **CA**, dissolved in 450 μL of $CDCl_3$. The synthetic procedure of **FPA** is left to be described in a future publication. The synthesis and sample preparation were performed by D. Yamano. Other reagents were purchased from Sigma-Aldrich, and used without further purification.

5.2.2 NMR Instrumentation

The ^{19}F solution-state NMR experiments were carried out on a 600 MHz Bruker Avance system equipped with a 5 mm Bruker TBO He probe. No ^{1}H decoupling was used throughout the experiments.

5.3 Results

Several solutions containing a fixed amount of the prochiral molecule **FPA** were titrated with varying amounts of the chiral amine **CA**. The isotropic chemical shift was perturbed by the addition of **CA**, suggesting that binding with **FPA** had taken place. Figure 5.3 shows the variation of the isotropic chemical shift δ_{iso} as a function of the concentration of **CA**. After a sharp initial decrease in the chemical shift for the solution containing exclusively unbound **FPA**, the prochiral molecule becomes fully saturated after the addition of approximately one equivalent of **CA**.

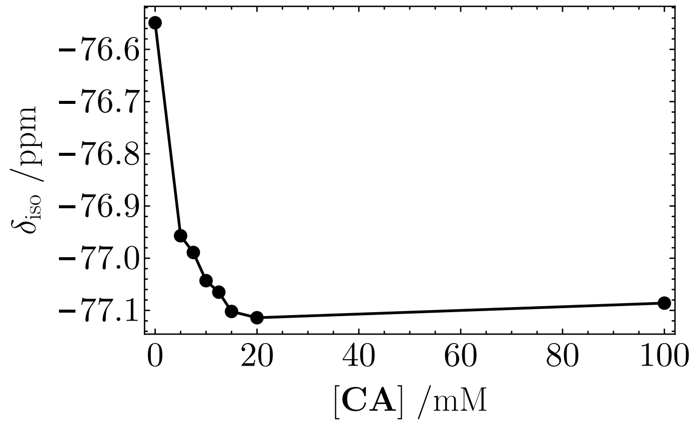

Figure 5.3: Isotropic chemical shift δ_{iso} for a solution of 20 mM of **FPA**, and varying concentrations of **CA** in $CDCl_3$ at 14.1 T and 298 K.

The system parameters associated with each solution that was studied are given in Table 5.1.

Table 5.1: Variation of the chemical shift difference Δ as a function of the concentration of **CA**. The values of Δ and θ_{ST} assume a field of 14.1 T. The concentration of **FPA** is fixed to 20 mM. Solutions were dissolved in $CDCl_3$.

[**CA**]/mM	$^2J_{\text{FF}}$ /Hz	$\Delta\delta$ /ppb	Δ /Hz	$\theta_{\text{ST}}/^\circ$
0	n.d.	0.0 ± 0.1	0.0 ± 0.1	0.0 ± 0.1
5	114.1 ± 1.1	14.0 ± 2.9	7.9 ± 0.9	3.1 ± 0.3
7.5	114.1 ± 1.1	16.3 ± 2.0	9.2 ± 0.9	3.7 ± 1.1
10	114.1 ± 1.1	27.0 ± 3.6	15.2 ± 1.0	6.0 ± 0.4
12.5	114.1 ± 1.1	45.6 ± 5.2	25.8 ± 3.0	10.1 ± 1.1
15	114.1 ± 1.1	33.6 ± 0.1	19.0 ± 0.5	7.5 ± 0.2
20	114.1 ± 1.1	33.6 ± 0.1	19.0 ± 0.5	7.5 ± 0.2
100	114.1 ± 1.1	33.6 ± 0.1	19.0 ± 0.5	7.5 ± 0.2

The J-coupling between the two ^{19}F nuclei of **FPA** was measured to be $^2J_{\text{FF}} \approx 114$ Hz for all solutions where the **CA** chiral guest was present. The first row of Table 5.1 corresponds to the case without **CA**. In this case, the ^{19}F nuclei of **FPA** are equivalent, meaning the J-coupling is not directly observable, and therefore could not be determined. The chemical shift difference Δ and the J-coupling were used to calculate the singlet-triplet mixing angle θ_{ST}, as described Equation 2.13.

The θ_{ST} angle displays an interesting variation as a function of the concentration of **CA**. This shows an increase from the solution containing 0 mM of **CA**, reaching a maximum for the solution containing 12.5 mM of **CA**, before decreasing slightly and stabilising at around $\theta_{\text{ST}} \approx 7.5^\circ$ for the solutions that have approximately one equivalent of **CA** with respect to **FPA**. The reason behind the spike observed at 12.5 mM concentration of **CA** remains without a clear explanation, so far.

The following sections discuss the double-quantum filtered and singlet filtered NMR spectra of these solutions, which lie in the near-equivalent regime.

5.3.1 Double-Quantum Filtered NMR

The double-quantum filtered ^{19}F NMR spectra of several solutions of a fixed amount of **FPA** (20 mM), and varying quantities of **CA** are illustrated in Figure 5.4, where the sample volume and room temperature were consistent across samples. The DQF procedure was implemented using the GeoDQ pulse sequence designed to operate in near-equivalent spin systems, as illustrated in Figure 4.4. The pulse sequence parameters are given in Table D.1.

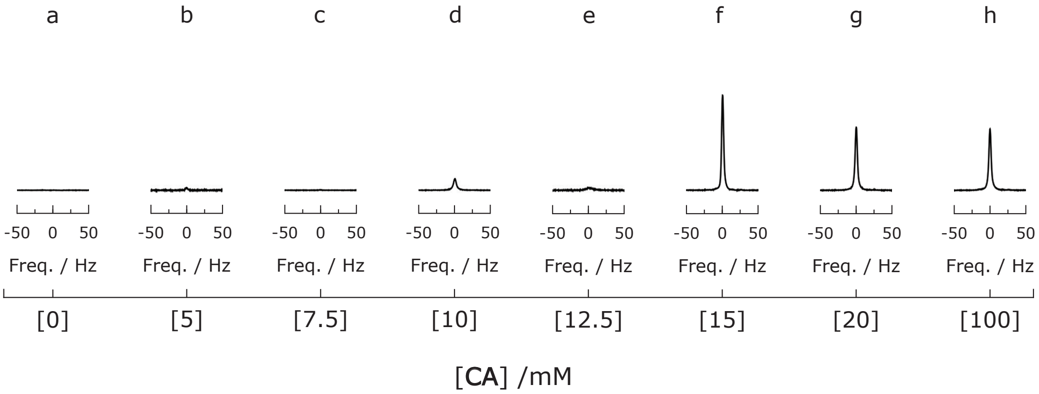

Figure 5.4: Double-quantum filtered ^{19}F NMR spectra of a solution of 20 mM of **FPA** and varying concentrations of **CA** in $CDCl_3$. Each spectrum was acquired at 14.1 T, 298 K, and averaged over 32 transients. ^{1}H decoupling was not used. All spectra have the same vertical scale. Double-quantum filtering amplitudes are in parentheses. All pulse sequence parameters are given in Table D.1. (**a**) [**CA**] = 0 mM. The frequency axis is centred around −76.549 ppm. [0.0 %] (**b**) [**CA**] = 5 mM. The frequency axis is centred around −76.957 ppm. [1.1 %]. (**c**) [**CA**] = 7.5 mM. The frequency axis is centred around −76.989 ppm. [0.0 %]. (**d**) [**CA**] = 10 mM. The frequency axis is centred around −77.043 ppm. [4.8 %]. (**e**) [**CA**] = 12.5 mM. The frequency axis is centred around −77.065 ppm. [1.1 %]. (**f**) [**CA**] = 15 mM. The frequency axis is centred around −77.102 ppm. [39.9 %]. (**g**) [**CA**] = 20 mM. The frequency axis is centred around −77.114 ppm. [26.4 %]. (**h**) [**CA**] = 100 mM. The frequency axis is centred around −77.086 ppm. [25.6 %].

Figure 5.4(a) shows the double-quantum filtered spectrum for a solution containing 0 mM of **CA**. As expected, the DQF-amplitude for this system that contains the symmetrical **FPA** molecule on its own, is zero. Figure 5.4(b-e) shows the double-quantum filtered spectra of the following solutions, where the DQF-amplitude is given in square brackets: 5 mM [1 %], 7.5 mM [0 %], 10 mM [5 %], and 12.5 mM [1 %] of **CA**, respectively.

The total double-quantum coherence excitation time values T_{DQ} for each solution shown in Figure 5.4(b-h) are depicted in Figure 5.5. These are inversely proportional with the θ_{ST} values depicted in Table 5.1, since a smaller θ_{ST} leads to a higher repetition number n in the GeoDQ sequence, and therefore a longer T_{DQ}.

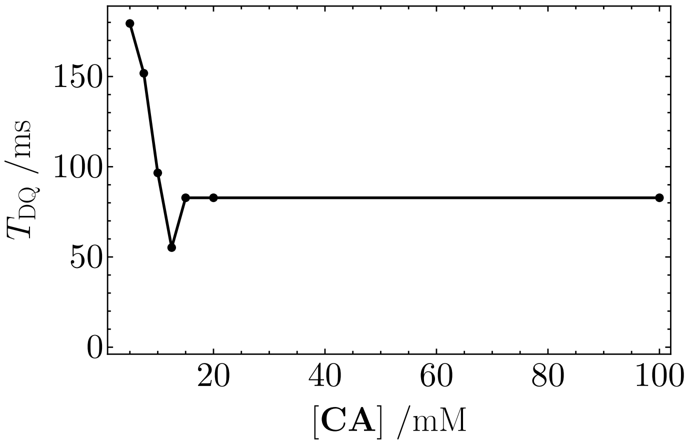

Figure 5.5: Total double-quantum coherence excitation time T_{DQ} for solutions of 20 mM of **FPA**, and varying concentrations of **CA** in $\mathrm{CDCl_3}$ at 14.1 T and 298 K. The data points correspond to the DQF spectra shown in Figure 5.4(b-h). The T_{DQ} values and GeoDQ pulse sequence parameters are given in Table D.1.

Figure 5.4(f-h) shows the double-quantum filtered spectra of the following solutions, where the DQF-amplitude is given in square brackets: 15 mM [40 %], 20 mM [26 %], and 100 mM [26 %] of **CA**, respectively. These solutions displayed the same θ_{ST} angle, and were optimised to identical pulse sequence parameters. Therefore, the T_{DQ} value was also identical across the three solutions. However, the highest DQF-amplitude was given by the 15 mM of **CA** solution. This result can be explained by the longer $T_1 \approx 500$ ms value of this solution (Table D.3), compared to the 20 mM, and 100 mM solutions, where $T_1 \approx 480$ ms, which mitigates the relaxation losses.

5.3.2 Singlet Filtered NMR

The singlet filtered ^{19}F NMR spectra of several solutions of a fixed amount of **FPA** (20 mM), and varying quantities of **CA** are illustrated in Figure 5.6, where the sample volume and room temperature were consistent across samples. The singlet excitation procedure was implemented using the M2S-S2M pulse sequence, as illustrated in Figures 2.6, and 2.5. The pulse sequence parameters are given in Table D.2.

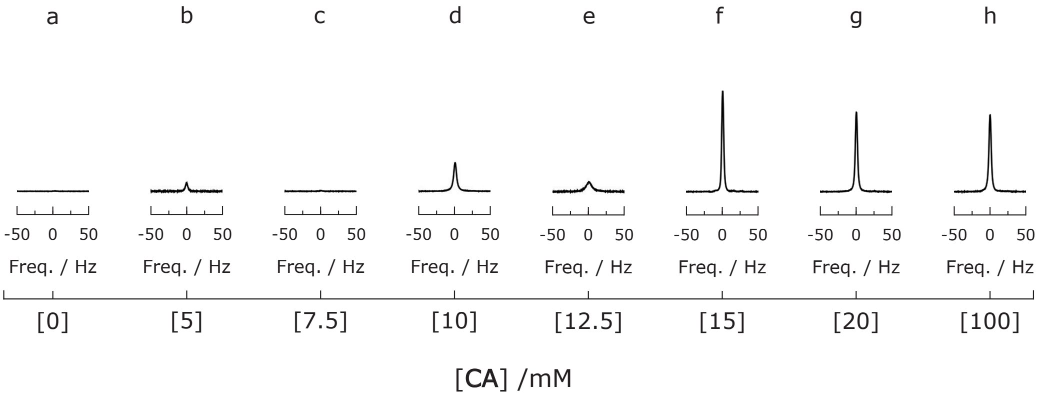

Figure 5.6: Singlet filtered ^{19}F NMR spectra of a solution of 20 mM of **FPA** and varying concentrations of **CA** in $CDCl_3$. Each spectrum was acquired at 14.1 T, 298 K, and averaged over 32 transients. ^{1}H decoupling was not used. All spectra have the same vertical scale. Singlet filtering amplitudes are in parentheses. All pulse sequence parameters are given in Table D.2. (**a**) [**CA**] = 0 mM. The frequency axis is centred around -76.549 ppm. [0.0 %] (**b**) [**CA**] = 5 mM. The frequency axis is centred around -76.957 ppm. [3.4 %]. (**c**) [**CA**] = 7.5 mM. The frequency axis is centred around -76.989 ppm. [0.0 %]. (**d**) [**CA**] = 10 mM. The frequency axis is centred around -77.043 ppm. [11.9 %]. (**e**) [**CA**] = 12.5 mM. The frequency axis is centred around -77.065 ppm. [4.0 %]. (**f**) [**CA**] = 15 mM. The frequency axis is centred around -77.102 ppm. [42.1 %]. (**g**) [**CA**] = 20 mM. The frequency axis is centred around -77.114 ppm. [33.2 %]. (**h**) [**CA**] = 100 mM. The frequency axis is centred around -77.086 ppm. [32.0 %].

Figure 5.6(a) shows the singlet filtered spectrum for a solution containing 0 mM of **CA**. As expected, the singlet filtering amplitude for this system is zero. Figure 5.4(b-e) shows the singlet filtered spectra of the following solutions, where the singlet filtering amplitude is given in square brackets: 5 mM

[3 %], 7.5 mM [0 %], 10 mM [12 %], and 12.5 mM [4 %] of **CA**, respectively. The higher efficiencies, compared to the DQF spectra, are due to a shorter overall total singlet order excitation time T_{SO}, depicted in Figure 5.7, since exciting DQC generally takes twice as long as exciting singlet order.

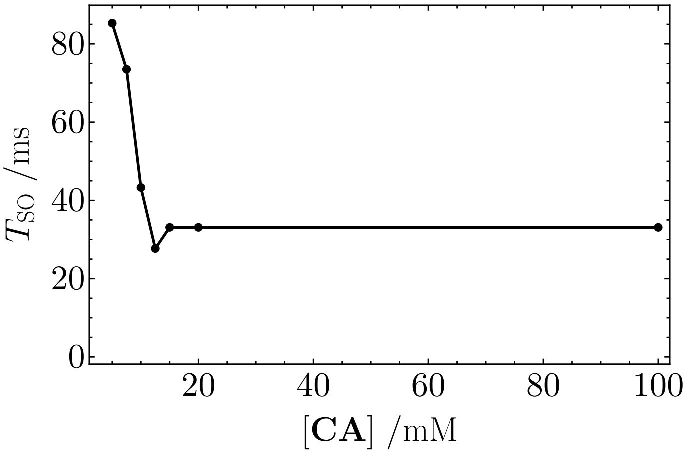

Figure 5.7: Total singlet order excitation time T_{SO} for solutions of 20 mM of **FPA**, and varying concentrations of **CA** in $CDCl_3$ at 14.1 T and 298 K. The data points correspond to the DQF spectra shown in Figure 5.6(b-h). The T_{SO} values and M2S-S2M pulse sequence parameters are given in Table D.2.

Figure 5.6(f-h) shows the singlet filtered spectra of the following solutions, where the singlet filtering amplitude is given in square brackets: 15 mM [42 %], 20 mM [33 %], and 100 mM [32 %] of **CA**, respectively.

5.3.3 Relaxation Measurements

The double-quantum, and singlet filtering efficiencies given in Figures 5.4(b-e), and 5.6(b-e), respectively, showed significant variations between one spectrum and another. An attempt at giving a possible explanation is as follows. The chemical shift difference determines determines how fast DQC/SO can be excited, whereas the T_1 value (and therefore T_2) regulates the efficiency the DQC/SO. In the cases where the **FPA**/**CA** complex is more strongly-coupled, *and* displays a shorter T_1, the DQF and singlet filtered signal amplitudes were observed to be very small. The different combinations of these events result in the observed signal amplitudes.

The T_1 time constants as a function of [**CA**] are depicted in Figure 5.8. As the **FPA**/**CA** complex forms, the T_1 decreases, since the rotational correlation time is longer. Appendix D contains the detailed parameters.

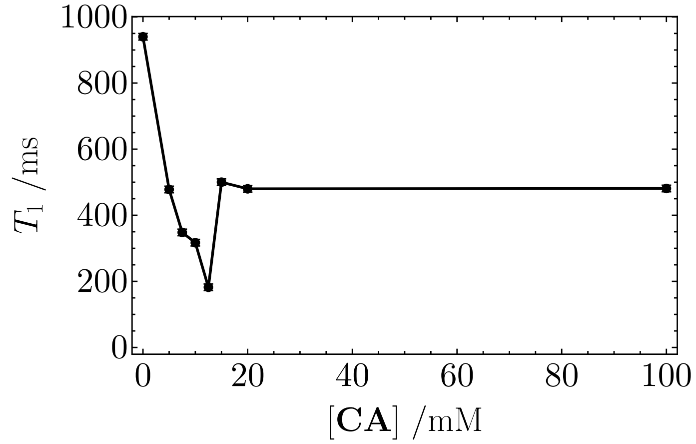

Figure 5.8: Longitudinal relaxation lifetime measurements for solutions of 20 mM of **FPA**, and varying concentrations of **CA** in $CDCl_3$ at 14.1 T and 298 K. The T_1 values are given in Table D.3. The GeoDQ pulse sequence parameters are given in Table D.1.

The T_S time constants as a function of [**CA**] are depicted in Figure 5.9.

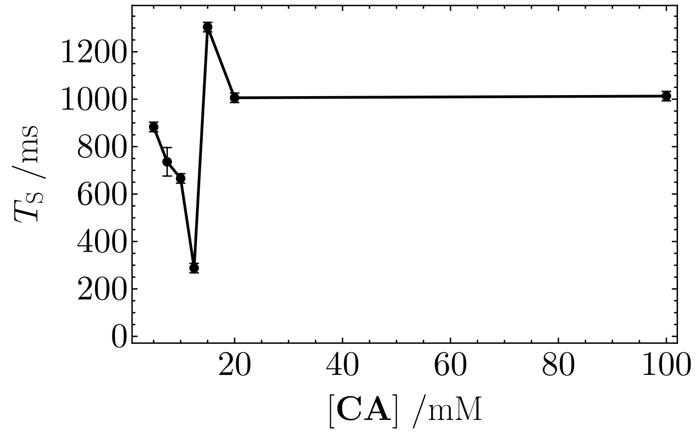

Figure 5.9: Singlet relaxation lifetime measurements for solutions of 20 mM of **FPA**, and varying concentrations of **CA** in $CDCl_3$ at 14.1 T and 298 K. The T_S values are given in Table D.3. The M2S-S2M pulse sequence parameters are given in Table D.2.

5.4 Discussion

The flourinated phenoxyacetic acid **FPA**, and the chiral amine **CA** species form a supramolecular complex in an isotropic liquid. Solutions containing a fixed amount of **FPA** were titrated with increasing amounts of **CA**. The first indication that binding had taken place, was the perturbation of the observed isotropic chemical shift Δ_{iso}. This parameter changed significantly once **CA** was added to a solution containing free **FPA**. The binding mechanism relies on the formation of hydrogen bonds between the two molecules, which are necessary to maintain the fixed structure of the complex[174]. The symmetry of the **FPA** molecule is broken upon binding with **CA**.

However, the conventional pulse-acquire ^{19}F NMR spectrum showed a single, strong peak for all the solutions that were examined, and not an AB type spectrum. This is due to the binding interaction generating a very small chemical shift difference, compared to the J-coupling between the two ^{19}F nuclei within **FPA**, i.e. the near-equivalence regime[68].

Double-quantum filtering methods are routinely used to detect coupled species. The ordinary procedures[108] are inefficient in the strong-coupling/near-equivalence regime. Therefore, we implemented the geometric double-quantum filtering method[1,2,128] described in previous chapters to successfully confirm that the binding event had taken place. This pulse sequence was designed to efficiently excite DQC in this coupling regime. Even so, the combination of a short T_1 relaxation time, and longer DQC-excitation times due to a small chemical shift difference $\Delta\delta$, resulted in generally low double-quantum filtering signal amplitudes being observed. This effect varied across samples, resulting in different DQF amplitudes being observed.

Singlet order may also be excited between the ^{19}F spin-pair. The singlet filtered spectra displayed better signal amplitudes, compared to the DQF spectra, since singlet excitation takes approximately half as long as DQC excitation, therefore resulting in fewer relaxation losses. The T_1 and T_{S} relaxation constants were recorded. The singlet lifetimes were approximately twice as long as the longitudinal relaxation time constant. The short T_{S} values are due to the large contribution of CSA to singlet relaxation from the ^{19}F nuclei, in addition to the high magnetic field used.

In this chapter, we demonstrated the detection of reversible binding interactions using the GeoDQ method. Nonetheless, the Spinor-DQ class of techniques may also be used for this purpose. These procedures could potentially be used for molecular binding assays to detect the reversible association of some types of molecules in solution, where these are properly designed and are able to sustain the necessary geometry for the symmetry-breaking event to occur. This could be useful as an additional tool among the NMR methods used in drug discovery. Some of the methods exploit the perturbation of diffusion rates or chemical shifts, or long-lived states as well[50,175–179]. It is possible that double-quantum filtering may provide a cleaner and less ambiguous indication of binding, in some cases.

Chapter 6

Conclusions

In this thesis, we explored pulse sequences that are able to efficiently excite double-quantum coherence in the strong-coupling/near-equivalence regime. The established methods, such as INADEQUATE, are inefficient in these conditions, which lead to substantial relaxation losses.

The first pulse sequence we explored, GeoDQ, exploits the geometric Aharonov-Anandan phase. To ultimately excite double-quantum coherence, this method employs a rotation of the system through π about the z-axis in the zero-quantum subspace spanned by the $\{|S_0\rangle, |T_0\rangle\}$ states.

We applied this pulse sequence to study two isotopologues of the squarate dianion that are able to support singlet order. To break the symmetry of this molecule, we used ^{18}O-enrichment. We observed rich splitting patterns in the ^{13}C NMR spectra at low and high pH in aqueous solution, and we were able to assign the positions of the peaks arising from several secondary isotope shifts.

A modification of this pulse sequence allowed the study of the singlet order relaxation of a previously inaccessible squarate isotopologue. Although we anticipated very long T_S values for this highly symmetrical species, the interactions of the singlet spin-pair with the surrounding environment still limited the singlet relaxation lifetime to a few minutes.

The second variety of pulse sequences we explored include SLIC, and PulsePol, which are well-known for the preparation of singlet order. To ultimately excite double-quantum coherence, both methods employ a rotation of the system through 2π in the single-quantum subspace spanned by the $\{|S_0\rangle, |T_{+1}\rangle\}$ states, exploiting spinor behaviour.

The SLIC-DQ sequence was attractive, due to the ease of its implementation, compared to GeoDQ and PulsePol-DQ. However, due to the poor robustness of the SLIC sequence with respect to deviations in the radiofrequency field amplitude, a compensated variant, cSLIC, was developed.

We applied these pulse sequences to near-equivalent $^{19}F_2$ spin-pairs in solution, whose molecular symmetry had been previously broken from the presence of a stereocentre within the molecule. In general, we observed that the GeoDQ pulse sequence displayed the highest double-quantum filtering efficiency, followed by the PulsePol-DQ sequence, the cSLIC-DQ sequence, the SLIC-DQ sequence, and the INADEQUATE pulse sequence.

Lastly, we investigated the symmetry-breaking interaction in the case of a molecule containing a diastereotopic fluorine spin-pair. In the correct conditions, hydrogen bonding has been previously known to cause a small chemical shift difference between the two spins when binding to another molecule occurred. In our case, the NMR spectrum showed a single peak.

Nonetheless, we were able to detect the binding interaction *via* the GeoDQ double-quantum filtering method. However, this method was hindered by the need to have at least one equivalent of the binding substrate to achieve good double-quantum filtering efficiency, and short T_1 relaxation times.

In summary, the outlook is fascinating, and there is scope for further research. Finer optimisation of the conditions and molecular candidates may ultimately lead to improvements in studies concerning ligand-binding assays, detecting coupled species within mixtures, or multiple-quantum coherence order filtering in larger spin systems, among other applications.

Bibliography

[1] U. D. Heramun, M. Sabba, C. Bengs, G. A. I. Moustafa and M. H. Levitt, *The Journal of Chemical Physics*, 2025, **163**, 074201.

[2] U. D. Heramun, M. Sabba, D. Yamano, C. Bengs, B. Legrady, G. Pileio, S. Thompson and M. H. Levitt, *The Journal of Chemical Physics*, 2026, **164**, 064201.

[3] I. I. Rabi, J. R. Zacharias, S. Millman and P. Kusch, *Physical Review*, 1938, **53**, 318–318.

[4] C. Gorter, *Physica*, 1936, **3**, 995–998.

[5] F. Bloch, *Physical Review*, 1946, **70**, 460–474.

[6] E. M. Purcell, H. C. Torrey and R. V. Pound, *Physical Review*, 1946, **69**, 37–38.

[7] J. Caceres-Cortes, B. Falk, L. Mueller and T. G. M. Dhar, *Journal of Medicinal Chemistry*, 2024, **67**, 1701–1733.

[8] P. C. Lauterbur, *Nature*, 1973, **242**, 190–191.

[9] P. Mansfield and P. K. Grannell, *Journal of Physics C: Solid State Physics*, 1973, **6**, L422–L426.

[10] P. Mansfield, *Journal of Physics E: Scientific Instruments*, 1988, **21**, 18–30.

[11] C. P. Grey and N. Dupré, *Chemical Reviews*, 2004, **104**, 4493–4512.

[12] M. Elsayed, A. Isah, M. Hiba, A. Hassan, K. Al-Garadi, M. Mahmoud, A. El-Husseiny and A. E. Radwan, *Journal of Petroleum Exploration and Production Technology*, 2022, **12**, 2747–2784.

[13] M. H. Levitt, *Spin Dynamics. Basics of Nuclear Magnetic Resonance*, Wiley, Chichester, 1st edn., 2001.

[14] R. Freeman, *Spin Choreography: Basic Steps in High Resolution NMR*, Oxford University PressOxford, 1998.

[15] J. Keeler, *Understanding NMR spectroscopy*, John Wiley and Sons, Chichester, U.K, 2nd edn., 2010.

[16] K. Jozef and M. Lena, *Nuclear Spin Relaxation in Liquids: Theory, Experiments, and Applications*, CRC Press, Second edition. | Boca Raton, FL : CRC Press, Taylor & Francis Group, [2018], 2nd edn., 2017.

[17] P. W. Atkins and R. Friedman, *Molecular quantum mechanics*, Oxford University Press, Oxford ; New York, 5th edn., 2011.

[18] R. R. Ernst, G. Bodenhausen and A. Wokaun, *Principles of Nuclear Magnetic Resonance in One and Two Dimensions*, Clarendon Press, 1990, vol. 1.

[19] Q. Stern and K. Sheberstov, *Magnetic Resonance*, 2023, **4**, 87–109.

[20] O. Sørensen, G. Eich, M. Levitt, G. Bodenhausen and R. Ernst, *Progress in Nuclear Magnetic Resonance Spectroscopy*, 1984, **16**, 163–192.

[21] M. H. Levitt and C. Bengs, *Magnetic Resonance*, 2021, **2**, 395–407.

[22] J. Jeener, in *Advances in Magnetic and Optical Resonance*, Elsevier, 1982, vol. 10, pp. 1–51.

[23] P. K. Madhu and A. Kumar, *Concepts in Magnetic Resonance*, 1997, **9**, 1–12.

[24] E. L. Hahn, *Physical Review*, 1950, **80**, 580–594.

[25] H. Y. Carr and E. M. Purcell, *Physical Review*, 1954, **94**, 630–638.

[26] S. Meiboom and D. Gill, *Review of Scientific Instruments*, 1958, **29**, 688–691.

[27] C. Bengs and M. H. Levitt, *Magnetic Resonance in Chemistry*, 2018, **56**, 374–414.

[28] H. J. Bernstein, J. A. Pople and W. G. Schneider, *Canadian Journal of Chemistry*, 1957, **35**, 67–83.

[29] S. A. Smith, W. E. Palke and J. T. Gerig, *Concepts in Magnetic Resonance*, 1992, **4**, 107–144.

[30] S. A. Smith, W. E. Palke and J. T. Gerig, *Concepts in Magnetic Resonance*, 1992, **4**, 181–204.

[31] F. A. L. Anet and D. J. O'leary, *Concepts in Magnetic Resonance*, 1992, **4**, 35–52.

[32] N. F. Ramsey, *Physical Review*, 1950, **77**, 567–567.

[33] N. F. Ramsey, *Physical Review*, 1950, **78**, 699–703.

[34] U. Haeberlen, *High Resolution NMR in Solids. Selective Averaging*, Academic, New York, 1976.

[35] G. Bodenhausen, R. Freeman and D. L. Turner, *Journal of Magnetic Resonance (1969)*, 1977, **27**, 511–514.

[36] G. Bodenhausen, H. Kogler and R. Ernst, *Journal of Magnetic Resonance (1969)*, 1984, **58**, 370–388.

[37] A. Bax, R. Freeman, T. A. Frenkiel and M. H. Levitt, *J. Magn. Reson.*, 1981, **43**, 478–483.

[38] A. D. Bain, *Journal of Magnetic Resonance (1969)*, 1984, **56**, 418–427.

[39] M. H. Levitt, P. Madhu and C. E. Hughes, *Journal of Magnetic Resonance*, 2002, **155**, 300–306.

[40] M. H. Levitt and R. Freeman, *Journal of Magnetic Resonance (1969)*, 1979, **33**, 473–476.

[41] S. Wimperis, *Journal of Magnetic Resonance, Series A*, 1994, **109**, 221–231.

[42] H. K. Cummins, G. Llewellyn and J. A. Jones, *Physical Review A*, 2003, **67**, 042308.

[43] M. Carravetta and M. H. Levitt, *Journal of the American Chemical Society*, 2004, **126**, 6228–6229.

[44] M. Carravetta, O. G. Johannessen and M. H. Levitt, *Physical Review Letters*, 2004, **92**, 153003.

[45] M. H. Levitt, in *Encyclopedia of Magnetic Resonance*, ed. R. K. Harris, John Wiley & Sons, Ltd, Chichester, UK, 2010, p. emrstm1036.

[46] M. H. Levitt, in *New Developments in NMR*, ed. G. Pileio, Royal Society of Chemistry, Cambridge, 2020, pp. 1–32.

[47] R. Sarkar, P. R. Vasos and G. Bodenhausen, *Journal of the American Chemical Society*, 2007, **129**, 328–334.

[48] C. Bengs, L. Dagys, G. A. I. Moustafa, J. W. Whipham, M. Sabba, A. S. Kiryutin, K. L. Ivanov and M. H. Levitt, *The Journal of Chemical Physics*, 2021, **155**, 124311.

[49] S. Cavadini, J. Dittmer, S. Antonijevic and G. Bodenhausen, *Journal of the American Chemical Society*, 2005, **127**, 15744–15748.

[50] R. Buratto, D. Mammoli, E. Chiarparin, G. Williams and G. Bodenhausen, *Angewandte Chemie International Edition*, 2014, **53**, 11376–11380.

[51] G. Pileio, S. Bowen, C. Laustsen, M. C. D. Tayler, J. T. Hill-Cousins, L. J. Brown, R. C. D. Brown, J. H. Ardenkjaer-Larsen and M. H. Levitt, *Journal of the American Chemical Society*, 2013, **135**, 5084–5088.

[52] M. C. D. Tayler, I. Marco-Rius, M. I. Kettunen, K. M. Brindle, M. H. Levitt and G. Pileio, *Journal of the American Chemical Society*, 2012, **134**, 7668–7671.

[53] P. R. Vasos, A. Comment, R. Sarkar, P. Ahuja, S. Jannin, J.-P. Ansermet, J. A. Konter, P. Hautle, B. Van Den Brandt and G. Bodenhausen, *Proceedings of the National Academy of Sciences*, 2009, **106**, 18469–18473.

[54] J.-N. Dumez, B. Vuichoud, D. Mammoli, A. Bornet, A. C. Pinon, G. Stevanato, B. Meier, G. Bodenhausen, S. Jannin and M. H. Levitt, *The Journal of Physical Chemistry Letters*, 2017, **8**, 3549–3555.

[55] G. Pileio, M. Carravetta, E. Hughes and M. H. Levitt, *J. Am. Chem. Soc.*, 2008, **130**, 12582–12583.

[56] G. Stevanato, S. Singha Roy, J. Hill-Cousins, I. Kuprov, L. J. Brown, R. C. D. Brown, G. Pileio and M. H. Levitt, *Physical Chemistry Chemical Physics*, 2015, **17**, 5913–5922.

[57] G. Pileio and S. Ostrowska, *Journal of Magnetic Resonance (San Diego, Calif.: 1997)*, 2017, **285**, 1–7.

[58] M. Carravetta and M. H. Levitt, *The Journal of Chemical Physics*, 2005, **122**, 214505.

[59] G. Pileio, *Progress in Nuclear Magnetic Resonance Spectroscopy*, 2017, **98-99**, 1–19.

[60] J. D. van Beek, M. Carravetta, G. C. Antonioli and M. H. Levitt, *J. Chem. Phys.*, 2005, **122**, 244510.

[61] M. H. Levitt, *Journal of Magnetic Resonance*, 2016, **262**, 91–99.

[62] O. W. Sørensen, *Journal of Magnetic Resonance (1969)*, 1990, **86**, 435 – 440.

[63] M. H. Levitt, *Annual Review of Physical Chemistry*, 2012, **63**, 89–105.

[64] G. Pileio and M. H. Levitt, *The Journal of Chemical Physics*, 2009, **130**, 214501–14.

[65] G. Pileio, M. Concistrè, M. Carravetta and M. H. Levitt, *Journal of Magnetic Resonance*, 2006, **182**, 353–357.

[66] S. Vega, *The Journal of Chemical Physics*, 1978, **68**, 5518–5527.

[67] A. Wokaun and R. R. Ernst, *The Journal of Chemical Physics*, 1977, **67**, 1752–1758.

[68] M. C. D. Tayler and M. H. Levitt, *Journal of the American Chemical Society*, 2013, **135**, 2120–2123.

[69] M. C. D. Tayler and M. H. Levitt, *Physical Chemistry Chemical Physics*, 2011, **13**, 5556.

[70] G. Stevanato, J. T. Hill-Cousins, P. Håkansson, S. S. Roy, L. J. Brown, R. C. D. Brown, G. Pileio and M. H. Levitt, *Angewandte Chemie International Edition*, 2015, **54**, 3740–3743.

[71] G. Pileio, M. Carravetta and M. H. Levitt, *Proceedings of the National Academy of Sciences*, 2010, **107**, 17135–17139.

[72] J.-N. Dumez, *Molecular Physics*, 2020, **118**, e1644382.

[73] K. F. Sheberstov, A. S. Kiryutin, C. Bengs, J. T. Hill-Cousins, L. J. Brown, R. C. D. Brown, G. Pileio, M. H. Levitt, A. V. Yurkovskaya and K. L. Ivanov, *Physical Chemistry Chemical Physics*, 2019, **21**, 6087–6100.

[74] C. Bengs, M. Sabba, A. Jerschow and M. H. Levitt, *Physical Chemistry Chemical Physics*, 2020, **22**, 9703–9712.

[75] M. H. Levitt and R. Freeman, *Journal of Magnetic Resonance (1969)*, 1981, **43**, 502–507.

[76] S. J. DeVience, R. L. Walsworth and M. S. Rosen, *Physical Review Letters*, 2013, **111**, 173002.

[77] S. J. DeVience and M. S. Rosen, in *Long-lived Nuclear Spin Order: Theory and Applications*, ed. G. Pileio, Royal Society of Chemistry, 2020, pp. 151 – 168.

[78] S. J. DeVience and M. S. Rosen, *Journal of Magnetic Resonance*, 2022, **341**, 107244.

[79] S. J. DeVience, M. Greer, S. Mandal and M. S. Rosen, *ChemPhysChem*, 2021, **22**, 2128–2137.

[80] K. F. Sheberstov, H.-M. Vieth, H. Zimmermann, K. L. Ivanov, A. S. Kiryutin and A. V. Yurkovskaya, *Applied Magnetic Resonance*, 2018, **49**, 293–307.

[81] K. F. Sheberstov, H.-M. Vieth, H. Zimmermann, B. A. Rodin, K. L. Ivanov, A. S. Kiryutin and A. V. Yurkovskaya, *Scientific Reports*, 2019, **9**, 20161.

[82] A. Sonnefeld, G. Bodenhausen and K. Sheberstov, *Physical Review Letters*, 2022, **129**, 183203.

[83] I. Schwartz, J. Scheuer, B. Tratzmiller, S. Müller, Q. Chen, I. Dhand, Z.-Y. Wang, C. Müller, B. Naydenov, F. Jelezko and M. B. Plenio, *Science Advances*, 2018, **4**, eaat8978.

[84] H. J. Mamin, M. Kim, M. H. Sherwood, C. T. Rettner, K. Ohno, D. D. Awschalom and D. Rugar, *Science*, 2013, **339**, 557–560.

[85] M. Sabba, N. Wili, C. Bengs, J. W. Whipham, L. J. Brown and M. H. Levitt, *The Journal of Chemical Physics*, 2022, **157**, 134302.

[86] H. Harbor-Collins, M. Sabba, G. Moustafa, B. Legrady, M. Soundararajan, M. Leutzsch and M. H. Levitt, *The Journal of Chemical Physics*, 2023, **159**, 104307.

[87] H. Harbor-Collins, M. Sabba, C. Bengs, G. Moustafa, M. Leutzsch and M. H. Levitt, *The Journal of Chemical Physics*, 2024, **160**, 014305.

[88] H. Harbor-Collins, M. Sabba, M. Leutzsch and M. H. Levitt, *Magnetic Resonance*, 2024, **5**, 121–129.

[89] A. Brinkmann and M. H. Levitt, *The Journal of Chemical Physics*, 2001, **115**, 357–384.

[90] A. Brinkmann, M. Carravetta, X. Zhao, M. Edén, J. Schmedt auf der Günne and M. H. Levitt, in *Perspectives on Solid State NMR in Biology*, ed. S. Kiihne and H. de Groot, Kluwer, Dordrecht, 2001, pp. 3–14.

[91] Y. K. Lee, N. D. Kurur, M. Helmle, O. G. Johannessen, N. C. Nielsen and M. H. Levitt, *Chemical Physics Letters*, 1995, **242**, 304–309.

[92] M. Carravetta, M. Edén, X. Zhao, A. Brinkmann and M. H. Levitt, *Chemical Physics Letters*, 2000, **321**, 205–215.

[93] M. H. Levitt, in *eMagRes*, John Wiley & Sons, Ltd, 2007.

[94] M. H. Levitt, *J. Chem. Phys.*, 2008, **128**, 052205–25.

[95] M. Sabba, C. Bengs, U. D. Heramun and M. H. Levitt, *The Journal of Physical Chemistry Letters*, 2026, acs.jpclett.6c00524.

[96] B. A. Rodin, K. F. Sheberstov, A. S. Kiryutin, L. J. Brown, R. C. D. Brown, M. Sabba, M. H. Levitt, A. V. Yurkovskaya and K. L. Ivanov, *The Journal of Chemical Physics*, 2019, **151**, 234203.

[97] S. J. Elliott, C. Bengs, L. J. Brown, J. T. Hill-Cousins, D. J. O'Leary, G. Pileio and M. H. Levitt, *The Journal of Chemical Physics*, 2019, **150**, 064315.

[98] *Long-lived Nuclear Spin Order: Theory and Applications*, ed. G. Pileio, Royal Society of Chemistry, S.l., 1st edn., 2020.

[99] M. C. D. Tayler, S. Marie, A. Ganesan and M. H. Levitt, *Journal of the American Chemical Society*, 2010, **132**, 8225–8227.

[100] R. Ian Storer, C. Aciro and L. H. Jones, *Chemical Society Reviews*, 2011, **40**, 2330.

[101] F. Neese, F. Wennmohs, U. Becker and C. Riplinger, *The Journal of Chemical Physics*, 2020, **152**, 224108.

[102] R. Radeglia, *Solid State Nuclear Magnetic Resonance*, 1995, **4**, 317–321.

[103] R. P. Young, C. R. Lewis, C. Yang, L. Wang, J. K. Harper and L. J. Mueller, *Magnetic Resonance in Chemistry*, 2019, **57**, 211–223.

[104] G. Pileio, J. T. Hill-Cousins, S. Mitchell, I. Kuprov, L. J. Brown, R. C. D. Brown and M. H. Levitt, *Journal of the American Chemical Society*, 2012, **134**, 17494–17497.

[105] G. Pileio, *Progress in Nuclear Magnetic Resonance Spectroscopy*, 2010, **56**, 217–231.

[106] P. Ahuja, R. Sarkar, P. R. Vasos and G. Bodenhausen, *The Journal of Chemical Physics*, 2007, **127**, 134112.

[107] A. D. Buckingham and S. M. Malm, *Molecular Physics*, 1971, **22**, 1127–1130.

[108] A. Bax and R. Freeman, *Journal of Magnetic Resonance (1969)*, 1980, **41**, 507–511.

[109] N. F. Ramsey, *Physical Review*, 1952, **87**, 1075–1079.

[110] H. Batiz-Hernandez and R. Bernheim, *Progress in Nuclear Magnetic Resonance Spectroscopy*, 1967, **3**, 63–85.

[111] C. J. Jameson, *The Journal of Chemical Physics*, 1977, **66**, 4983–4988.

[112] P. E. Hansen, *Progress in Nuclear Magnetic Resonance Spectroscopy*, 1988, **20**, 207–255.

[113] C. J. Jameson, in *Isotopes in the Physical and Biomedical Science*, Elsevier Science, Amsterdam, Netherlands, 1991, vol. 2.

[114] P. Lantto, S. Kangasvieri and J. Vaara, *The Journal of Chemical Physics*, 2012, **137**, 214309.

[115] P. Lantto, S. Kangasvieri and J. Vaara, *Physical Chemistry Chemical Physics*, 2013, **15**, 17468–17478.

[116] M. Bendall and D. Doddrell, *Australian Journal of Chemistry*, 1978, **31**, 1141.

[117] P. E. Hansen, H. D. Dettman and B. D. Sykes, *Journal of Magnetic Resonance (1969)*, 1985, **62**, 487–496.

[118] S. Pinchas and E. Meshulam, *J. Chem. Soc. D*, 1970, **0**, 1147–1148.

[119] J. M. Risley and R. L. Van Etten, *Journal of the American Chemical Society*, 1979, **101**, 252–253.

[120] K. U. Buckler, A. R. Haase, O. Lutz, M. Müller and A. Nolle, *Zeitschrift für Naturforschung A*, 1977, **32**, 126–130.

[121] M. Cohn and A. Hu, *Proceedings of the National Academy of Sciences*, 1978, **75**, 200–203.

[122] C. J. Jameson and H. J. Osten, in *Annual Reports on NMR Spectroscopy*, Elsevier, 1986, vol. 17, pp. 1–78.

[123] A. Bax, R. Freeman and S. P. Kempsell, *Journal of the American Chemical Society*, 1980, **102**, 4849–4851.

[124] J. Eills, G. Stevanato, C. Bengs, S. Glöggler, S. J. Elliott, J. Alonso-Valdesueiro, G. Pileio and M. H. Levitt, *Journal of Magnetic Resonance*, 2017, **274**, 163–172.

[125] T. Nakai and C. A. McDowell, *Molecular Physics*, 1993, **79**, 965–983.

[126] S. Pancharatnam, *Proceedings of the Indian Academy of Sciences - Section A*, 1956, **44**, 247–262.

[127] Y. Aharonov and L. Susskind, *Physical Review*, 1967, **158**, 1237–1238.

[128] C. Bengs, M. Sabba and M. H. Levitt, *The Journal of Chemical Physics*, 2023, **158**, 124204.

[129] Y. Aharonov and J. Anandan, *Physical Review Letters*, 1987, **58**, 1593–1596.

[130] M. Berry, *Proceedings of the Royal Society of London. A. Mathematical and Physical Sciences*, 1984, **392**, 45–57.

[131] D. Suter, G. C. Chingas, R. A. Harris and A. Pines, *Molecular Physics*, 1987, **61**, 1327–1340.

[132] A. Bax, R. Freeman and T. A. Frenkiel, *Journal of the American Chemical Society*, 1981, **103**, 2102–2104.

[133] M. C. D. Tayler, *phd*, University of Southampton, 2012.

[134] J. W. Zwanziger, M. Koenig and A. Pines, *Annual Review of Physical Chemistry*, 1990, **41**, 601–646.

[135] D. Suter, K. T. Mueller and A. Pines, *Physical Review Letters*, 1988, **60**, 1218–1220.

[136] M. C. D. Tayler, in *Long-lived Nuclear Spin Order: Theory and Applications*, ed. G. Pileio, Royal Society of Chemistry, 2020, pp. 188 – 208.

[137] E. Cartan, *The theory of Spinors*, Dover Publications, Inc., New York, 1981.

[138] M. E. Stoll, A. J. Vega and R. W. Vaughan, *Physical Review A*, 1977, **16**, 1521–1524.

[139] E. K. Wolff and M. Mehring, *Physics Letters A*, 1979, **70**, 125–126.

[140] M. Mehring, P. Höfer and A. Grupp, *Physical Review A*, 1986, **33**, 3523–3526.

[141] D. Suter, A. Pines and M. Mehring, *Physical Review Letters*, 1986, **57**, 242–244.

[142] M. J. Thrippleton, T. J. Ball, S. Steuernagel, S. E. Ashbrook and S. Wimperis, *Chemical Physics Letters*, 2006, **431**, 390–396.

[143] M. J. Thrippleton, T. J. Ball and S. Wimperis, *The Journal of Chemical Physics*, 2008, **128**, 034507.

[144] B. Tratzmiller, *Dissertation*, Universität Ulm, 2021.

[145] S. J. DeVience, R. L. Walsworth and M. S. Rosen, *NMR in Biomedicine*, 2013, **26**, 1204–1212.

[146] S. J. Elliott, L. J. Brown, J.-N. Dumez and M. H. Levitt, *Physical Chemistry Chemical Physics*, 2016, **18**, 17965–17972.

[147] S. J. Elliott, L. J. Brown, J.-N. Dumez and M. H. Levitt, *Journal of Magnetic Resonance*, 2016, **272**, 87–90.

[148] D. E. Korenchan, J. Lu, M. Sabba, L. Dagys, L. J. Brown, M. H. Levitt and A. Jerschow, *Physical Chemistry Chemical Physics*, 2022, **24**, 24238–24245.

[149] A. Sonnefeld, A. Razanahoera, P. Pelupessy, G. Bodenhausen and K. Sheberstov, *Science Advances*, 2022, **8**, eade2113.

[150] A. Razanahoera, A. Sonnefeld, K. Sheberstov, P. Narwal, M. Minaei, K. Kouřil, G. Bodenhausen and B. Meier, *The Journal of Physical Chemistry Letters*, 2024, **15**, 9024–9029.

[151] K. F. Sheberstov, A. Sonnefeld and G. Bodenhausen, *The Journal of Chemical Physics*, 2024, **160**, 144308.

[152] I. Mandzhieva, F. Theiss, X. He, A. Ortmeier, A. Koirala, S. J. McBride, S. J. DeVience, M. S. Rosen, V. Blum and T. Theis, *Journal of Chemical Information and Modeling*, 2025, **65**, 7554–7568.

[153] D. P. Weitekamp, *Time-domain multiple-quantum NMR*, Lawrence Berkeley National Lab. (LBNL), Berkeley, CA (United States) Technical Report LBL–10593, 1982.

[154] L. E. Kay and R. McClung, *Journal of Magnetic Resonance (1969)*, 1988, **77**, 258–273.

[155] A. Wilman and P. Allen, *Journal of Magnetic Resonance, Series B*, 1994, **105**, 58–60.

[156] U. Haeberlen and J. S. Waugh, *Physical Review*, 1968, **175**, 453–467.

[157] M. Hohwy and N. C. Nielsen, *The Journal of Chemical Physics*, 1997, **106**, 7571–7586.

[158] C. Wiame, S. Van Dyck, K. Sheberstov, A. Razanahoera and G. Bodenhausen, *Magnetic Resonance Discussions*, 2025, 1–11.

[159] C. Cohen-Tannoudji, B. Diu and F. Laloë, *Quantum Mechanics*, Wiley, London, 1977.

[160] M. Edén, *Concepts in Magnetic Resonance Part A*, 2015, **43**, 109–126.

[161] M. Chávez and M. Ernst, *Solid State Nuclear Magnetic Resonance*, 2022, **122**, 101834.

[162] J. T. Hill-Cousins, I.-A. Pop, G. Pileio, G. Stevanato, P. Håkansson, S. S. Roy, M. H. Levitt, L. J. Brown and R. C. D. Brown, *Organic Letters*, 2015, **17**, 2150–2153.

[163] M. Rance, O. W. Sørensen, G. Bodenhausen, G. Wagner, R. R. Ernst and K. Wüthrich, *Biochemical and Biophysical Research Communications*, 1983, **117**, 479–485.

[164] L. Emsley, I. Burghardt and G. Bodenhausen, *J. Magn. Reson.*, 1990, **90**, 214–220.

[165] K. Elbayed and D. Canet, *Molecular Physics*, 1990, **71**, 979–993.

[166] J. Zhou, C. Ye and B. Sanctuary, *Molecular Physics*, 1996, **87**, 679–689.

[167] S. J. F. Vincent, C. Zwahlen and G. Bodenhausen, *Journal of the American Chemical Society*, 1993, **115**, 9202–9209.

[168] R. Konrat, I. Burghardt and G. Bodenhausen, *Journal of the American Chemical Society*, 1991, **113**, 9135–9140.

[169] R. Konrat, G. Zieger, H. Sterk and W. Bermel, *Journal of Magnetic Resonance, Series A*, 1994, **106**, 23–31.

[170] S. Mamone, N. Rezaei-Ghaleh, F. Opazo, C. Griesinger and S. Glöggler, *Science Advances*, 2020, **6**, eaaz1955.

[171] S. Mamone, A. B. Schmidt, N. Schwaderlapp, T. Lange, D. v. Elverfeldt, J. Hennig and S. Glöggler, *NMR in Biomedicine*, 2021, **34**, e4400.

[172] D. H. Lysak, F. V. C. Kock, S. Mamone, R. Soong, S. Glöggler and A. J. Simpson, *Chemical Science*, 2023, **14**, 1413–1418.

[173] S. J. McBride, M. Pike, E. Curran, A. Zavriyev, B. Adebesin, L. Tucker, J. M. Harzan, I. M. Senanayake, M. Abdulmojeed, F. Theiss, S. Shen, T. Boele, S. B. Duckett, B. M. Goodson, M. S. Rosen, E. Y. Chekmenev, H. Yuan, C. Dedesma, T. Gade, S. Kadlecek, T. Theis and P. TomHon, *Angewandte Chemie International Edition*, 2025, **64**, e202501231.

[174] S. Ishihara, J. Labuta, Z. Futera, S. Mori, H. Sato, K. Ariga and J. P. Hill, *The Journal of Physical Chemistry B*, 2018, **122**, 5114–5120.

[175] C. Dalvit, P. Pevarello, M. Tatò, M. Veronesi, A. Vulpetti and M. Sundström, *Journal of biomolecular NMR*, 2000, **18**, 65–68.

[176] B. J. Stockman and C. Dalvit, *Progress in Nuclear Magnetic Resonance Spectroscopy*, 2002, **41**, 187–231.

[177] C. Dalvit, *Progress in Nuclear Magnetic Resonance Spectroscopy*, 2007, **51**, 243–271.

[178] R. Buratto, A. Bornet, J. Milani, D. Mammoli, B. Vuichoud, N. Salvi, M. Singh, A. Laguerre, S. Passemard, S. Gerber-Lemaire, S. Jannin and G. Bodenhausen, *ChemMedChem*, 2014, **9**, 2509–2515.

[179] R. Buratto, D. Mammoli, E. Canet and G. Bodenhausen, *Journal of Medicinal Chemistry*, 2016, **59**, 1960–1966.

[180] P. Lesot, C. Aroulanda, H. Zimmermann and Z. Luz, *Chemical Society Reviews*, 2015, **44**, 2330–2375.

[181] J. Courtieu, P. Lesot, A. Meddour, D. Merlet and C. Aroulanda, in *Encyclopedia of Magnetic Resonance*, ed. R. K. Harris, John Wiley & Sons, Ltd, Chichester, UK, 2007, p. emrstm0078.

[182] B. Gouilleux, F. Moussallieh and P. Lesot, *ChemPhysChem*, 2023, **24**, e202200508.

[183] C. Aroulanda and P. Lesot, *Chirality*, 2022, **34**, 182–244.

[184] V. Chiapolino, F.-M. Moussallieh, P. Lesot and B. Gouilleux, *Journal of Pharmaceutical Analysis*, 2025, 101469.

[185] J. Labuta, J. P. Hill, S. Ishihara, L. Hanyková and K. Ariga, *Accounts of Chemical Research*, 2015, **48**, 521–529.

[186] J. Labuta, S. Ishihara, D. T. Payne, K. Takimoto, H. Sato, L. Hanyková, K. Ariga and J. P. Hill, *Chemosensors*, 2021, **9**, 259.

[187] R. R. Fraser, M. A. Petit and M. Miskow, *Journal of the American Chemical Society*, 1972, **94**, 3253–3254.

Appendix A

Spherical Tensor Operators

The spherical tensor operators for a one-spin-1/2 system are given as follows:

$$\begin{aligned}\mathbf{T^{1}_{1,0}} &= I_{1z},\\ \mathbf{T^{1}_{1,\pm 1}} &= \mp\frac{1}{\sqrt{2}}I_1^{\pm},\end{aligned} \tag{A.1}$$

and for a two-spin-1/2 system:

$$\begin{aligned}\mathbf{T^{12}_{0,0}} &= -\frac{1}{\sqrt{3}}\left(I_1 I_2\right),\\ \mathbf{T^{12}_{1,0}} &= \frac{1}{2\sqrt{2}}\left(I_1^{+}I_2^{-} - I_1^{-}I_2^{+}\right),\\ \mathbf{T^{12}_{1,\pm 1}} &= -\frac{1}{2}\left(I_1^{\pm}I_{2z} - I_{1z}I_2^{\pm}\right),\\ \mathbf{T^{12}_{2,0}} &= \frac{1}{\sqrt{6}}\left(3I_{1z}I_{2z} - I_1 I_2\right),\\ \mathbf{T^{12}_{2,\pm 1}} &= \mp\frac{1}{2}\left(I_1^{\pm}I_{2z} + I_{1z}I_2^{\pm}\right),\\ \mathbf{T^{12}_{2,\pm 2}} &= \frac{1}{2}\left(I_1^{\pm}I_2^{\pm}\right).\end{aligned} \tag{A.2}$$

Appendix B

Supplementary Information - Chapter 3

B.1 Computational Chemistry

B.1.1 CSA Tensors

Estimates of the ^{13}C nuclear shielding tensors for the four carbon sites in the squarate dianion were obtained using the B3LYP functional using the ORCA[101] package. The calculations do not take into account secondary isotope shifts. The shielding tensors are given in Equation B.1.1.

$$
\begin{aligned}
\sigma_1 &= \begin{pmatrix} -86.787 & 0.457 & -0.552 \\ 0.478 & -112.518 & 0.23 \\ -0.468 & 0.22 & 66.533 \end{pmatrix} \text{ppm}, \\
\sigma_2 &= \begin{pmatrix} -112.52 & -0.362 & -0.546 \\ -0.41 & -86.786 & 0.109 \\ -0.554 & 0.189 & 66.516 \end{pmatrix} \text{ppm}, \\
\sigma_3 &= \begin{pmatrix} -86.740 & 0.451 & -0.402 \\ 0.435 & -112.491 & 0.233 \\ -0.493 & 0.220 & 66.523 \end{pmatrix} \text{ppm}, \\
\sigma_4 &= \begin{pmatrix} -112.489 & -0.405 & -0.548 \\ -0.416 & -86.737 & 0.258 \\ -0.553 & 0.163 & 66.540 \end{pmatrix} \text{ppm}.
\end{aligned}
\tag{B.1}
$$

The calculated values of the isotropic parts of the shielding tensors are given in Equation B.2.

$$
\begin{aligned}
\sigma_1^{\text{iso}} &= -44.258 \text{ ppm}, \\
\sigma_2^{\text{iso}} &= -44.263 \text{ ppm}, \\
\sigma_3^{\text{iso}} &= -44.236 \text{ ppm}, \\
\sigma_4^{\text{iso}} &= -44.229 \text{ ppm}.
\end{aligned}
\tag{B.2}
$$

B.1.2 Scalar Couplings

The scalar couplings were estimated using the ORCA[101] open-source quantum chemistry package, reported in Table B.1. The main text reports the average value of the J-couplings shown in the table below as the J_{calc} parameter (see Table 3.3).

Table B.1: Keyword specifics used in computational calculations performed by ORCA, along with the different scalar coupling estimates for 1,2-$^{13}C_2$-squarate and 1,3-$^{13}C_2$-squarate. Adapted from Heramun *et al.*[1], *J. Chem. Phys.* 163, 074201 (2025), Supporting Info; licensed under a Creative Commons Attribution (CC BY) license.

Keywords	$^1J_{12}$ **/Hz**	$^2J_{13}$ **/Hz**
B3LYP pcJ-3 TightSCF	56.31	47.35
B3LYP pcJ-3 VeryTightSCF	56.31	47.35
B3LYP pcJ-3 VeryTightSCF CPCM(water)	56.48	46.36
TPSSh pcJ-3 TightSCF	56.56	48.98
TPSSh pcJ-3 VeryTightSCF	56.56	48.98
TPSSh pcJ-3 VeryTightSCF CPCM(water)	56.68	47.97

B.2 Isotope Shifts - Peak Assignment

B.2.1 pH 0.9

Table B.2 details how each of the $^{13}C_1$-squarate isotopologues at pH 0.9 (shown in Figure 3.11) were assigned to their respective peaks. Each species' position is the result of the relevant isotope shift interactions, summed together.

Table B.2: Isotope shift effect calculation for each individual isotopomer present at pH 0.9, as shown in Figure 3.11. The relative shift position is taken with respect to peak 1 in Figure 3.11, which experiences no isotope shifts. Within the molecular structures, an orange filled circle indicates a ^{16}O atom, and a blue circle with a white star in the centre indicates a ^{18}O atom. A filled black circle denotes a ^{13}C atom.

Peak	**Species**	**Isotope Shifts**	**Position /ppb**
1	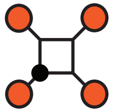	No isotope effects	0
2	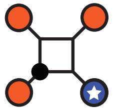	$^{2}\Delta^{13}\mathrm{C}(^{18}\mathrm{O})$	-14.9 ± 0.5
2	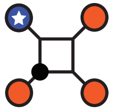	$^{2}\Delta^{13}\mathrm{C}(^{18}\mathrm{O})$	-14.9 ± 0.5
3	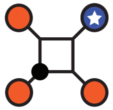	$^{3}\Delta^{13}\mathrm{C}(^{18}\mathrm{O})$	-22.1 ± 0.5
4	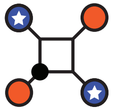	$2(^{2}\Delta^{13}\mathrm{C}(^{18}\mathrm{O}))$	-29.8 ± 0.5
5	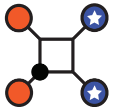	$^{2}\Delta^{13}\mathrm{C}(^{18}\mathrm{O}) + {}^{3}\Delta^{13}\mathrm{C}(^{18}\mathrm{O})$	-37.0 ± 0.5

Peak	Species	Isotope Shifts	Position /ppb
5	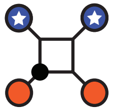	${}^{2}\Delta^{13}\mathrm{C}({}^{18}\mathrm{O}) + {}^{3}\Delta^{13}\mathrm{C}({}^{18}\mathrm{O})$	-37.0 ± 0.5
6	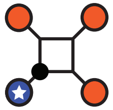	${}^{1}\Delta^{13}\mathrm{C}({}^{18}\mathrm{O})$	-40.1 ± 0.5
7	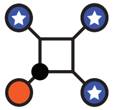	$2({}^{2}\Delta^{13}\mathrm{C}({}^{18}\mathrm{O})) + {}^{3}\Delta^{13}\mathrm{C}({}^{18}\mathrm{O})$	-51.9 ± 0.5
8	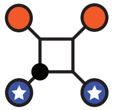	${}^{1}\Delta^{13}\mathrm{C}({}^{18}\mathrm{O}) + {}^{2}\Delta^{13}\mathrm{C}({}^{18}\mathrm{O})$	-54.9 ± 0.5
8	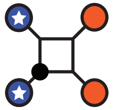	${}^{1}\Delta^{13}\mathrm{C}({}^{18}\mathrm{O}) + {}^{2}\Delta^{13}\mathrm{C}({}^{18}\mathrm{O})$	-54.9 ± 0.5
9	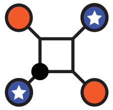	${}^{1}\Delta^{13}\mathrm{C}({}^{18}\mathrm{O}) + {}^{3}\Delta^{13}\mathrm{C}({}^{18}\mathrm{O})$	-62.2 ± 0.5
10	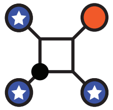	${}^{1}\Delta^{13}\mathrm{C}({}^{18}\mathrm{O}) + 2({}^{2}\Delta^{13}\mathrm{C}({}^{18}\mathrm{O}))$	-69.8 ± 0.5

Peak	**Species**	**Isotope Shifts**	**Position /ppb**
11	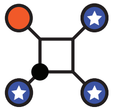	$^{1}\Delta^{13}\mathrm{C}(^{18}\mathrm{O}) + {}^{2}\Delta^{13}\mathrm{C}(^{18}\mathrm{O}) + {}^{3}\Delta^{13}\mathrm{C}(^{18}\mathrm{O})$	-77.1 ± 0.5
11	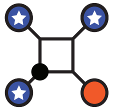	$^{1}\Delta^{13}\mathrm{C}(^{18}\mathrm{O}) + {}^{2}\Delta^{13}\mathrm{C}(^{18}\mathrm{O}) + {}^{3}\Delta^{13}\mathrm{C}(^{18}\mathrm{O})$	-77.1 ± 0.5
12	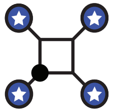	$^{1}\Delta^{13}\mathrm{C}(^{18}\mathrm{O}) + 2({}^{2}\Delta^{13}\mathrm{C}(^{18}\mathrm{O})) + {}^{3}\Delta^{13}\mathrm{C}(^{18}\mathrm{O})$	-91.9 ± 0.5

B.2.2 pH 13.3

Table B.3 details how each of the $^{13}C_1$-squarate, 1,2-$^{13}C_2$-squarate and 1,3-$^{13}C_2$-squarate isotopologues were assigned to their respective peaks (shown in Figure 3.12). In the case of coupled spins, each species' position is the result of the sum of the relevant isotope shift interactions viewed from the perspective of one ^{13}C-spin, averaged with the sum of the isotope shifts viewed from the second ^{13}C-spin. For single ^{13}C-spins, each species' position is the result of the relevant isotope shift interactions, summed together.

Table B.3: Isotope shift effect calculation for each individual isotopologue present at pH 13.3, as shown in Figure 3.12. The relative shift position is taken with respect to peak 1 in Figure 3.12 (a), which experiences no isotope shifts. Within the molecular structures, an orange filled circle indicates a ^{16}O atom, and a blue circle with a white star in the centre indicates a ^{18}O atom. The grey filled circle can be either a ^{16}O or ^{18}O atom. A filled black circle denotes a ^{13}C atom.

Peak	Species	Isotope Shifts	Position /ppb
1	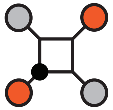	No isotope effects	0
2	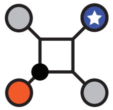	${}^{3}\Delta^{13}C(^{18}O)$	-2.7 ± 0.5
3	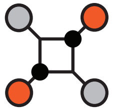	${}^{2}\Delta^{13}C(^{13}C)$	-7.1 ± 0.5
4	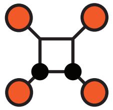	${}^{1}\Delta^{13}C(^{13}C)$	-21.3 ± 0.5
4	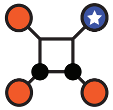	$[{}^{3}\Delta^{13}C(^{18}O) + 2({}^{1}\Delta^{13}C(^{13}C))]/2$	-22.7 ± 0.5

Peak	**Species**	**Isotope Shifts**	**Position /ppb**
4	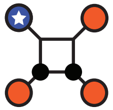	$[{}^{3}\Delta^{13}\mathrm{C}({}^{18}\mathrm{O}) + 2({}^{1}\Delta^{13}\mathrm{C}({}^{13}\mathrm{C}))]/2$	-22.7 ± 0.5
4	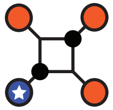	$[{}^{1}\Delta^{13}\mathrm{C}({}^{18}\mathrm{O})+{}^{3}\Delta^{13}\mathrm{C}({}^{18}\mathrm{O})+2({}^{2}\Delta^{13}\mathrm{C}({}^{13}\mathrm{C}))]/2$	-21.4 ± 0.5
4	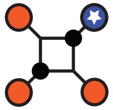	$[{}^{1}\Delta^{13}\mathrm{C}({}^{18}\mathrm{O})+{}^{3}\Delta^{13}\mathrm{C}({}^{18}\mathrm{O})+2({}^{2}\Delta^{13}\mathrm{C}({}^{13}\mathrm{C}))]/2$	-21.4 ± 0.5
4	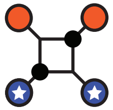	$[{}^{1}\Delta^{13}\mathrm{C}({}^{18}\mathrm{O})+{}^{3}\Delta^{13}\mathrm{C}({}^{18}\mathrm{O})+2({}^{2}\Delta^{13}\mathrm{C}({}^{13}\mathrm{C}))]/2$	-21.4 ± 0.5
4	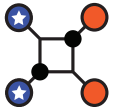	$[{}^{1}\Delta^{13}\mathrm{C}({}^{18}\mathrm{O})+{}^{3}\Delta^{13}\mathrm{C}({}^{18}\mathrm{O})+2({}^{2}\Delta^{13}\mathrm{C}({}^{13}\mathrm{C}))]/2$	-21.4 ± 0.5
4	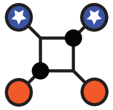	$[{}^{1}\Delta^{13}\mathrm{C}({}^{18}\mathrm{O})+{}^{3}\Delta^{13}\mathrm{C}({}^{18}\mathrm{O})+2({}^{2}\Delta^{13}\mathrm{C}({}^{13}\mathrm{C}))]/2$	-21.4 ± 0.5
4	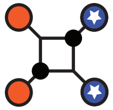	$[{}^{1}\Delta^{13}\mathrm{C}({}^{18}\mathrm{O})+{}^{3}\Delta^{13}\mathrm{C}({}^{18}\mathrm{O})+2({}^{2}\Delta^{13}\mathrm{C}({}^{13}\mathrm{C}))]/2$	-21.4 ± 0.5

Peak	Species	Isotope Shifts	Position /ppb
5	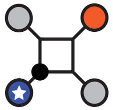	${}^{1}\Delta^{13}\mathrm{C}({}^{18}\mathrm{O})$	-25.7 ± 0.5
6	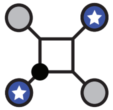	${}^{1}\Delta^{13}\mathrm{C}({}^{18}\mathrm{O}) + {}^{3}\Delta^{13}\mathrm{C}({}^{18}\mathrm{O})$	-28.5 ± 0.5
7	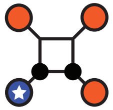	$[{}^{1}\Delta^{13}\mathrm{C}({}^{18}\mathrm{O}) + 2({}^{1}\Delta^{13}\mathrm{C}({}^{13}\mathrm{C}))]/2$	-34.2 ± 0.5
7	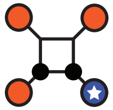	$[{}^{1}\Delta^{13}\mathrm{C}({}^{18}\mathrm{O}) + 2({}^{1}\Delta^{13}\mathrm{C}({}^{13}\mathrm{C}))]/2$	-34.2 ± 0.5
7	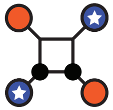	$[{}^{1}\Delta^{13}\mathrm{C}({}^{18}\mathrm{O}) + {}^{3}\Delta^{13}\mathrm{C}({}^{18}\mathrm{O}) + 2({}^{1}\Delta^{13}\mathrm{C}({}^{13}\mathrm{C}))]/2$	-35.6 ± 0.5
7	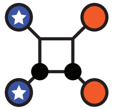	$[{}^{1}\Delta^{13}\mathrm{C}({}^{18}\mathrm{O}) + {}^{3}\Delta^{13}\mathrm{C}({}^{18}\mathrm{O}) + 2({}^{1}\Delta^{13}\mathrm{C}({}^{13}\mathrm{C}))]/2$	-35.6 ± 0.5
7	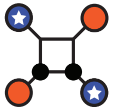	$[{}^{1}\Delta^{13}\mathrm{C}({}^{18}\mathrm{O}) + {}^{3}\Delta^{13}\mathrm{C}({}^{18}\mathrm{O}) + 2({}^{1}\Delta^{13}\mathrm{C}({}^{13}\mathrm{C}))]/2$	-35.6 ± 0.5

Peak	**Species**	**Isotope Shifts**	**Position /ppb**
7	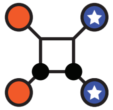	$[{}^{1}\Delta^{13}\mathrm{C}({}^{18}\mathrm{O}) + {}^{3}\Delta^{13}\mathrm{C}({}^{18}\mathrm{O}) + 2({}^{1}\Delta^{13}\mathrm{C}({}^{13}\mathrm{C}))]/2$	-35.6 ± 0.5
7	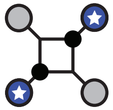	${}^{1}\Delta^{13}\mathrm{C}({}^{18}\mathrm{O}) + {}^{3}\Delta^{13}\mathrm{C}({}^{18}\mathrm{O}) + {}^{2}\Delta^{13}\mathrm{C}({}^{13}\mathrm{C})$	-35.6 ± 0.5
7	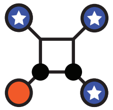	$[{}^{1}\Delta^{13}\mathrm{C}({}^{18}\mathrm{O}) + 2({}^{3}\Delta^{13}\mathrm{C}({}^{18}\mathrm{O}) + {}^{1}\Delta^{13}\mathrm{C}({}^{13}\mathrm{C}))]/2$	-37.0 ± 0.5
7	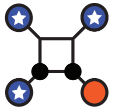	$[{}^{1}\Delta^{13}\mathrm{C}({}^{18}\mathrm{O}) + 2({}^{3}\Delta^{13}\mathrm{C}({}^{18}\mathrm{O}) + {}^{1}\Delta^{13}\mathrm{C}({}^{13}\mathrm{C}))]/2$	-37.0 ± 0.5
8	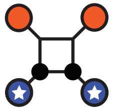	${}^{1}\Delta^{13}\mathrm{C}({}^{18}\mathrm{O}) + {}^{1}\Delta^{13}\mathrm{C}({}^{13}\mathrm{C})$	-47.1 ± 0.5
8	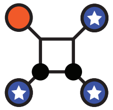	$[{}^{3}\Delta^{13}\mathrm{C}({}^{18}\mathrm{O}) + 2({}^{1}\Delta^{13}\mathrm{C}({}^{18}\mathrm{O}) + {}^{1}\Delta^{13}\mathrm{C}({}^{13}\mathrm{C}))]/2$	-48.5 ± 0.5
8	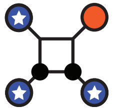	$[{}^{3}\Delta^{13}\mathrm{C}({}^{18}\mathrm{O}) + 2({}^{1}\Delta^{13}\mathrm{C}({}^{18}\mathrm{O}) + {}^{1}\Delta^{13}\mathrm{C}({}^{13}\mathrm{C}))]/2$	-48.5 ± 0.5

Peak	**Species**	**Isotope Shifts**	**Position /ppb**
8	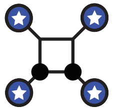	${}^{1}\Delta^{13}\mathrm{C}({}^{18}\mathrm{O}) + {}^{3}\Delta^{13}\mathrm{C}({}^{18}\mathrm{O}) + {}^{1}\Delta^{13}\mathrm{C}({}^{13}\mathrm{C})$	-49.8 ± 0.5

B.3 Filtration Parameters

The parameters used for the singlet order destruction filter, and the T_{00} filter are given in Table B.4.

Table B.4: T_{00} filter z-pulse gradient parameters used, and details of the SOD loop numbers, m and j. Adapted from Heramun *et al.*[1], *J. Chem. Phys.* 163, 074201 (2025), Supporting Info; licensed under a Creative Commons Attribution (CC BY) license.

	T_{00}	
z-Gradient	**Strength / %**	**Duration / ms**
G_1	+15	4.4
G_2	−7.5	2.4
G_3	−7.5	2.0

	SOD	
Parameter	**1,2-$^{13}C_2$-sq.**	**1,3-$^{13}C_2$-sq.**
m	14	10
j	4	4

B.4 Additional ^{13}C NMR Spectra

Below are illustrated some additional spectra containing further double-quantum and singlet filtered ^{13}C NMR spectra of 1,2-$^{13}C_2$-squarate (Figure B.1), and 1,3-$^{13}C_2$-squarate (Figure B.2). The spectra obtained by applying the M2S-S2M sequence both contain interference due to the imperfect filtration of the ^{13}C species in solution, which are most abundant. In the case of 1,3-$^{13}C_2$-squarate in Figure B.2(e), this meant that the 1,3-$^{13}C_2$-squarate species was altogether unobservable.

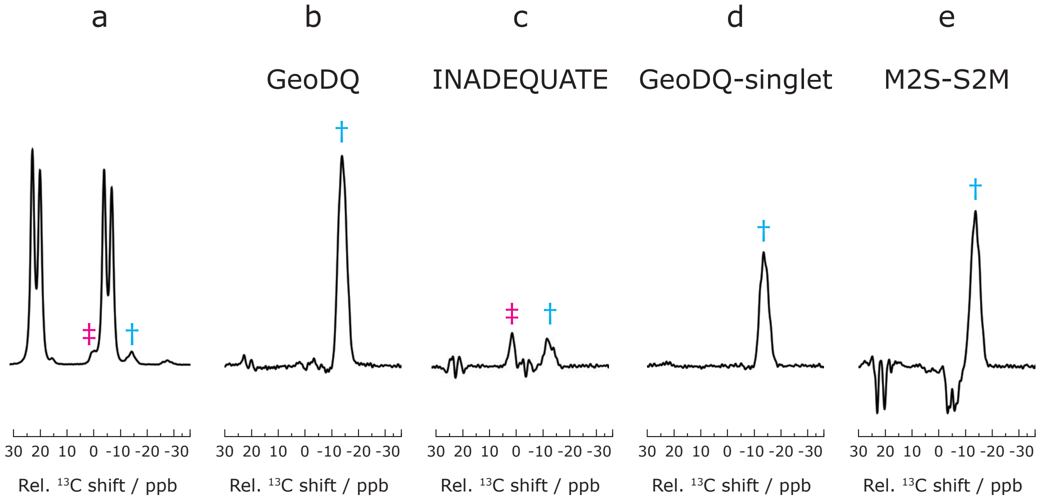

Figure B.1: Selective ^{13}C NMR of 1,2-$^{13}C_2$-squarate. All spectra are for a solution of $^{13}C_1$ squarate at pH 13.3 and 298 K. The chemical shift scale is centred at 203.05 ppm. Blue dagger: 1,2-$^{13}C_2$ squarate signals; Magenta double-dagger: 1,3-$^{13}C_2$ squarate signals. (**a**) A 90° pulse-acquire ^{13}C NMR spectrum of the $^{13}C_1$-squarate solution in a magnetic field of 9.4 T, averaged over 512 transients. Only given as a positional reference for the 1,2-$^{13}C_2$-squarate and 1,3-$^{13}C_2$-squarate signals. (**b**) Double-quantum filtered spectrum obtained using the GeoDQ pulse sequence. The spectrum was acquired over 1024 transients at 16.4 T and 298 K. (**c**) Double-quantum filtered spectrum obtained using the refocused INADEQUATE pulse sequence. The spectrum was acquired over 1024 transients at 16.4 T and 298 K. (**d**) Singlet-filtered spectrum obtained using the GeoDQ-singlet pulse sequence. The spectrum was acquired over 1024 transients at 16.4 T and 298 K. (**e**) Singlet-filtered spectrum obtained using the M2S-S2M pulse sequence. The spectrum was acquired over 1024 transients at 16.4 T and 298 K. See Table B.5 for the experimentally optimised parameters.

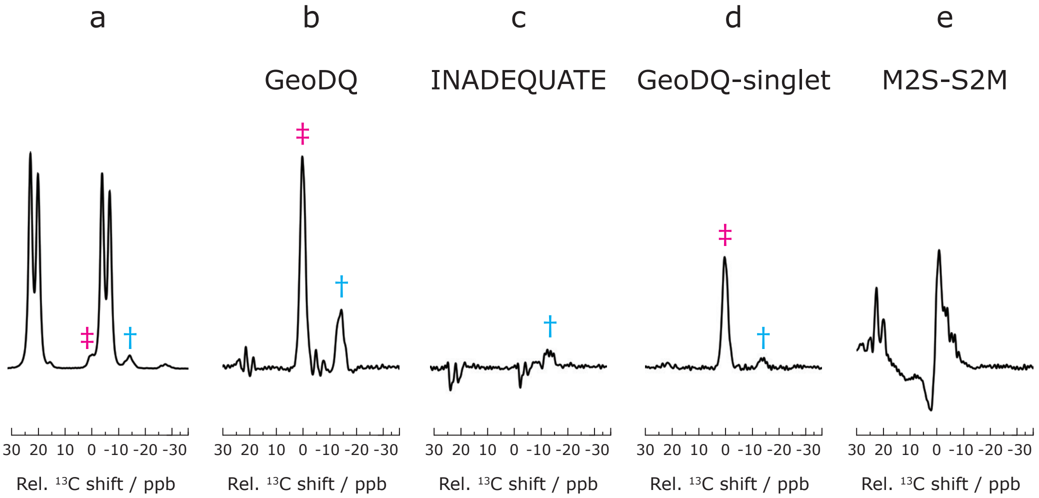

Figure B.2: Selective ^{13}C NMR of 1,3-$^{13}C_2$-squarate. All spectra are for a solution of $^{13}C_1$ squarate at pH 13.3 and 298 K. The chemical shift scale is centred at 203.05 ppm. Blue dagger: 1,2-$^{13}C_2$ squarate signals; Magenta double-dagger: 1,3-$^{13}C_2$ squarate signals. (**a**) A 90° pulse-acquire ^{13}C NMR spectrum of the $^{13}C_1$-squarate solution in a magnetic field of 9.4 T, averaged over 512 transients. Only given as a positional reference for the 1,2-$^{13}C_2$-squarate and 1,3-$^{13}C_2$-squarate signals. (**b**) Double-quantum filtered spectrum obtained using the GeoDQ pulse sequence. The spectrum was acquired over 1024 transients at 16.4 T and 298 K. (**c**) Double-quantum filtered spectrum obtained using the refocused INADEQUATE pulse sequence. The spectrum was acquired over 1024 transients at 16.4 T and 298 K. (**d**) Singlet-filtered spectrum obtained using the GeoDQ-singlet pulse sequence. The spectrum was acquired over 1024 transients at 16.4 T and 298 K. (**e**) Singlet-filtered spectrum obtained using the M2S-S2M pulse sequence. The spectrum was acquired over 1024 transients at 16.4 T and 298 K. See Table B.5 for the experimentally optimised parameters.

The experimentally optimised pulse sequence parameters are given in Tables 3.3 in the main text, and Table B.5 below.

Table B.5: Pulse sequence parameters used for the double-quantum and singlet filtered experiments of 1,2-$^{13}C_2$-squarate and 1,3-$^{13}C_2$-squarate at 16.4 T and 298 K for a pH 13.3 sample.

Pulse Sequence	**Parameter**	**1,2-$^{13}C_2$-sq.**	**1,3-$^{13}C_2$-sq.**
GeoDQ	τ_1 /ms	4.53	6.21
	τ_2 /ms	9.06	12.42
	n	20	16
INADEQUATE	τ /ms	3325	2437
M2S-S2M	τ_J /ms	4.54	6.24
	n_1	9	8
	n_2	18	16

Appendix C

Supplementary Information - Chapter 4

C.1 Control Experiments

To confirm that the origin of the symmetry-breaking mechanism observed in molecules **I** (Table 4.1) and **K** (Table 4.3) is due to the presence of a chiral site within each molecule, DQF experiments were attempted using a "control" molecule. This is a carboxylic acid, and one of the starting materials used to synthesise the amides; It contains the ^{19}F spin-pair and the neighbouring phenyl ring, but the chiral site is absent. The molecular structure is shown in Figure C.1.

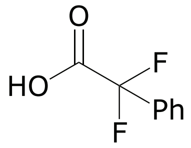

Figure C.1: Molecular structure of 2,2-difluoro-2-phenylacetic acid.

The DQF methods applied to molecules **I** (Table 4.1) and **K** (Table 4.3), shown in Figures 4.11 and 4.14, were repeated for this carboxylic acid control molecule. Attempts were made to experimentally optimise the pulse sequence parameters, given in Table C.1. The resulting double-quantum

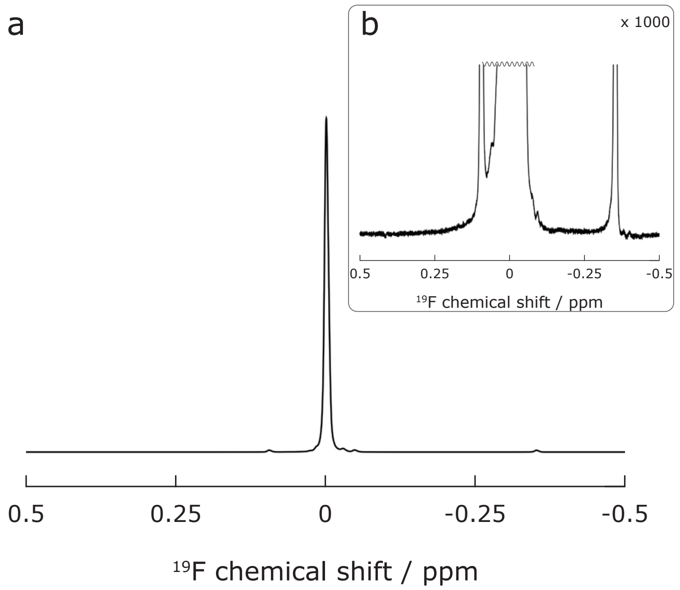

Figure C.2: (**a**) A 90° pulse-acquire ^{19}F NMR spectrum of a solution of the fluorinated carboxylic acid molecule shown in Figure C.1 in $CDCl_3$, acquired at 14.1 T, 298 K, and averaged over 5120 transients. The frequency scale is centred around -105.148 ppm. (**b**) A zoomed in view of the spectrum shown in part a. The vertical scale is given. Note the absence of an AB pattern.

filtered spectra are shown in Figure C.3. We can observe that the double-quantum filtering efficiency is approximately zero for all the double-quantum excitation methods. This confirms that the fluorine pair is chemically equivalent to each other, i.e. there is no evidence of a chemical shift difference between the two nuclei.

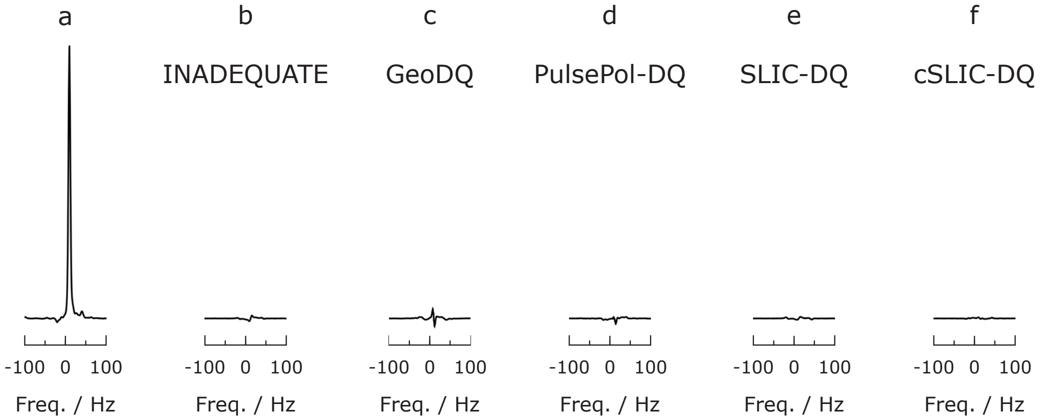

Figure C.3: ^{19}F spectra of a solution of the "control" A_2 spin system in $CDCl_3$, acquired at 14.1 T, 298 K, and averaged over 4 transients. ^{1}H decoupling was not used. The frequency axis is centred around -105.148 ppm. All spectra have the same vertical scale. All pulse sequence parameters are given in table C.1. (**a**) A 90° pulse-acquire spectrum. (**b**) Double-quantum filtered spectrum obtained using the refocused INADEQUATE pulse sequence. (**c**) Double-quantum filtered spectrum obtained using the GeoDQ pulse sequence. (**d**) Double-quantum filtered spectrum obtained using the PulsePol-DQ pulse sequence. (**e**) Double-quantum filtered spectrum obtained using the SLIC-DQ pulse sequence. (**f**) Double-quantum filtered spectrum obtained using the cSLIC-DQ pulse sequence.

Table C.1: Pulse sequence parameters used for the control double-quantum filtering experiments.

Pulse Sequence	**Parameter**	**Value**
Hard pulses	$\omega_{\mathrm{nut}}/(2\pi)$ / kHz	22.8 ± 0.1
INADEQUATE	τ_1 / ms	500.00
GeoDQ	τ_1^{Geo} / μs	976.0
	τ_2^{Geo} / μs	1952
	n	26
PulsePol-DQ	τ_2 / μs	2400
	m	9
SLIC-DQ	$\omega_{\mathrm{nut}}^{\mathrm{SLIC}}/(2\pi)$ / Hz	226 ± 3
cSLIC-DQ	$\omega_{\mathrm{nut}}^{\mathrm{SLIC}}/(2\pi)$ / Hz	256 ± 3
	n_J	21
	τ_J / μs	3940
	α	–

C.2 Double-Quantum Coherence Buildup Curves

The DQC buildup curves for the INADEQUATE pulse sequence are shown in Figure C.4, where the experimental, and simulated curves are depicted for the experiments using $^{13}C_2$-DAND (Table 4.5).

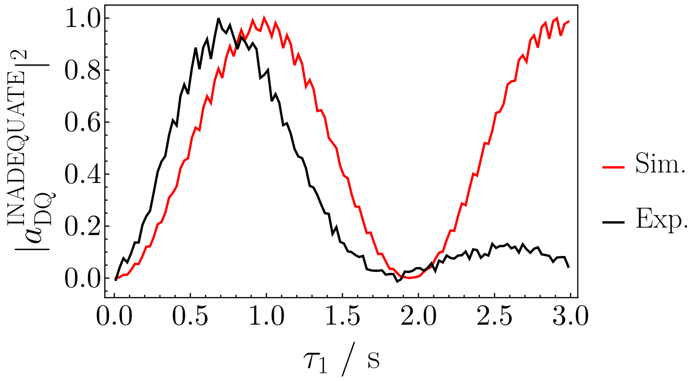

Figure C.4: Experimental and simulated buildup of DQC for the INADEQUATE pulse sequence, as a function of the delay τ_1, and for the solution of $^{13}C_2$-DAND at 9.4 T and 298 K. The *SpinDynamica*[27] parameters used were $J = 54.4$ Hz, and $\Delta = 7.5$ Hz.

Similarly, the curves are shown for the SLIC-DQ sequence in Figure C.5.

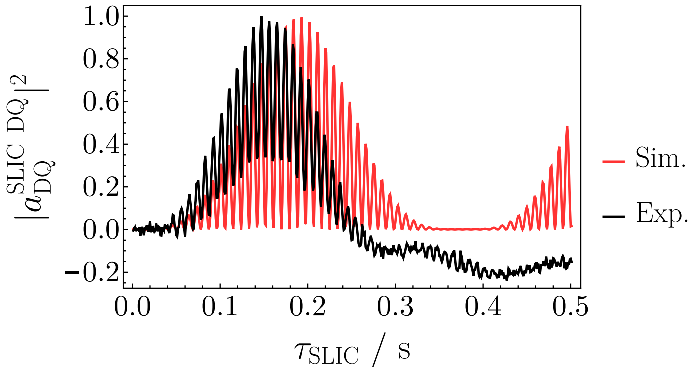

Figure C.5: Experimental and simulated buildup of DQC for the SLIC-DQ pulse sequence, as a function of the delay τ_{SLIC}, and for a solution of $^{13}C_2$-DAND at 9.4 T and 298 K. The *SpinDynamica*[27] parameters used were $J = 54.4$ Hz, and $\Delta = 7.5$ Hz.

The DQC buildup curves for the GeoDQ pulse sequence are shown in Figure C.6, where the experimental, and simulated curves are depicted for variations in the delay (Figure C.6(a)), and repetition number (Figure C.6(b)). Note that double-quantum coherence continues to be generated with good efficiency, even when far off-resonance from the optimal delay value, as shown in Figure C.6(a).

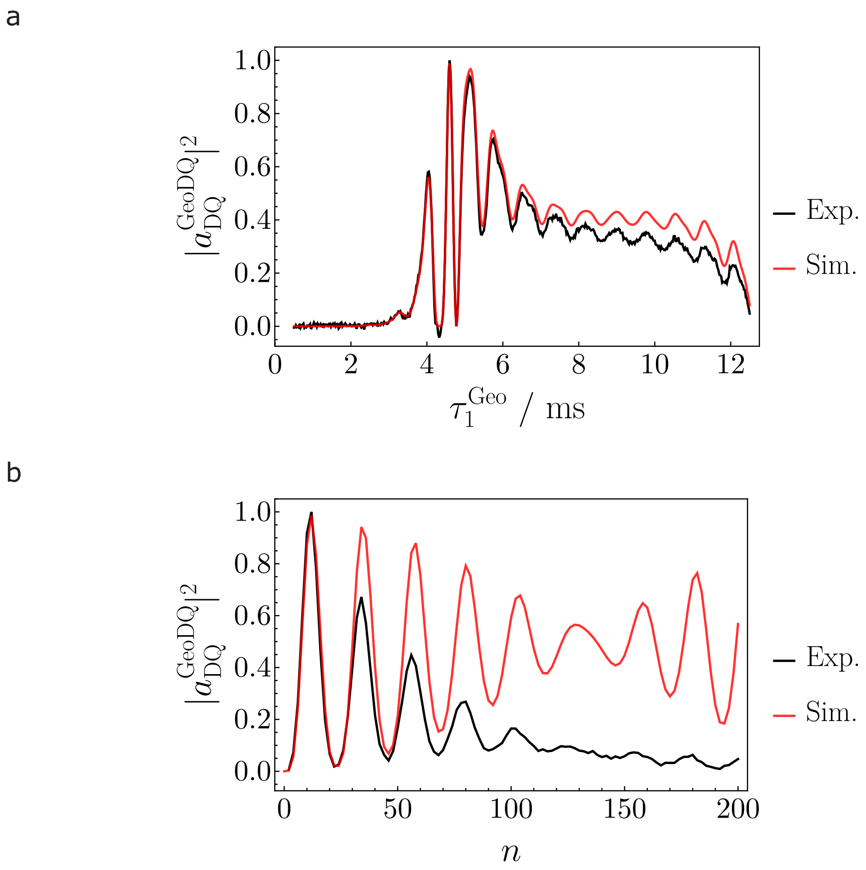

Figure C.6: Experimental and simulated buildup of DQC for the GeoDQ pulse sequence, for a solution of ^{13}C$_2$-DAND at 9.4 T and 298 K. (**a**) As a function of the delay τ_1^{Geo}. (**b**) As a function of the repetition number n. The *SpinDynamica*[27] parameters used were $J = 54.4$ Hz, and $\Delta = 7.5$ Hz.

The DQC buildup curves for the PulsePol-DQ pulse sequence are shown in Figure C.7, where the experimental, and simulated curves are depicted for variations in the delay (Figure C.7(a)), and repetition number (Figure C.7(b)). Note that double-quantum coherence is only generated when on-resonance with the optimal delay value, as shown in Figure C.7(a).

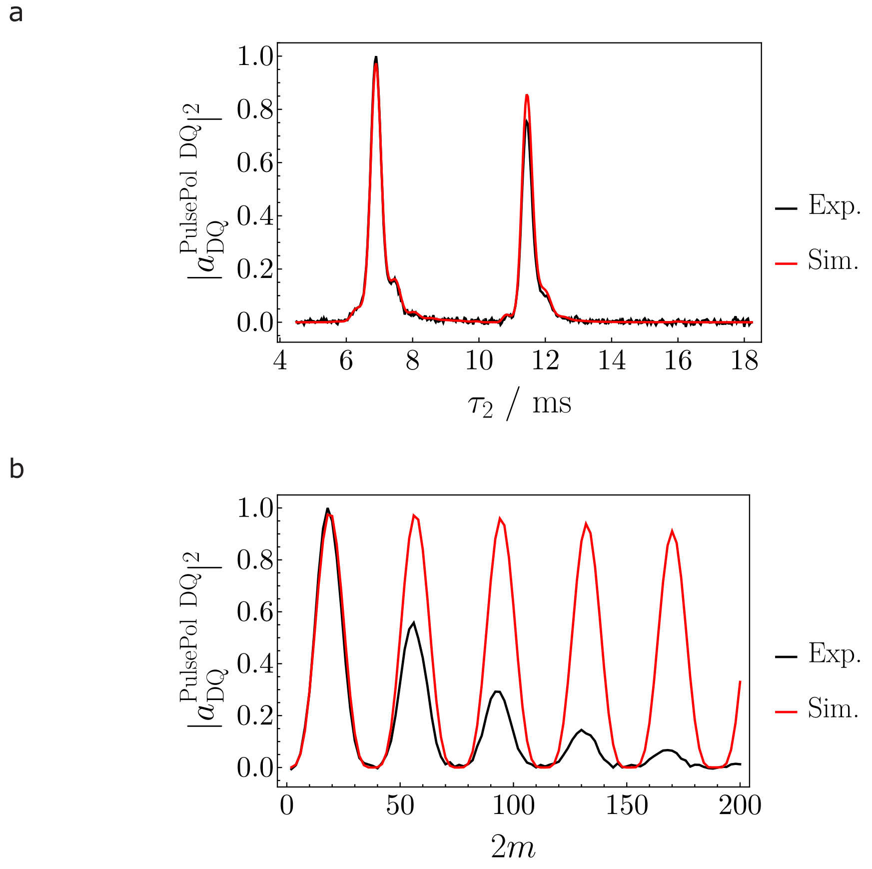

Figure C.7: Experimental and simulated buildup of DQC for the PulsePol-DQ pulse sequence, for a solution of $^{13}C_2$-DAND at 9.4 T and 298 K. (**a**) As a function of the delay τ_2. (**b**) As a function of the repetition number $2m$. The *SpinDynamica*[27] parameters used were $J = 54.4$ Hz, and $\Delta = 7.5$ Hz.

The DQC buildup curves for the cSLIC-DQ pulse sequence are shown in Figure C.8, where the experimental curves are depicted for variations in the delay (Figure C.8(a-b)), and repetition number (Figure C.8(b)). Note that double-quantum coherence is only generated when on-resonance with the optimal delay value, as shown in Figure C.8(b), displaying the high selectivity of the SLIC-type sequences.

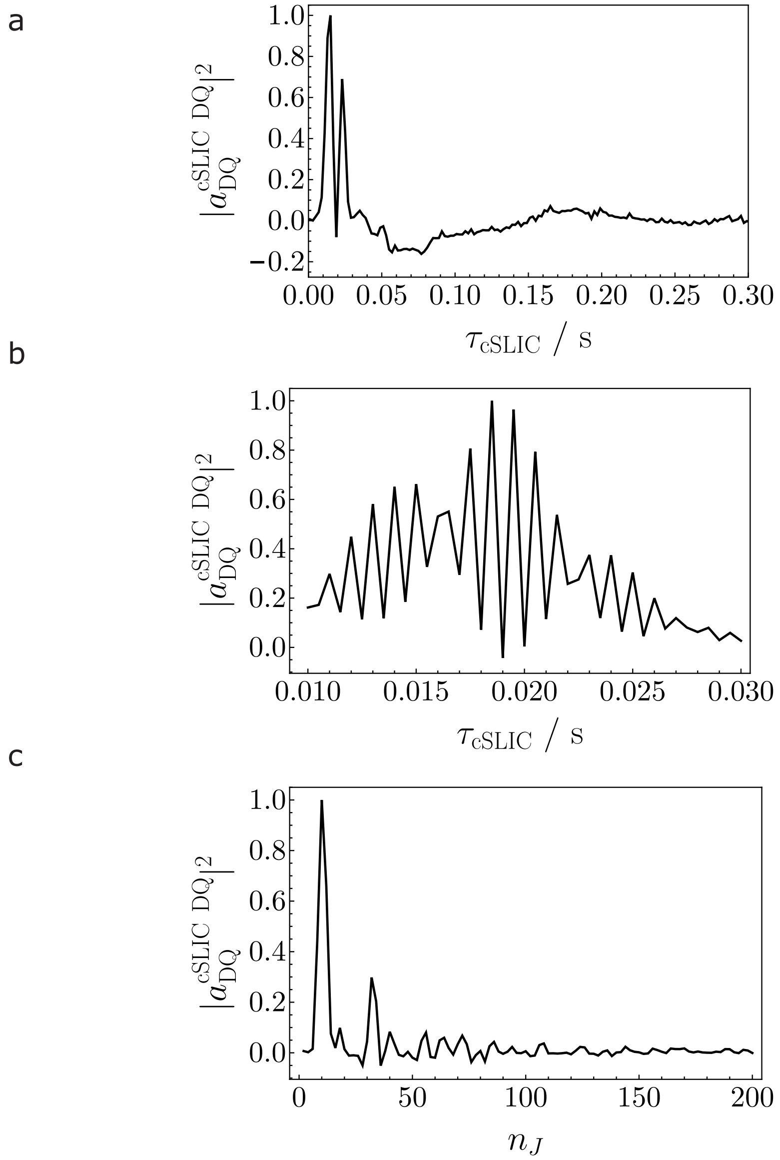

Figure C.8: Experimental buildup of DQC for the cSLIC-DQ pulse sequence, for the solution of $^{13}C_2$-DAND at 9.4 T and 298 K. (**a**) As a function of the delay τ_{cSLIC}. (**b**) As a function of τ_{cSLIC}, in a zoomed-in view of **a**. (**c**) As a function of the repetition number n_J.

Appendix D

Supplementary Information - Chapter 5

The following sections provide the exact numerical details for the parameters used to obtain the experimental results discussed in Chapter 5, and the T_1 and T_S relaxation time constants.

D.1 Double-Quantum Filtered NMR

The GeoDQ pulse sequence parameters used in the double-quantum filtered ^{19}F NMR spectra shown in Figure 5.4 are given in Table D.1. The pulse sequence is illustrated in Figure 4.4.

D.2 Singlet Filtered NMR

The M2S-S2M pulse sequence parameters for the singlet-filtered ^{19}F NMR spectra shown in Figure 5.6 are given in Table D.2. The pulse sequence is illustrated in Figures 2.6, and 2.5.

D.3 Relaxation Measurements

The T_1 and T_S relaxation constants are given in Table D.3.

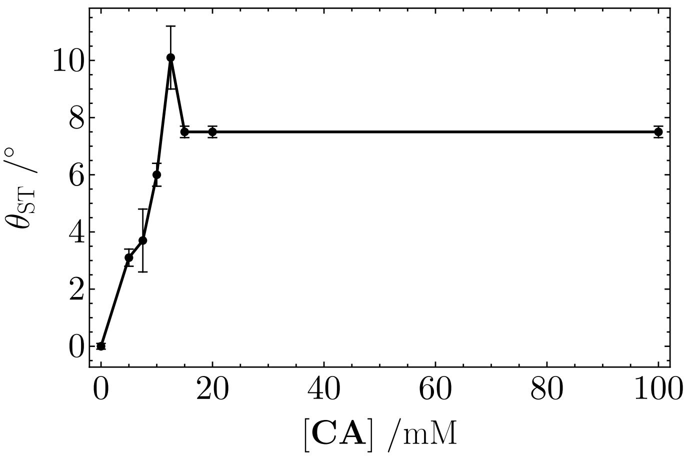

Figure D.1: Singlet-triplet mixing angle θ_{ST} for solutions of 20 mM of **FPA**, and varying concentrations of **CA** in $CDCl_3$ at 14.1 T and 298 K. The data points correspond to the DQF spectra shown in Figure 5.4(a-h).

Table D.1: Pulse sequence parameters used to obtain the double-quantum filtered spectra shown in Figure 5.4. The GeoDQ pulse sequence parameters were optimised at a field of 14.1 T. The concentration of **FPA** is fixed to 20 mM, whereas the concentration of **CA** varies. T_{DQ} is the total double-quantum excitation time. The sequence was implemented as described in Figure 4.4.

[**CA**]/mM	τ_1 /ms	n	T_{DQ}/ms
0	–	–	–
5	3.45	26	179.4
7.5	3.45	22	151.8
10	3.45	14	96.6
12.5	3.45	8	55.2
15	3.45	12	82.8
20	3.45	12	82.8
100	3.45	12	82.8

Table D.2: Pulse sequence parameters used to obtain the singlet filtered spectra shown in Figure 5.6. The M2S-S2M pulse sequence parameters were optimised at a field of 14.1 T. The concentration of **FPA** is fixed to 20 mM, whereas the concentration of **CA** varies. T_{SO} is the total singlet order excitation time. The sequence was implemented as described in Figures 2.5, and 2.6.

[**CA**]/mM	τ_J /ms	n_2	T_{SO}/ms
0	–	–	–
5	1.74	32	85.3
7.5	1.71	28	73.5
10	1.73	16	43.3
12.5	1.73	10	27.7
15	1.74	12	33.1
20	1.74	12	33.1
100	1.74	12	33.1

Table D.3: Variation of the T_1 and T_S relaxation lifetimes as a function of the concentration of **CA**. The values were measured at a field of 14.1 T. The concentration of **FPA** is fixed to 20 mM, whereas the concentration of **CA** varies.

[**CA**]/mM	T_1 /ms	T_S /ms	T_S/T_1
0	940 ± 10	–	–
5	478 ± 10	883 ± 20	1.9
7.5	348 ± 10	736 ± 60	2.1
10	317 ± 10	666 ± 20	2.1
12.5	182 ± 10	288 ± 20	1.6
15	500 ± 10	1304 ± 20	2.6
20	480 ± 10	1006 ± 20	2.1
100	481 ± 10	1013 ± 20	2.1

D.4 Magnification of the Outer Singlet-Triplet Transitions

The M2S, and PulsePol pulse sequences operate differently, which can be observed in Figure D.2. The M2S sequence induces transitions between both outer-singlet triplet states (Figure D.2(b)), while in PulsePol the choice of symmetry number influences which transition is induced (Figure D.2(c-d)). As a consequence, either both AB outer peaks are magnified, like in the M2S case, or one of the two, like in the PulsePol case.

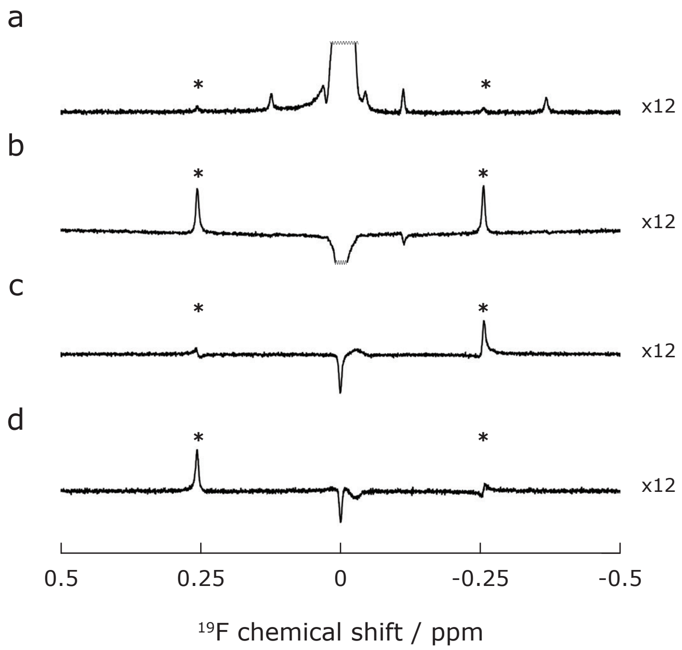

Figure D.2: ^{19}F spectra of a solution of of 20 mM of **FPA** and 100 mM of **CA**, showing various methods to magnify the outer singlet-triplet transitions. Each spectrum was acquired at 14.1 T, 298 K, and averaged over 32 transients. ^{1}H decoupling was not used. The frequency axis is centred around -77.086 ppm. The vertical scales are given. The asterisks indicate the position of the AB outer peaks. (**a**) A 90° pulse-acquire spectrum. (**b**) Spectrum obtained after applying the first J-synchronised CPMG-based echo-train of the M2S pulse sequence: $\{90^{\circ}_{y} - [\tau_J - 180^{\circ}_{y} - \tau_J]_{n_2}\}$ (see Figure 2.6(a)). Transitions are induced between both outer singlet-triplet states. (**c**) Spectrum obtained after applying the following pulse sequence, in its riffled implementation: $\{90^{\circ}_{y} - R4^{1}_{3}\}$ (see Figure 2.12). Transitions are induced between one outer singlet-triplet state. (**d**) Spectrum obtained after applying the following pulse sequence, in its riffled implementation: $\{90^{\circ}_{y} - R4^{-1}_{3}\}$ (see Figure 2.12). Transitions are induced between the other outer singlet-triplet state.